THE UNIVERSITY OF ASTON IN BIRMINGHAM

PROTON INDUCED X-RAY ANALYSIS

Thesis Submitted for the Degree of

DOCTOR OF PHILOSOPHY

by

MD. RASHIDUZZAMAN KHAN

December 1975

Department of Physics

SUMMARY

Proton induced thick target X-ray yields have been measured from the elements Ti, V, Fe, Ni, Cu, Zn, Mo, Ag, Cd, In and Sn for the K shell, and from In, Sn, Nd, Dy, Pt and Au for the L shell X-rays in the energy region 1 - 3 MeV. K shell ionization cross-sections and L shell production cross-sections have been derived from the respective yields. The K shell ionization cross-sections have been compared with the results of other workers and the predictions of the Binary Encounter Approximation (BEA), Constrained Binary Encounter Approximation (CBEA), Plane Wave Born Approximation (PWBA) and PWBA with different modifications.

The Lα, Lβ, Lγ and total L X-ray production cross-sections and $\sigma_{L\alpha}/\sigma_{L\ell}$, $\sigma_{L\alpha}/\sigma_{L\beta}$ and $\sigma_{L\alpha}/\sigma_{L\gamma}$ ratios for the elements Au, Pt, Dy and Nd and the total L X-ray production cross-sections for In and Sn have been calculated. These have been compared with the results of other workers and the predictions of PWBA and CBEA. Thin target measurements have been made to check the ratios obtained from the thick targets.

Exploratory analysis has been performed and equations useful to the multielemental thin target analysis have been proposed.

ACKNOWLEDGEMENTS

I am very much indebted to my supervisor, Dr. D. Crumpton, for his continued guidance throughout the research project and I thank Professor S. E. Hunt, Head of the Department of Physics, for his interest in the work. I gratefully acknowledge Dr. P. E. Francois for his interest in the project and for many useful discussions.

I am very grateful to Mr. M. Stillman and Mr. A. Hopkins for their assistance.

Thanks are also due to the Physics Workshop Staff and the technical and academic staff in the Radiation Centre, Birmingham.

I acknowledge the Commonwealth Scholarship Commission, U.K., for the award of a Scholarship and the University of Dacca for granting me study leave for the period. Thanks are also due to the University of Aston for the award of a studentship for one term.

I am very grateful to Mrs. Harris for typing the thesis.

Finally, I wish to thank my wife Lila for her patience and understanding and my son Upal for being a source of pleasure through the period.

TABLE OF CONTENTS

CHAPTER I

Introduction

INTRODUCTION

Studies of inner-shell ionization cross-sections by protons and other light ions have received considerable attention in the past few years for the following reasons.

Firstly, such studies help in the understanding of the phenomena of interactions between the incident charged particle and the inner shell electrons in the presence of the nuclear coulomb field. The measured cross-sections may be used to test the assumptions involved in the different theories. Discrepancies between the predictions of a given theory and these cross-sections very often prompt modifications to the theories. The measured data also provide a basis for the comparison between theories.

Secondly, due to the development of high resolution Si(Li) X-ray detecting systems, proton induced X-ray analysis is being increasingly employed for simultaneous multielemental analysis requiring very high sensitivities.

Early experimental works and theoretical developments have been summarized by Merzbacher and Lewis (MerE58), who formulated the non-relativistic Plane Wave Born Approximation (PWBA) in great detail. This theory predicts a universal function which was found to be in qualitative agreement with the limited experimental data available.

Basbas et.al (BasG73) on the basis of more accurate data from K shell measurement on low Z elements with protons and other light ions, tested the universal function predicted by non-relativistic PWBA for quantitative agreement and found that the universal function over-esimated the cross-section substantially, particularly at low energies. They proposed corrections to the non-relativistic PWBA on the following

basis, (1) that the binding energy of the inner shell electron increases at the time of interaction, (2) that the incident particle deviates from its straight path in the nuclear coulomb field. These modifications applied to the PWBA (PWBABC) were found to remove the discrepancy between the theory and the experimental data.

Recent measurements (present, KheN75) of proton induced cross-sections on medium Z elements are however found to suggest that though the application of either of these correction factors produces a good empirical fit to the experimental data, the application of both of the corrections together underestimates the cross-sections.

Garcia et.al (GarJ73) has made an extensive review of the theoretical and experimental development on inner shell ionization induced by heavy charged particles. In particular, the Binary Encounter Approximation (BEA) theory was dealt with in great detail. Hansen (HanJ73) modified the BEA theory and reformulated it. In the case of L shell ionizations 2s non-relativistic hydrogenic wave functions were employed, whereas BEA uses 1s non-relativistic wave functions for the description of L shell ionizations.

It should be noted, however, that the theories discussed so far are non-relativistic in the sense that the motions of the inner shell electrons are described by the non-relativistic hydrogenic wave functions. When the binding energy of the electron exceeds 10 keV the need for relativistic description of the motion of electron may arise. The preliminary calculations of Hansen (HanJ73) and Choi (ChoB71) show that for medium and heavy elements relativistic correction increase the cross-sections significantly.

Most of the measurements on the inner shell ionization have been made for the K shells. Coupled to this, the relatively simpler structure of the K shell spectrum and simpler wave functions, have made

K shell ionization phenomena more clearly understood than the L shell ionization . The disagreement between the theories, in the energy region 1 - 3 MeV are within a factor of 2. Although the uncertainties quoted in recent measurements are typically less than 10% the disagreement between authors is sometimes as high as 60% which does not allow discrimination between theories on the basis of all available experimental data.

On the other hand, the measurements on the L shell ionization cross-sections are relatively sparse and limited mainly to high Z elements. Due to the complexity in the L shell spectrum and the close spacing of the energies of most of the transitions, the present day Si(Li) detector has proved to be inadequate for the study of most of the important individual transitions. For these reasons most of the workers have studied total L X-ray cross-sections and other gross-features, namely, Lα, Lβ and Lγ cross-sections, and finer details of the subshell ionization cross-sections have been rather obscured. Recently, authors have used complex mathematical techniques to separate the semiresolved transitions in L X-ray spectra and derived subshell ionization cross-sections. These results support the PWBA and CBEA prediction of the presence of a structure in σ_{LI} cross-sections. These subshell cross-sections agree only qualitatively with PWBA predictions. The experimental data disagrees with the shape and the extent of the structure predicted by CBEA. In general the energy dependence of the measured cross-section data does not agree with the prediction of CBEA. Theoretical developments on L shell ionization processes include binding energy and coulomb deflection corrections applied to PWBA (BraW74) and relativistic corrections applicable to all non-relativistic theories. Clearer understanding of the L shell phenomena requires more detailed experimental measurements which demand, among other things, the development of detectors of much

better resolution.

A compilation of K shell ionization cross-sections has been reported by Rutledge and Watson (RutC73). Lists of proton induced X-ray measurements on K and L shells have been compiled by the present author and are presented in Appendix 1 and Appendix 2 respectively.

The recent trend in cross-section measurements is to use thin targets on the basis that they allow more accurate determination of the cross-sections. These measurements are difficult to perform, and require more sophistication in the instrumentation. The potential for thick target measurements for the accurate determination of cross-sections for medium Z elements in the energy region 1 - 3 MeV was neglected. Thick targets were used in the present measurements because of the simplicity in the measuring technique and on the assumption that such measurement would produce cross-section data comparable to thin target data in terms of accuracy and consistency. The energy region was chosen due to the importance of cross-section data in this region for practical analysis.

Johansson et.al (JohT70) were the first people to show the tremendous potential that proton induced X-ray analysis possess as a method for multielemental trace analysis.

Comparisons of the analytical capabilities of proton induced X-ray analysis were made with the other competitive techniques (α-particle induced X-ray analysis, X-ray fluorescence analysis, electron microprobe analysis, neutron activation analysis, etc.) by Duggan et.al (DugJ71), Folkmann et.al (FolF74a), Cooper et.al (CooJ71), Perry and Brady (PerS73) and other workers.

Limitations imposed by different facets of proton induced X-ray analysis were studied by Verba et.al (VerJ71) and improvements were suggested by them.

R. K. Jolly (JolR71) described a method for preparing uniform thin

target samples from tissues and other biological and pathological samples. An array of commercially available plastic materials Kapton, Mylar, Millipore, Nuclepore, Formvar, etc. used as a backing, are found to have one or more problems associated with them. Problems with the backing materials, sample preparation and data analysis are also discussed with the scores of practical analysis reported (JohT70, JohT72, ManN74, GorB71, FloR72, WalR74, ValV74, ThoJ74, BarB74, DecD75).

At present the limiting factors in any analysis seem to be the problems with the backing material in terms of purity, conductivity and strength of the material, detector resolution and sample preparation from non-evaporable material and background associated with the measurements.

With the growing worldwide concern about pollution and the need for accurate determination of trace elements in biological, pathological and other samples, demand for quick and efficient routine analysis is continually increasing. Due to the availability of a few hundred small accelerators throughout the world, small on-line computers and continuous improvement in the detecting system, proton induced X-ray analysis is proving to be a major analytical technique. In the present work empirical equations based on experimental data, for the calculation of cross-sections at 1.0, 1.5, 2.0, 2.5 and 3.0 MeV, for different elements, have been proposed which may be very useful in multielemental thin target analysis.

Practical analysis, in the present study, however, was of exploratory nature. The aim of this analysis was to gain some first hand experience in the technique.

CHAPTER II

Origin of X-rays

2.1 ELECTRONIC STRUCTURE OF AN ATOM

An atom consists of a central positive nucleus encircled by a number of shells populated by negative electrons.

The Schrödinger equation:

$$\nabla^2\psi + \frac{2m}{\hbar^2}(E - V)\ \psi = 0 \qquad 2.1.1$$

describes quantum mechanically the motion of an electron in hydrogen and hydrogen-like atoms. The solution of equation 2.1.1 in polar coordinates r, θ and ϕ yields three quantum numbers n, ℓ and m_ℓ, known respectively as total, angular and magnetic quantum numbers. Quantum mechanical considerations allow the quantum numbers to assume values:

$$\begin{aligned} n &= 1, 2, 3, \ldots \\ \ell &= 0, 1, 2, \ldots\ n - 1 \\ m_\ell &= 0, \pm1, \pm2, \ldots. \pm(n - 1) \end{aligned} \qquad 2.1.2$$

These three quantum numbers along with the spin quantum number of the electrons determine the state of an electron in the atom. The number of electrons in a shell or subshell can be determined from the Pauli exclusion principle viz: 'No two electrons can have the same set of quantum numbers'. Accordingly, the maximum number of electrons in a subshell is $2(2\ell+1)$. Adding over all subshells the total number of electrons in a given shell is:

$$\sum_{\ell=0}^{n-1} 2(2\ell+1) = 2n^2 \qquad 2.1.3$$

The transition of electrons between different quantum states is guided jointly by selection rules and the Pauli exclusion principle. The selection rules for different quantum numbers are:

$$\Delta \ell = \pm 1$$

$$\Delta m_{\ell} = 0, \pm 1 \qquad 2.1.4$$

and Δn has no restriction. A schematic diagram of the shells and subshells of an atom together with possible transitions with their conventional nomenclature is shown in figure 2.1.1.

2.2 ELECTRON TRANSITIONS AND APPEARANCE OF X-RAYS

When radiation passes through matter there is an appreciable probability that it will interact with an atomic electron causing its ejection from the atom. There are three ways by which the vacancy thus produced can be filled and the ejected electron can dissipate its energy.

1) Fluorescence : The vacancy may be filled by an electron from an outer shell with higher energy. A photon may be emitted with an energy:

$$h\nu = E_{final} - E_{initial} \qquad 2.2.1$$

where E_{final} and $E_{initial}$ are respectively the energies of final and initial states of the electron. The X-ray photons thus emitted are characteristic of the elements and the shells or subshells between which the transitions take place.

2) Auger effect : The X-ray photon produced in fluorescence possess sufficient energy to excite an electron from a higher shell of the same atom. If it does so the photon disappears and the electron emerges with energy E_A given by:

$$E_A = h\nu - E_B \qquad 2.2.2$$

where E_B is the binding energy of the electron. Clearly no Auger

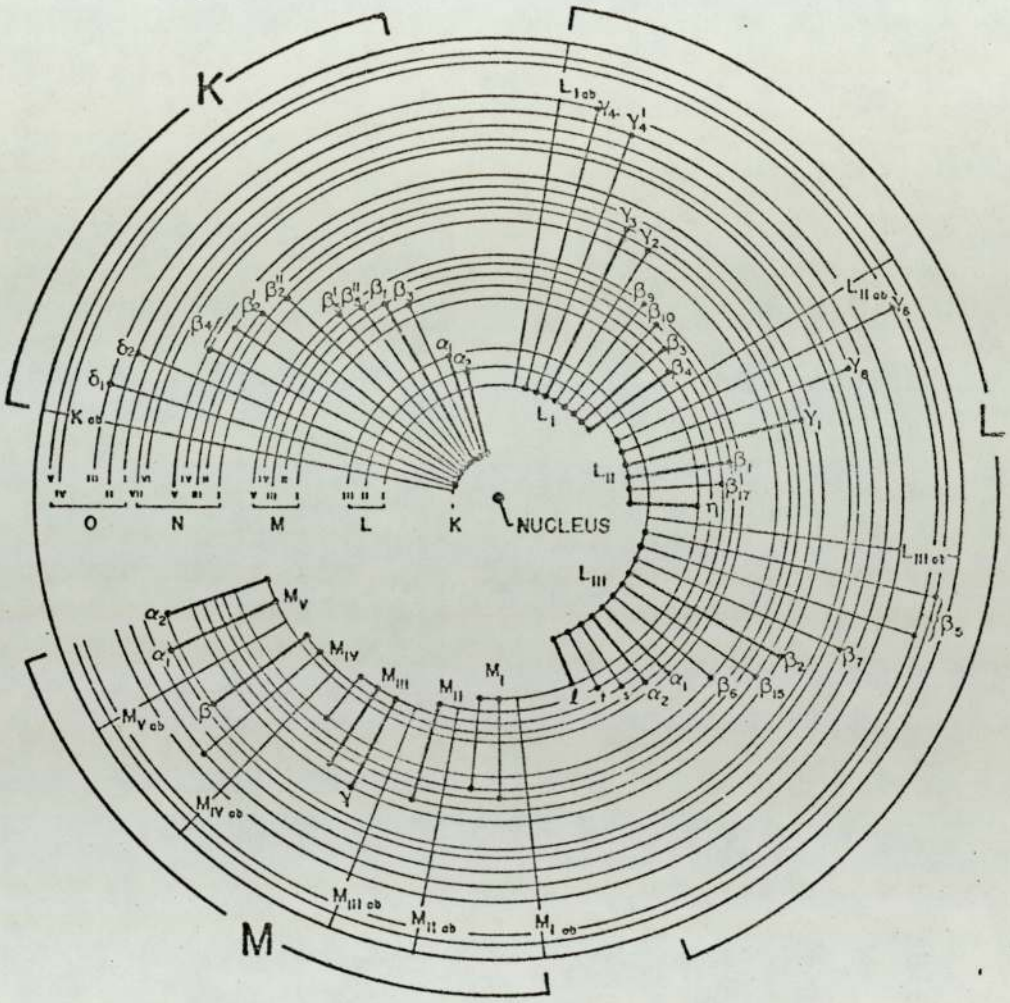

Figure 2.1.1. Atomic model, showing electron transitions that may follow electron vacancies. Transitions are labeled with conventional notation for associated emission lines.

electron can be produced from the K shell. The innermost shell from which the Auger electrons may be produced is L shell.

From the figure 2.2.1 it is clear that the X-ray photon emitted from K shell is lost in the process producing an L Auger electron. Thus two vacancies are left in the L shell which may be filled by electrons from M or any of the higher shells. The Auger electron thus produced, if sufficiently energetic, may initiate vacancies in the higher shells or may dissipate its energy in the atomic lattice.

3) Coster-Kronig transitions : There may be transitions between the subshells of the same shell due to the difference in their angular momentum quantum numbers. By the process a vacancy may move to a higher subshell before the vacancy is filled by intershell transition. These transitions are known as Coster-Kronig transitions. The net effect of such a transition is the change in the primary vacancy distribution in the subshell of a shell of an atom.

The fluorescence yield of an atomic shell or subshell is defined as the probability that a vacancy in that shell or subshell is filled in through the radiative transition. The total width Γ of an excited state in an atom with a vacancy is related to the mean life time τ by:

$$\Gamma = h/\tau \qquad 2.2.3$$

and if we define the total width as the sum of

$$\Gamma = \Gamma_R \text{ (Radiative width)} + \Gamma_A \text{ (Auger width or non-radiative width)} + \Gamma_{CK} \text{ (Coster-Kronig width)}$$

The fluorescence yield

$$\omega = \frac{\Gamma_R}{\Gamma} \qquad 2.2.4$$

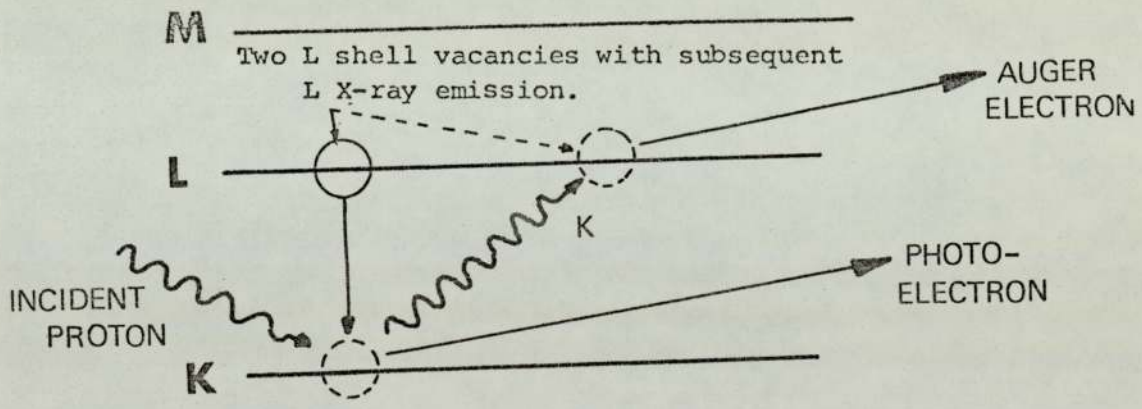

Figure 2.2.1

Production of Auger Electron.

In the case of vacancies in a set of large numbers of atoms the fluorescence yield of a shell is equal to the ratio of the vacancies filled in that particular shell by the emission of characteristic X-rays to that of the primary vacancies originally existing in that particular shell. For the K shell, normally containing two $S_{\frac{1}{2}}$ electrons, the fluorescence yield is:

$$\omega_K = I_K/n_K \qquad 2.2.5$$

where

I_K = Total number of characteristic K X-ray photons emitted from the sample.

n_K = Total number of primary K shell vacancy.

for L shells and higher the definition is not so straightforward for the following reasons:

(1) These shells consist of subshells in which the electrons have different angular momentum quantum numbers. The average fluorescence yield thus depends on the mode of ionization of these shells because different ionization methods produce different sets of primary vacancies.

(2) Due to the Coster-Kronig transitions the primary vacancy distribution is very often changed before they are filled.

Let us define the fluorescence yield of i^{th} subshell of a shell X (X = L, M ...) by ω_i^x, then

$$\omega_i^x = \frac{I_i^x}{n_i^x} \qquad 2.2.6$$

where I_i^x is the number of X-rays emitted from that subshell and n_i^x is the number of vacancies that existed there. The average fluorescence yield, $\bar{\omega}_x$ of the shell X is given by

$$\bar{\omega}_x = \sum_{i=1}^{k} N_i^x \, \omega_i^x \qquad 2.2.7$$

where N_i^x is the relative number of primary vacancies in i^{th} subshell of the shell X, where

$$N_i^x = \frac{n_i^x}{\sum_i^k n_i^x} \quad \text{and} \quad \sum_{i=1}^{k} N_i^x = 1 \qquad 2.2.8$$

The summation $\sum_{i=1}^{k}$ extends over all the k subshells of the shell X.

If we define the total number of vacancies in all the subshells of the shell X by n_x i.e.

$$n_x = \sum_{i=1}^{k} n_i^x \qquad 2.2.9$$

then the average fluorescent yield of the X shell is

$$\bar{\omega}_x = I_x / n_x \qquad 2.2.10$$

where I_x = Total number of X-ray photons emitted from all the subshells of the shell X.

For this definition of $\bar{\omega}_x$ to be valid, the primary vacancy distribution among the subshells must not alter before all the vacancies are filled. But the presence of Coster-Kronig transition violates this definition and makes the situation complex.

Since the average fluorescent yield depends on the primary vacancy distribution, hence on the mode of ionization, fluorescent yield is not strictly an intrinsic property of the atom.

Two alternative approaches are taken to incorporate the effect of Coster-Kronig transition in the definition of $\bar{\omega}_x$.

(1) $\bar{\omega}_x$ may be considered as a linear combination of subshell yields ω_i^x with a new vacancy distribution V_i^x in the i^{th} subshell taking into

account the vacancies shifted to each subshell by Coster-Kronig transition and is given by

$$\bar{\omega}_x = \sum_{i=1}^{k} V_i^x \omega_i^x \qquad 2.2.11$$

The probability of Coster-Kronig transitions for shifting a vacancy from the subshell X_i to a higher subshell X_j is denoted by f_{ij}^x, hence the quantity V_i^x can be related to N_i^x of primary vacancy as

$$\begin{aligned} V_1^x &= N_1^x \\ V_2^x &= N_2^x + f_{12}^x N_1^x \\ V_3^x &= N_3^x + f_{23}^x N_2^x + (f_{13}^x + f_{12}^x f_{23}^x) N_1^x \end{aligned} \qquad 2.2.12$$

2) The alternative approach is to express the average fluorescence yield as

$$\bar{\omega}_x = \sum_{i=1}^{k} N_i^x v_i^x$$

where v_i^x is the total number of characteristic X-rays resulting per primary vacancy in the X_i subshell. The relations between v_i^x and ω_i^x are quite involved and are given by Bambynek et. al (BamW72).

However for L subshell

$$\begin{aligned} \nu_I &= \omega_1 + f_{12} \omega_2 + (f_{13} + f_{12} f_{23}) \omega_3 \\ \nu_{II} &= \omega_2 + f_{23} \omega_3 \\ \nu_{III} &= \omega_3 \end{aligned} \qquad 2.2.14$$

And the relation between the average L shell X-ray production σ_{LX} and ionization cross-section σ_L, and with the subshell ionization cross-section σ_{LI}, σ_{LII} and σ_{LIII} are given by

$$\sigma_{LX} = \bar{\omega}_L \, \sigma_L \qquad \text{and} \qquad 2.2.15$$

$$\sigma_{LX} = \nu_I \, \sigma_{LI} + \nu_{II} \, \sigma_{LII} + \nu_{III} \, \sigma_{LIII} \qquad 2.2.16$$

CHAPTER III

Interaction of heavy charged particles with matter.

3.1 PASSAGE OF CHARGED PARTICLES THROUGH MATTER

An energetic charged particle passing through matter loses its energy mainly through its interaction with the atomic electrons. These interactions produce excitation and ionization. A vacancy in a shell or subshell of such an ionized atom is filled either by radiative (X-ray emission) or non-radiative (Auger or Coster-Kronig) decay.

The maximum energy that can be transferred by an ionizing particle of mass M and energy E to a free electron of mass m is

$$E_{max} = \frac{4mM}{(M+m)^2} E \qquad 3.1.1$$

for heavy charged particles this reduces to

$$E_{max} = \frac{4m}{M} E \qquad 3.1.2$$

The energetic electrons thus emitted (delta rays) may produce secondary ionizations.

If the loss of energy of the incident particle in an encounter is very small compared with its own energy the process is assumed elastic and the deviation of the particle from its straight path is considered negligible. The particle thus carries on losing its energy in successive encounters until it no longer possesses sufficient energy for further ionization, and reverts to a neutral atom. The distance traversed by the particle is known as range. The probability of losing energy through nuclear reactions and inelastic processes leading to inner shell ionization is negligible compared to the energy loss by elastic and near elastic collisions.

An encounter between the projectile and the nucleus may produce a sudden acceleration to the particle, and the particle may lose energy giving out bremsstrahlung radiation. Due to the importance of

bremsstrahlung radiation to the present measurements the process will be discussed in some detail in the next section.

Another form of radiation loss is through Cerenkov radiation, which appears from longitudinal polarization of a transparent medium when a charged particle moves in it with a velocity higher than the phase velocity of light in the medium.

On the basis of quantum mechanics Bethe and Bloch derived a formula for 'specific energy loss' which is the energy loss per unit distance. The formula in SI unit is given by:

$$-\frac{dE}{dx} = \frac{e^4}{4\pi\varepsilon_o^2}\ \frac{Z_1^2}{mv^2}\ NZ_2\ \log\ \frac{2mv^2}{I}\ \text{Joules/m} \qquad 3.1.3$$

where v and Z_1 are respectively the velocity and atomic number of the projectile, Z_2, I and N respectively are the atomic number, mean ionization potential and number of atoms/m^3 of the target material. Using the Thomas-Fermi distribution function for electrons in the atom I can approximately be related to the atomic number through the following relation

$$I \simeq kZ_2 \quad \text{where} \qquad 3.1.4$$

$$k \simeq 11.5 \text{ ev.}$$

The formula 3.1.3 can be extended to take care of the relativistic velocity of the particle as follows:

$$-\frac{dE}{dx} = \frac{e^4}{4\pi\varepsilon_o^2}\ \frac{Z_1^2}{mv^2}\ NZ_2\ \left[\log\ \frac{2mv^2}{I} - \log\ (1-\beta^2) - \beta^2\right] \text{Joules/m} \qquad 3.1.5$$

where $\beta = \frac{v}{c}$

c being the velocity of light.

The formula 3.1.3 obviously breaks down when the log term

$$\frac{2mv^2}{I} < 1$$

$$\text{or } \frac{4mE}{MI} < 1 \text{ or } E < 450\ I \qquad 3.1.6$$

The log term is also found to be a very slowly varying function of the incident energy. In non-relativistic cases, for a particular medium, to a good approximation

$$\frac{dE}{dx} \alpha \frac{Z_1^2}{v^2} \qquad 3.1.7$$

An empirically modified formula is given by Williamson et al. (WilC67) and the tabulation of $\frac{dE}{dx}$ and ranges are reported by Williamson et al. (WilC67), Janni (JanJ66) and Northcliffe et al. (NorL70).

3.2 BREMSSTRAHLUNG RADIATION PRODUCED BY HEAVY CHARGED PARTICLES

A heavy charged particle can produce bremsstrahlung while passing through matter, directly, when accelerated in the coulomb field of the nucleus or indirectly, by the secondary electrons produced by ionization.

Experimentally one finds that the bremsstrahlung intensity is very high at lower energy and decreases rapidly as the energy of the radiation approaches E_{max}, the maximum energy the projectile may transfer to a free electron. The radiations produced at the lower end of the bremsstrahlung spectrum is mainly the contribution of the secondary electrons whereas their contribution is zero at radiation energies greater than E_{max}.

Higher energy bremsstrahlung radiation is produced when the projectile experiences large acceleration in a close encounter with the nucleus. The differential cross-sections for the production of

bremsstrahlung photons of energy E_r by a projectile (A_1, Z_1, E_1) on a target (A_2, Z_2) is given by Alder et.al (AldK56).

$$\frac{d\sigma_r^B}{dE_r} = C \frac{A_1 Z_1^2 Z_2^2}{E_1 E_r} \left[\left(\frac{Z_1}{A_1} - \frac{Z_2}{A_2} \right) + \text{higher multipolarities} \right] \qquad 3.2.1$$

The term $\left(\frac{Z_1}{A_1} - \frac{Z_2}{A_2} \right)$ arises from the interference between the radiation of the projectile and the recoiling nucleus and implies that one can make the electric dipole bremsstrahlung vanish by a suitable $\left(\frac{A_1}{Z_1} = \frac{A_2}{Z_2} \right)$ projectile target combination . In those cases higher multipolarities become important but they are of much lesser intensity (FolF74).

Folkmann et.al (FolF74) calculated the production of bremsstrahlung by indirect process in two steps. They used the binary encounter approximation to calculate the probability that a projectile with energy E_1 will produce an electron of energy E_δ in the range E_e and $E_e + dE_e$. They also calculated the cross section that an electron with energy E_δ will produce a photon of energy between E_r and $E_r + dE_r$. Combining them and integrating over all possible energy exchanges they found that such a cross-section is proportional to E_1^4 and decreases as E_r^{-8}. Which shows that the probability for the production of high energy photon by indirect processes is negligible, whereas from the equation 3.2.1, we find that the probability for the direct production of bremsstrahlung radiation varies as E^{-1} and E_r^{-1}, making the distribution of higher energy radiation along the energy spectrum very flat. The graph, Fig.3.2.1 of ref.(FolF74) illustrates these points.They also found that for all practical purposes, emission of bremsstrahlung photons is isotropic.

So in choosing the projectile energy for a heavy charged

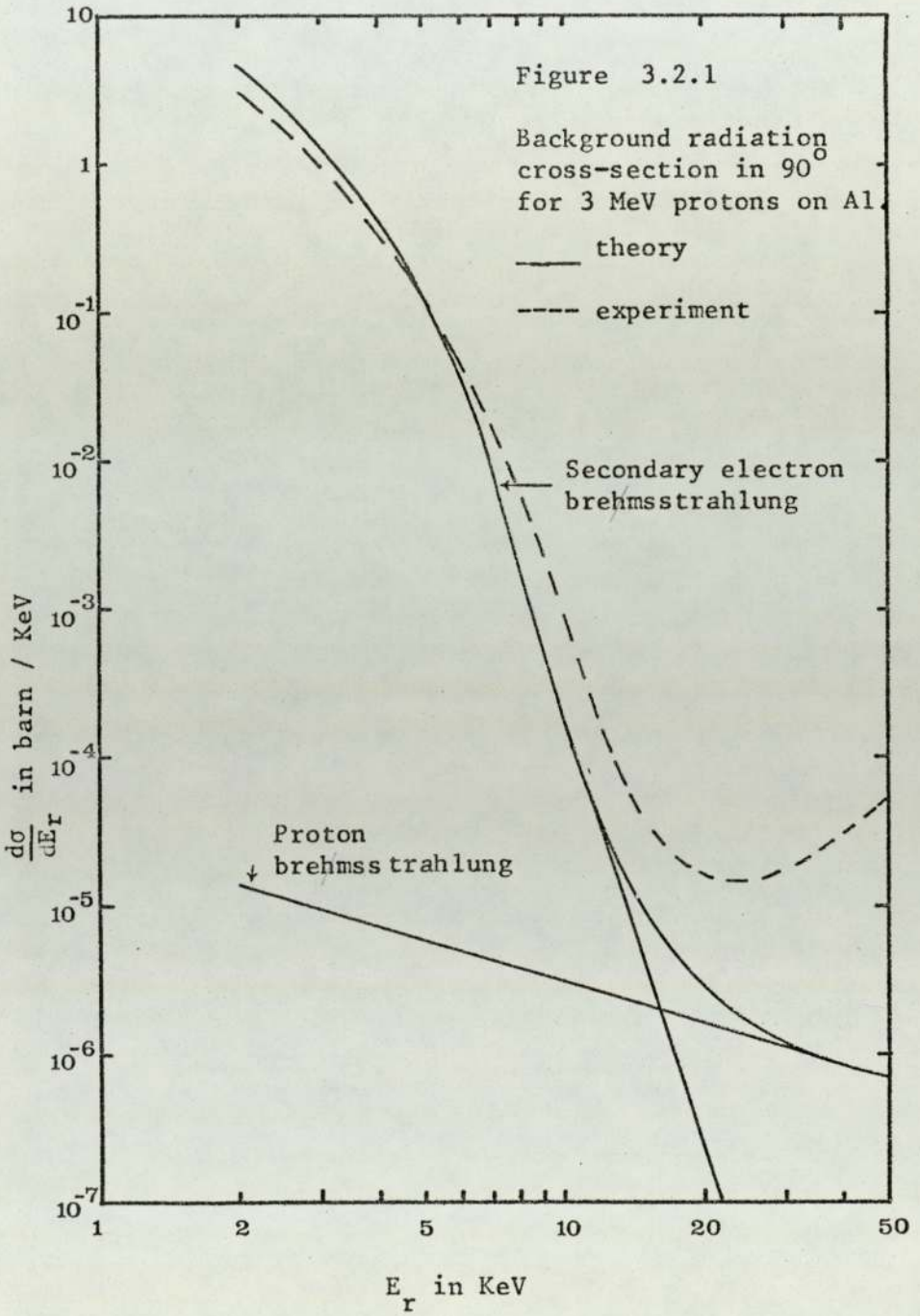
Figure 3.2.1
Background radiation cross-section in 90° for 3 MeV protons on Al.
theory
experiment
Secondary electron brehmsstrahlung
Proton brehmsstrahlung
$\frac{d\sigma}{dE_r}$ in barn / KeV
E_r in KeV
10
1
10^{-1}
10^{-2}
10^{-3}
10^{-4}
10^{-5}
10^{-6}
10^{-7}
1
2
5
10
20
50

particle induced X-ray analysis one has to take care that the energy, E_x, of the excited X-ray line is greater than E_{max} to avoid large bremsstrahlung background from secondary electrons.

3.3 PRODUCTION OF INNER SHELL IONIZATION BY HEAVY CHARGED PARTICLES

The inelastic collision between the charged particle and the electron may produce inner-shell ionization of the atom. The threshold energy E_{th} in eV for such an ionization is expressed in terms of a dimensionless parameter $\eta_s = 10^{-3}$ Madison et.al (MadD74).

where $\eta_s = \frac{m E_{th}}{M Z_s^2 R_\alpha}$ and Z_s = the effective atomic number of the s shell and R_α = 13.6 eV.

Basically, three different theoretical approaches have been developed to describe the inner shell ionization by charged particles.

The Plane Wave Born Approximation describes both the projectile and the atom quantum mechanically, and the projectile is depicted as a plane wave.

Whereas in Binary Encounter Approximation a classical collision is assumed to occur between the projectile and the electron, the rest of the target atom takes no part in the interaction other than providing the necessary binding energy, which determines the velocity distribution of the electrons.

In the semiclassical concept the relative motion of the projectile target system is described classically whereas the electron is accorded full quantum properties. Most attempts to derive a quantitative criteria for the applicability of such a model for collisions has produced limits, that appear to be unnecessarily restrictive, Madison et.al (MadD74).

Common to all the theories mentioned here is the assumption that the collision producing one or more inner-shell vacancies, takes place

in a time short compared to the subsequent decay of the excited atom. The deexcitation may happen through radiative or non-radiative decay. Experimental observation of any of these transitions enables one to test these theories.

3.3.1 PLANE WAVE BORN APPROXIMATION

In the Plane Wave Born Approximation the projectile is represented in its initial and final state by plane waves. The atomic coulomb field acts as a scattering centre. The scattered projectiles leave some of their energy with the atom raising it to its final state f from its initial state i. If an inner shell is ionized in the process, the final state is described as a vacancy in the inner shell of the atom plus an electron emitted with finite energy.

The basic assumptions in PWBA are:

(1) The distortions of the projectile wave functions by the atomic coulomb field are very small and can be considered as a perturbation, and the perturbation exists only when the projectile is in the atomic coulomb field.

(2) The perturbation of the atomic orbit between which transition takes place is neglected and the states of the atomic electrons are considered to be the states of the electrons of an unperturbed atom. Non-relativistic hydrogenic wave functions are used for electronic states and the screening due to other electrons are accounted for only arbitrarily.

The screening of the nuclear charge by other inner shell electrons is thought to reduce the nuclear charge from Z_2 to Z_{2S} where for K-shell

$$Z_{2S} = Z_{2K} = Z_2 - .3$$

and for L shell

$$Z_{2L} = Z_2 - 4.15 \text{ is used.}$$

(3) The projectile acts as a point charge.

To verify the validity of the first assumption Hansen et al (HanH66, HanH64) measured the inner shell ionization of medium to heavy elements by positron and electron impact. If the projectile wave functions were distorted appreciably contrary to this assumption, the cross-sections should differ significantly. Their results agreed within the experimental uncertainties of 10-20% for incident energies .1 - 1.4 MeV.

All of these assumptions are thought to be valid for the production of inner shell ionization by protons from elements with $Z_2 > 10$.

For any inner shell S the ionization cross-section σ_S has been derived by Merzbacher and Lewis (MerE58) in their pioneering work on the quantum mechanical derivation of inner shell ionization by heavy charged particles, and is given by

$$\sigma_S = \frac{8\pi Z_1^2 a_o^2}{Z_{2S}^4 \eta_S} f_S(\eta_S/\theta_S^2) \qquad 3.3.1.1$$

where

$$\theta_S = \frac{E_S S^2}{Z_{2S}^2 R_\alpha} \qquad 3.3.1.2$$

is the screening parameter for the s^{th} shell and a_o is the Bohr radius.

This formula predicts a scaling law in that the cross-section σ_S divided by Z_1^2 is the same for all particles incident on a specific target with the same velocity. The scaling in equation 3.3.1.1. is expected to be obeyed at low impact velocities, i.e. velocity v_1 of the projectile is less than the velocity v_{2S} of the target S shell electron. The cross-section reaches its maximum when $\eta_S/\theta_S^2 \simeq 1$ i.e. when $v_1 \approx v_{2S}$. For K shell the values of the function $f_K(\eta_K/\theta_K^2)$ against η_K for selected values of θ_K have been tabulated by Khandelwal et al (KhaG69).

The same formula 3.3.1.1 has also been used for individual subshells. For i^{th} subshell in L shell the ionization cross-section can be written as

$$\sigma_{Li} = \frac{8\pi Z_1^2 a_o^2}{Z_{2L}^4 \eta_L} f_{Li}\left(\eta_L / \theta_{2Li}^2\right) \qquad 3.3.1.3$$

The total L shell ionization cross-section is the sum of the subshell ionization cross-sections and is given by

$$\sigma_L = \sum_{i=1}^{3} \sigma_{Li} = \frac{8\pi Z_1^2 a_o^2}{Z_{2L}^4 \eta_L} \left(f_{LI} + f_{LII} + f_{LIII}\right) \qquad 3.3.1.4$$

The L subshell ionization cross-sections are related to the total L shell production cross-section σ_{LX}, through the equation 2.2.16. The values of f_{LI} and f_{LII} are tabulated by Choi et al. (Cho B73), f_{LIII} is calculated from f_{LII} for the values of θ_{2LIII}.

For K shell ionization cross-sections, Basbas et al. (BasG73) transformed equation 3.3.1.1 to a more convenient form by separating the target features from the function as

$$\sigma_K^{PWBA}(\eta_K, \theta_K)/(\sigma_{OK}/\theta_K) = f(\eta_K/\theta_K^2)/\eta_K \qquad 3.3.1.5$$

where $$\sigma_{OK} = 8\pi a_{2K}^2 (Z_1/Z_{2K})^2 \qquad 3.3.1.6$$

replacing right hand side of the equation 3.3.1.5 by $F(\eta_K/\theta_K^2)$ and re-writing as

$$\sigma_K^{PWBA}(\eta_K, \theta_K)/(\sigma_{OK}/\theta_K) = F(\eta_K/\theta_K^2) \qquad 3.3.1.7$$

they argued that the PWBA cross-section should predict universality. Replacing

$$\eta_K/\theta_K^2 = y$$

they tabulated the values of F(y) against y. The prediction of univer-

sality based on equation 3.3.1.7 states, 'All cross-sections should follow a universal curve if reduced as prescribed in the left hand side of the equation 3.3.1.7. and plotted versus η_K/θ_K^2.' They tested this prediction by reducing the measured ionization cross-section values according to the specification of equation 3.3.1.7 and plotting them against η_K/θ_K^2. They found that the PWBA prediction was in error both in magnitude and in universality. They attributed these discrepancies to the fact that the PWBA neglects (i) the nuclear coulomb deflection of the particle and (ii) increased binding of the inner shell electron at deeper penetration of the projectile.

At low energies nuclear coulomb deflection inhibits the particle from deeper penetration of the inner shell, thus reducing the probability of inner-shell ionization. Following the semiclassical treatment of Bang and Hansteen (BanJ59), Basbas et al (BasG73) derived the relation between σ_K^{PWBA} and nuclear deflection corrected ionization cross-section σ_K^{PWBAC} as follows:

$$\sigma_K^{PWBAC} = 9\, E_{1O}\,(\pi dq_o)\ \sigma_K^{PWBA} \qquad 3.3.1.8$$

where $\pi dq_o = \tfrac{1}{2}\pi Z_1\ (m/M)\ \theta_K^{-2}\ (\eta_K/\theta_K^2)^{-3/2}$ 3.3.1.9

and $E_{1O}(\pi dq_o)$ is given by the following approximate relation

$$E_{1O}(\pi dq_o) = \frac{e^{-\pi dq_o}}{9+\pi dq_o} \qquad 3.3.1.10$$

At high velocity of the particle the coulomb deflection effect disappears and $9E_{1O}(\pi dq_o) \sim 1$.

At low velocities, particles which penetrate deep into the K shell spend longer time in the K-shell orbit compared to the interaction time of the K-shell electron and the particle. So the electron

experiences a larger binding energy $(Z_{2K} + Z_1)^2\ \theta_K\ R_\alpha$ instead of $Z_{2K}^2\ \theta_K\ R_\alpha$. This increase in binding energy decreases the probability of ionization. This effect is taken into account through the replacement of θ_K by $\varepsilon\theta_K$ in the cross-section equation 3.3.1.7 where

$$\varepsilon = 1 + 2\ (Z_1\ Z_{2K}^{-1}\ \theta_K^{-1})\ g\ (\sqrt{\eta_K}\ /\ \theta_K) \qquad 3.3.1.11$$

The values of $g(\sqrt{\eta_K}\ /\ \theta_K)$ against η_K/θ_K^2 are tabulated by Basbas et.al. (BasG73). This modification relates σ_K^{PWBA}, with binding energy corrected K-shell ionization σ_K^{PWBAB} through the following relation

$$\sigma_K^{PWBAB} = \sigma_K^{PWBA}(\eta_K, \varepsilon\theta_K) = (\sigma_{OK}/\varepsilon\theta_K)\,F\left(\eta_K/(\varepsilon\theta_K)^2\right) \qquad 3.3.1.12$$

and σ_K^{PWBABC} which includes all the corrections becomes

$$\sigma_K^{PWBABC} = 9E_{1O}(\pi dq_o\varepsilon)(\sigma_{OK}/\varepsilon\theta_K)\ F\ (\eta_K/(\varepsilon\theta_K)^2) \qquad 3.3.1.13$$

They (BasG73) have shown that these modifications to PWBA removes an order of magnitude discrepancy between the scaled experimental cross-sections and the prediction of PWBA theory.

3.3.2 BINARY ENCOUNTER APPROXIMATION

The basic assumptions in the binary encounter description of ion atom collisions are

(i) that the incident particle interacts with only one target particle (electron or nucleus) at a time (ii) that the mutual interaction between the nucleus and an atomic electron may be disregarded during a collision. The first assumption is justified only if the effective interaction between the projectile and one of the scattering centres take place in a

region small compared with the atomic dimension. In this case the momentum transfer to one of the atomic particles is large compared with the momentum of the atomic electron. And in such a situation the energy transfer by the particle to the electron is larger than the binding energy of the electron.

In the calculation of cross-section in binary encounter collision, a target system is viewed as a system of free static nuclei and free electrons with the velocity distribution as in the atom. The derivation of cross-section for collision between two structureless free charged particles, by both classical and quantum mechanics produces results identical to the coulomb scattering cross-section in the case of unlike particles. For like particles the difference arises from the interference between direct and exchange terms. Approximations are involved when this cross-section is related to those for charged particle atom collisions.

In Binary Encounter Approximation (BEA) the dominant interaction leading to a transition is direct exchange of energy between the incident particle and the atomic electron. The presence of nucleus modifies the momentum distribution. To calculate the cross-section for collision between an incident particle with momentum $\underline{k}$, with a free electron of momentum $\underline{k_e}$ one has to sum over all momentum exchange compatible with an energy exchange ΔE, which again has to be integrated over all permitted energy exchanges and finally weighted by the distribution of electron momenta associated with the bound state. Since the quantum mechanical cross-section for the collision between two free charged particles is identical with the classical results, all the steps in the above description are calculated classically except the determination of the distribution of initial momenta of the electron in the bound state. Though quantum mechanically one has to add the amplitudes rather than the cross-sections, Vriens (VriL69)

showed that for large momentum transfer only one amplitude is important for an electron in a particular bound state, and sum of the squares of the amplitudes become equal to the square of the sums.

The ionization cross-section for a heavy charged particle has been derived by Gerjouy (GerE66), Garcia et.al (GarJ68),(GarJ70a) and all the derivation and results have been summarized and critically discussed by Garcia et.al (GarJ73). They have shown that the ionization cross-section for any shell or subshell derived on the basis of hydrogenic velocity distribution of electrons was found to obey a scaling law, expressed as $\sigma_s = \frac{Z_1^2}{E_s^2} f\left[E/\lambda E_s, \lambda\right]$ 3.3.2.1

where λ is the mass of the projectile in electron mass units and E_s is the binding energy of the S shell or subshell.

When $\lambda >> 1$ the separate dependence of λ in equation 3.3.2.1 ceases to exist and a plot of $E_s^2 \sigma_s / Z_1^2$ vs $E/\lambda E_s$ should produce a universal curve for all target elements bombarded by heavy charged particles. Numerical values of such a universal function against $E/\lambda E_s$ have been tabulated by Garcia et.al (GarJ73).

The main advantage of BEA theory is that it gives a reasonable estimate of cross-sections for a wide variety of target-projectile combinations in a direct and simple way. In this theory no assumption is needed about the classical orbits of electrons, only knowledge of the velocity distribution of the target electrons is required. No assumptions are made for the position of target electrons. The BEA theory gives the most exact description of the close collisions.

The main argument against the BEA theory is that the distant collisions are not described adequately by them.

3.3.3 CONSTRAINED BINARY ENCOUNTER APPROXIMATION

Hansen (HanJ73) transformed the BEA description from momentum space to configuration space. In doing so firstly he formulated in configuration space a model for the interaction of a bound electron and a projectile of fixed trajectory with respect to a nucleus. Secondly he proposed a modification to BEA to account for the discrepancies which arise due to the differences between the real system of a complex atom and particle and the theoretical system of hydrogenlike atom and incident particle. This version of BEA, known as CBEA (Constrained Binary Encounter Approximation), predicts cross-sections which are lower in general than those of the BEA theory.

Whereas the general BEA predictions for higher shell and subshells are derived on the basis of classical momentum distributions of 1s state, the similar predictions of CBEA uses the momentum distribution of the individual shells and subshells. He also presented the tables for the CBEA cross-section calculations.

CHAPTER IV

Instrumentation

4. EXPERIMENTAL ARRANGEMENTS

The instruments used in the present measurement, their relevant characteristics along with their place in the entire set up will be discussed in this chapter. The measured performance characteristics will be reported at the end of this chapter under the heading 'System performance'.

The experimental arrangement is shown in (Fig.4.1) and can be broadly divided in four parts:

1) Dynamitron; providing the proton beam
2) Target chamber, housing the targets and acting as a Faraday Cage for charge collection.
3) Keithley Electrometer and Voltage to Frequency converter for charge integration.
4) Kevex X-ray Detector System with Hewlett Packard Nuclear Data Acquisition System and Computer System for the detection and processing of the X-ray signals.

4.1 DYNAMITRON AT THE JOINT RADIATION CENTRE, BIRMINGHAM.

The Dynamitron at the Joint Radiation Centre, Birmingham, was used to provide beams of energetic protons.

The Dynamitron is a variable energy high current accelerator. The DC potential is built up at the high voltage terminal by the rectification of radiofrequency across 64 rectifiers. A 130 KHz RF oscillator supplies the power which is fed to two semicircular plates inside the pressure vessel. The semicircular plates are capacitively coupled to semicircular rings in the acceleration column. (Fig.4.1.1) The rectifier tubes separate these rings thus making a chain from the bottom to the top. The terminal voltage can be varied between 1 - 3 MeV.

In the positive mode H_1^+, H_2^+, H_3^+ ions are produced in a duoplas-

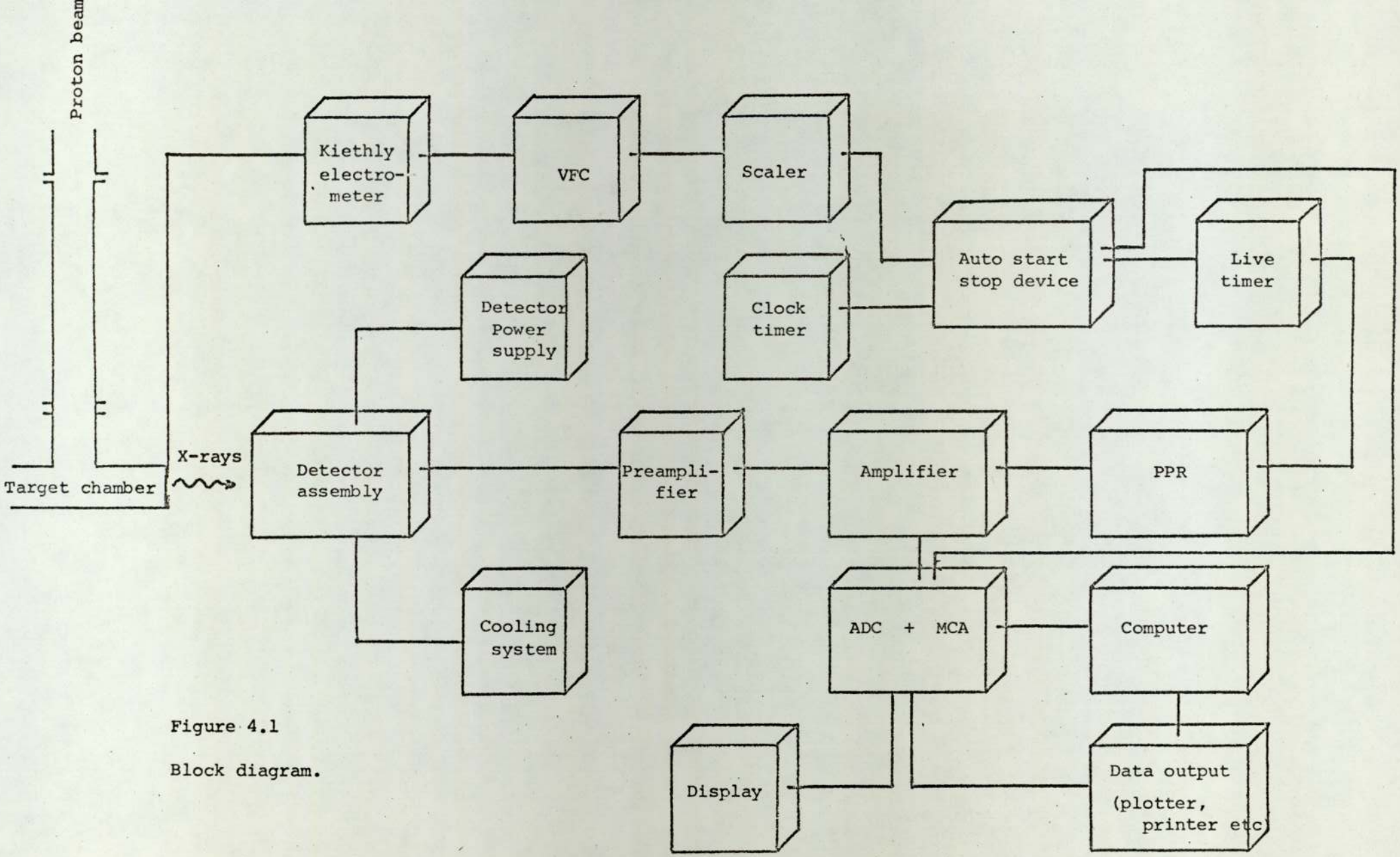

Figure 4.1

Block diagram.

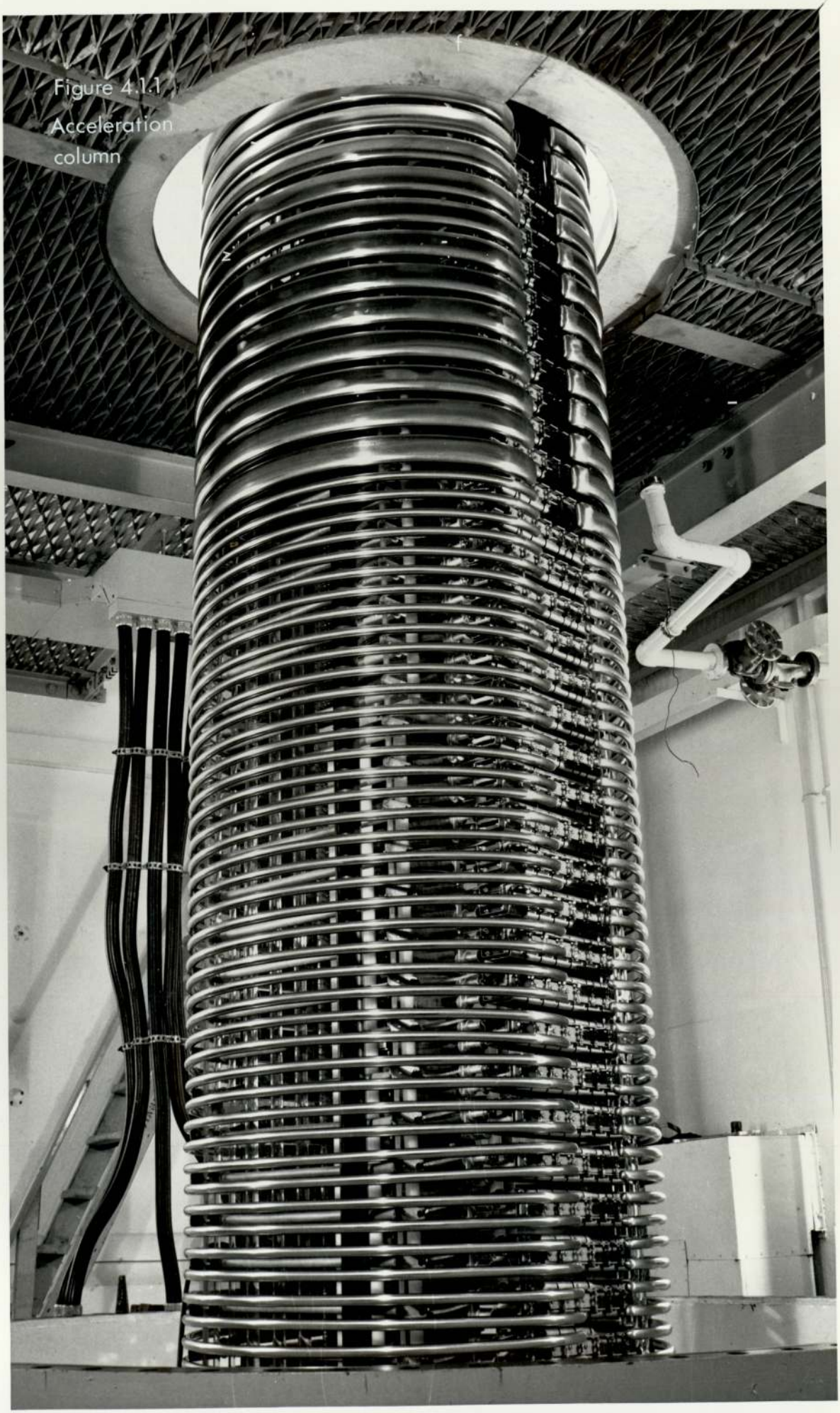

Figure 4.1.1
Acceleration column

matron ion source. The ion source is placed at an angle to the acceleration column and ions are bent to the line of the column by subjecting them to the field of a permanent magnet. The separation of the component ions is accomplished by using different extraction voltages prior to the beam entering the field of the permanent magnet.

Beam currents from a few nanoampere to about 2mA can be obtained.

The beam accelerated vertically downward can be used in the electron gamma room or could be subjected to the field of an H magnet in the magnet room and be bent at 45^{o} in either of the two directions leading to 'Aston beam' room or 'Low Scatter lower' room (Fig.4.1.2). For our measurements we have used two of these lines in 'Aston beam' room and 'Low Scatter lower' room. The C magnet in the Aston beam was degaussed prior to each measurement.

The dynamitron is stabilized through the current drawn down a series of resistors along the acceleration tube. The total value of the resistors is $10^{10}\Omega$. Then the current is monitored by a digital voltmeter across a 500Ω resistor. The energy of the beam was read through the DVM reading.

A ripple of ∿ 3 KeV FWHM was reported (WeaD74) in case of the proton beam. But the drift in mean energy over an hour was claimed to be <100eV.

4.2 TARGET CHAMBER

The target chamber was made from a 2" stainless steel 'dependex' T piece (Fig.4.2.1).A target holder made from a solid cylindrical copper rod was cut and machined at an angle 45^{o} at one end, appropriate grooves for the viton gaskets compatible with 2" dependex vacuum seal were made at the other end of the rod. A hole of about ¾" diameter was drilled through the elliptical cut face of the copper rod along the line of the beam. The outer flat end of the holder was marked so

Figure 4.1.2

Beam transport

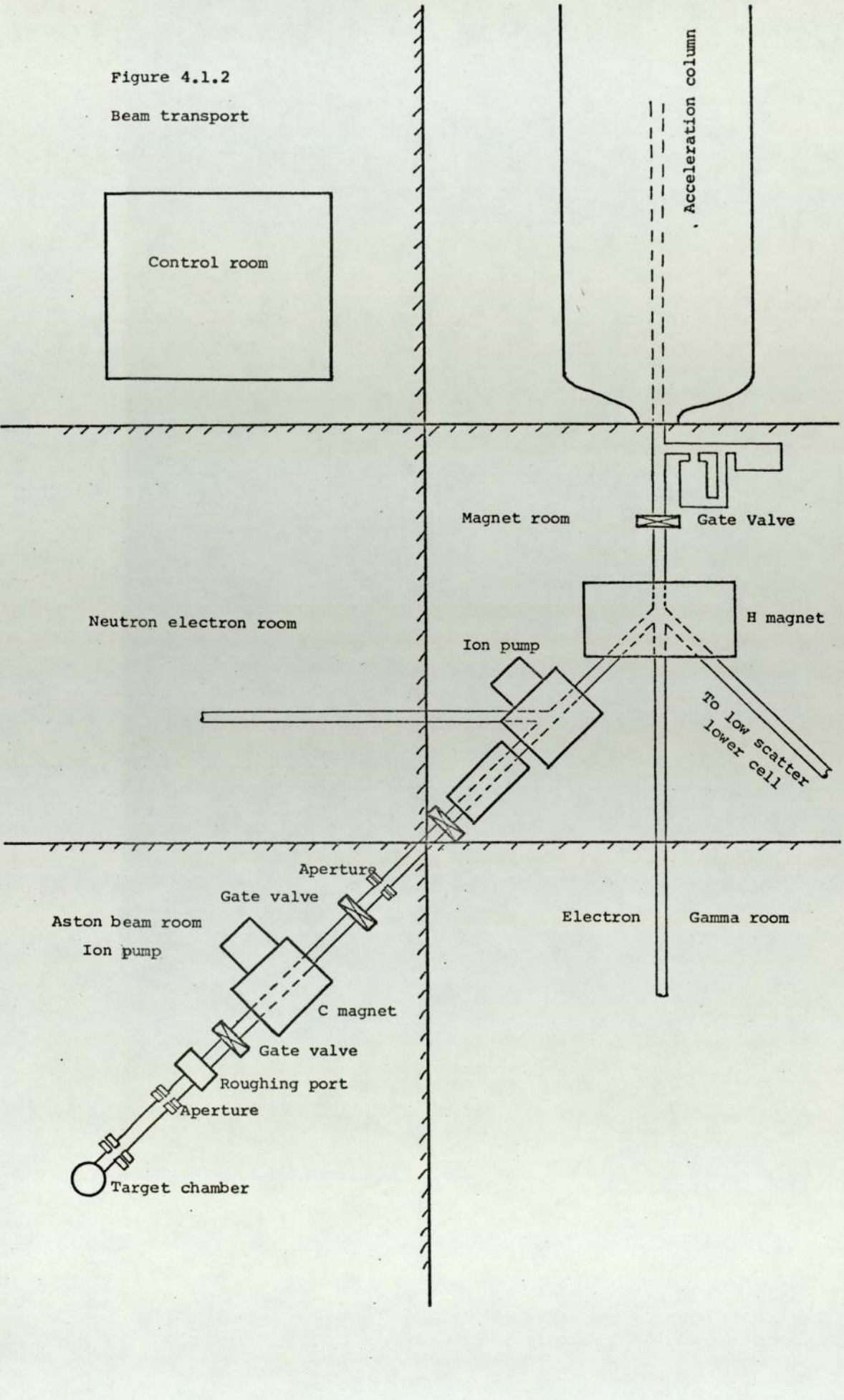

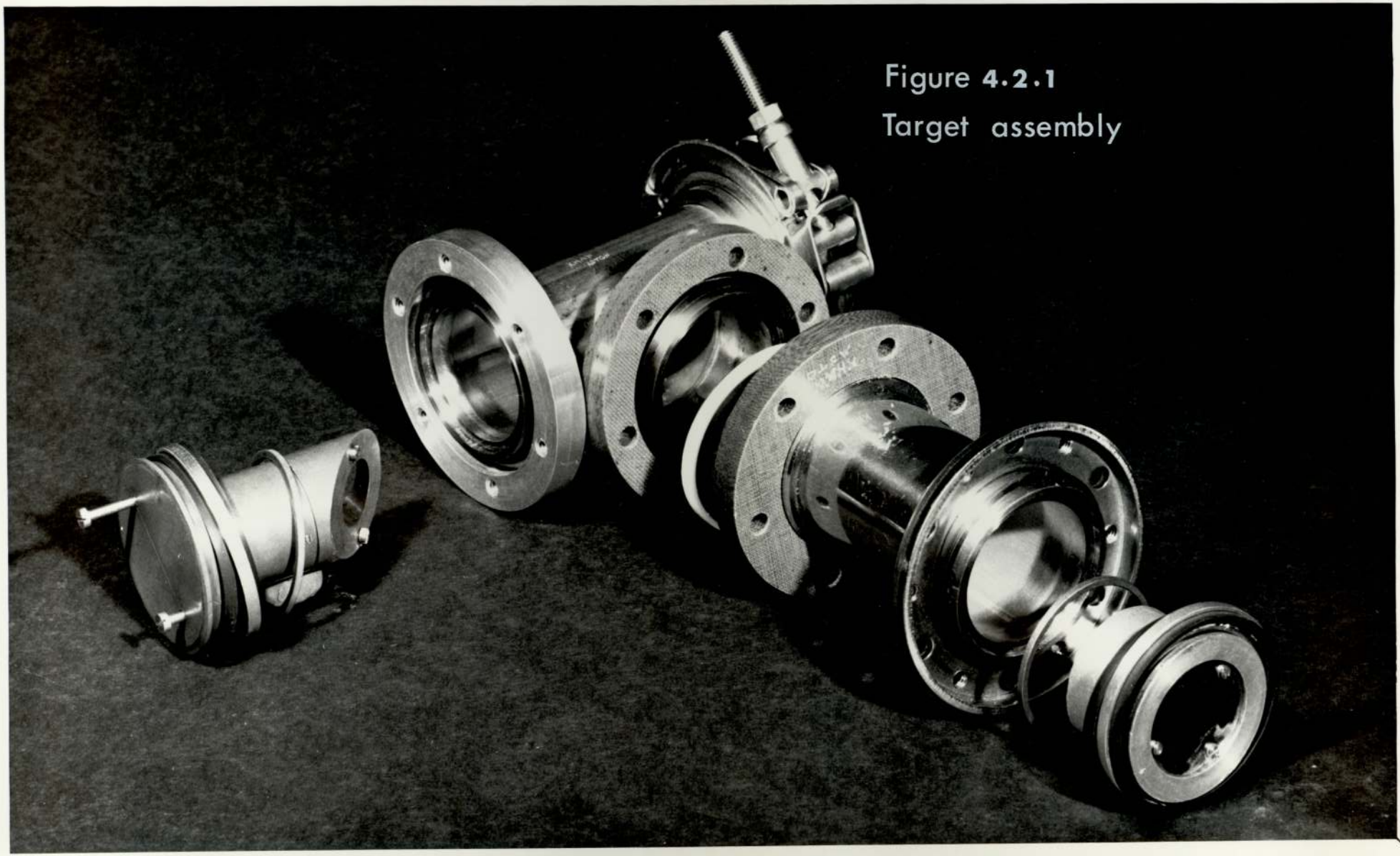

Figure 4.2.1
Target assembly

as to facilitate the setting of the elliptical plane perpendicular to the beam direction. Suitable clamping arrangements were made to hold the target in the elliptical plane. The holder was introduced through the end A of the T piece. A thin window was mounted on the end B of the T piece for the exit of the X-rays produced in the target. The thin windows were fixed with araldite onto the 2cm diameter hole on the end plate.

Three tantalum apertures A_1, A_2, A_3 of diameters 1mm, 2mm and 5mm respectively, were placed along the beam line. Aperture A_1 defined the beam profile, while A_2 connected electrically with A_1 prevented partially any scattered protons or secondary electrons released at A_1, from reaching the target. Aperture A_3 was connected electrically to the target and T piece and the whole assembly was insulated from the main beam line. Thus the T piece along with the aperture A_3 acted as a Faraday Cage collecting the incident beam and the majority of the backscattered protons and secondary electrons. (Fig.4.2.2).

4.3 KEITHLEY ELECTROMETER AND VOLTAGE TO FREQUENCY CONVERTER.

The current from the target was integrated by a Keithley electrometer. The electrometer can be switched on to one of the various ranges 10^{-10}A-10^{-3}A. Changing the range switch automatically changes the impedence so as to keep the output voltage corresponding to full scale deflection constant at 1V.

The output was fed to a voltage to frequency converter which produces 10^5Hz at 1V. The output of the VFC was again fed to a scaler through a decade dividing circuit. The decade dividing unit divides the input signal in multiples of 10. The scaler and the divider were controlled by an automatic start/stop device.

For the majority of the measurements low currents $\sim(10^{-9}$A - 10^{-7}A)

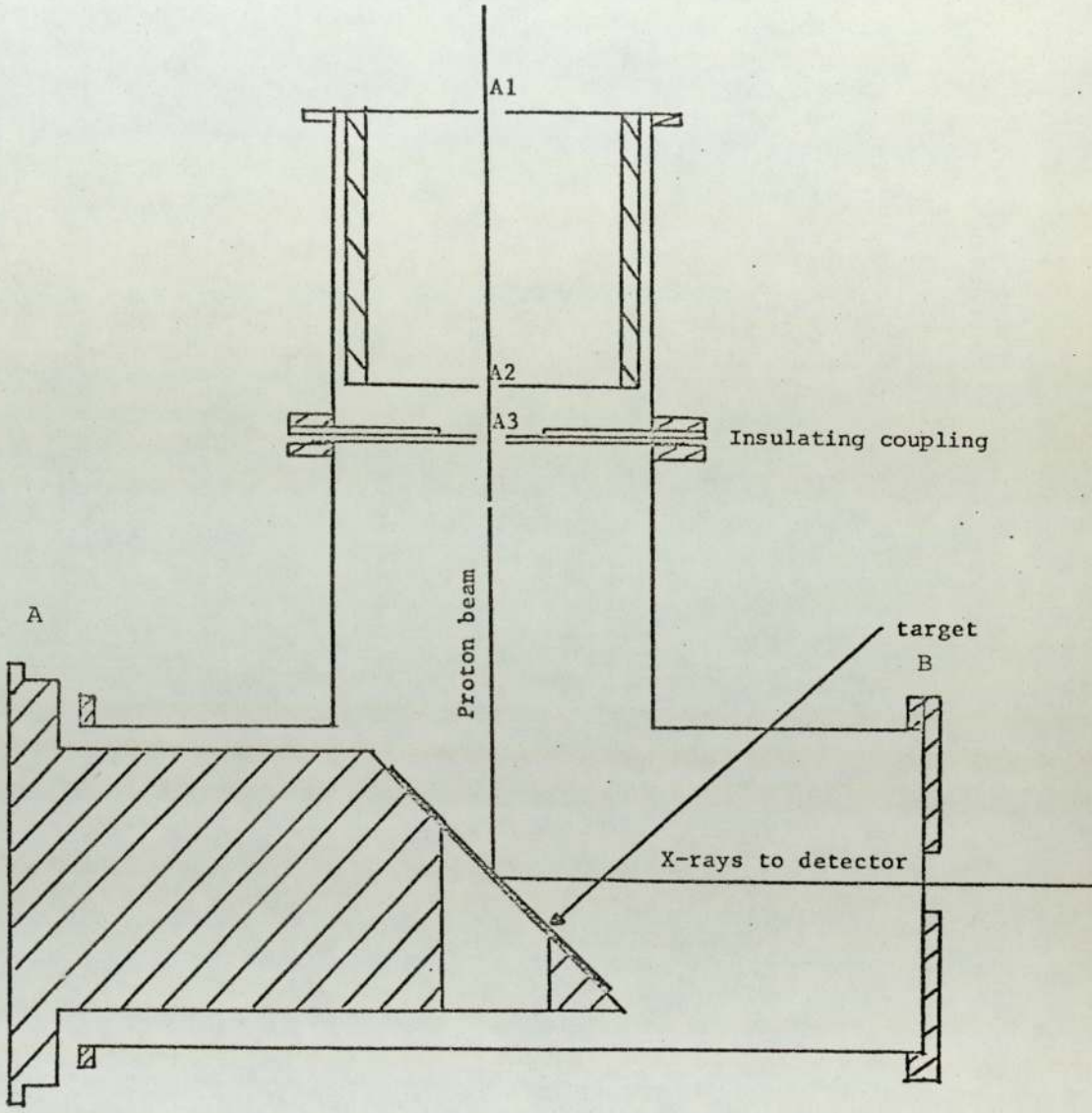

Figure 4.2.2

Target Assembly.

were used so as to make the count rate compatible with the input requirement of the detection system. The corresponding output impedances of the electrometer are $\sim 10^9 - 10^7\ \Omega$. Comparison of these impedances with that of standard insulating coupling $\sim 10^9 - 10^{10}\ \Omega$ shows that a variable leakage path for the beam current may exist through the insulating coupling. This was evidenced in the step changes in the thick target yield curve when ranges were changed. Such step changes in the nickel thick target yield curve are shown in (Fig.4.3.1).

To improve the insulation a PTFE T section was inserted in the insulating coupling. The T section was of $\sim$ 3mm thick and of $\sim 10^{16}\Omega$ resistance. No such step changes were observed after this modification. The specified uncertainty in the current measurement at FSD is < 1%.

4.4 THE JIG

A diagram of the jig used for the measurement of the distance between the target and the detector is shown Fig.4.4.1. Two stands pass through the holes drilled at the ends of a meter scale and can be held in the desired place by suitable clamps. Two pointers on their bases can be slid along the rule. The bases are marked along the central lines of the pointers. The lengths of the two pointers are such that when the respective pointers touch the bottom of the detector aperture and the bottom of the target holder and made horizontal using a spirit level the detector centre comes in the same horizontal plane as the beam spot on the target. The bottom of the target holder is marked along the line of the beam spot. Using these pointers the distance between the beam spot and the detector can be measured with an accuracy better than 1mm.

4.5 KEVEX 3201 CRYOGENIC SUBSYSTEM

A Kevex 3201 cryogenic subsystem used in the present measurements

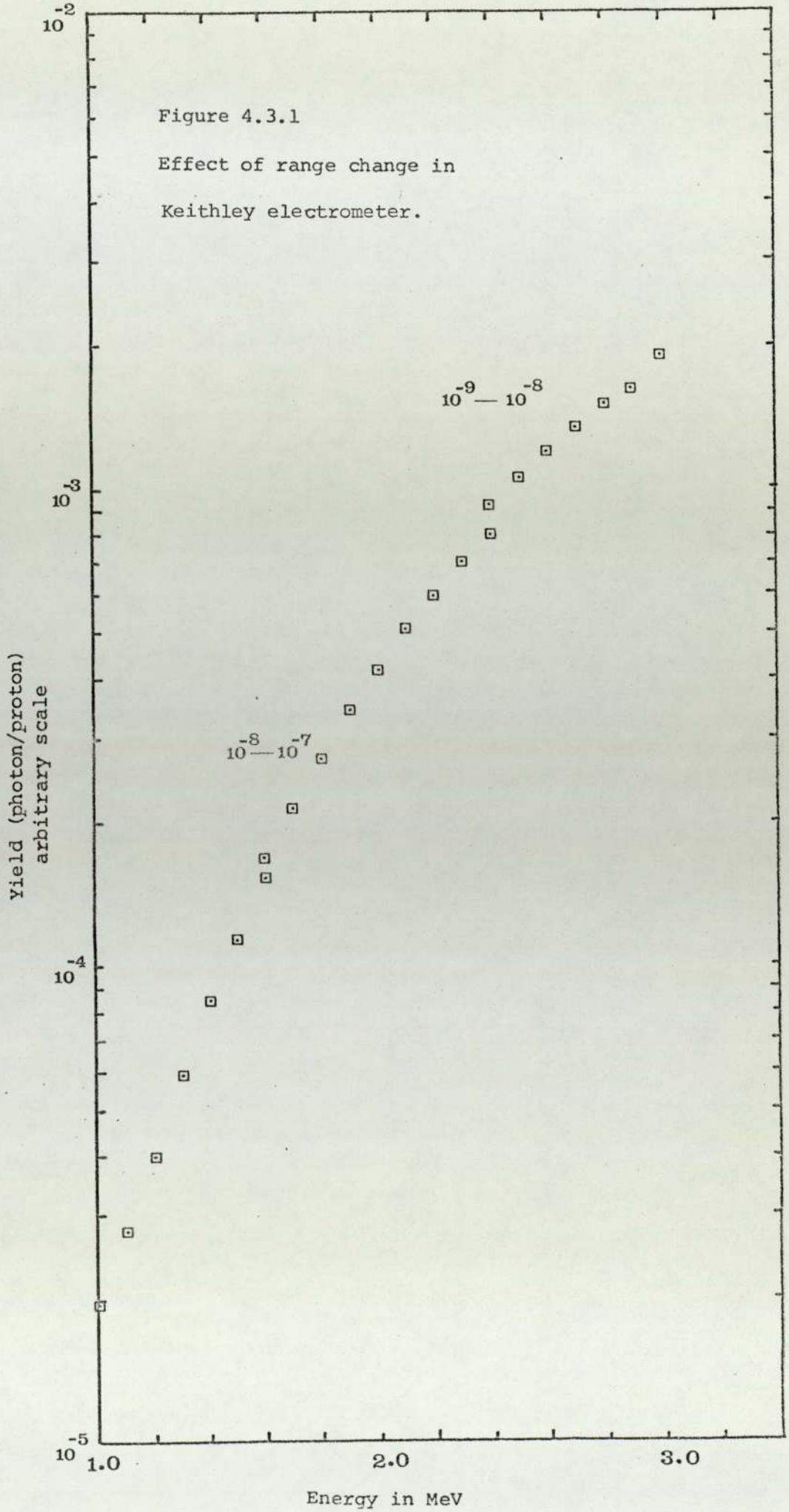

Figure 4.3.1

Effect of range change in

Keithley electrometer.

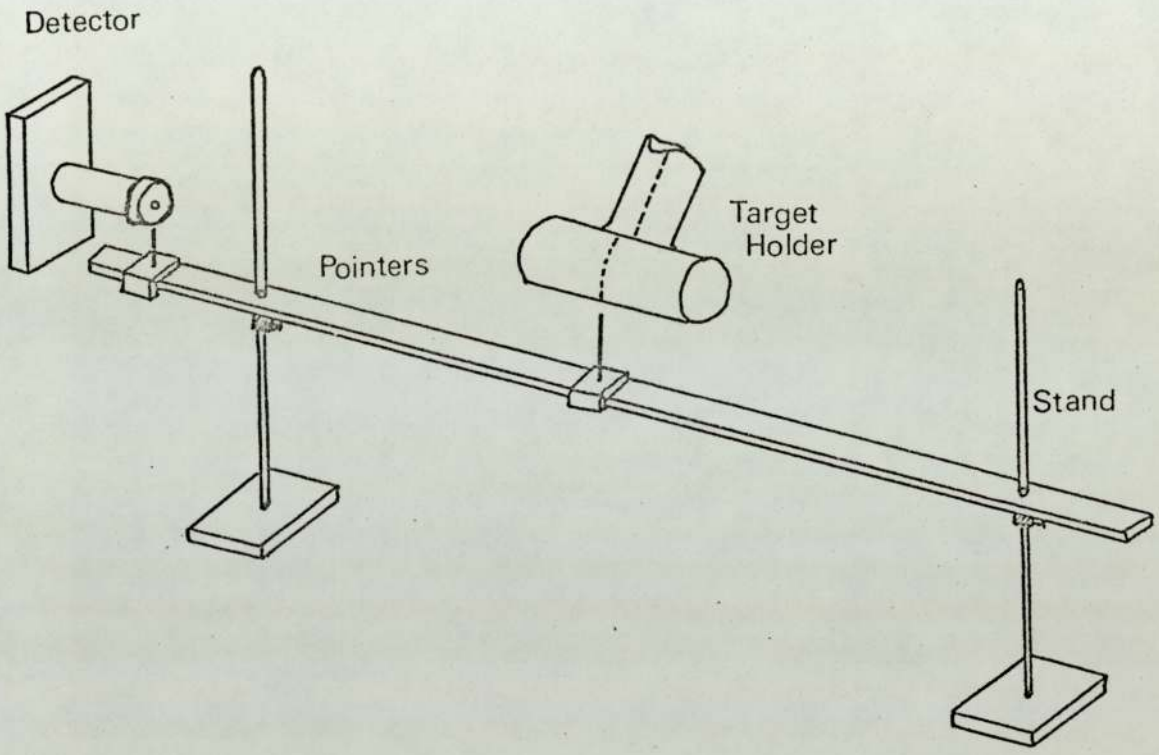

Figure 4.4.1

The Jig

consists of a lithium drifted silicon detector head assembly, a cryostat with beryllium window, pulse optical feedback preamplifier and a liquid nitrogen dewar. The beryllium window of 12.7μm thickness provides the vacuum seal and optical shield. A machined plexiglass protective cover with an adjustable stainless steel strap protects the extremely fragile beryllium window.

The crystal is 30.3 sq. mm area and of 3mm thickness. The crystal is mounted in contact with a surface cooled by the liquid nitrogen from the dewar. A field effect transistor acting as a first stage of the preamplifier is placed in contact with the detector crystal to minimize noise.

Layers of $\sim$ 200Å gold on both sides of the crystal act as electrical contact. A bias of 1000V across them sweeps the charges produced in the crystal by incident radiation. The vacuum acting as an insulation to the liquid nitrogen in the system, is provided either by a molecular sieve or by an ion pump to ensure that the vacuum environment is free from materials affecting the detector surface state.

The detector was placed outside the target holder window. The jig was used to measure accurately the distance between the face of the detector crystal and the beam spot on the target. Specular reflection of a laser beam from the target was used to fix the position of the detector.

Lead apertures of appropriate diameters were used to define the detector area and eliminate the dead layer effect predominant at the boundary of the crystal.

The manufacturers specification of resolution was $\sim$ 161 eV at 5.9 KeV at 1000cps.

A photograph of the experimental set up is shown in Fig.4.5.1.

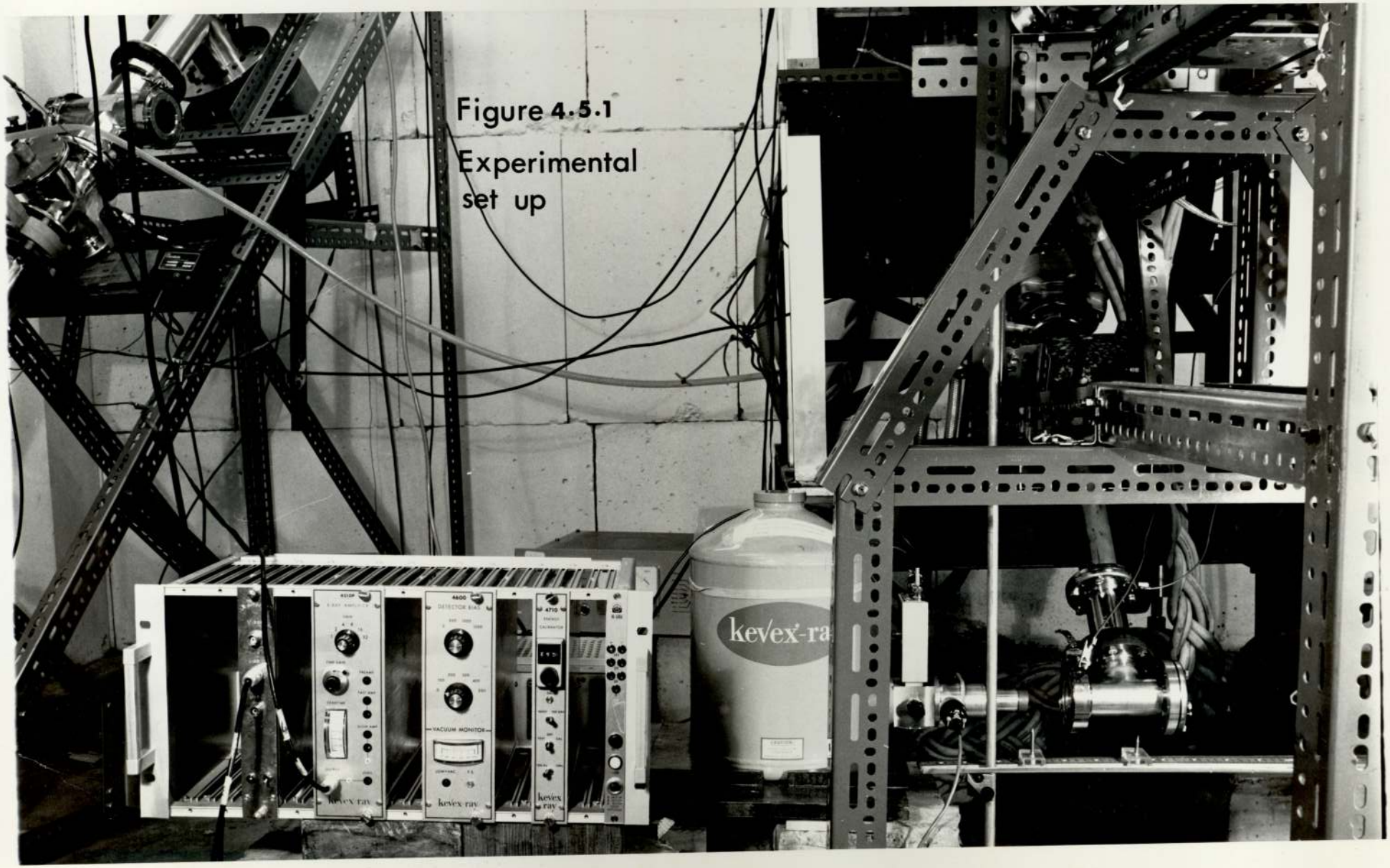

Figure 4.5.1

Experimental set up

4.6 KEVEX 4600 DETECTOR BIAS SUPPLY

A Kevex Model 4600 Detector Bias Supply was used to provide the EHT for the detector. This has a voltage range of 0 to -2000 volts in 100 volt increments, an impedance of 65 megohms and ripple and noise <100μV rms. The temperature stability is <.02%/C^{o} and line stability is <.02%.

A vacuum monitor is incorporated in the cryogenic subsystem. A heated thermocouple provides an output voltage proportional to the pressure. If the pressure in the vacuum system exceeds 20 microns, the output initiates the sensing circuit to disconnect the high voltage supply from the detector. Otherwise the corona discharge that may result in the cryostat at higher pressure will damage the charge sensitive amplifier input FET. At readings lower than 90% of the full scale on the vacuum monitor which correspond to about 25 micron, a vacuum light is lit.

4.7 KEVEX 2002 PULSED OPTICAL FEEDBACK PREAMPLIFIER

A preamplifier integrates the charges produced in the detector and presents them as a voltage signal to the amplifier. To obtain optimum noise suppression and hence better resolution, the first stage in the form of a FET of the Kevex 2002 preamplifier, used in the present experiment, is placed close to the detector and cooled with it.

To keep the operating condition of the FET unaltered, the pulses must be provided through a by-pass. In a resistor feedback preamplifier a resistor is connected in parallel with FET to provide a by-pass. But the resistor itself acts as a noise source and lengthens the shaping time of the pulses which affects the count rate capability adversely.

In a pulsed optical feedback system of Kevex 2002 the use of a resistor is eliminated by providing a by-pass in the following way.

The voltage in the FET is allowed to build up in steps to a certain level, at which point a level sensor triggers a light emitting diode (Fig.4.7.1).Light shines on the FET drain gate junction momentarily and makes it conductive and the capacitance discharges. A pulsed optical system like this is a high performer in terms of resolution and low noise characteristics but loses certain count rate capability.

The Kevex 2002 preamplifier gives an output with negative reset pulses. The input charge conversion is approximately 4.5 mV per 10 KeV.

The output of the impedance of the preamplifier is 50 ohms.

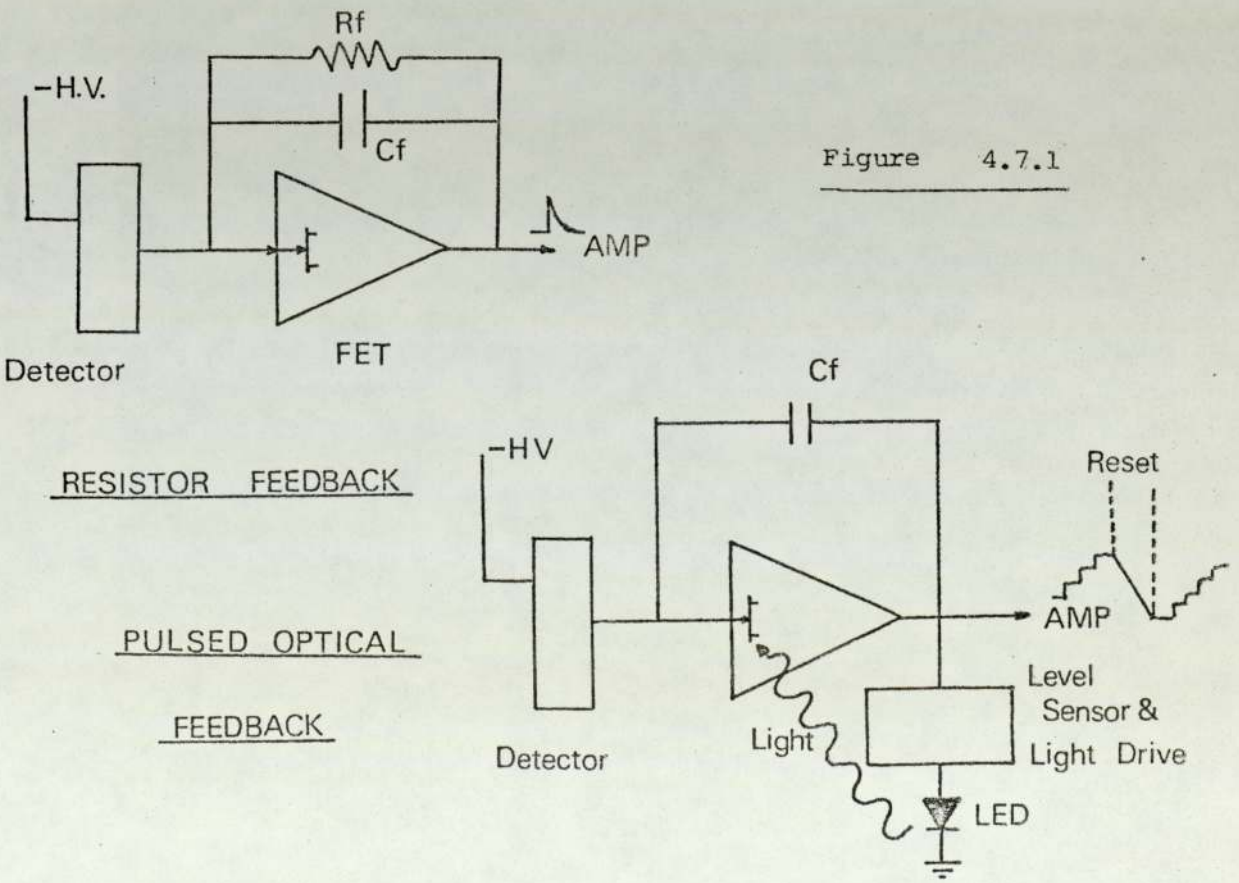

Figure 4.7.1

4.8 KEVEX 4500P X-RAY AMPLIFIER

In order to amplify pulses from a 2002 Kevex pulsedoptical feedback preamplifier and process them so as to make them compatible with the subsequent data analysis and storage system, a 4500P Kevex pulsed optical feedback type X-ray amplifier was employed.

The Kevex 4500P amplifier provides coarse gain from 1 to 16 in multiples of 2 and the fine gain is a ten turn control from 1 to 2.2. There is also available a post gain facility of 1,2,4 above base line setting. The gain and base-line stabilities are $\pm.01/^{o}C$ and $\pm200\mu V/^{o}C$ respectively. The maximum output is + 10V direct coupled. The output pulses are flat topped and of 2μS duration. Input and output polarity control switches are provided. The pulsed optical dead time is adjustable from 50μS to 500μS and a busy output provides a busy signal for pulse duration and optical reset time.

The amplifier uses a long shaping time for efficient noise suppression. A number of plug in time constant cards provide the freedom in choosing the desired pulse shaping time. The total width of the shaped pulse is 10 times the time constant.

The longer the pulse shaping time the more efficient is the noise suppression. But longer pulse shaping times increase the probability that a second pulse may arrive while the first pulse is being processed.

Let us define the pulse peaking time as the time taken by a pulse to attain its maximum amplitude. Let us also divide the pulses in two halves through their maximum amplitude.

Three types of pile up that may occur, are illustrated in the Fig.4.8.1.

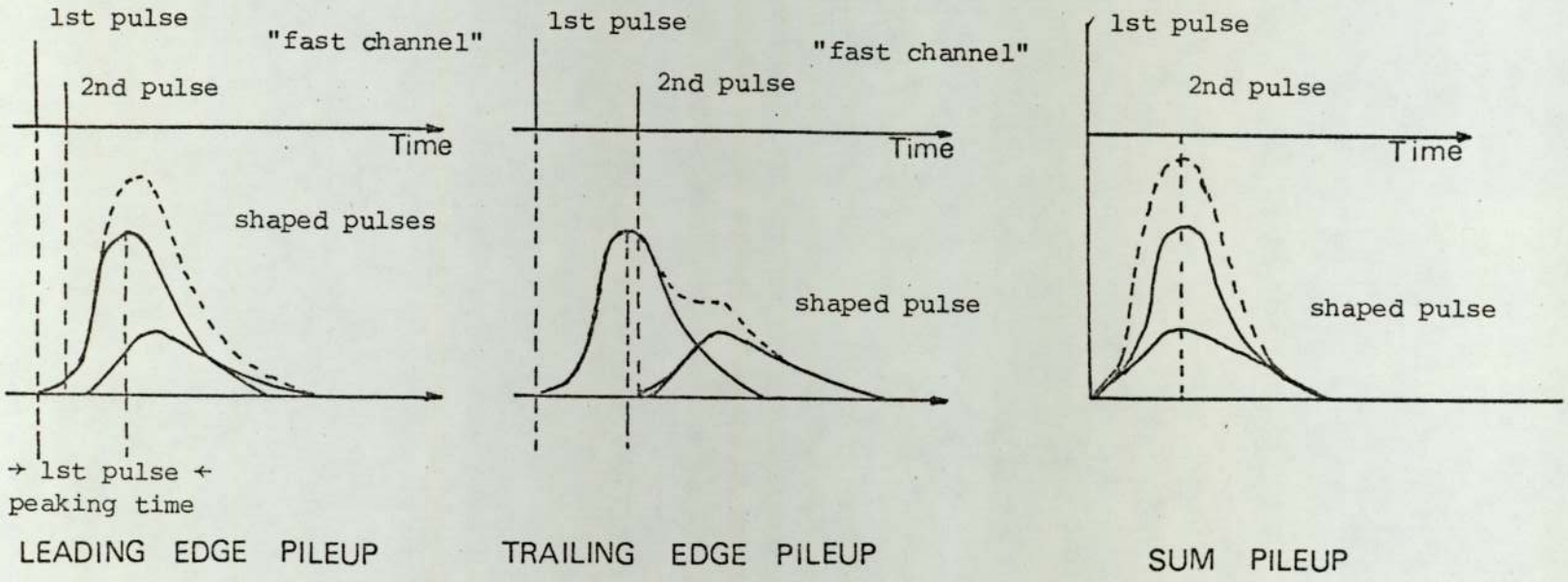

Figure 4.8.1

Pulse pile up.

(1) leading edge : A second pulse might arrive when the first pulse is in the first half of its processing time.

(2) trailing edge : A second pulse may arrive after the first pulse has crossed its peak amplitude and is in the second half of its processing time.

(3) Sum pile up : Two pulses may arrive together (in the eye of the processing system).

Since in pulse height analysis mode, pulses are analysed for their energy by measuring their pulse height, a change in pulse amplitude is extremely undesirable, because it signifies the presence of a pulse with a different energy.

In the leading edge pile up both the pulses lose their original amplitude and shape, and have to be discarded. In the trailing edge pile up, though both of the pulses lose their shape, the amplitude of the first pulse remains unaltered and may be retained. Only the second pulse has to be rejected. Since the system cannot identify sum pulses as the sum of the two pulses, additional information has to be used to deal with these.

The rejection of distorted pulses may be accomplished by the use of a pulse pile up rejector.

4.9 4590 KEVEX PULSE PILE UP REJECTOR

In order to reject pulses distorted due to leading and trailing edge pile up and to correct for the dead time, and pulsed optical reset, a Kevex 4590 PPR is incorporated in the circuit.

As discussed in the previous section, for optimum use of the available signals, the first signal in trailing edge pile up, having unchanged amplitude, has to be retained. While in the leading edge pile up both pulses are distorted and are rejected.

A fast amplifier with good pulse pair resolution provides the time discrimination of events for the slower shaping amplifier. The total width of a shaped pulse is 10τ i.e. for 8μS time constant it is 80μS whereas the pulse pair resolution $\sim$ 1μS. Knowing the total width of the quasigaussian shaped pulse in the shaping amplifier and comparing the arrival of successive events, the discriminator sets up a gate prohibiting passage of both the pulses in case of leading edge pile up and only the second pulse in the case of trailing edge pile up.

The Kevex PPR incorporates an analog meter for estimating the dead time. Though the optical pulse resetting time is small compared with the total dead time, their contributions to it become more prominent for higher energy pulses. Because of the larger number of charges/photon, more frequent resetting is required.

A 'Lowes Live Time Corrector', Woldseth (WolR73) incorporated in the 4590 PPR accounts for the dead times due to pulse pile up rejection, pulse reset, and multichannel analyser busy time and prolongs the counting time of the live time clock to compensate for them. Alternatively, a'busy signal' output which is either busy high +5V or busy low +0V, can be used for correcting the dead time.

4590 PPR is provided with a time constant switch to match with the time constant of the amplifier. The preamp input accepts positive or negative tail pulse or staircase. The Kevex PPR incorporates an analog meter for estimating the dead time.

4.10 LIVE TIME MEASURING SYSTEM

For quantitative measurement the dead time incurred in the preamp-amp-PPR system has to be accounted for. This dead time, as was explained earlier, arises from pulsed optical reset time and the extendible dead time per pulse of the PPR system. To facilitate dead time correction the PPR provides a +5V busy output signal when the system is inoperative. Normally this signal is used to gate the live timer of the multichannel analyser. In the case of the Hewlett-Packard data acquisition system, no convenient access is available.

In order to measure the dead time the busy signal was used to gate a 1MHz crystal oscillator employed as a clock. The circuit was arranged so that when the output of the busy signal was +5V the oscillator output was inhibited, and when the busy output was zero, i.e. the system was live, the oscillator output was passed to a scaler via appropriate dividing circuits.

The logic was achieved by the use of 3 NAND gates incorporated in a commercial microcircuit SN7400N available from Texas Instruments. Details of the circuit are shown in Fig.4.10.1. The busy signal was fed to the first NAND gate and an inverted output obtained. Using the second NAND gate this inverted output was used to gate the crystal oscillator output. The 3rd NAND gate simply inverted the output of the second NAND gate. The truth table shows that the final output is zero when the output of the busy signal is +5V and is that of the crystal oscillator when the busy output is zero. The following truth table refers to Figure 4.10.1.

Truth Table

A (busy)	$\bar{A}$	B (C.O.)	$\overline{\bar{A}.B.}$	$\overline{\overline{\bar{A}.B.}}$
1	0	1	1	0
0	1	1	0	1

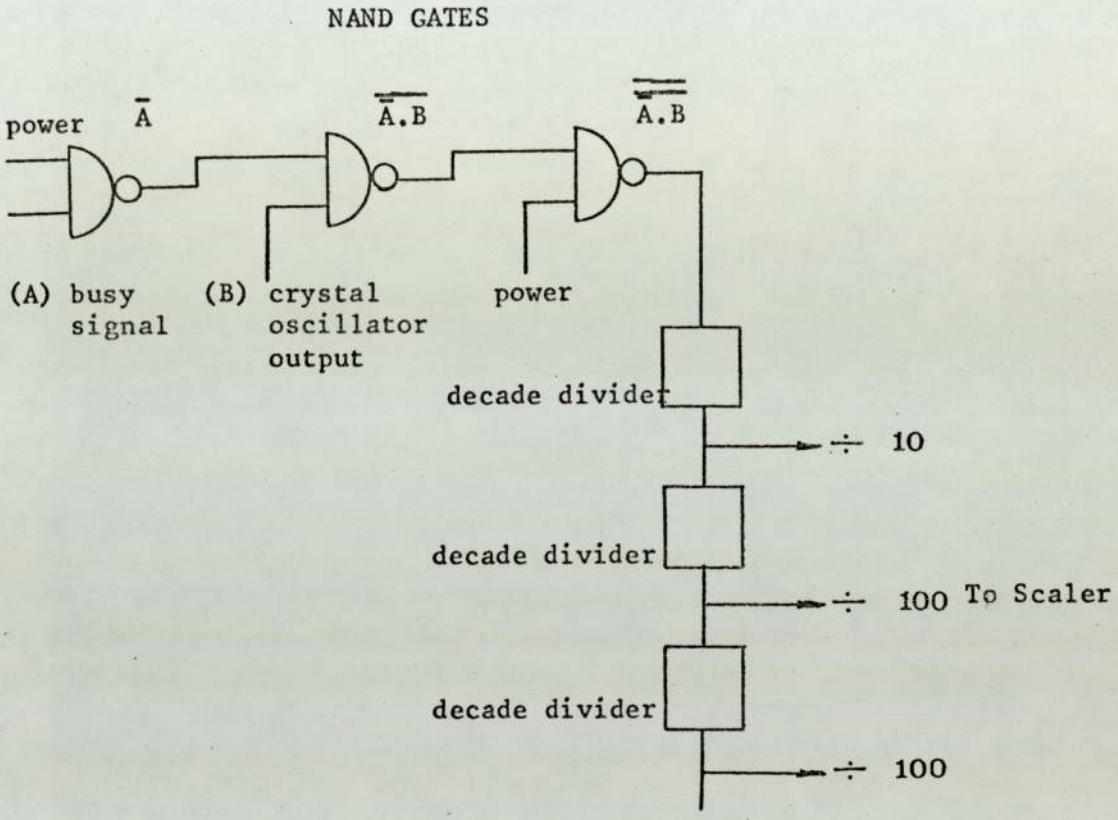

Figure 4.10.1

Circuit diagram of the live timer.

The final output was then fed to a scaler via a number of decade dividing counters. The three decade counters were connected in series and a total dividing factor of 10, 100 and 1000 may be achieved respectively at the output of 1st, 2nd and 3rd dividing circuit. A 5V voltage regulator used the 12V power supply of the NIM bin to supply power to the microcircuit. The board with the circuit was mounted in a standard NIM bin. BNC connectors were provided for input and output. An on-off microswitch with an indicator light was mounted on the front. A provision was made for a power supply from any 12V source when the unit was used outside the NIM bin.

A seven decade NE scaler was used to count the output pulses from this system.

4.11 5406B NUCLEAR DATA ACQUISITION SYSTEM

The 5406B HP Nuclear data acquisition system is a multiparameter or multiplex multichannel analyser which uses a digital computer for processing and control of measured data. Three 5416B 200MHz ADC's can be used at a time but only one ADC was used in the present measurement. The system takes commands from a teleprinter.

Any of the 2^n output channels can be chosen in the ADC with $4 \leq n \leq 13$. A digital offset in multiples of 2 is available. Upper and lower level discriminators can be set to select an input window. An analog offset control is adjustable from -1V to +1V. The input is dc coupled and accepts inputs between +0V to +10V. Either fixed or variable analysis time on clock time or live time mode can be selected. The ADC can be operated either on normal, coincidence or anticoincidence mode.

The ADC is also provided with a multidimensional display with XY markers to choose individual or groups of channels. A dual purpose meter can be used to monitor either the count rate or the dead time.

An X-Y plotter can be used to record the spectrum.

In pulse height analysis mode amplitudes of the input pulses are converted in binary codes and sent into the computer which in turn represents them by channel numbers. Each time the ADC processes a signal of the same amplitude the memory location of that corresponding channel is incremented by 1. An overflow takes place when the memory location exceeds 2^{16}.

The ADC analysis time in either fixed mode or variable dead time mode is related to the output range channel as

Output range channel selected	Fixed mode timing	Variable mode timing
512	6.5 μs	3.4 + (.005n) μs
1024	9.5 μs	3.7 + (.005n) μs
2048	16.5 μs	4.3 + (.005n) μs
4096	30.5 μs	5.8 + (.005n) μs

where n is the channel number at which the pulse is located.

The data accumulation is displayed on the screen for study, manipulation and analysis using available routines. The spectrum can also be outputed in (1) line printer, (2) paper tape, (3) magnetic tape (4) X-Y plotter or may be stored in the computer file for further analysis. A photograph of the data acquisition system is shown in Fig.4.11.1.

4.12 SYSTEM PERFORMANCE

Important performance characteristics of the different instruments are discussed in the following subsections:

4.12.1 Energy calibration of the detector system

The following standard x-ray sources were used to calibrate the detector:

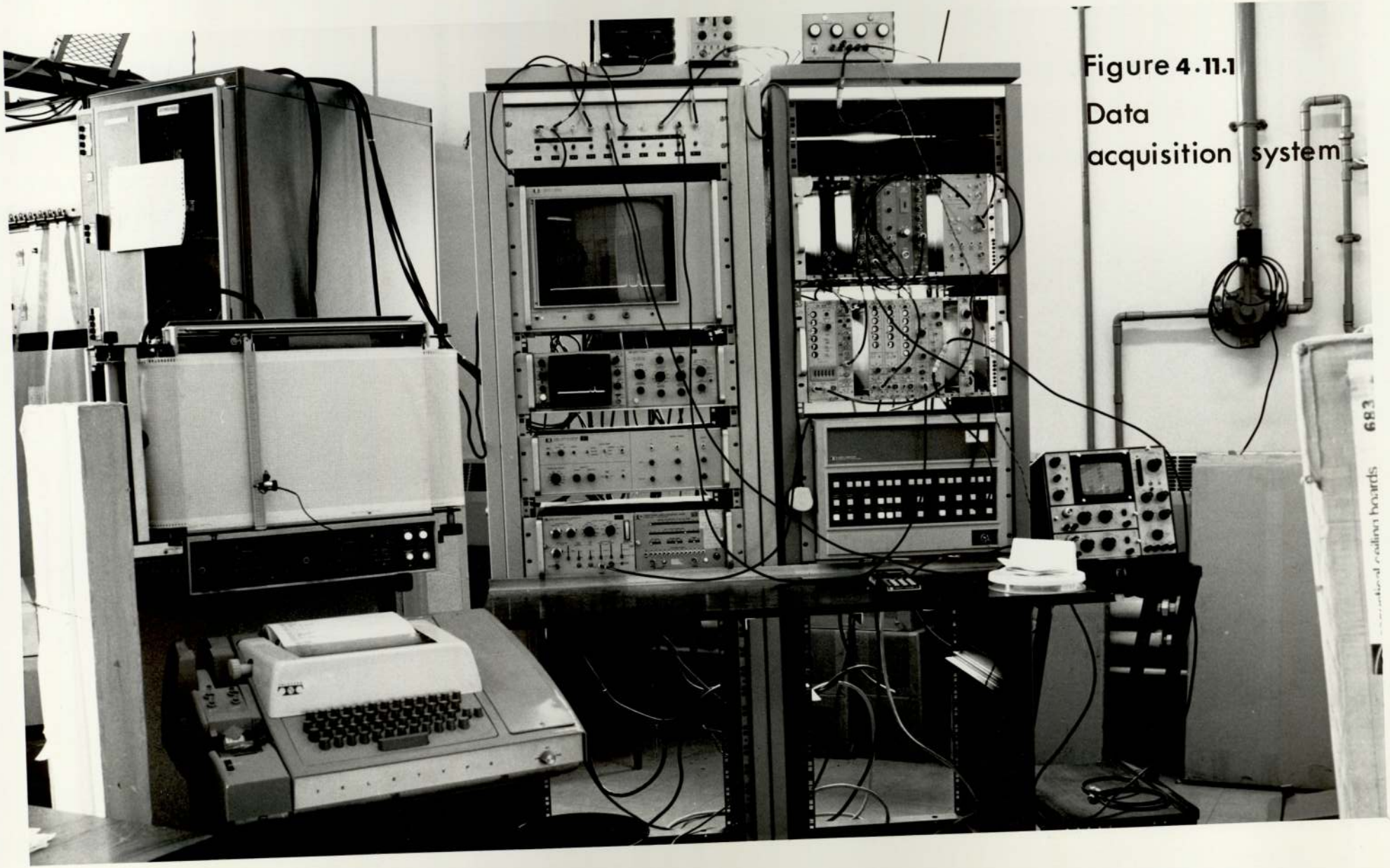

Figure 4.11.1
Data
acquisition system

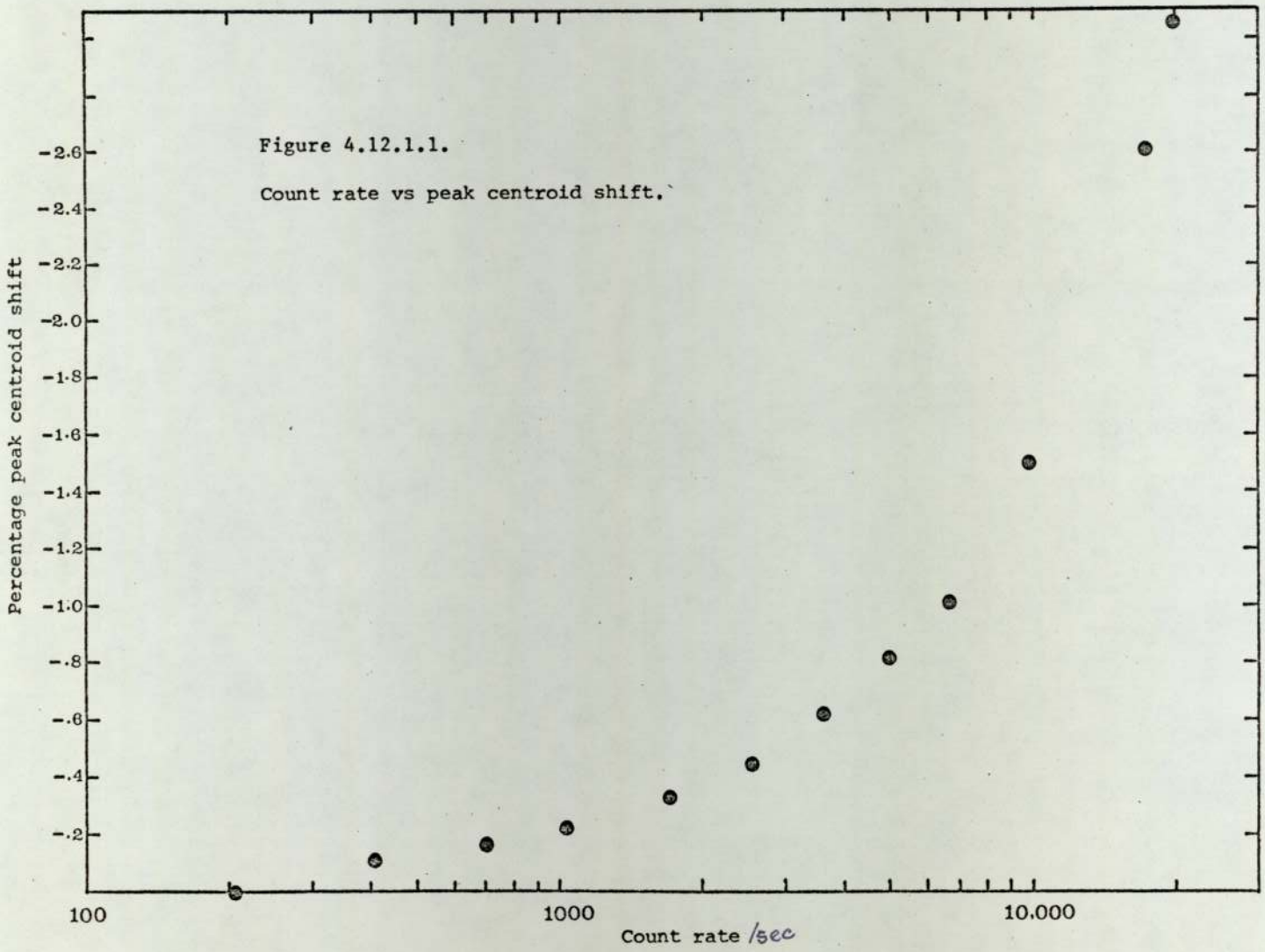

Figure 4.12.1.1.

Count rate vs peak centroid shift.

	Source	Kα energy in keV	Kβ energy in keV
1)	Mn	5.89	6.49
2)	Cu	8.04	8.91
3)	Rb	13.37	14.97
4)	Mo	17.44	19.63
5)	Ag	22.10	24.99
6)	Ba	32.06	36.55

All the X-ray lines 2) - 6) were provided by a variable X-ray source, and Mn X-rays were provided by a 330μc Fe^{55} source.

At a fixed count rate, a linear relation between the X-ray energies and their respective channels was always observed. The calibration was made prior to each measurement.

The peak centroid stability with the count rate was studied using a Mn X-ray source at 8μs time constant. The shift of peak centroid at 20000 cps compared to the peak position at 1000 cps was found to be ∿ 3% (Fig.4.12.1.1) whereas the manufacturers specification claims this to be < 1%.

4.12.2 Detector Efficiency

In estimating the detector efficiency the following measures were taken: (i) Dead layer effects were minimized using collimators, (ii) Detector window (12.7μm thick Beryllium) was treated separately, (iii) Gold layer absorption was neglected.

The detector efficiency d_e for a photon energy E was then calculated by using the formula

$$d_e = 1 - e^{-\mu_s(E)X_d}$$

where $\mu_s(E)$ = linear absorption coefficient of silicon for photons of energy E.

X_d = Detector crystal thickness ∿ .3cm.

A graph of detector efficiency plus the absorption in the window is shown (Fig.4.12.2.1). The decrease in efficiency at energies above the flat top is due to the crystal transparency, and the absorption in the window is negligible, whereas that below the top is due entirely to the absorption in the window.

4.12.3 Detector Collimation

The detector itself sometimes contributes to the background (GouF71,JakJ70). This arises for incomplete charge collection due to the edge effect near the lateral surface of the sensitive volume. The dead layers absorbing low energy X-rays extend deeper near the boundary demanding non linear correction. These two effects were minimized by introducing collimators of precise apertures.

4.12.4 Pulse pile-up rejection and dead time

The performance of the rejection circuit is shown (Fig.4.12.4.1). This graph also shows the background, the pile-up continuum can render to the peaks at higher energy. And the discrete strength of sum peaks which could add itself to a peak at higher energy producing false information.

Curve a (Fig.4.12.4.2) shows the variation of the percentages of pile-up continuum to their parent peak, at different count rate. Use of pulse pile-up rejector reduces these percentages to a negligible amount , curve b (Fig.4.12.4.2).

Curve a in (Fig.4.12.4.3) shows the real time throughput whereas curve b shows the dead time corrected output count vs input count rate. Since the output pulses from the detecting system were separated by at least 80μs (8μs x 10) and since ADC dead time was much smaller than this, no correction for ADC dead time was necessary. The output

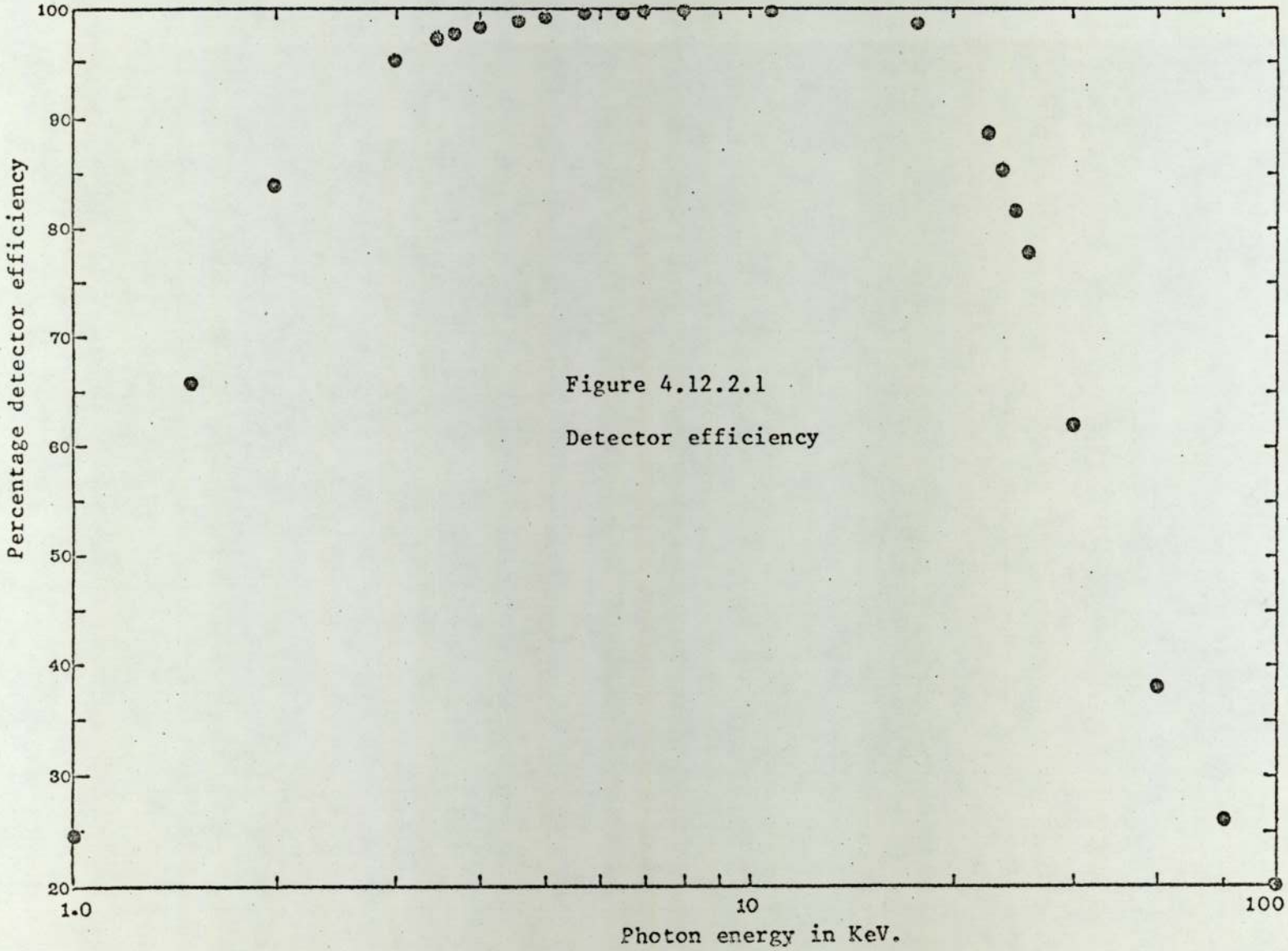

Figure 4.12.2.1

Detector efficiency

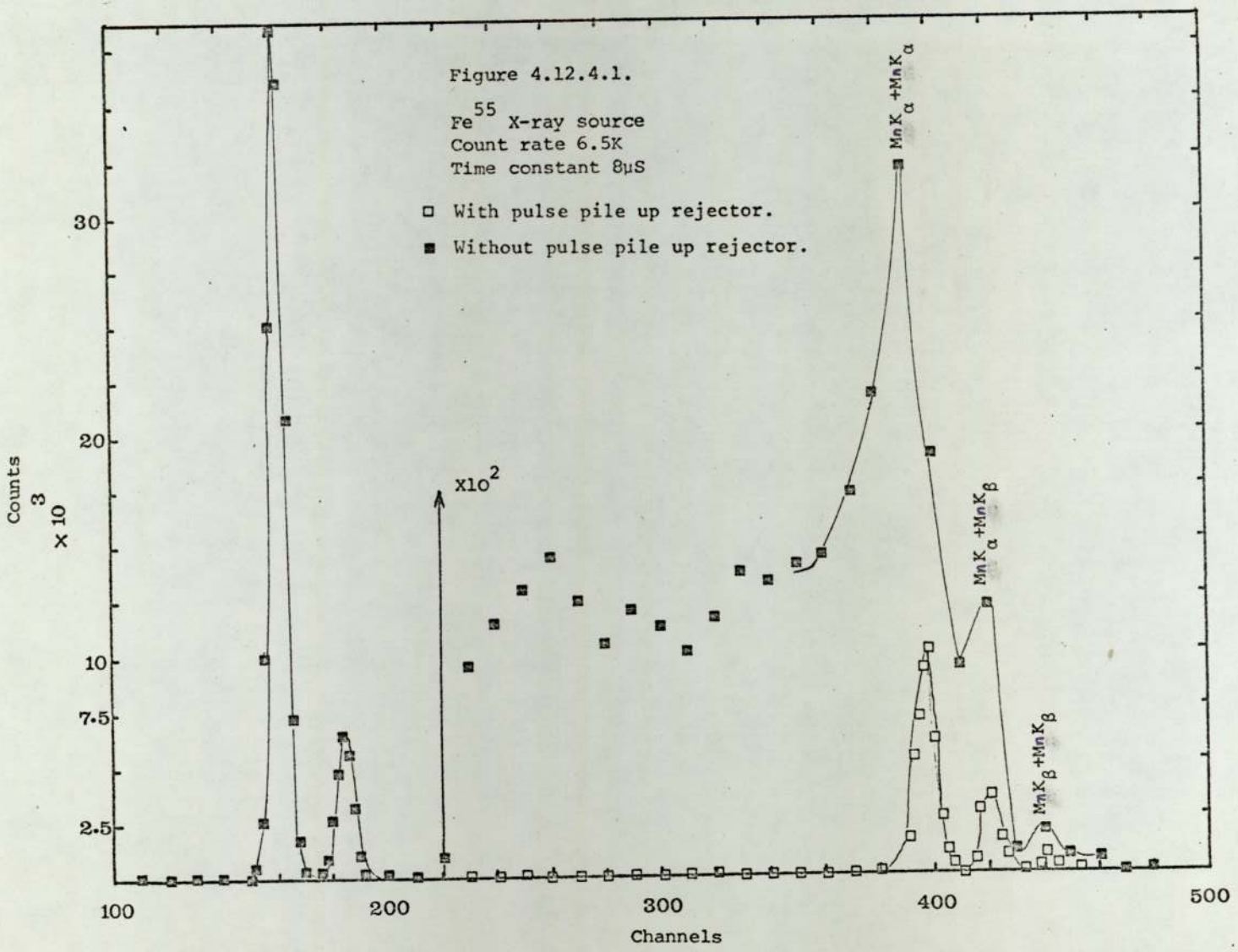
Figure 4.12.4.1.
Fe55 X-ray source
Count rate 6.5K
Time constant 8μS
With pulse pile up rejector.
Without pulse pile up rejector.
Counts
x 10^3
30
20
10
7.5
2.5
x10^2
MnKα+MnKα
MnKα+MnKβ
MnKβ+MnKβ
100
200
300
400
500
Channels

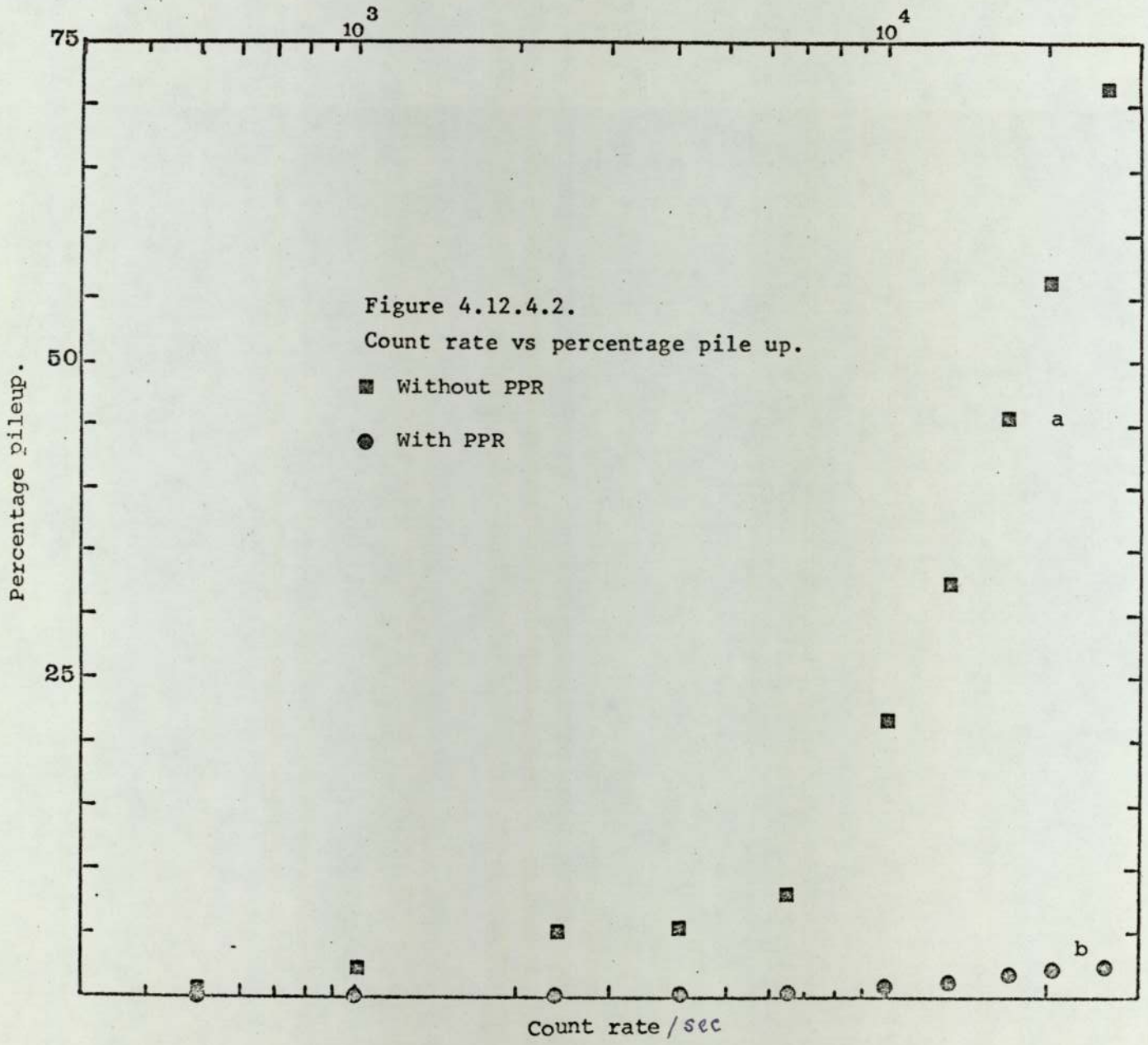

Figure 4.12.4.2.
Count rate vs percentage pile up.

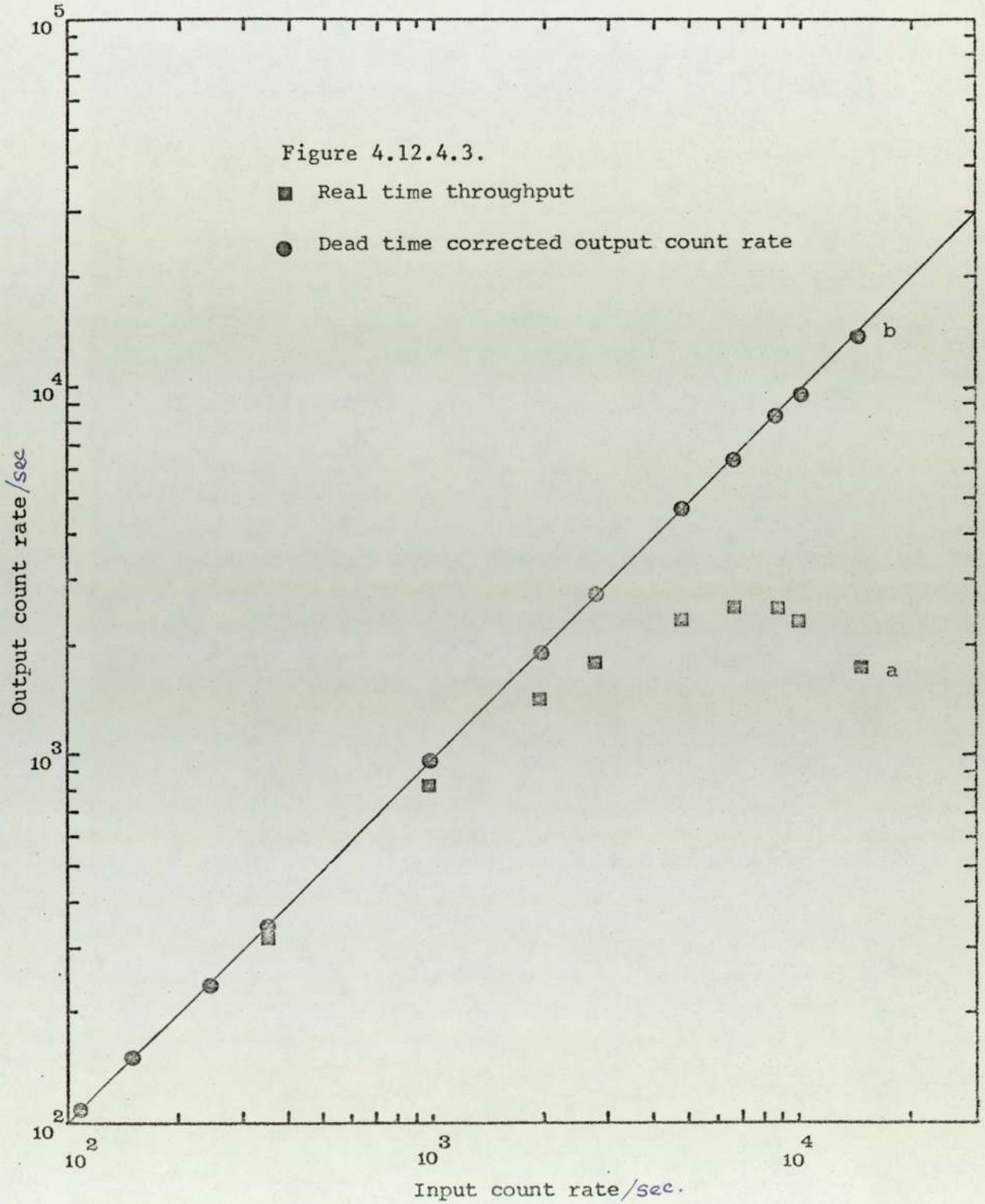
Figure 4.12.4.3.
Real time throughput
Dead time corrected output count rate
b
a
10^5
10^4
10^3
10^2
Output count rate/sec
10^2
10^3
10^4
Input count rate/sec.

count was corrected using the simple formula,

$$\text{corrected output} = \text{input} \times \frac{\text{clock time}}{\text{live time}} .$$

From the real time throughput curve it is evident that increase in input count rate after $\sim$ 17000 cps results in the decrease in corresponding output count rate.

The curve b also shows that even at input count rate as high as 15000 cps our dead time correction procedure is correct within 2%.

4.12.5 Resolution

The resolution of an X-ray detecting system is conventionally defined as the Full Width at Half Maximum (FWHM) of MnKα (5.89 KeV) peak at an input rate of 1000 cps. The FWHM due to 'intrinsic resolution' or 'statistical spread is

$$(\Delta E)_{det} = 2.35 \sqrt{F\varepsilon E} \text{ eV} \qquad 4.12.5.1$$

where F = Fano factor (dimensionless)

ε = eV/electron hole pair

E = Energy of the incident photon in eV

The effective resolution of the detector contains the contribution from the electronic noise, which is considered random and independent and is added quadratically to the detector resolution. So the total resolution is

$$\text{FWHM} = \sqrt{(\Delta E)^2_{det} + (\Delta E)^2_{noise}} \qquad 4.12.5.2$$

The working resolution of our detector was found to be $\sim$ 170 eV. Using a KeVex pulser the electronic noise width was estimated to be

$\sim$ 117 eV. Using this value in eqn 4.12.5.2, the detector FWHM was found to be 123 eV. The corresponding manufacturers specification of noise width is $\sim$ 98 eV which makes the total resolution $\sim$ 153 eV.

The variation of resolution with count rate was studied and presented in Fig.412.5.1.According to manufacturers specification the degradation of resolution at 20000 cps should be < 1%, whereas our measurement shows the increase in FWHM at 20K cps compared to the FWHM at 1000 cps, is $\sim$ 33%. However, all our measurements were done $\sim$ 1000 cps to use optimum resolution.

4.12.5a Microphonics

In certain high resolution X-ray detectors with specific mounting configurations serious problems can arise due to their sensitivity to microphonics. The detector used in the present study was found to be very sensitive to microphonics. Fig.4.12.5.2 shows a typical spectrum of copper X-rays from a variable energy fluorescent X-ray source. The spectrum was recorded in a noise-free environment and the FWHM for copper Kα X-rays was measured to be 200 eV.

Serious degradation of resolution (Fig.4.12.5.3) was observed when the detector was employed to collect copper X-rays induced by protons generated from a 500 kV Van de Graaf accelerator. The beam room was noisy due to the presence of running belt and blower.

A series of experiments weredone to pinpoint the part of the detection system most sensitive to microphonics. In all these experiments noise generated from the running of the belt and blower in the Van de Graaf assembly was used as a source of microphonics and the standard copper source provided the X-ray spectrum. A cardboard box filled with foam acted as a microphonics shield. The following measurements were made:

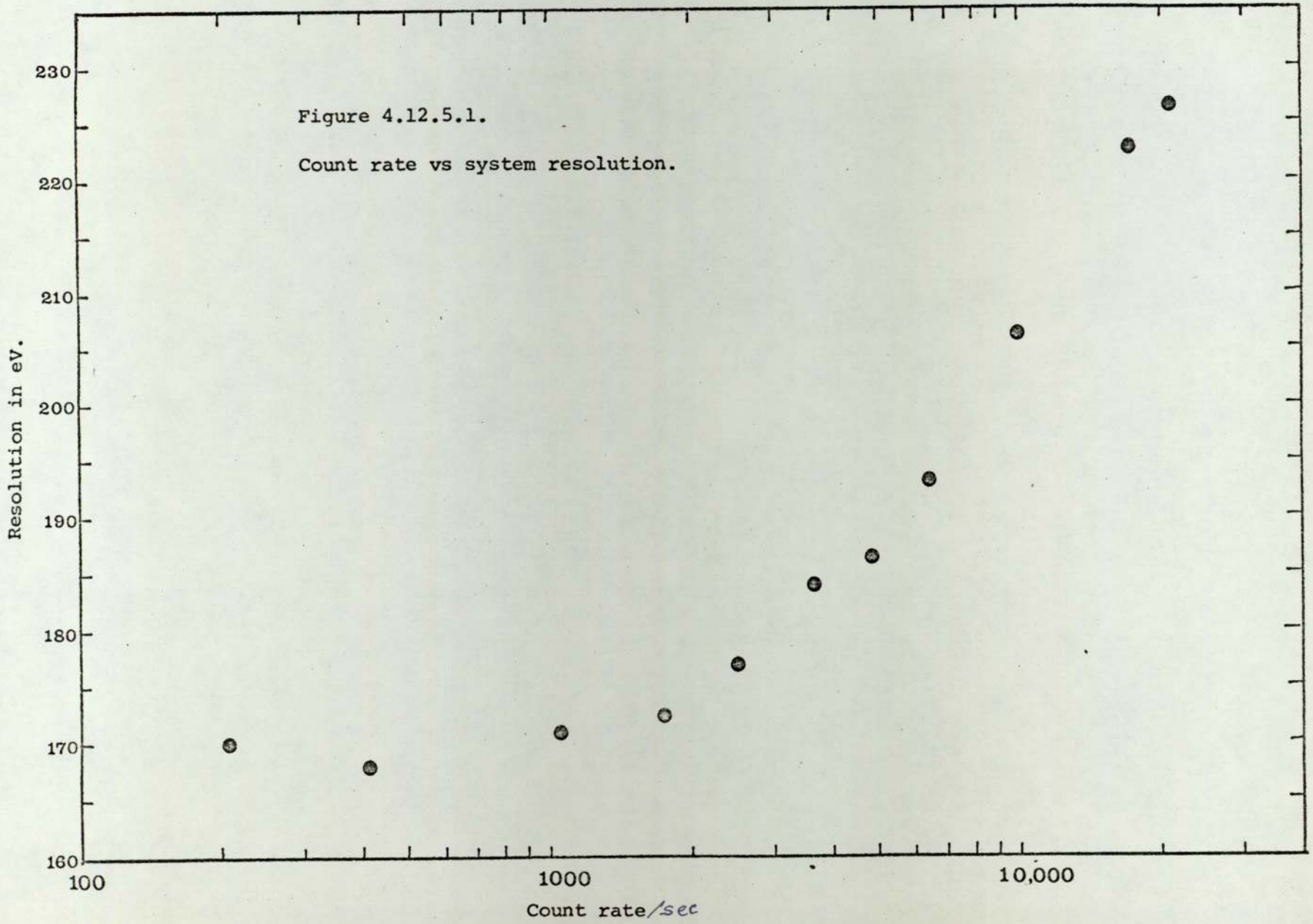

Figure 4.12.5.1.

Count rate vs system resolution.

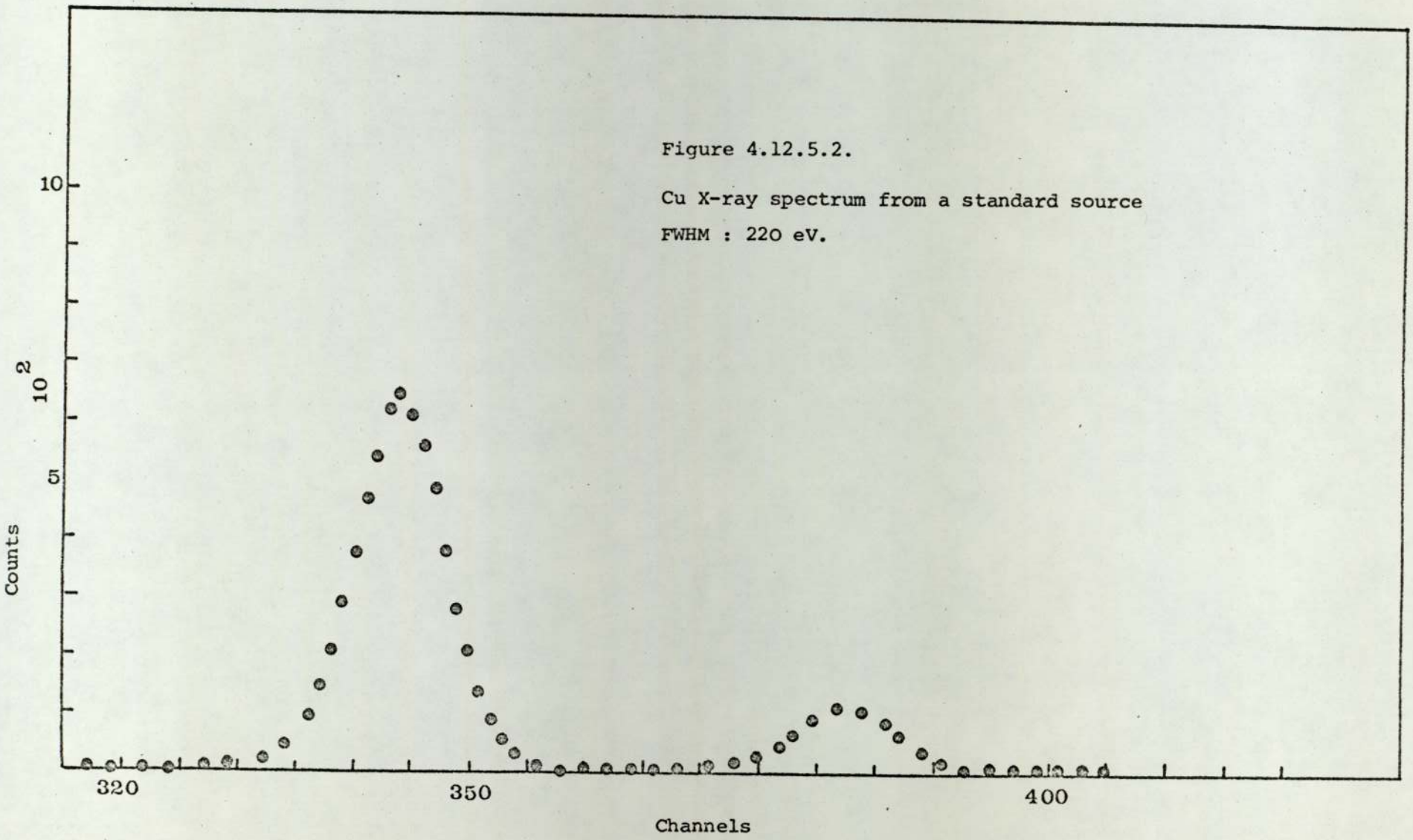

Figure 4.12.5.2.

Cu X-ray spectrum from a standard source

FWHM : 220 eV.

Figure 4.12.5.3.

Degradation of Cu spectrum due to microphonics.

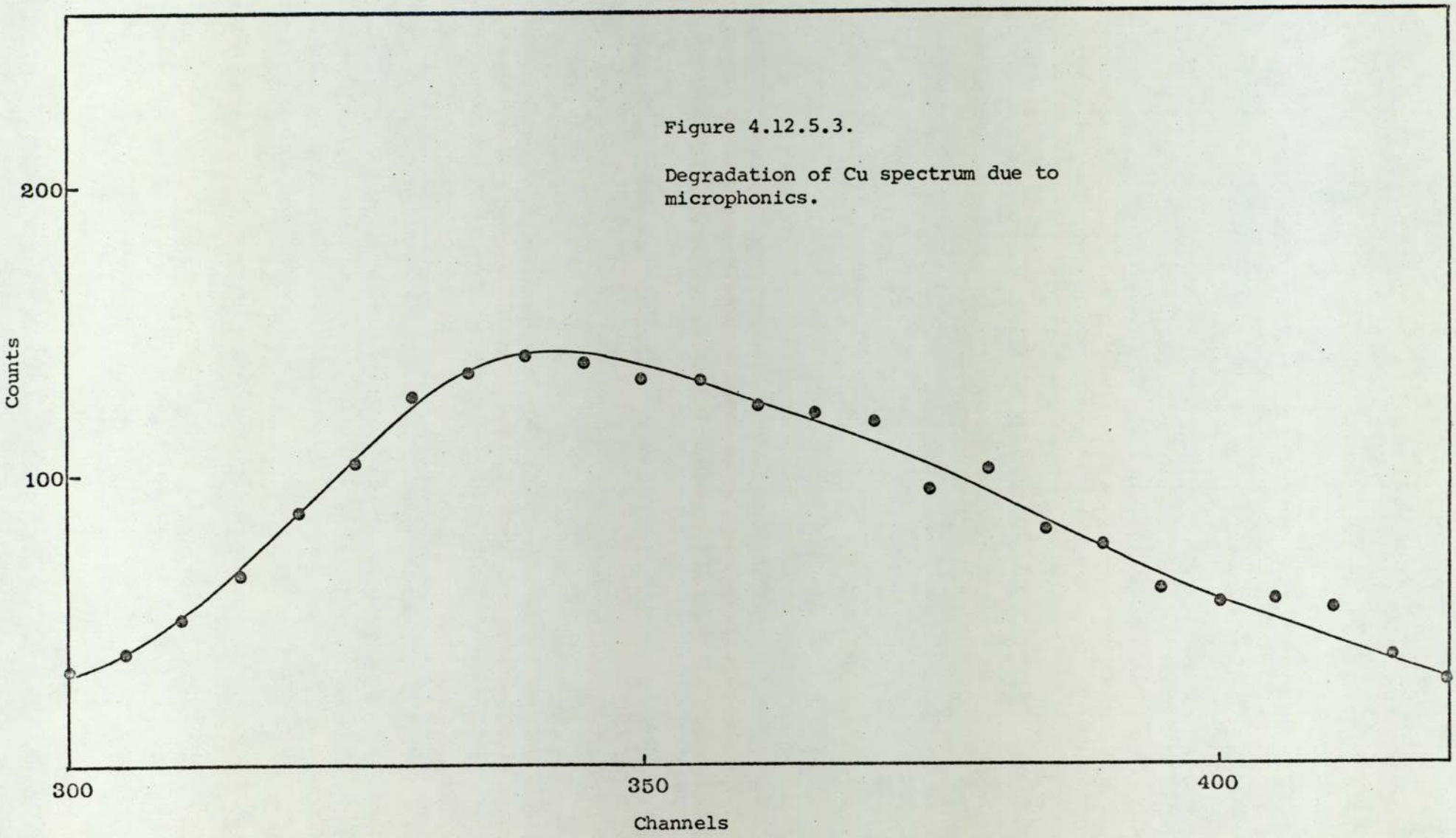

(i) Dewar and preamplifier was put inside the box. The resolution was found to be improved. FWHM was found to be 411 eV (Fig.4.12.5.4).

(ii) Dewar and preamplifier inside the box, with the top of the detector covered. No significant improvement was noted (Fig.4.12.5.5).

(iii) Dewar, preamplifier and detector head along with the source inside the box. The improvement in FWHM ($\sim$ 302 eV) was significant, Fig.4.12.5.6 and shows the inadequacy of the shielding.

No conclusive inference in terms of finding the most sensitive part could be drawn from these measurements.

It was found that even the bubbling of the liquid nitrogen when the dewar is just filled produces significant resolution degradation (Fig.4.12.5.7).

A survey of the scanty literature (MugA72, KeVI72) available suggests that any movements in the input circuit components relative to the surfaces at different potential may generate noise in the detector system. The sensitivity of this movement to the production of microphonics was illustrated by Elad et.al(ElaE65) as follows:

In order to produce a noise signal of amplitude 10eV in silicon a change of capacitance of only 5×10^{-7}pF between FET gate and high voltage (1000V) is required. The usual stray capacitance between the FET gate and high voltage is of the order of 1pF and hence a movement $\sim 10^{-7}$cm should contribute sufficiently. Most of the vibration problems are at relatively low energy and hence use of a limited amplifier pass band should filter out much of the microphonics noise. Consequently, the longer the shaping time constant the more serious should be the problem of microphonics.

Muggleton (MugA72) suggested that the following precaution be observed in the fabrication of detector-preamplifier package to improve the problem of microphonics:

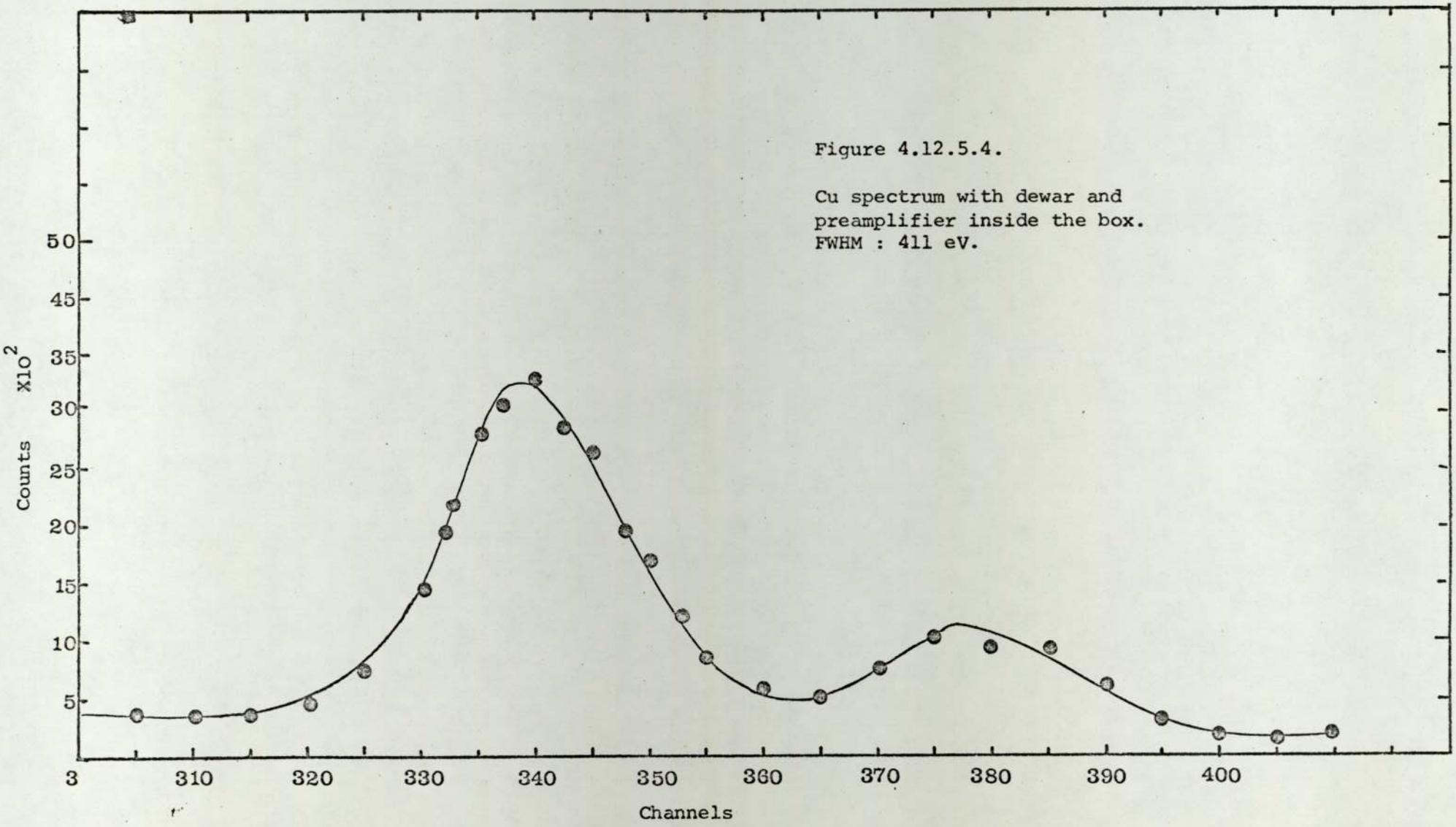

Figure 4.12.5.4.

Cu spectrum with dewar and preamplifier inside the box.
FWHM : 411 eV.

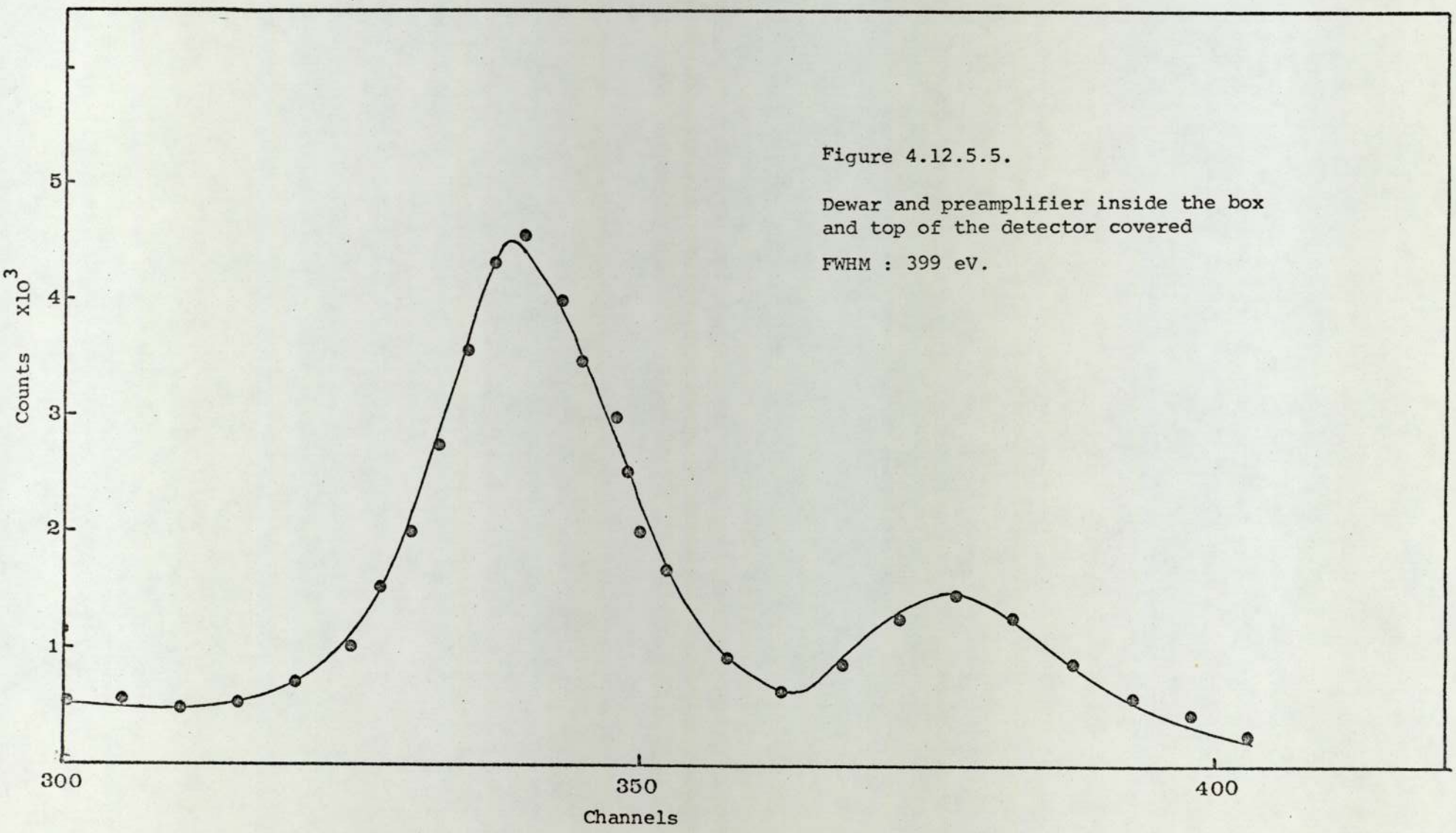

Figure 4.12.5.5.

Dewar and preamplifier inside the box and top of the detector covered

FWHM : 399 eV.

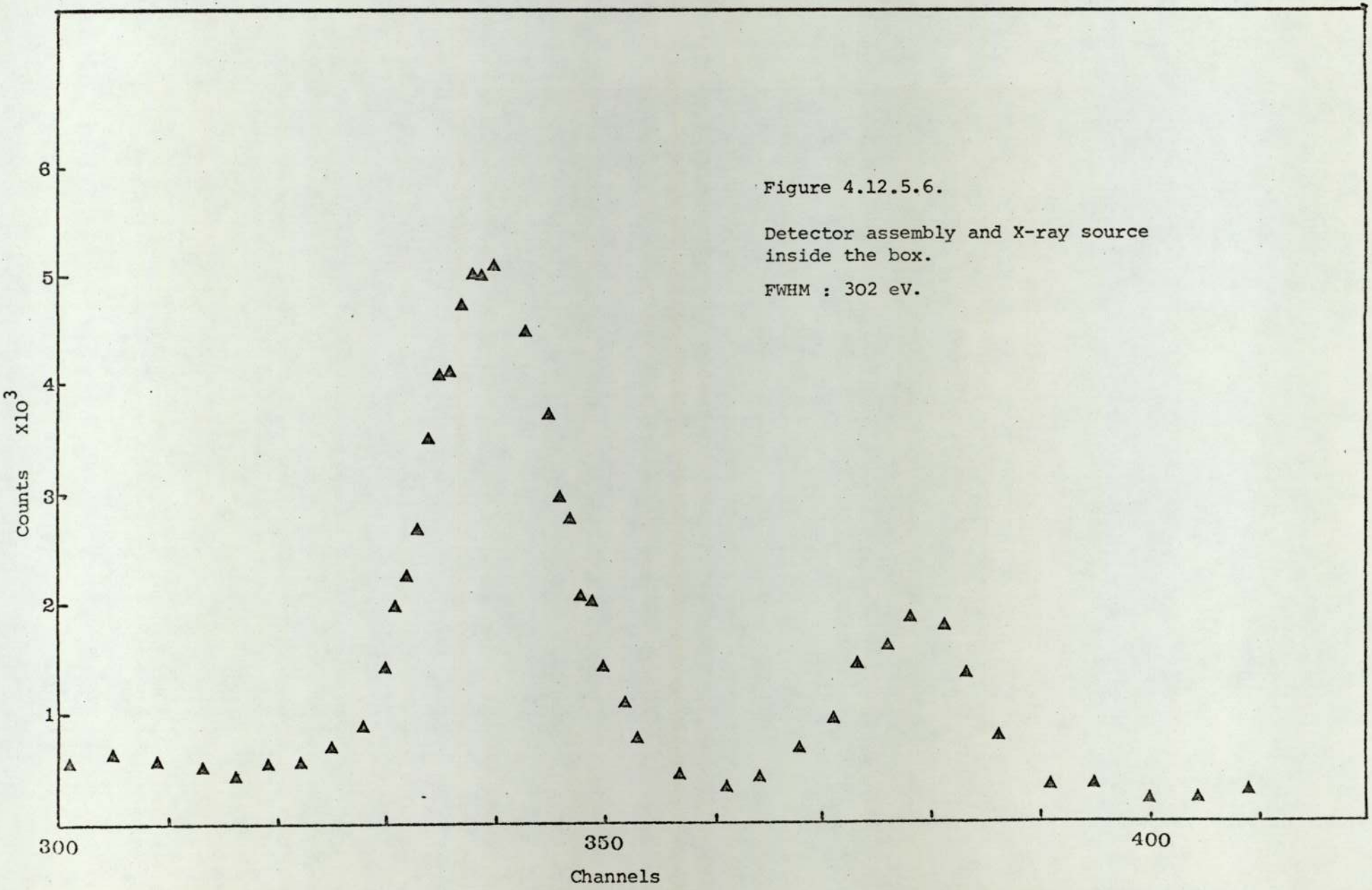

Figure 4.12.5.6.

Detector assembly and X-ray source inside the box.

FWHM : 302 eV.

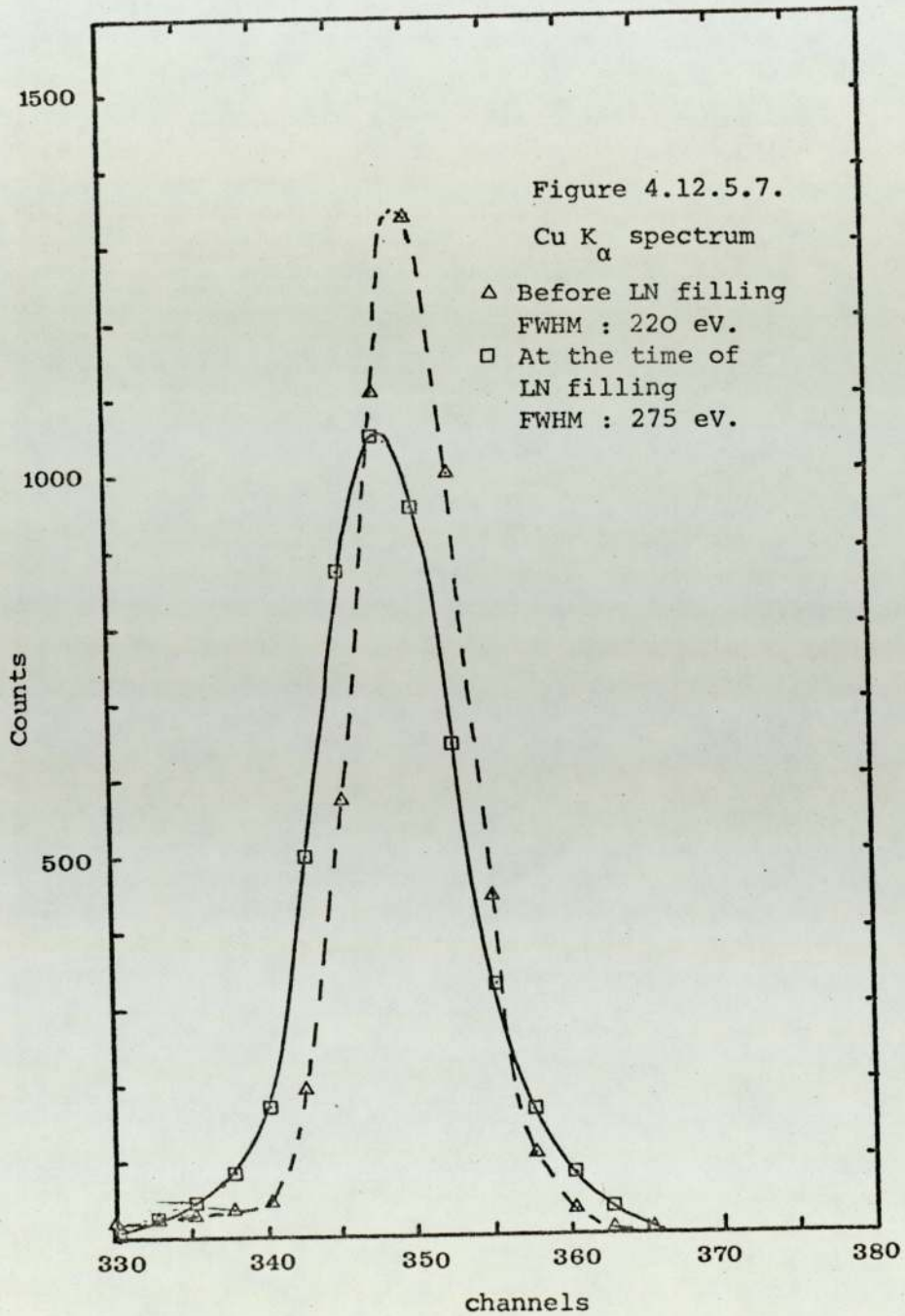
1500
1000
500
Counts
330
340
350
360
370
380
channels
Figure 4.12.5.7.
Cu K_α spectrum
△ Before LN filling
FWHM : 220 eV.
□ At the time of
LN filling
FWHM : 275 eV.

(i) Connectors between the detector and preamplifier should be of minimum length.

(ii) All wiring should be securely tied down.

(iii) Proper care should be taken to shield the FET from the high voltage lead and the internal connections should be such as to avoid any possibility of earth loops.

Though the use of foam and other materials may reduce the microphonics considerably, it is advisable to avoid noisy environments.

CHAPTER V

K X-ray Measurements

5.1 PROTON INDUCED K X-RAY THICK TARGET YIELDS

5.1.1 Theoretical

A thick target for an energetic proton, by definition, has a thickness greater than the range of the incident proton. However, it should be noted that in the case of proton induced X-ray production the contribution to the total X-ray yield by those X-rays produced deep in the target is insignificant for two reasons:

(i) At the present range of proton energies 1-3 MeV, for all elements studied, the production cross-section is a steeply increasing function of proton energy. The proton, as it goes deeper, loses its energy and its X-ray production efficiency decreases sharply.

(ii) The deeper the X-rays are produced within the target the longer the absorbing path they encounter while emerging from the target.

Consequently, under these conditions even a semi thick target acts as a thick target in the case of proton induced X-ray production. More than 90% of the total X-ray yield arises from the target thickness in which protons lose 30% of their energy. The contribution to the total thick target yield by the X-rays produced by protons after they have lost 70% of their energy is negligible.

If n is the number of atoms/cc in the target material, and E is the energy of the incident proton beam, the theoretical thick target yield $I_\mu(E)$ in photons/proton is given by

$$I_\mu(E) = n \int_E^0 \sigma(E_i) \frac{dE}{S(E_i)} e^{-\mu x} \text{ photons/proton} \qquad 5.1.1.1.$$

where $\sigma(E_i)$ = X-ray production cross-section

$S(E_i)$ = Stopping power of the material

μ = Linear absorption coefficient of the target for its own radiation

$$x = \int_{E}^{E_i} \frac{dE}{S(E)} \quad \frac{\cos\theta_i}{\cos\theta_e} \qquad 5.1.1.2$$

where

θ_i and θ_e are respectively the angle of incidence of the proton beam and angle of emergence of the X-rays to the target normal. These parameters are illustrated in Fig.5.1.1.1. In the present experimental arrangement where $\theta_i = \theta_e = 45^o$ equation 5.1.1.1 becomes

$$I_\mu(E) = n\int_{E}^{o} \sigma(E_i) \quad \frac{1}{S(E_i)} \exp\left[-\mu\int_{E}^{E_i}\frac{dE}{S(E_i)}\right] dE \qquad 5.1.1.3$$

In the particular case of low energy protons where $E<<450\ E_K$, E_K being the binding energy of the K shell, Merzbacher et al (MerE58) deduced an approximate relation for the inner shell ionization cross-section, which is directly proportional to E^4 and inversely proportional to z_2^{12},

$$\text{i.e.} \quad \sigma_I \ \alpha \ \frac{E^4}{z_2^{12}} \qquad 5.1.1.4$$

using the relation 5.1.1.4 and the non-relativistic approximation

$$\frac{dE}{dx} \ \alpha \ \frac{z_2}{E} \qquad 5.1.1.5$$

and assuming $\ell n \frac{2mv^2}{I}$ is a slowly varying function of energy, Dyson (DysN73) deduced a relation for $I_\mu(E)$ which can be shown to be proportional directly to E^6 and inversely to z_2^{13} i.e.

$$I_\mu(E) \ \alpha \ \frac{E^6}{z_2^{13}} \qquad 5.1.1.6$$

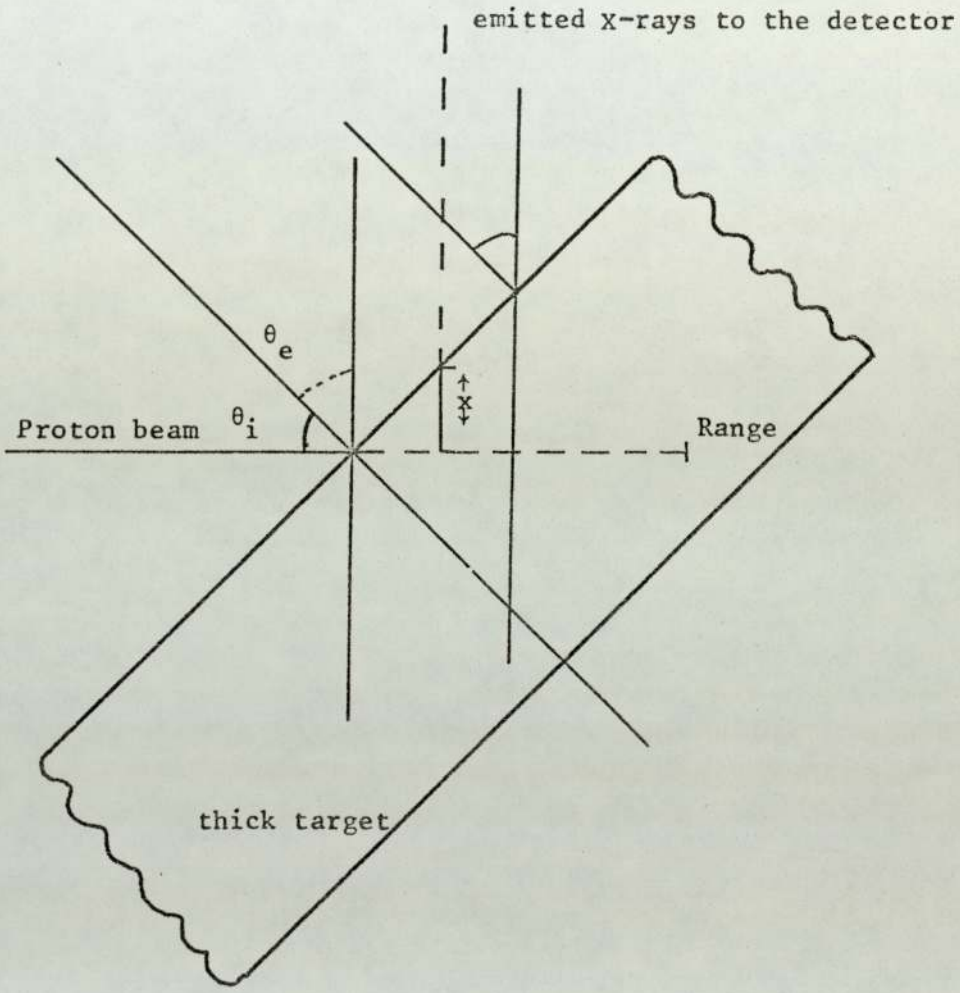

Fig. 5.1.1.1.

Meaning of the parameters used in the derivation of thick target formula.

5.1.2 Thick target yield measurements and data analysis

The X-rays produced in the target by the incident protons were detected by the detecting system and were accumulated in the nuclear data acquisition system for a fixed live time. The accumulated spectrum was displayed and the area under Kα and Kβ peak was estimated after proper back-ground substraction. The data thus represent the number of K X-ray photons produced by a certain number of protons, their charges being measured in microcoulombs by the beam current integration. A sample thick target spectrum is shown in Fig.5.1.2.1.

Each of our data points were measured several times to check for consistency and the mean was taken. Reproducibility of the measured data and any drift in Dynamitron energy during the measurements were checked by going back in several steps in energy and repeating one or two data. For energy stability the Dynamitron was also conditioned for several hours before any experiment. Where discrepancies were observed the whole set was remeasured and checked. The long term reproducibility was tested by measuring nickel thick target yieldsafter about a year in an entirely different set-up. The results were found to be reproduced satisfactorily. The effect of change in the range switch was tested and eliminated (section 4.3). All these precautions produced an entirely consistent set of data.

In order to calculate the experimental thick target yield Y_μ from the experimental data let us define

A = area of the detector exposed to the incident X-rays

N = number of X-rays counted under the peak

N_t = number of X-rays emitted from the target in a solid angle $d\Omega$ subtended by the detector area

then

$$N_t = N. C_{air}. C_{dw}. C_{thw}. C_{dt}/d_e \qquad 5.1.2.1$$

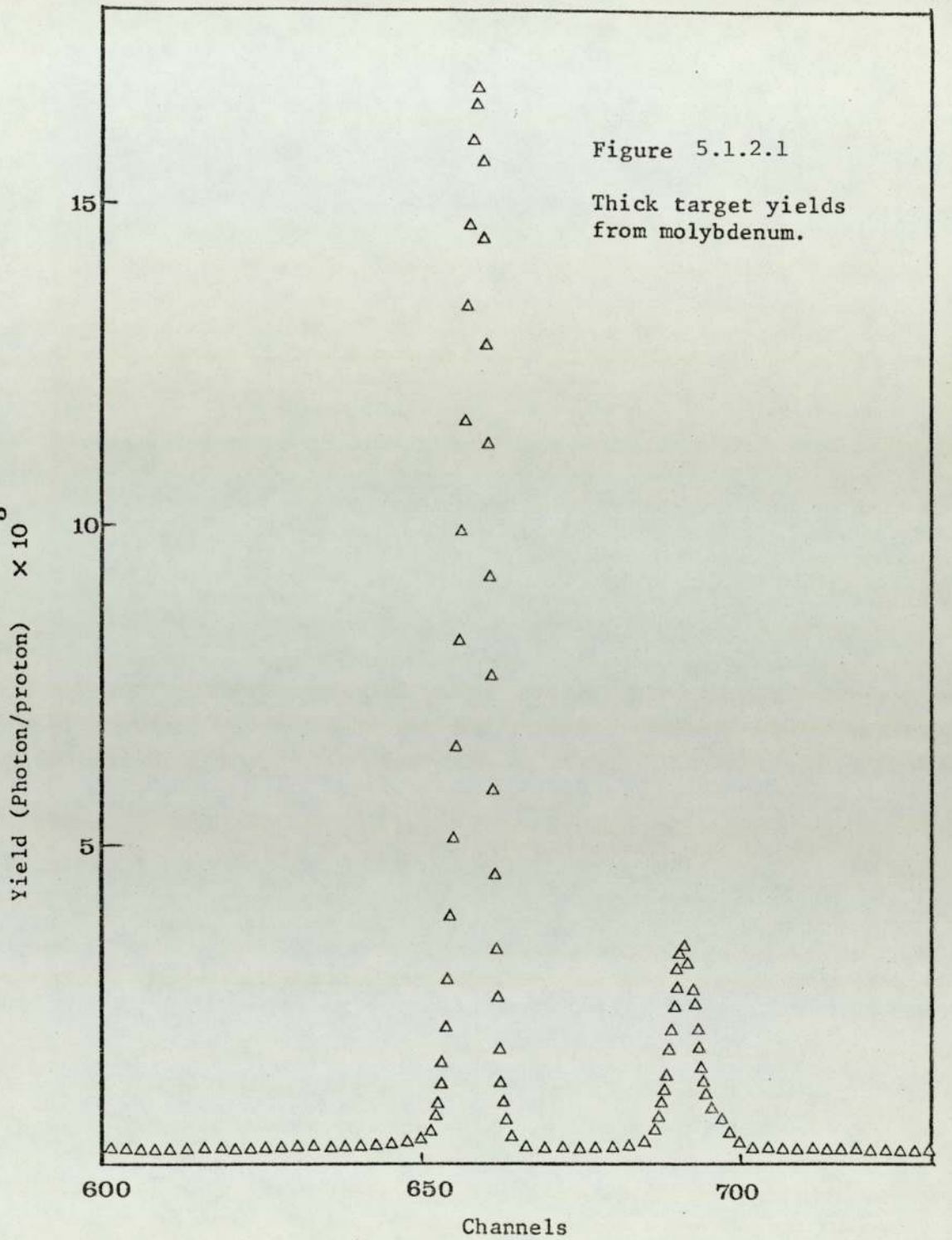

Figure 5.1.2.1

Thick target yields from molybdenum.

where

C_{air} = correction for the absorption in the airpath between the detector face and the target holder window.

= exp (air path length x μ_m of air x air density)

C_{dw} = correction for absorption in detector window.

= exp (det. window thickness x μ_m of det. window x density)

C_{thw} = correction for the absorption in target holder window.

= exp (target holder window thickness x μ_m of target holder window x density)

C_{dt} = dead time corrections

d_e = detector efficiency

Lewis et al (LewC72) have measured the angular distribution of charged particle induced X-rays at different energies and from different targets. They found that the emission was isotropic within 2%. On this assumption of isotropy the experimental thick target yield Y_μ in photons/proton at a given energy is found by integrating N_t over the solid angle $d\Omega$ and dividing by the number of protons. If Q is the integrated charge in μC, then N_p, the number of protons corresponding to this charge is given by

$$N_p = Q/(1.6 \times 10^{-13}) \qquad 5.1.2.2$$

and Y_μ is then given by

$$Y_\mu = \frac{4\pi d^2}{A} N_t/N_p \quad \text{Photons/proton} \qquad 5.1.2.3$$

where

d = distance between the point at which the beam hits the target and the centre of the detector crystal.

As discussed earlier (section 4.12.3) the detector area was defined by placing a lead aperture of precisely known area (area 13.077mm^2) on top of the detector crystal. The distance d was chosen to suit individual targets, such that the X-ray yield produced offered a count rate compatible with the input requirement of the detector characteristics, at the same time maintaining a reasonable current on the target. Two target holder windows were used. One made of 50μm thick aluminium foil and another 50μm thick melinex film. Melinex is the trade name of polyethyleneteraphthalate having the formula $(C_{10}H_8O_4)_n$. The average density is 1.39gm/cc and the mass absorption coefficients are tabulated in CRC Handbook of Chemical and Physical Constants (53rd Edition).

The live time of the detecting system was measured by feeding the busy output of the PPR into the live time measuring device (section 4.10). A clock timer was run together with the live timer and the current integrating system. A start stop device was used to stop the clock timer, current integrator and ADC data accumulation when the live timer stopped at a preset count. Dead time correction d_t was made by using the relation

$$d_t = \frac{\text{clock time}}{\text{live time}} \qquad 5.1.2.4$$

The live timer was set so that the statistical uncertainty in the accumulated data was at least better than 1%.

The detector efficiency d_e was calculated to a good approximation by the formula

$$d_e = 1 - e^{-\mu_m \times d_s} \qquad 5.1.2.5$$

as discussed in section 4.12.2.

Compilations of Storm and Israel (StoE74) and Miller and Greening (MilR74) were used for different mass absorption coefficients. Four to six order polynomials were fitted on different mass absorption coefficient data and their values at the specific energy were calculated from the polynomials. For air absorption at energies below the compilation of Miller and Greening (MilR74), data of Storm and Israel (StoE74) for nitrogen, oxygen and argon were used along with their respective percentage weight abundance to calculate the mass absorption coefficient of air. Where these calculated data overlapped with the tabulation of Miller and Greening they were found to agree within 1%.

The density of air was calculated using the formula given by

$$d = \frac{.001293}{1+.00367t} \quad \frac{H}{76} \qquad 5.1.2.6$$

where t is the temperature in ^{o}C and H is the atmospheric pressure in cm. A $2^{o}C$ change in temperature produces .7% change in air density and 1cm change in pressure produces 1.4% change in air density and hence 1cm increase in pressure with a $2^{o}C$ decrease in temperature produces a change of 1.56% in the density. Since this change in density in some cases produces a change $\sim$ 5% in the total absorption correction, temperatures and pressures were monitored in the beam room at the time of experiment.

The integration of X-ray peaks was achieved using the following formula:

$$\text{PEAK Area} = \sum_{a}^{b} (C_i - Y_i) \qquad 5.1.2.7$$

where C_i is the number of counts in the i^{th} channel and Y_i is the estimated background in the same channel, a and b are the specified starting and ending channel respectively. Y_i is calculated from a

straight line fit $Y_i = mX_i + C$ on the averaged background counts on the endpoints. The average is estimated on a specified number of channels. The programme PEAK that uses this formula is available in Hewlett Packard data acquisition system.

5.1.3 Error Analysis

The total uncertainty in the measured thick target yields consists of the uncertainty in the estimate of the following parameters:

(1) Absorption corrections, (a) C_{air}, corrections due to the absorption in the air path, (b) C_{thw}, corrections due to the absorption in the target holder window, (c) C_{dw}, corrections due to the absorption in detector window, (d) detector efficiency. (2) Source to detector distance and detector area. (3) Dead time corrections. (4) Peak integration. (5) Current integration. (6) Statistical uncertainty.

(1) Absorption corrections, (a) C_{air} : For the K shell yield measurement for the X-rays from low atomic numbers the correction factor due to absorption in the air path was largest. The uncertainty in the estimate of this correction factor arises due to the uncertainty in the density of air, airpath length and the error in the mass absorption coefficient values. Assuming an uncertainty of 2mm in pressure and $1^{o}C$ uncertainty in the temperature, produces an uncertainty in the density measurement $\sim$ .3%, combining this to the .5% uncertainty (on the basis of 2mm error in the distance measurement) on the airpath length and 1% uncertainty in the mass absorption coefficient (1% uncertainty is quoted by Miller and Greening) the total uncertainty in $\mu_m \times \ell \times d$ is 1.16%. If this uncertainty is incorporated in $C_{air} = \exp(\mu_m \ell d)$ for titanium, the highest value of uncertainty in C_{air}, $\sim$ 3.8%, is obtained. The values of total air absorption corrections with associated uncertainties are

given in column 2 of table 5.1.3.1. The same column shows that for higher atomic numbers the corrections involved are only a few per cent and the errors in them are negligible.

(b) C_{thw} : The uncertainty in the absorption corrections for the target holder window material arises due to the uncertainty in the thickness, density and μ_m, the mass absorption coefficient of the window material. In the case of titanium measurements an aluminium window was used. Assuming a 2% uncertainty in the foil thickness and 1% uncertainty in the μ_m values and incorporating them in C_{thw} an uncertainty of 7.3% is estimated for titanium. For the other measurements a melinex window was used and the absorption corrections are small. Even allowing a 5% uncertainty in the thickness of melinex, a 5% uncertainty in the quoted mass absorption coefficient together with a 2% uncertainty in the density then the combined uncertainty in $\mu_m xd$ is found to be about 7.4% which produces 2.5% uncertainty in the value of C_{thw} for vanadium. The values of C_{thw} along with their percentage uncertainty is given in column 3 of table 5.1.3.1.

For the higher Z elements $Z \geq 42$ total C_{thw} corrections are <1% and uncertainties in them are negligible.

(c) C_{dw} : The maximum correction for the absorption of radiation in the detector window is $\sim$ 1.01 and is given in column 4 of the table 5.1.3.1. The uncertainties are negligible.

(d) d_e : Detector efficiency d_e was the largest correction factor for higher Z elements ($Z \geq 42$). Assigning an arbitrary uncertainty of 10% to the specified value of thickness, 3mm for the crystal and 1% uncertainty in μ_m the maximum uncertainty in d_e in case of tin K X-rays is estimated to be $\sim$ 4.6%. They are given in column 5 along with d_e in the table 5.1.3.1.

Table 5.1.3.1

Correction factors involved in different parameters in the measurements of K shell thick target yields and uncertainties in them.

Element	C_{air}	C_{thw}	C_{dw}	d_e	Total	Total uncertainty
Titanium	27.2 ± 3.8%	29.2 ± 7.8%	1.01 ± .04%	1.00	804 ± 8.2%	8.4%
Vanadium	7.0 ± 2.2%	1.29 ± 2.5%	1.01 ± .04%	1.00	9.03 ± 3.3%	3.9%
Iron	4.5 ± 1.7%	1.12 ± 1.1%	1.00	1.00	5.09 ± 2.0%	3.8%
Nickel	2.1 ± .9%	1.10 ± 1.0%	1.00	1.00	2.29 ± 1.4%	2.7%
Nickel*	2.2 ± .9%	1.10 ± 1.0%	1.00	1.00	2.38 ± 1.4%	2.7%
Copper	1.8 ± .7%	1.05 ± .5%	1.00	1.00	1.85 ± .9%	2.4%
Zinc	1.4 ± .4%	1.05 ± .5%	1.00	1.00	1.51 ± .6%	2.1%
Molybdenum	1.06 ± .1%	1.04 ± .4%	1.00	.986 ± .7%	1.11 ± .8%	2.2%
Silver	1.04	1.00	1.00	.89 ± 3.0%	1.17 ± 3.0%	3.6%
Cadmium	1.04	1.00	1.00	.85 ± 3.6%	1.22 ± 3.6%	4.1%
Indium	1.02	1.00	1.00	.82 ± 4.2%	1.26 ± 4.2%	4.7%
Tin	1.02	1.00	1.00	.78 ± 4.6%	1.32 ± 4.6%	5.0%

* Repeat.

(2) Detector area A and the distance between the target and the centre of detector : Source to detector distance measured with the jig (section 4.4) is estimated to be accurate within 2mm. This uncertainty in the distance produces negligible error in the yield measurement. The error in the detector area is considered negligible.

All the uncertainties discussed so far are systematic and are added together to produce the total in column 6 of the table 5.1.3.1. This systematic uncertainty was then combined to the maximum random uncertainty of one per cent each on the measurement of dead time (section 4.12.4), current (section 4.3), peak integration and statistical uncertainty and is given in the last column of table 5.1.3.1.

5.1.4 Results and discussions on measured thick target yields.

The results of proton induced thick target yields in the energy region 1-3 MeV from the elements Ti, V, Fe, Ni, Cu, Zn, Mo, Ag, Cd, In and Sn are shown along with the results of other workers in the figures 5.1.4.1 to 5.1.4.3. The lack of experimental thick target yields, in this energy region is clearly demonstrated in these figures. Where measurements have been reported there is little agreement between authors. In addition the internal consistency of the reported measurements is often very poor. Whereas the internal consistency of the present data is very good. This was evidenced when fourth to sixth order polynomials were fitted to log Y_μ and log E. The difference between the thick target yield calculated from the polynomial and the experimental data was usually less than 2% and never exceeded 5% (column 4, Table 5.2.2.1). The numerical thick target yield data are presented in column 2 and those calculated from the polynomial fit are given in column 3 in tables 5.2.3.1 to 5.2.3.12.

No thick target yield data was found to be reported in this

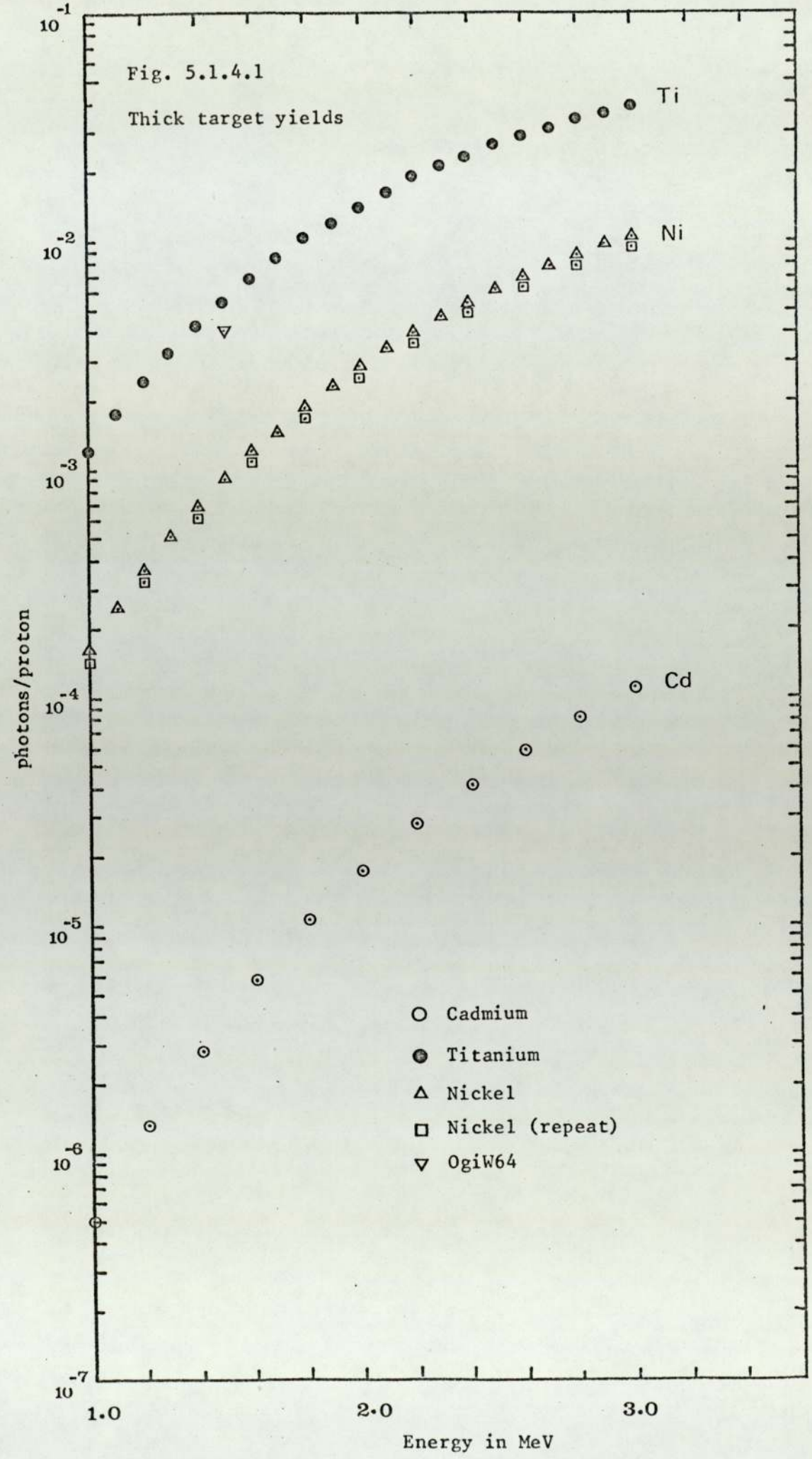
Fig. 5.1.4.1
Thick target yields
Ti
Ni
Cd
photons/proton
Energy in MeV
1.0
2.0
3.0
Cadmium
Titanium
Nickel
Nickel (repeat)
OgiW64

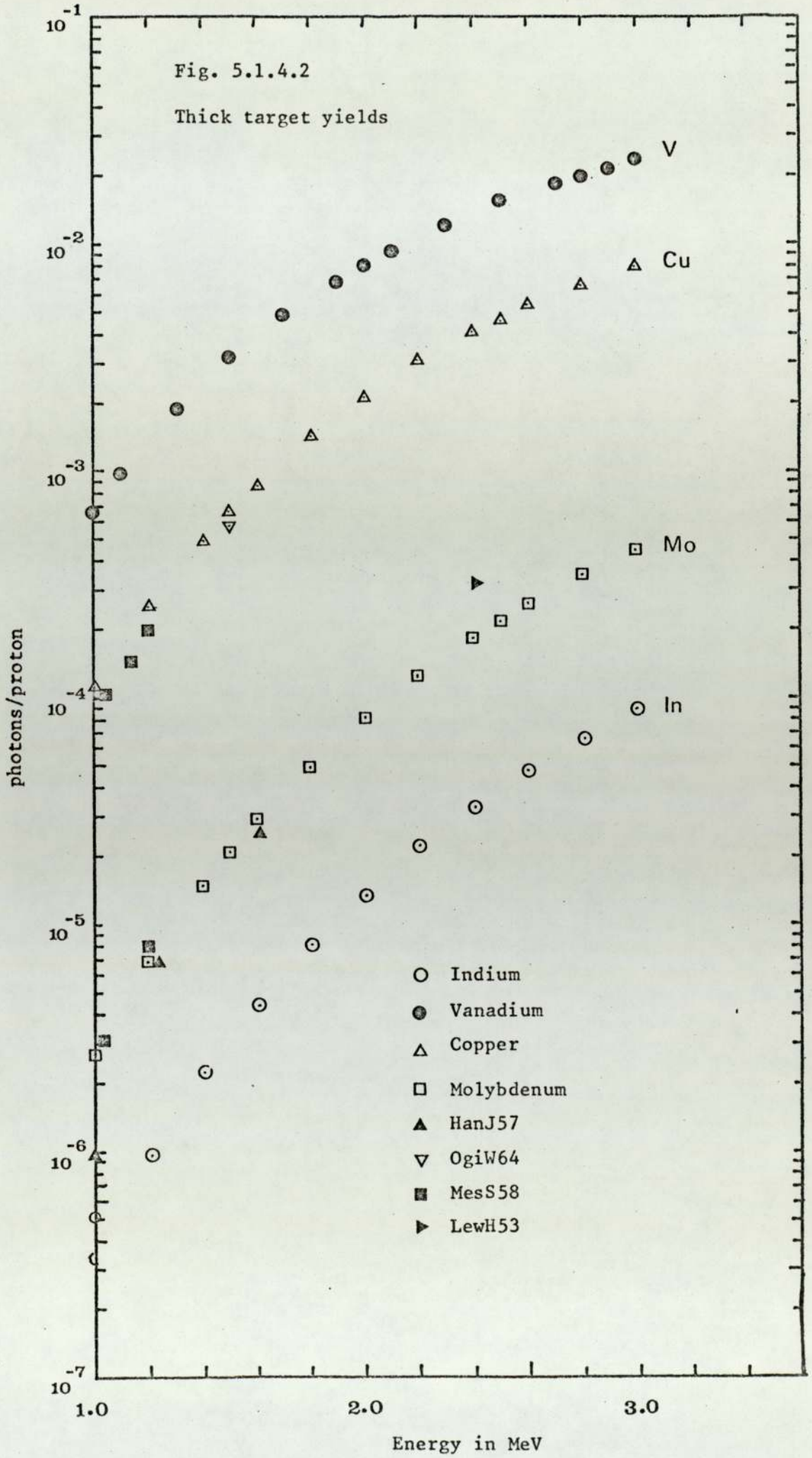
Fig. 5.1.4.2
Thick target yields
V
Cu
Mo
In
photons/proton
Energy in MeV
1.0
2.0
3.0
Indium
Vanadium
Copper
Molybdenum
HanJ57
OgiW64
MesS58
LewH53

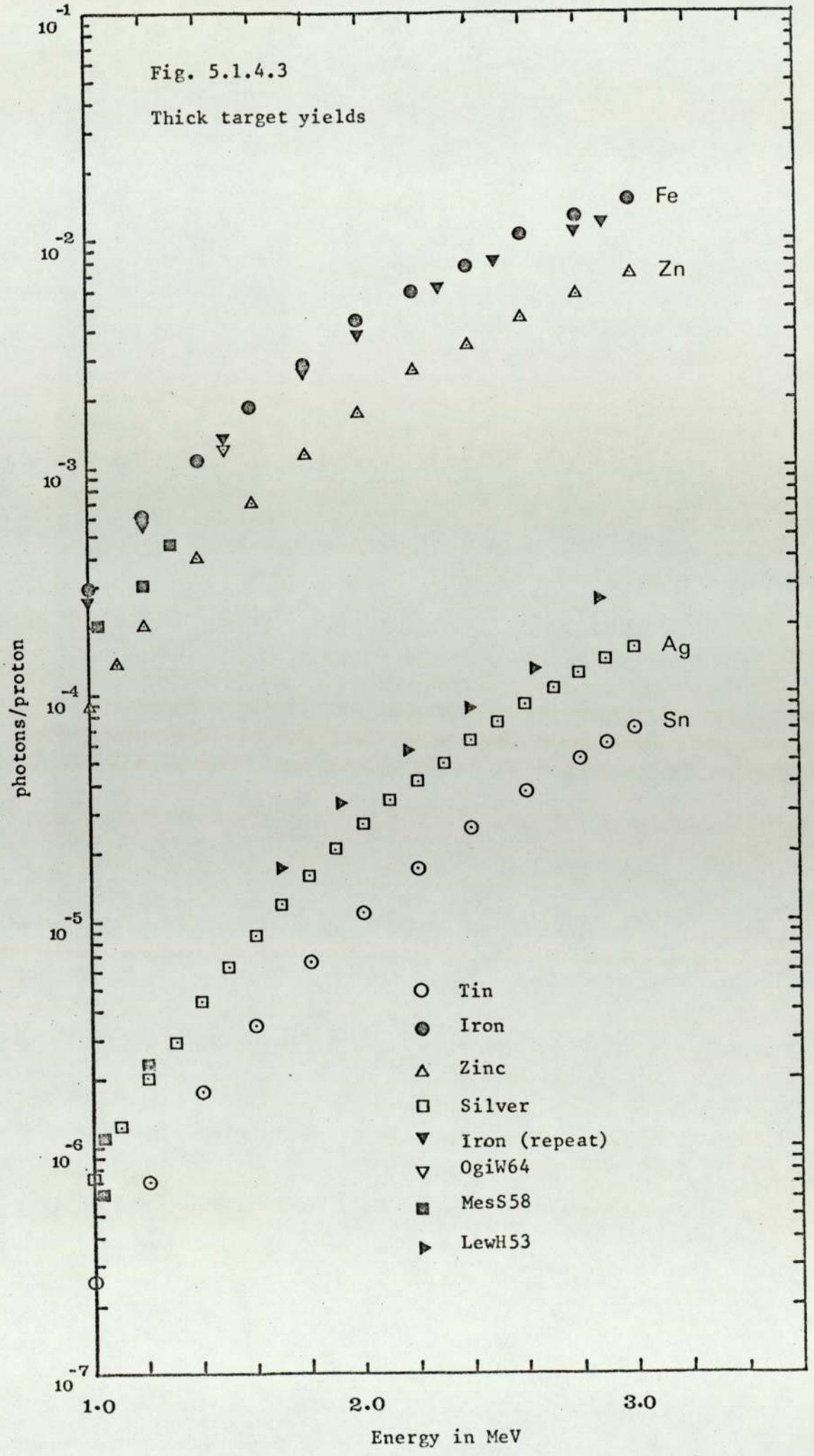
Fig. 5.1.4.3
Thick target yields
photons/proton
Energy in MeV
1.0
2.0
3.0
Fe
Zn
Ag
Sn
Tin
Iron
Zinc
Silver
Iron (repeat)
OgiW64
MesS58
LewH53

energy region for the elements vanadium, nickel, cadmium and indium (Fig.5.1.4.1 - Fig.5.1.4.3). A thick target yield for titanium measured by Ogier (OgiW64) at 1.5 MeV is lower than the present measurement by ∿ 30% (Fig.5.1.4.1) whereas for iron at the same energy his measurement agrees with the present work within experimental error. The values reported by Messelt (MesS58) for iron up to 1.3 MeV are consistently below present measurements by ∿ 70% (Fig.5.1.4.3).

Measurements reported by Messelt (MesS58) and Ogier (OgiW64) on copper are lower than the present work by ∿ 20% whereas a solitary measurement at 1 MeV by Hansteen and Messelt (HanJ57) is above the present measurement by ∿ 20% (Fig.5.1.4.2). Reported values of Messelt (MesS58) and Hansteen and Messelt (HanJ57) on molybdenum agree reasonably well with the present measurement except one point of Hansteen et.al at 1 MeV (Fig.5.1.4.2).

The data of Lewis et.al (LewH53) on silver thick target yields are systematically higher than the present measurement by ∿ 25% except the last point at 2.88 MeV which shoots up abnormally, whereas the corresponding measurements of Messelt (MesS58) are in agreement with the present work (Fig.5.1.4.3).

A solitary measurement at 1.04 MeV by Messelt (MesS58) exists in this energy region for tin and is much higher than the present work (Fig.5.1.4.3).

To check the inter-element consistency the measured thick target yields of different elements at 1, 2 and 3 MeV are plotted against their atomic numbers (Fig.5.1.4.4). The majority of the data points agree within experimental error with the smooth curves drawn except for (1) titanium at 1 and 2 MeV, where they are above the curve by about 30%. (2) vanadium, which is lower by about 40% at 3 MeV, and (3) silver, which is above the curves at all the three energies by

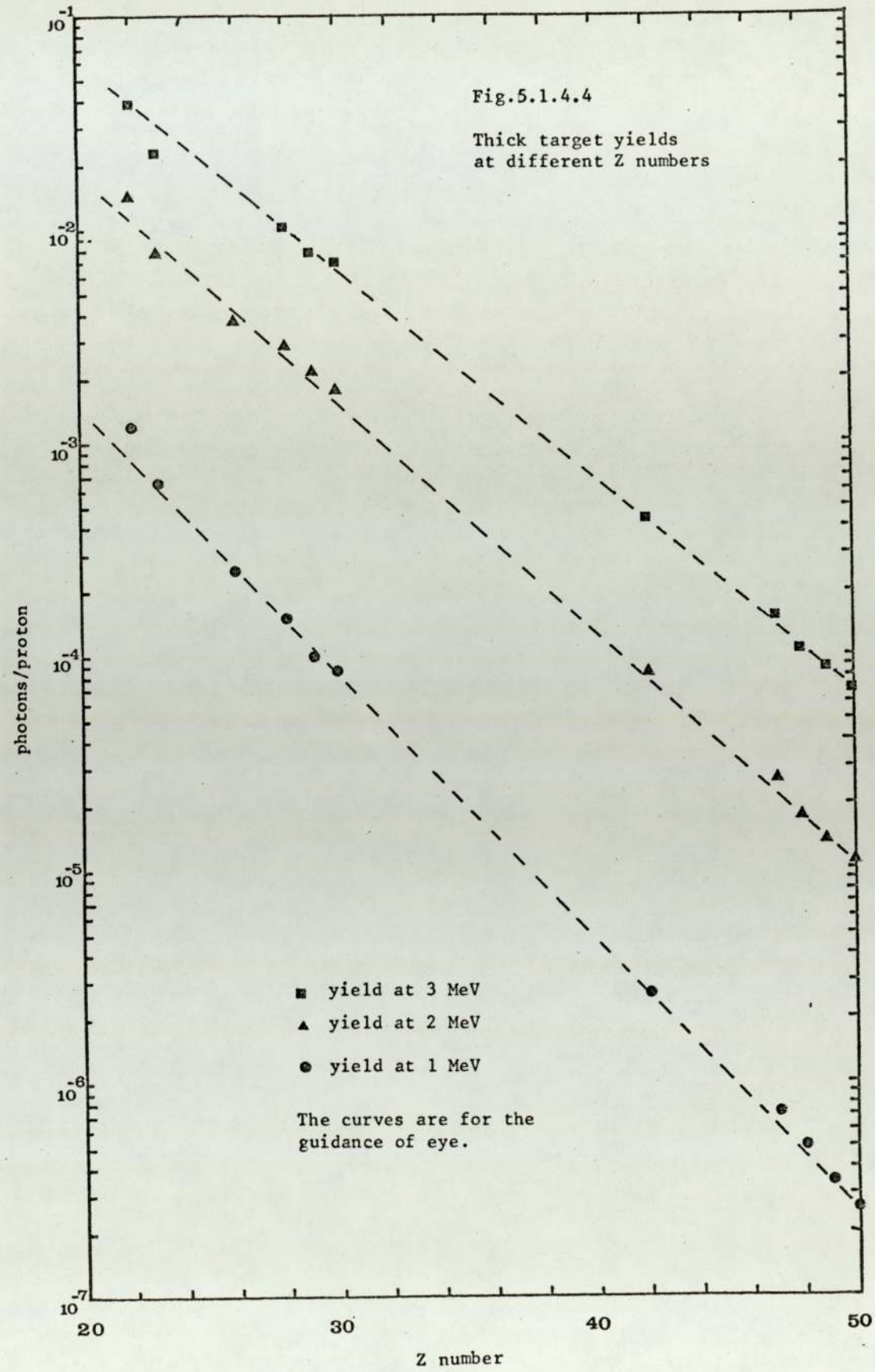
Fig.5.1.4.4
Thick target yields
at different Z numbers
photons/proton
Z number
yield at 3 MeV
yield at 2 MeV
yield at 1 MeV
The curves are for the
guidance of eye.
10^-1
10^-2
10^-3
10^-4
10^-5
10^-6
10^-7
20
30
40
50

about 15-20%. This may indicate the presence of systematic over-estimation of silver thick target yields.

To test the validity of Z^{-13} dependence (section 5.1.1) of thick target yield in the energy region $E<<450\ E_K$, (meaning of << is assumed to be less at least by a factor of 10) which among the present measurements is only valid for silver, cadmium, indium and tin at 1 MeV, the log yield for these elements at 1 MeV is plotted against log Z(Fig.5.1.4.5). The slope obtained from a least square fit on these points is found to be greater than predicted and is ~ -16.8. However, any rigorous conclusion on Z^{-13} dependence on the basis of the present measurement might be misleading for (1) the energy and Z combination just satisfy the condition $E<<450\ E_K$ and (2) the range of Z number used here is very small. To make any conclusive remark one has to make measurements on a wider range of z number within the restriction $E<<450\ E_K$.

To check the reproducibility of the measured thick target yield data, measurements were repeated on nickel in an almost entirely different experimental configuration after about a year. The thick target yields were found to be reproduced within experimental error (Fig.5.1.4.1).

5.2 K SHELL IONIZATION CROSS-SECTIONS

5.2.1 Derivation of cross-section from thick target yields.

K Shell production cross-sections can be derived from the formula 5.1.1.1 by the application of Liebnitz rule which gives:

$$\sigma_x(E) = \frac{1}{n}\left[\frac{dI_\mu(E)}{dE}\cdot S(E)\frac{dx}{dx_o} + \mu\frac{\cos\theta_i}{\cos\theta_e} I_\mu(E)\right] \qquad 5.2.1.1$$

where θ_i and θ_e are illustrated in Fig.5.1.1.1, S(E) is the stopping power of the material and $\frac{dx}{dx_o}$ is known as the detour factor. x and

Fig. 5.1.4.5

Thick target yield vs log Z.

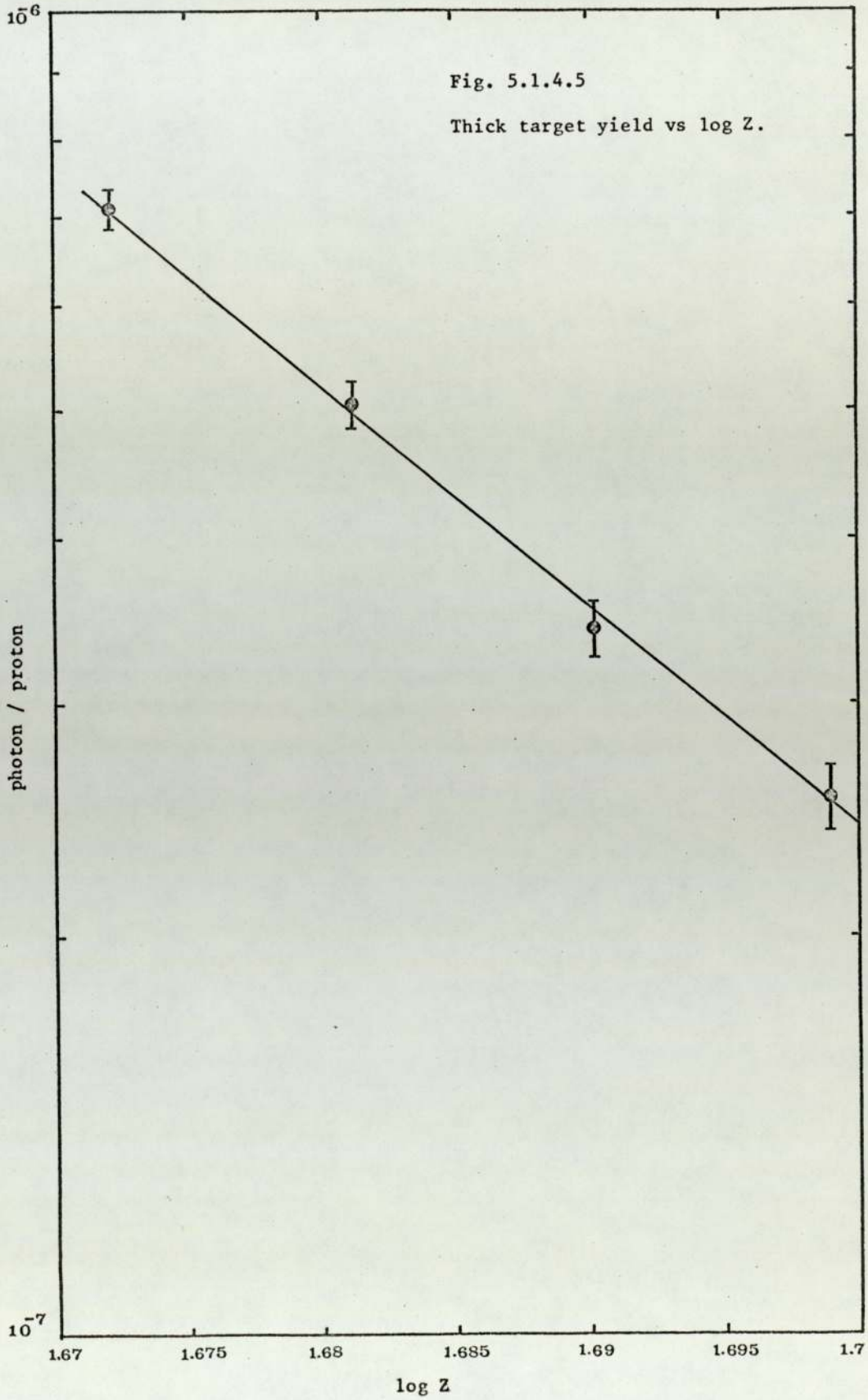

x_o are respectively measured along the actual beam path in the target and along the projected path of the beam. The detour factor takes account of the deviation of the beam from the projected path inside the target. For a proton beam however the detour factor $\frac{dx}{dx_o} = 1$ to a good approximation.

Implicit in equation 5.2.1.1 are the assumptions,
(i) that the trajectory of the beam inside the target is a straight line and is along the line of incidence of the beam (ii) stopping power S(E) is smooth and there exists a unique relation between the energy of the particle and its distance from the point of incidence. (iii) X-ray production by back-scattered protons is negligible, (iv) the total X-ray production by the protons at a certain depth is that due to protons having the average energy at that point.

In the rigorous sense none of these assumptions hold true. The deeper the beam penetrates into the target the more the particles deviate from a straight path due to multiple coulomb scattering thus violating the first assumption. Spread in particle energy from their mean energy also increases for the same reason. If the energy distribution of the particle at a certain depth is assumed Gaussian, the X-rays produced by the particle having energies greater than the mean energy cannot be assumed equal to those produced by the same number of particles having energies lower than the mean energy due to the steep dependence of the production efficiency on energy. Thus energy straggling violates assumption ii, iii and iv together. Moreover, as the particles deviate from the straight path, X-rays produced are subjected to different absorption paths while emerging from the target. However, for protons and other light ions all these assumptions hold true to a very good approximation, McKnight et al (McKR75).

To derive the X-ray production cross-section from the measured thick target yield $Y_\mu(E)$ at an energy E, equation 5.2.1.1 is

rewritten in terms of $Y_\mu(E)$ and is given by:

$$\sigma_x(E_1) = \frac{1}{n}\left[\frac{dY_\mu(E)}{dE} S(E) + \mu \frac{\cos\theta_i}{\cos\theta_o} Y_\mu(E)\right]_{E = E_1} \qquad 5.2.1.2$$

A fourth to sixth order polynomial was fitted to the log $Y_\mu(E)$ and log E data and the values of fitted thick target yield $Y'_\mu(E)$ were obtained from the polynomials. The internal consistency of the present data was such that the values of $Y'_\mu(E)$ agree within 2% with the experimental thick target yield $Y_\mu(E)$. The difference never exceeded 5%. The slope $\frac{dY'_\mu(E)}{dE}$ was then calculated from the equation of the polynomial. Replacing $\frac{dY_\mu(E)}{dE}$ in equation 5.2.1.2. by $\frac{dY'_\mu(E)}{dE}$ and applying the experimental condition $\theta_i = \theta_o$ (section 4.5) equation 5.2.1.2. is rewritten as:

$$\sigma_x(E_1) = \frac{1}{n}\left[\frac{dY'_\mu(E)}{dE} S(E) + \mu Y_\mu(E)\right]_{E = E_1} \qquad 5.2.1.3$$

from which $\sigma_x(E)$ is calculated.

The values of $\frac{dE}{dx}$ were taken from the compilation of Janni (JanJ66) except in the case of indium where calculations done by O'Connel (ConB75) were used. $\frac{dE}{dx}$ values used in the cross-section evaluation are presented in column four of table 5.2.3.1 to table 5.2.3.12.

For the values of linear absorption coefficients μ, the photon absorption cross-section tabulations of Storm and Israel (StoE74) were used. Their cross-section values were converted to mass absorption coefficients and fourth to sixth order polynomials were fitted to them. Values of mass absorption coefficients at the required energy were calculated from the polynomials and were multiplied by the appropriate density to obtain the linear absorption coefficients μ.

Table 5.2.1.1

22/ 9/75 PROG. SIGMAFIT

CALCULATION OF PROTON INDUCED X-RAY PRODUCTION AND INNER SHELL IONISATION
CROSS-SECTION OF COPPER K (8.136 KEV) WITH AT.WT.= 63.54 DENSITY= 8.92
MASS ABSORPTION COEFFICIENT FOR THE TARGET ITSELF= 49.61
FLUORESCENT YIELD= .445 USING JANNI'S SPECIFIC ENERGY LOSS DATA

E	Y(M)	Y(M)F	%DIFF	DY(M)F/DE	DE/DX	SIGMA(P)	SIGMA(I)	RATIO
1.0	1.12E-04	1.12E-04	0.00	5.39E-04	1.084E+03	7.51E-24	1.68E-23	11.746
1.2	2.55E-04	2.55E-04	-0.00	9.17E-04	9.764E+02	1.19E-23	2.68E-23	7.923
1.4	4.92E-04	4.93E-04	-0.15	1.49E-03	8.905E+02	1.83E-23	4.12E-23	6.102
1.5	6.65E-04	6.60E-04	0.66	1.86E-03	8.563E+02	2.23E-23	5.02E-23	5.464
1.6	8.60E-04	8.68E-04	-0.90	2.28E-03	8.211E+02	2.67E-23	6.00E-23	4.882
1.8	1.43E-03	1.41E-03	1.04	3.21E-03	7.650E+02	3.64E-23	8.19E-23	3.921
2.0	2.12E-03	2.15E-03	-1.51	4.15E-03	7.172E+02	4.65E-23	1.04E-22	3.125
2.2	3.11E-03	3.06E-03	1.62	4.97E-03	6.759E+02	5.58E-23	1.25E-22	2.476
2.4	4.12E-03	4.13E-03	-0.22	5.61E-03	6.401E+02	6.41E-23	1.44E-22	1.966
2.5	4.62E-03	4.70E-03	-1.75	5.87E-03	6.233E+02	6.79E-23	1.52E-22	1.758
2.6	5.38E-03	5.30E-03	1.48	6.11E-03	6.084E+02	7.17E-23	1.61E-22	1.583
2.8	6.56E-03	6.57E-03	-0.18	6.59E-03	5.805E+02	7.97E-23	1.79E-22	1.316
3.0	7.95E-03	7.95E-03	-0.00	7.28E-03	5.559E+02	8.95E-23	2.01E-22	1.150

The production cross-section, σ_x, calculated from equation 5.2.1.3 is divided by the appropriate fluorescent yield ω_K to obtain the ionization cross-section σ_I. The values of the fluorescent yields are taken from the fitted values of Bambynek et. al. (BamW72). The values of μ, ω_K and E_K for different elements are presented at the top of the table 5.2.3.1 - table 5.2.3.12. A sample computer output for the calculation of ionization cross-section is given in table 5.2.1.1.

The first column of this table gives the proton energy E. The experimental yield Y(μ) and the fitted yield Y(μ)F are presented in column 2 and 3 respectively. The percentage difference, % DIFF, between the experimental and fitted yields are given in column 4. Slope of the excitation function dY(μ)F/dE, and dE/dx are tabulated in colums 5 and 6 respectively. Columns 7 and 8 SIGMA(P), represent the production cross-section and SIGMA(I) the ionization cross-section. The ratio of $\frac{dY'_\mu}{dE} \cdot S(E)$ and μY_μ, the two additive terms in equation 5.2.1.3 are given in the final column. These ratios have been calculated to facilitate assignment of weights on errors in the two terms of the equation 5.2.1.3 for the calculation of uncertainty in the derived cross-sections.

5.2.2 Discussion of different parameters and error analysis:

The cross section equation 5.2.1.3 contains the following parameters, $n, \frac{dY'_\mu}{dE}, \frac{dE}{dx}, \mu$ and Y_μ. The number of scattering centres per unit volume, n, is calculated from the formula

$$n = \frac{N_o \rho}{A} \quad \text{where}$$

N_o = Avogadros number

ρ = density of the material and

A = atomic number of the target

No appreciable error is expected in the evaluation of the value of n.

To check the values of $\frac{dY'_\mu}{dE}$ calculated from the polynomials, the following procedures were adopted.

i) The slopes were calculated from the experimental data by different persons using graphical methods. The results agreed within 4% and scattered around the smooth curve formed by the slopes obtained from the polynomial.

ii) Numerical values of Y'_μ at an energy step of 10 KeV were calculated from the polynomial and the slopes were calculated at experimental energy E, using values at eneries E - .01 MeV and E + .01 MeV. These values were found to be indistinguishable from those calculated from the differentiation of the polynomial.

Though most authors reporting cross-sections derived from the thick target yield assign uncertainty usually between 10 - 20% to the values of $\frac{dY_\mu}{dE}$, an uncertainty < 4% is assigned to the values of $\frac{dY'_\mu}{dE}$ in the present work. This has been possible due to very good internal consistency of the present thick target yield values (column 4 of the table 5.2.1.1).

The values of $\frac{dE}{dx}$ are taken from Janni's table because for almost all elements Janni's values lie between two other major tabulations reported, namely Northcliffe and Schilling (NorL70), and Williamsons (WilC67). The deviations of Northcliffe and Schilling and Williamsons $\frac{dE}{dx}$ values from Janni's is maximum at 1 MeV for all elements studied. The worst deviation at 1 MeV for the elements studied, was for Sn and is 8.2%, whereas the deviation at 3 MeV is < 3%. The deviations in percentage of the $\frac{dE}{dx}$ values of Northcliffe and Schilling and Williamsons from those of Janni for silver are shown in Fig.5.2.2.1. The uncertainties assigned to the values of $\frac{dE}{dx}$ are the maximum deviations of $\frac{dE}{dx}$ of other tabulations from Janni's.

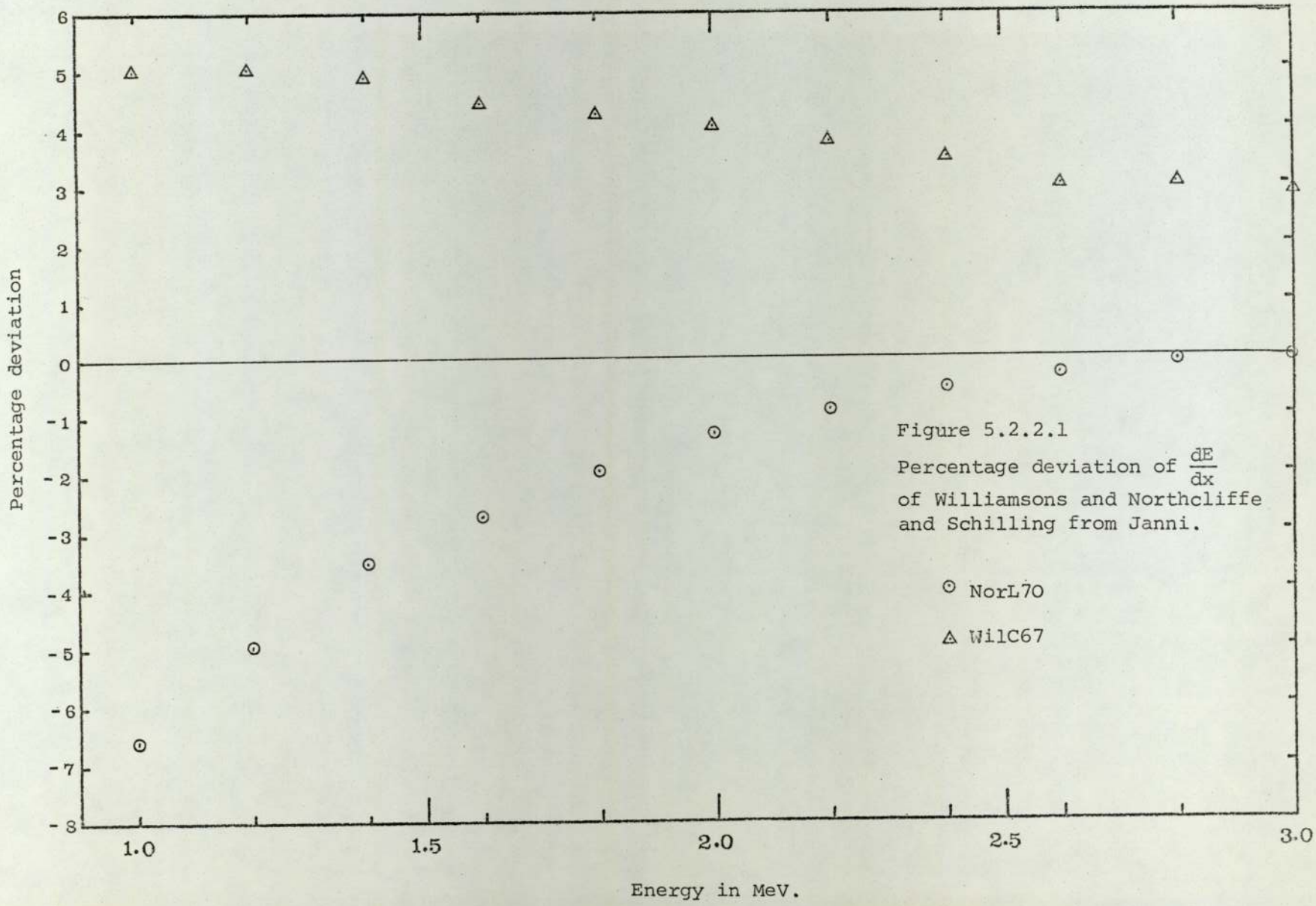

Figure 5.2.2.1

Percentage deviation of $\frac{dE}{dx}$ of Williamsons and Northcliffe and Schilling from Janni.

The uncertainty in μ_m (StoE74) is < 3% for all elements except for titanium and vanadium. An uncertainty of 5% is assigned to the values of μ_m for these two elements. The uncertainty in Y_μ are those assigned to different elements in the table 5.1.3.1.

The relative contribution to the total uncertainty in the production cross section values from the uncertainties in the values of $\frac{dY'_\mu}{dE}\ \frac{dE}{dx}$ and Y_μ depends on the ratio R defined as

$$R = \frac{dY'_\mu}{dE} \cdot \frac{dE}{dx} \Big/ \mu Y_\mu \qquad 5.2.2.1$$

The quantitative and qualitative nature of R in two regions of atomic number are completely different, as can be seen from Fig.5.2.2.2. For high Z materials in the energy region studied, the values of μ decreases rapidly with increasing Z and hence the contribution to the values of production cross section comes almost entirely from $\frac{dY'_\mu}{dE}\ \frac{dE}{dx'}$. And hence any uncertainty in $\frac{dY_\mu}{dE} \cdot \frac{dE}{dx}$ will almost singularly constitute the uncertainty in the production cross-section.

On the other hand, for low Z elements the first term dominates around 1 MeV, the two terms are comparable about 2 MeV and the second term dominates in 3 MeV region.

In order to calculate the uncertainty in the cross section values, Y_μ is assumed to be a product of two terms

$$Y_\mu = cY \qquad 5.2.2.2.$$

where c contains all the multiplicative factors e.g. absorption corrections, detector area and distance and contain only the systematic errors, whereas Y represents the excitation function and contains all the random errors in Y_μ, e.g. statistics, beam measurements, dead time corrections and uncertainty in peak integration,

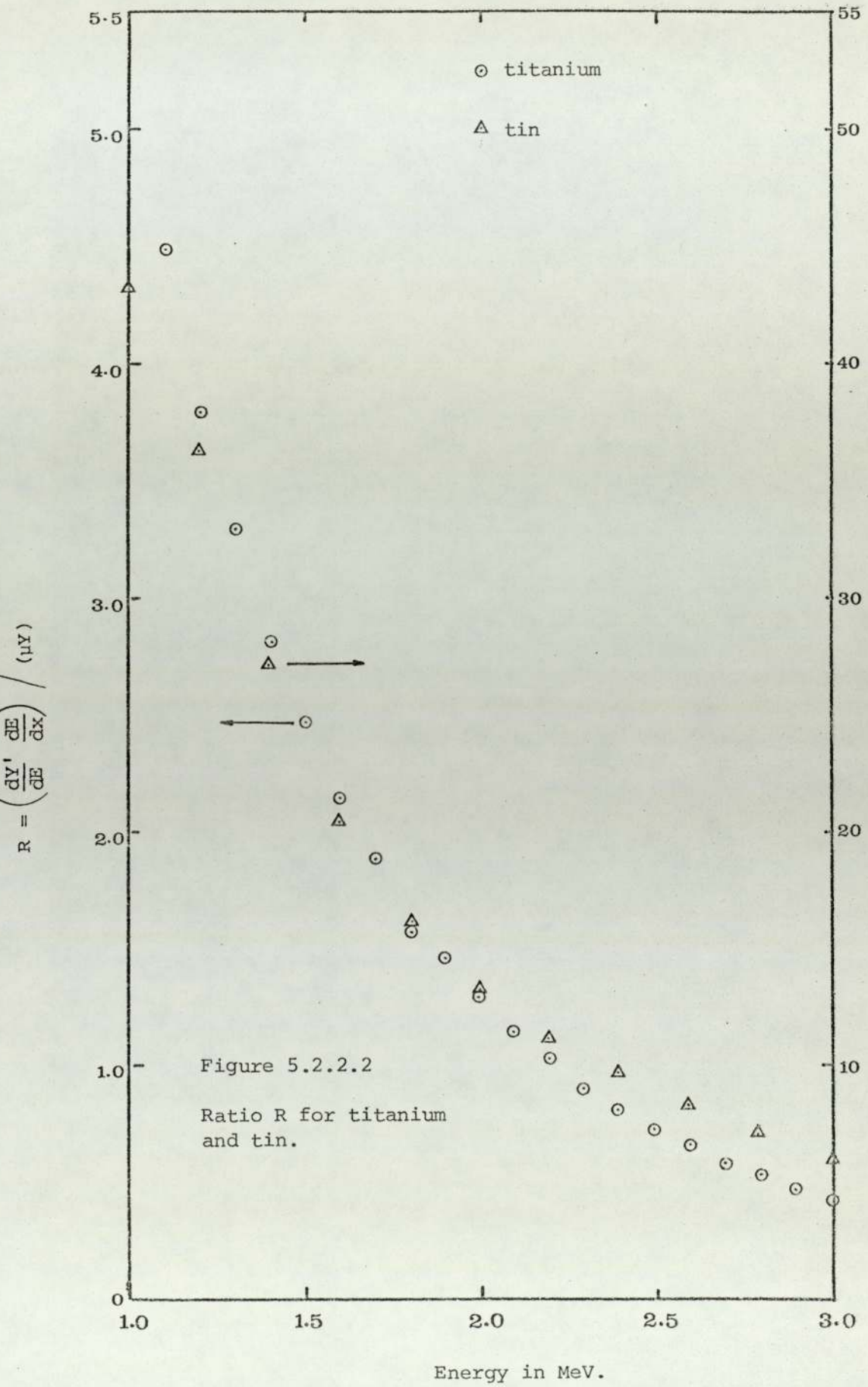

Figure 5.2.2.2

Ratio R for titanium and tin.

The equation 5.2.1.3 in terms of equation 5.2.2.2 becomes

$$\sigma_x(E) = \frac{c}{n}\left[\frac{dY}{dE}\frac{dE}{dx} + \mu Y\right] \qquad 5.2.2.3$$

The errors in $\frac{dY}{dE}$ are assumed to be the random errors in $\frac{dY'_\mu}{dE}$ and those in Y are the random errors in Y_μ. If we write $T_1 = \frac{dY}{dE}\frac{dE}{dx}$ and $T_2 = \mu Y$ the percentage error ΔT_1 in T_1 is found by combining 4% assigned uncertainty in $\frac{dY}{dE}$ with the percentage uncertainty in $\frac{dE}{dx}$. Similarly, uncertainty ΔT_2 in T_2 expressed in percentage is obtained by combining percentage uncertainty in μ with that of Y. The total percentage uncertainty ΔT in $T_1 + T_2$ is obtained by multiplying ΔT_1 and ΔT_2 with proper weights and combining them quadratically as follows:

$$\Delta T = \sqrt{(w_1 \Delta T_1)^2 + (w_2 \Delta T_2)^2}$$

where

$$w_1 = \frac{R}{R+1} \quad \text{and} \quad w_2 = \frac{1}{R+1}$$

ΔT is again added quadratically with the systematic uncertainty in Y_μ (i.e. uncertainty in c) to get the total uncertainty in production cross-section.

On the basis of the above discussion table 5.2.2.1 is prepared. The uncertainties for production cross-sections are calculated at 1, 2 and 3 MeV and are presented in this table. For the sake of brevity different steps in the calculation are shown only for 1 MeV. The uncertainty in ω_K (presented in column 3 of table 5.2.2.1) has been combined with the uncertainty in the production cross-section to estimate the uncertainty in the calculated ionization cross-section and are also presented.

Table 5.2.2.1

Major uncertainties in the calculation of proton induced K shell X-ray cross-sections (all uncertainties are in percentage).

Element	ΔY_μ	$\Delta\omega_K$	ΔT_2	1 MeV					2 MeV		3 MeV	
				$\Delta(dE/dx)$	Ratio	ΔT	$\Delta\sigma_x$	$\Delta\sigma_I$	$\Delta\sigma_x$	$\Delta\sigma_I$	$\Delta\sigma_x$	$\Delta\sigma_I$
Ti	8.4	8.2	5.4	6.0	5.2	6.1	10.2	13.1	9.0	12.2	9.2	12.3
V	3.9	2.8	5.4	6.0	6.4	6.3	7.1	7.6	4.9	5.6	5.1	5.8
Fe	3.8	2.3	3.6	6.2	10.6	6.8	7.5	7.8	3.4	4.1	4.1	4.7
Ni	2.7	6.8	3.6	3.7	10.5	5.0	5.3	8.6	3.6	7.7	3.5	7.6
Cu	2.4	2.0	3.6	4.0	11.7	5.3	5.5	5.9	3.4	3.9	3.1	3.7
Zn	2.1	6.3	3.6	4.0	12.1	5.3	5.3	8.2	3.5	7.2	3.2	7.1
Mo	2.2	4.2	3.6	3.7	30.0	5.3	5.4	6.8	3.8	5.7	3.5	5.5
Ag	3.6	3.0	3.6	6.6	35.0	7.5	8.1	8.6	6.1	6.8	5.1	5.9
Cd	4.1	3.5	3.6	8.0	39.0	8.7	9.4	10.0	5.5	6.5	5.0	6.1
In	4.7	3.4	3.6	8.0	42.0	8.7	9.7	10.0	5.9	6.8	5.5	6.5
Sn	5.0	3.3	3.6	8.2	43.4	8.9	10.0	10.5	6.2	7.0	5.8	6.6

5.2.3 Results and Discussions

The K shell ionization cross-section data obtained in the present measurements in the proton energy range 1-3 MeV for the elements Ti, V, Fe, Ni, Cu, Zn, Mo, Ag, Cd, In and Sn are presented along with those of other workers in figures 5.2.3.1 - 5.2.3.10. Also presented in the same figures are the curves predicted by PWBA, PWBABC and BEA theories (Chapter III). In the case of vanadium and nickel the results are presented together, figure 5.2.3.3.

A brief summary of the comparisons between the prediction of various theories are given below. For titanium and vanadium BEA curve lies between PWBA and PWBABC at low energy and crosses over PWBA at ∿ 2.2 MeV and ∿ 2.4 MeV respectively (figure 5.2.3.1 and figure 5.2.3.3). For the elements Fe, Ni, Cu and Zn (figures 5.2.3.2 - 5.2.3.5) BEA lies between PWBA and PWBABC in the present proton energy range. For Mo, Ag, Cd, In and Sn BEA and PWBABC curves are very close, the energy of the cross-over points between them being different for each element (figures 5.2.3.6 - 5.2.3.10). PWBABC values are in all these cases lower than those of PWBA.

The maximum differences between the theories have been calculated at 1, 2 and 3 MeV for the elements studied. At 1 MeV these differences, as predicted, are found to be an increasing function of the atomic number ranging from 52% for titanium to 110% for tin. At 2 MeV the corresponding values are respectively ∿ 30% and ∿ 50%. At 3 MeV the situation is more complex due to the cross-over of PWBA by BEA (figure 5.2.3.1 and 5.2.3.3).

It should be noted that the PWBA cross-sections presented here are derived from the universal function of Basbas et.al (BasG73). Though the universal function was derived from aluminium values, cross-section for the other elements derived from this function agree within few per cent with the more exact calculation of Khandelwal et.al. (KhaG69).

The numerical values of the experimental thick target yields, fitted yields, $\frac{dE}{dx}$ and the experimental ionization cross-section of different elements are presented in tables 5.2.3.1 - 5.2.3.11. The ionization cross-sections predicted by various theories are also tabulated. The tables also contain self absorption coefficients, μ, fluorescent yields, ω_k, and a reference to the $\frac{dE}{dx}$ values used in the derivation of ionization cross-sections.

Most of the cross-section data of other workers, presented in the figures for comparison with our data, are obtained from thin target measurements. In some cases authors have derived ionization cross-sections using fluorescent yield values different from those used in the present work. To facilitate comparison these ionization cross-sections were recalculated using the fluorescent yield values employed in the present measurement. Where agreement is claimed within the experimental errors, it should be noted that the experimental errors do not contain uncertainty in the fluorescent yield values.

For titanium below 2 MeV the present data are systematically higher than BEA by $\sim$ 15%. At 2.2 MeV BEA crosses PWBA and the present data follow PWBA above 2.2 MeV and are higher than PWBA by $\sim$ 12%. The present data agree within the experimental error with the thin target measurements of Aksselsson et.al (AksR74) and Bissinger et.al (BisG70) and is systematically lower than the similar measurements of Bodart et.al (BodF75) by $\sim$ 15% and McCoy et.al (McCJ73) by $\sim$ 12%. The thin target measurements of Bearse et.al (BeaR73) and Ogier's (OgiW64) thick target measurement at 1.5 MeV are systematically lower than the present measurement by $\sim$ 30% (Fig.5.2.3.1).

For iron the present ionization cross-section values lie between BEA and PWBABC at lower energy and falls back to PWBABC at higher energy (Fig.5.2.3.2). The thin target measurements of Bearse et.al (BeaR73) are consistently lower than the present work by $\sim$ 30%. The

TABLE 5.2.3.1

K-SHELL THICK TARGET YIELDS AND DERIVED IONIZATION CROSS-SECTIONS, AND THEIR COMPARISONS WITH THE PREDICTIONS OF DIFFERENT THEORIES FOR THE ELEMENT TITANIUM WITH WK=0.219 MU= 23.26 AND DE/DX VALUES FROM REFERENCE JAN166

E(P)	YIELD	YIELDFIT	DE/DX	SIGMA(I)	PWBA	PWBAB	PWBAC	PWBABC	BEA	CBEA
1.0	1.02E-03	1.02E-03	6.42E 02	2.49E-22	3.15E-22	2.12E-22	3.05E-22	2.05E-22	2.35E-22	2.40E-22
1.1	1.50E-03	1.49E-03	6.13E 02	3.12E-22	3.81E-22	2.62E-22	3.70E-22	2.55E-22	2.94E-22	3.02E-22
1.2	2.10E-03	2.09E-03	5.74E 02	3.82E-22	4.50E-22	3.16E-22	4.39E-22	3.08E-22	3.60E-22	3.70E-22
1.3	2.82E-03	2.82E-03	5.50E 02	4.65E-22	5.20E-22	3.72E-22	5.09E-22	3.64E-22	4.30E-22	4.42E-22
1.4	3.71E-03	3.71E-03	5.22E 02	5.37E-22	5.92E-22	4.30E-22	5.80E-22	4.22E-22	5.04E-22	5.19E-22
1.5	4.69E-03	4.75E-03	5.02E 02	6.21E-22	6.64E-22	4.90E-22	6.52E-22	4.82E-22	5.81E-22	5.99E-22
1.6	5.94E-03	5.94E-03	4.81E 02	7.06E-22	7.37E-22	5.51E-22	7.25E-22	5.42E-22	6.61E-22	6.82E-22
1.7	7.32E-03	7.29E-03	4.63E 02	7.93E-22	8.09E-22	6.13E-22	7.97E-22	6.04E-22	7.43E-22	7.67E-22
1.8	8.88E-03	8.78E-03	4.46E 02	8.79E-22	8.81E-22	6.75E-22	8.69E-22	6.66E-22	8.27E-22	8.53E-22
1.9	1.03E-02	1.04E-02	4.30E 02	9.51E-22	9.52E-22	7.38E-22	9.41E-22	7.29E-22	9.12E-22	9.41E-22
2.0	1.22E-02	1.28E-02	4.18E 02	1.05E-21	1.02E-21	8.00E-22	1.01E-21	7.91E-22	9.98E-22	1.03E-21
2.1	1.40E-02	1.40E-02	4.03E 02	1.14E-21	1.09E-21	8.62E-22	1.08E-21	8.53E-22	1.08E-21	1.12E-21
2.2	1.61E-02	1.60E-02	3.93E 02	1.22E-21	1.16E-21	9.23E-22	1.15E-21	9.14E-22	1.17E-21	1.21E-21
2.3	1.80E-02	1.81E-02	3.80E 02	1.30E-21	1.23E-21	9.84E-22	1.21E-21	9.75E-22	1.26E-21	1.29E-21
2.4	2.02E-02	2.02E-02	3.71E 02	1.37E-21	1.29E-21	1.04E-21	1.28E-21	1.04E-21	1.34E-21	1.38E-21
2.5	2.22E-02	2.23E-02	3.60E 02	1.45E-21	1.35E-21	1.10E-21	1.34E-21	1.09E-21	1.43E-21	1.46E-21
2.6	2.46E-02	2.45E-02	3.52E 02	1.51E-21	1.42E-21	1.16E-21	1.41E-21	1.15E-21	1.51E-21	1.55E-21
2.7	2.65E-02	2.67E-02	3.43E 02	1.58E-21	1.48E-21	1.22E-21	1.47E-21	1.21E-21	1.59E-21	1.63E-21
2.8	2.90E-02	2.89E-02	3.35E 02	1.64E-21	1.53E-21	1.27E-21	1.52E-21	1.27E-21	1.67E-21	1.71E-21
2.9	3.11E-02	3.11E-02	3.27E 02	1.70E-21	1.59E-21	1.33E-21	1.58E-21	1.32E-21	1.75E-21	1.79E-21
3.0	3.33E-02	3.32E-02	3.20E 02	1.76E-21	1.65E-21	1.38E-21	1.64E-21	1.37E-21	1.83E-21	1.87E-21

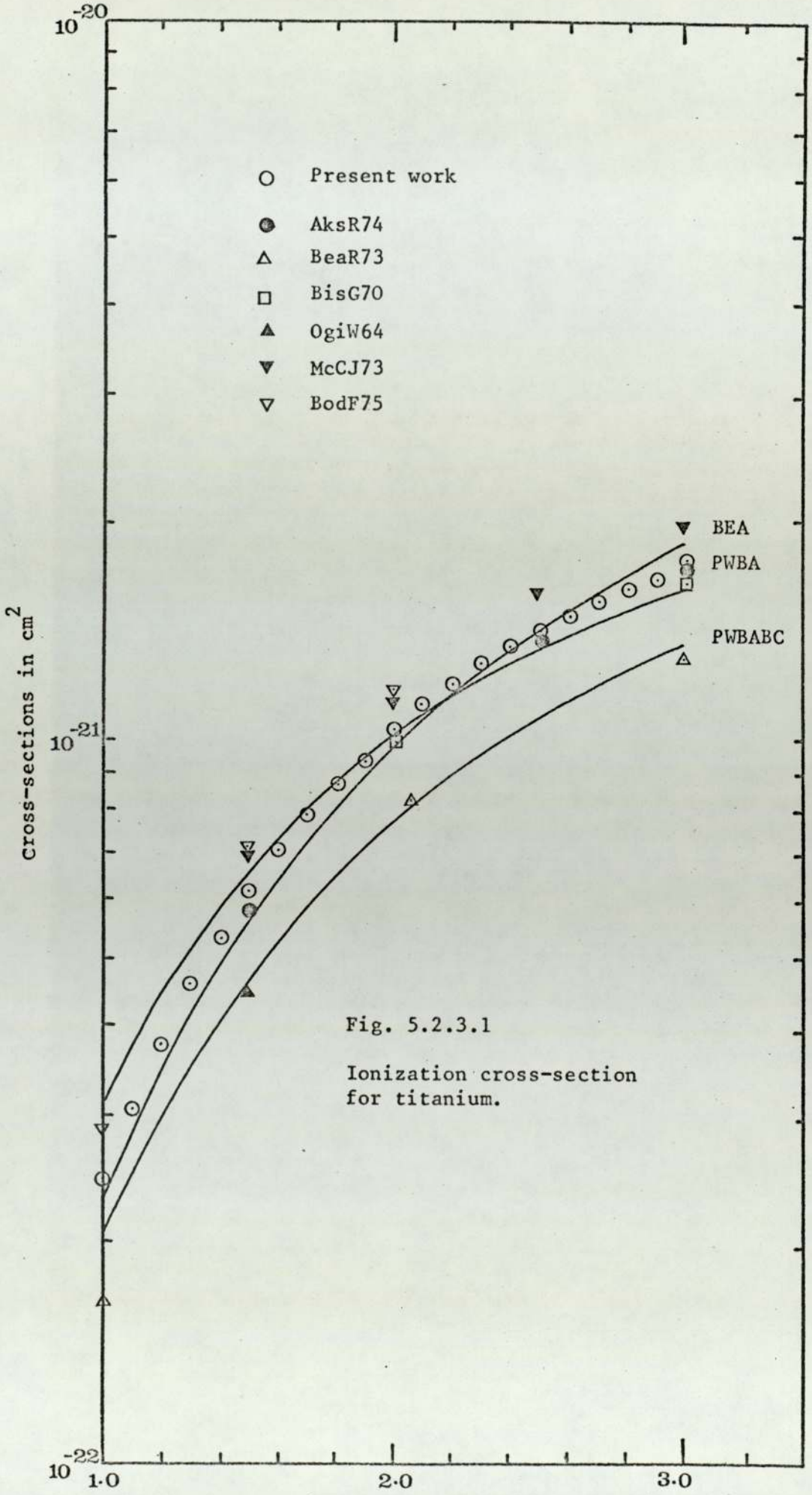

Fig. 5.2.3.1

Ionization cross-section for titanium.

TABLE 5.2.3.2

K-SHELL THICK TARGET YIELDS AND DERIVED IONIZATION CROSS-SECTIONS, AND THEIR COMPARISONS WITH THE PREDICTIONS OF DIFFERENT THEORIES FOR THE ELEMENT VANADIUM WITH WK=0.250 MU= 15.38 AND DE/DX VALUES FROM REFERENCE JAN166

E(P)	YIELD	YIELDFIT	DE/DX	SIGMA(I)	PWBA	PWBAB	PWBAC	PWBABC	BEA	CBEA
1.0	6.53E-04	6.50E-04	8.24E 02	1.49E-22	2.12E-22	1.42E-22	2.04E-22	1.37E-22	1.53E-22	1.57E-22
1.1	9.56E-04	9.66E-04	7.87E 02	1.87E-22	2.59E-22	1.77E-22	2.50E-22	1.72E-22	1.93E-22	1.98E-22
1.3	1.85E-03	1.84E-03	7.00E 02	2.67E-22	3.59E-22	2.55E-22	3.50E-22	2.49E-22	2.87E-22	2.94E-22
1.5	3.13E-03	3.10E-03	6.38E 02	3.58E-22	4.65E-22	3.41E-22	4.55E-22	3.34E-22	3.93E-22	4.05E-22
1.7	4.73E-03	4.76E-03	5.91E 02	4.59E-22	5.73E-22	4.31E-22	5.64E-22	4.24E-22	5.09E-22	5.25E-22
1.9	6.80E-03	6.83E-03	5.53E 02	5.67E-22	6.82E-22	5.25E-22	6.72E-22	5.17E-22	6.32E-22	6.52E-22
2.0	7.98E-03	8.01E-03	5.36E 02	6.21E-22	7.36E-22	5.72E-22	7.26E-22	5.64E-22	6.95E-22	7.17E-22
2.1	9.33E-03	9.29E-03	5.20E 02	6.76E-22	7.89E-22	6.19E-22	7.80E-22	6.11E-22	7.59E-22	7.83E-22
2.3	1.20E-02	1.20E-02	4.92E 02	7.83E-22	8.94E-22	7.13E-22	8.85E-22	7.05E-22	8.88E-22	9.15E-22
2.5	1.51E-02	1.51E-02	4.65E 02	8.80E-22	9.95E-22	8.05E-22	9.86E-22	7.98E-22	1.02E-21	1.05E-21
2.7	1.84E-02	1.83E-02	4.41E 02	9.72E-22	1.09E-21	8.96E-22	1.08E-21	8.88E-22	1.15E-21	1.18E-21
2.8	1.98E-02	1.99E-02	4.30E 02	1.01E-21	1.14E-21	9.40E-22	1.13E-21	9.33E-22	1.21E-21	1.24E-21
2.9	2.15E-02	2.15E-02	4.20E 02	1.04E-21	1.19E-21	9.83E-22	1.18E-21	9.76E-22	1.27E-21	1.30E-21
3.0	2.31E-02	2.31E-02	4.11E 02	1.08E-21	1.23E-21	1.03E-21	1.22E-21	1.02E-21	1.33E-21	1.36E-21

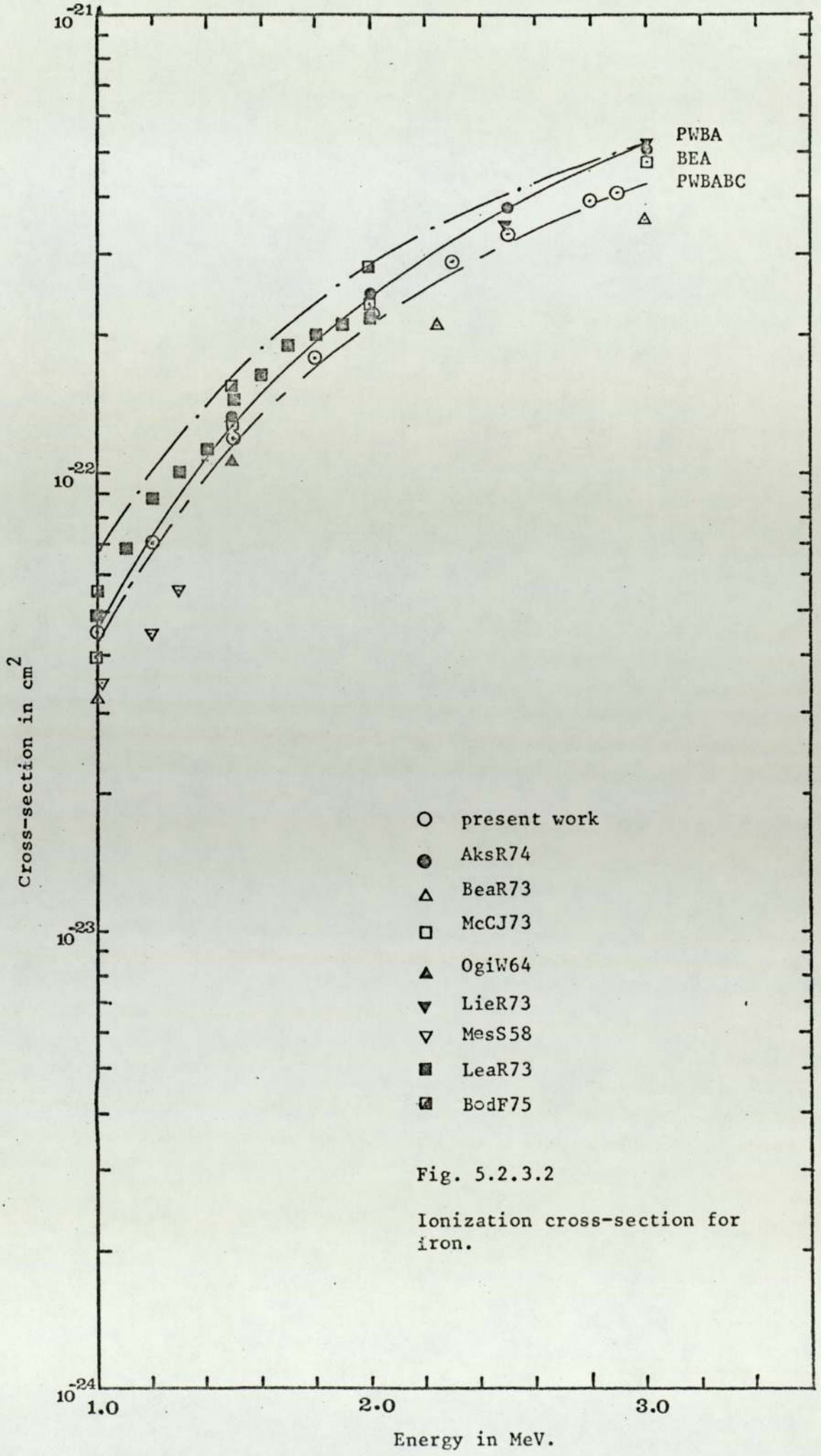

Fig. 5.2.3.2

Ionization cross-section for iron.

TABLE 5.2.3.3

K-SHELL THICK TARGET YIELDS AND DERIVED IONIZATION CROSS-SECTIONS, AND THEIR COMPARISONS WITH THE PREDICTIONS OF DIFFERENT THEORIES FOR THE ELEMENT IRON
WITH WK=0.347 MU= 8.63 AND DE/DX VALUES FROM REFERENCE JAN.166

E(P)	YIELD	YIELDFIT	DE/DX	SIGMA(I)	PWBA	PWBAB	PWBAC	PWBABC	BEA	CBEA
1.0	2.53E-04	2.53E-04	1.05E 03	4.51E-23	6.75E-23	4.51E-23	6.39E-23	4.27E-23	4.53E-23	4.65E-23
1.2	5.48E-04	5.51E-04	9.42E 02	7.01E-23	1.03E-22	7.13E-23	9.87E-23	6.84E-23	7.35E-23	7.52E-23
1.5	1.34E-03	1.32E-03	8.21E 02	1.18E-22	1.65E-22	1.20E-22	1.60E-22	1.16E-22	1.28E-22	1.31E-22
1.8	2.61E-03	2.61E-03	7.34E 02	1.78E-22	2.35E-22	1.76E-22	2.29E-22	1.72E-22	1.94E-22	2.00E-22
2.0	3.77E-03	3.80E-03	6.87E 02	2.23E-22	2.83E-22	2.16E-22	2.78E-22	2.12E-22	2.44E-22	2.52E-22
2.3	6.07E-03	6.08E-03	6.30E 02	2.92E-22	3.57E-22	2.80E-22	3.51E-22	2.76E-22	3.25E-22	3.35E-22
2.5	8.00E-03	7.89E-03	5.97E 02	3.36E-22	4.06E-22	3.23E-22	4.01E-22	3.19E-22	3.81E-22	3.93E-22
2.8	1.07E-02	1.08E-02	5.54E 02	3.91E-22	4.79E-22	3.88E-22	4.74E-22	3.84E-22	4.68E-22	4.83E-22
2.9	1.19E-02	1.19E-02	5.43E 02	4.06E-22	5.03E-22	4.10E-22	4.98E-22	4.06E-22	4.97E-22	5.13E-22

thick target measurements of Messelt (MesS58) and Ogier (OgiW64) are also lower than the present measurement by ∿ 30% and ∿ 10% respectively whereas the thin target measurements of Akselsson et.al (AksR74) and McCoy et.al (McCJ73) are higher by ∿ 13%. Similar thin target measurements of Liebert et.al (LieR73) agree at 2.5 MeV but are ∿ 18% higher at 3 MeV. Similar measurements of Lear et.al (LeaR73) from 1 MeV to 2 MeV are above ours by ∿ 1 - 15%.

For vanadium the present values follow PWBABC and are consistently higher than PWBABC by ∿ 10%. A solitary thin target measurement of Bearse et.al (BeaR73) at 2.5 MeV is below the present work by ∿9% whereas similar measurements by Bodart et.al (BodF75) are higher by ∿ 10-20% (Fig.5.2.3.3).

For nickel, the thin target measurements of Aksselsson et.al (AksR74) agree with the present work within experimental error whereas those of Bodart et.al (BodF75) and McCoy et.al (McCJ73) are systematically higher than the present work by ∿ 22% and 36% respectively. One data point of McCoy et.al, however, is abnormally lower than his other points by ∿ 30% and coincides with the present results. The thin target data of Liebert et.al compares well with the present data whereas those of Bearse et.al (BeaR73) spread over the entire energy region are below the present measurement by ∿ 15 - 25%.

For copper the present cross-section data lie between the prediction of BEA and PWBA except the 3 higher energy points which curl over to the PWBABC curve (Fig.5.2.3.4). Thin target measurements of Aksselsson et.al (AksR74) and Liebert et.al (LieR73) agree within experimental uncertainty. Those of Lear et.al (LeaR73) and the thick target measurements of Messelt (MesS58) and Ogier (OgiW64) agree within 10-20%. The thin target data of Bodart et.al (BodF75) are consistently above the present work and those of Bearse et.al (BeaR73) are below the present measurement by ∿ 17% and 15-40% respectively.

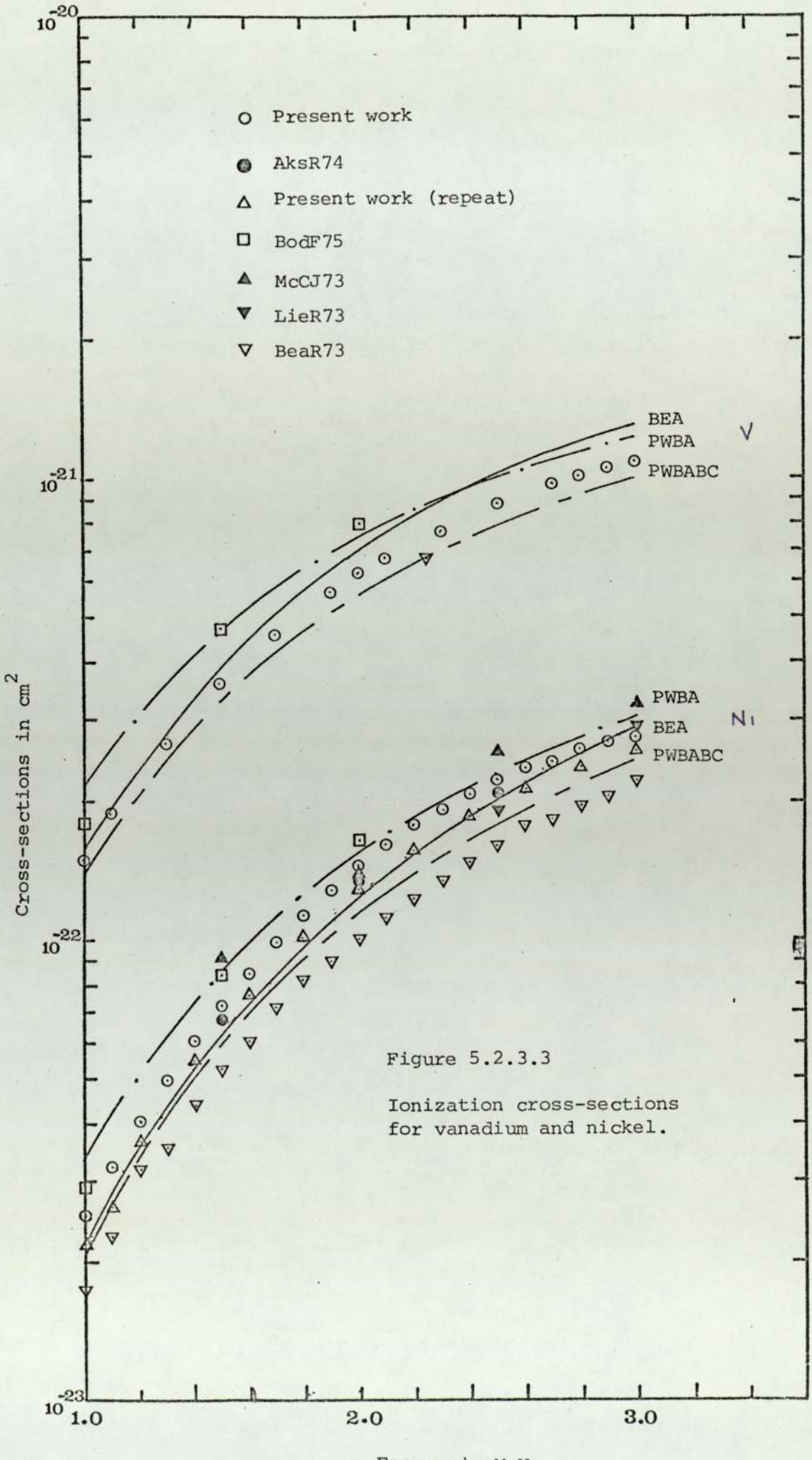

Figure 5.2.3.3

Ionization cross-sections for vanadium and nickel.

TABLE 5.2.3.4

K-SHELL THICK TARGET YIELDS AND DERIVED IONIZATION CROSS-SECTIONS, AND THEIR COMPARISONS
WITH THE PREDICTIONS OF DIFFERENT THEORIES FOR THE ELEMENT NICKEL1
WITH WK=0.414 MU= 6.43 AND DE/DX VALUES FROM REFERENCE JAN166

E(P)	YIELD	YIELDFIT	DE/DX	SIGMA(I)	PWBA	PWBAB	PWBAC	PWBABC	BEA	CBEA
1.0	1.62E-04	1.62E-04	1.15E 03	2.51E-23	3.28E-23	2.19E-23	3.06E-23	2.04E-23	2.13E-23	2.19E-23
1.1	2.48E-04	2.50E-04	1.08E 03	3.20E-23	4.17E-23	2.83E-23	3.92E-23	2.67E-23	2.78E-23	2.85E-23
1.2	3.68E-04	3.65E-04	1.03E 03	4.04E-23	5.15E-23	3.56E-23	4.88E-23	3.38E-23	3.52E-23	3.61E-23
1.3	5.10E-04	5.12E-04	9.82E 02	4.97E-23	6.21E-23	4.36E-23	5.93E-23	4.16E-23	4.36E-23	4.47E-23
1.4	6.98E-04	6.96E-04	9.38E 02	6.01E-23	7.35E-23	5.23E-23	7.05E-23	5.02E-23	5.29E-23	5.42E-23
1.5	9.25E-04	9.23E-04	9.04E 02	7.20E-23	8.54E-23	6.17E-23	8.25E-23	5.95E-23	6.31E-23	6.47E-23
1.6	1.22E-03	1.19E-03	8.67E 02	8.46E-23	9.83E-23	7.17E-23	9.50E-23	6.93E-23	7.42E-23	7.60E-23
1.7	1.46E-03	1.52E-03	8.39E 02	9.87E-23	1.12E-22	8.23E-23	1.08E-22	7.98E-23	8.60E-23	8.82E-23
1.8	1.90E-03	1.90E-03	8.07E 02	1.13E-22	1.25E-22	9.33E-23	1.22E-22	9.07E-23	9.86E-23	1.01E-22
1.9	2.35E-03	2.34E-03	7.83E 02	1.28E-22	1.39E-22	1.05E-22	1.36E-22	1.02E-22	1.12E-22	1.15E-22
2.0	2.87E-03	2.84E-03	7.56E 02	1.44E-22	1.54E-22	1.17E-22	1.50E-22	1.14E-22	1.26E-22	1.29E-22
2.1	3.40E-03	3.40E-03	7.35E 02	1.60E-22	1.68E-22	1.29E-22	1.65E-22	1.26E-22	1.40E-22	1.44E-22
2.2	4.02E-03	4.02E-03	7.12E 02	1.76E-22	1.83E-22	1.42E-22	1.79E-22	1.39E-22	1.55E-22	1.60E-22
2.3	4.68E-03	4.69E-03	6.93E 02	1.91E-22	1.98E-22	1.54E-22	1.95E-22	1.51E-22	1.71E-22	1.76E-22
2.4	5.42E-03	5.42E-03	6.75E 02	2.07E-22	2.14E-22	1.67E-22	2.10E-22	1.64E-22	1.87E-22	1.93E-22
2.5	6.16E-03	6.19E-03	6.57E 02	2.21E-22	2.29E-22	1.81E-22	2.25E-22	1.77E-22	2.04E-22	2.10E-22
2.6	6.99E-03	7.00E-03	6.41E 02	2.34E-22	2.44E-22	1.94E-22	2.40E-22	1.91E-22	2.20E-22	2.27E-22
2.7	7.84E-03	7.84E-03	6.25E 02	2.46E-22	2.60E-22	2.07E-22	2.56E-22	2.04E-22	2.37E-22	2.45E-22
2.8	8.76E-03	8.71E-03	6.12E 02	2.58E-22	2.75E-22	2.21E-22	2.71E-22	2.18E-22	2.55E-22	2.63E-22
2.9	9.52E-03	9.58E-03	5.97E 02	2.67E-22	2.90E-22	2.35E-22	2.86E-22	2.31E-22	2.72E-22	2.81E-22
3.0	1.04E-02	1.04E-02	5.85E 02	2.75E-22	3.06E-22	2.48E-22	3.02E-22	2.45E-22	2.90E-22	2.99E-22

TABLE 5.2.3.5

K-SHELL THICK TARGET YIELDS AND DERIVED IONIZATION CROSS-SECTIONS, AND THEIR COMPARISONS
WITH THE PREDICTIONS OF DIFFERENT THEORIES FOR THE ELEMENT NICKEL
WITH UK=0.414 MU= 6.43 AND DE/DX VALUES FROM REFERENCE JAN166

E(P)	YIELD	YIELDFIT	DE/DX	SIGMA(I)	PWBA	PWBAB	PWBAC	PWBABC	BEA	CBEA
1.0	1.46E-04	1.46E-04	1.15E 03	2.20E-23	3.28E-23	2.19E-23	3.06E-23	2.04E-23	2.13E-23	2.19E-23
1.2	3.28E-04	3.28E-04	1.03E 03	3.65E-23	5.15E-23	3.56E-23	4.88E-23	3.38E-23	3.52E-23	3.61E-23
1.4	6.26E-04	6.29E-04	9.38E 02	5.46E-23	7.35E-23	5.23E-23	7.05E-23	5.02E-23	5.29E-23	5.42E-23
1.6	1.08E-03	1.08E-03	8.67E 02	7.64E-23	9.83E-23	7.17E-23	9.50E-23	6.93E-23	7.42E-23	7.60E-23
1.8	1.71E-03	1.71E-03	8.07E 02	1.01E-22	1.25E-22	9.33E-23	1.22E-22	9.07E-23	9.86E-23	1.01E-22
2.0	2.54E-03	2.54E-03	7.56E 02	1.27E-22	1.54E-22	1.17E-22	1.50E-22	1.14E-22	1.26E-22	1.29E-22
2.2	3.58E-03	3.58E-03	7.12E 02	1.55E-22	1.83E-22	1.42E-22	1.79E-22	1.39E-22	1.55E-22	1.60E-22
2.4	4.83E-03	4.82E-03	6.75E 02	1.84E-22	2.14E-22	1.67E-22	2.10E-22	1.64E-22	1.87E-22	1.93E-22
2.6	6.24E-03	6.24E-03	6.41E 02	2.11E-22	2.44E-22	1.94E-22	2.40E-22	1.91E-22	2.20E-22	2.27E-22
2.8	7.79E-03	7.80E-03	6.12E 02	2.36E-22	2.75E-22	2.21E-22	2.71E-22	2.18E-22	2.55E-22	2.63E-22
3.0	9.45E-03	9.45E-03	5.85E 02	2.57E-22	3.06E-22	2.48E-22	3.02E-22	2.45E-22	2.90E-22	2.99E-22

Figure 5.2.3.4

Ionization cross-section
for copper.

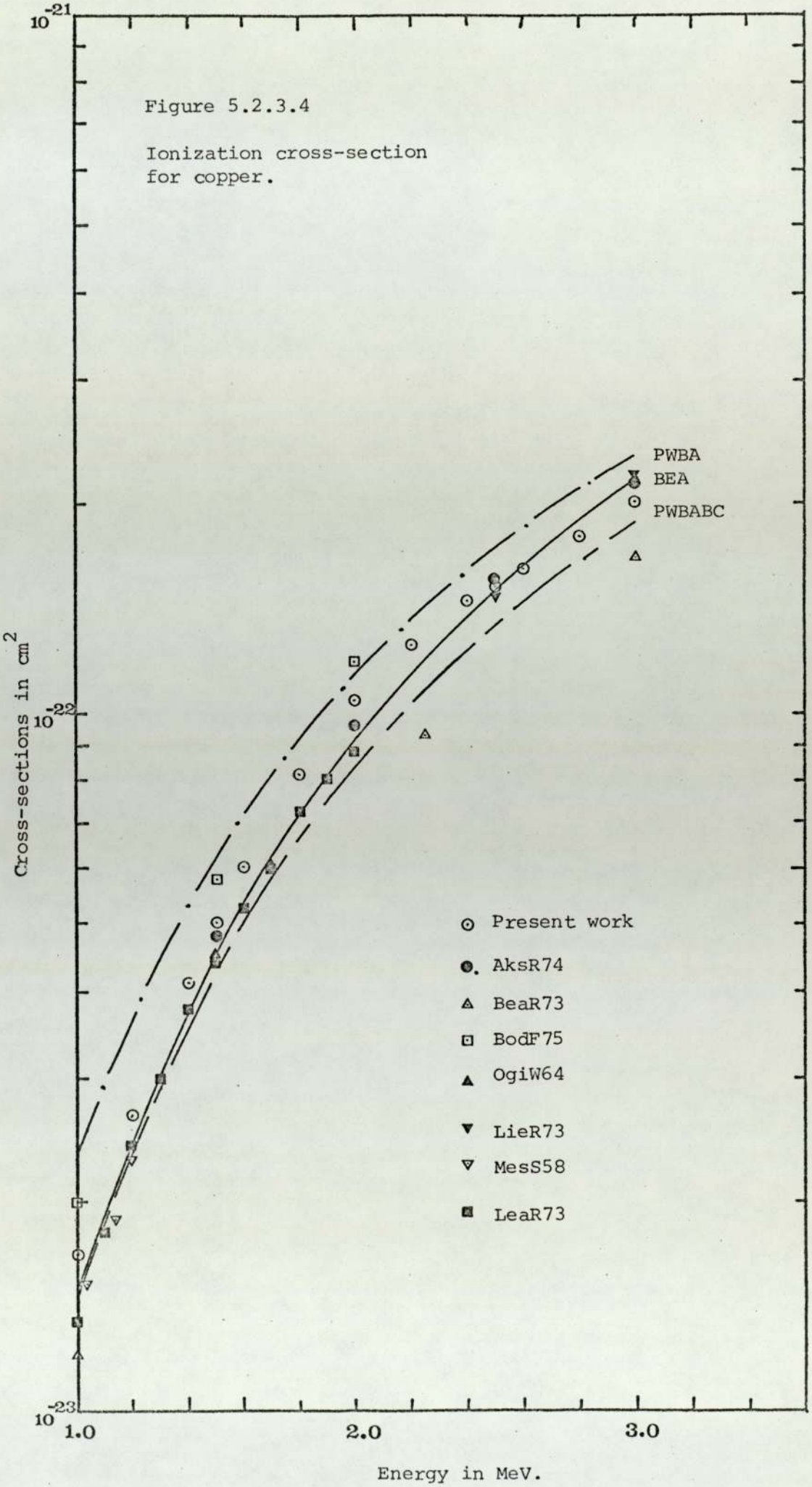

TABLE 5.2.3.6

K-SHELL THICK TARGET YIELDS AND DERIVED IONIZATION CROSS-SECTIONS, AND THEIR COMPARISONS WITH THE PREDICTIONS OF DIFFERENT THEORIES FOR THE ELEMENT COPPER WITH UK=0.445 MU= 5.56 AND DE/DX VALUES FROM REFERENCE JAN.66

E(P)	YIELD	YIELDFIT	DE/DX	SIGMA(I)	PWBA	PWBAB	PWBAC	PWBABC	BEA	CBEA
1.0	1.12E-04	1.12E-04	1.08E 03	1.68E-23	2.31E-23	1.54E-23	2.14E-23	1.43E-23	1.48E-23	1.53E-23
1.2	2.55E-04	2.55E-04	9.76E 02	2.68E-23	3.67E-23	2.54E-23	3.46E-23	2.39E-23	2.47E-23	2.54E-23
1.4	4.92E-04	4.93E-04	8.91E 02	4.12E-23	5.31E-23	3.77E-23	5.07E-23	3.60E-23	3.75E-23	3.84E-23
1.5	6.65E-04	6.60E-04	8.56E 02	5.02E-23	6.21E-23	4.47E-23	5.96E-23	4.29E-23	4.49E-23	4.59E-23
1.6	8.60E-04	8.68E-04	8.21E 02	6.00E-23	7.17E-23	5.22E-23	6.90E-23	5.03E-23	5.29E-23	5.42E-23
1.8	1.43E-03	1.41E-03	7.65E 02	8.19E-23	9.21E-23	6.85E-23	8.93E-23	6.64E-23	7.09E-23	7.27E-23
2.0	2.12E-03	2.15E-03	7.17E 02	1.04E-22	1.14E-22	8.63E-23	1.11E-22	8.40E-23	9.12E-23	9.36E-23
2.2	3.11E-03	3.06E-03	6.76E 02	1.25E-22	1.37E-22	1.05E-22	1.34E-22	1.03E-22	1.13E-22	1.17E-22
2.4	4.12E-03	4.13E-03	6.40E 02	1.44E-22	1.61E-22	1.25E-22	1.57E-22	1.23E-22	1.37E-22	1.41E-22
2.5	4.62E-03	4.70E-03	6.23E 02	1.52E-22	1.73E-22	1.36E-22	1.69E-22	1.33E-22	1.50E-22	1.54E-22
2.6	5.38E-03	5.30E-03	6.08E 02	1.61E-22	1.85E-22	1.46E-22	1.82E-22	1.44E-22	1.63E-22	1.68E-22
2.8	6.56E-03	6.57E-03	5.81E 02	1.79E-22	2.09E-22	1.68E-22	2.06E-22	1.65E-22	1.89E-22	1.95E-22
3.0	7.95E-03	7.95E-03	5.56E 02	2.01E-22	2.34E-22	1.89E-22	2.31E-22	1.86E-22	2.17E-22	2.24E-22

For zinc the present data lie between BEA and PWBA. The thin target measurements of Lear et.al (LeaR73) agrees well with the present work upto 1.4 MeV and deviates gradually to ∿ 20% at 2 MeV, whereas Liebert et.al's measurement at 3 MeV coincides with ours but disagrees at 2.5 MeV by ∿ 17%. (Fig.5.2.3.5).

For molybdenum the present data lie between the theories. The present data agrees well with the thin target data reported by Criswell et.al (CriT74). Similar data of Liebert et.al at 3 MeV coincides with the present measurement but disagrees at 2.5 MeV by ∿ 23%. The present data is higher than the thick target data of Hansteen and Messelt (HanJ57) by ∿ 25% and lower than the corresponding data of Messelt (MesS58) almost by the same amount (Fig.5.2.3.6).

Silver cross-section data in the present measurement again fall between theories except in the energy region 1.8 MeV to 2.6 MeV where the data coincides with the PWBA curve. There is excellent agreement between the present data and thin target data of Bearse et.al (BeaR73) over the entire energy region studied and those of Aksselsson et.al (AksR74) and Bissinger et.al, (BisG70) whereas present data lie above the measurements of Khelil et.al (KheN75) and Liebert et.al. (LieR73) by ∿ 20 - 30%, and ∿ 15 - 40% respectively. The thick target measurement of Lewis et.al (LewH53) in the energy region 1.7 MeV - 2.88 MeV is above the present work and others, and increases abnormally at higher energies, whereas those of Messelt (MesS58) at 1.04 and 1.2 MeV are above the present measurement by ∿ 40%. (Fig.5.2.3.7).

For cadmium all the cross-section data of the present measurements lie between the theories. The agreement with the thin target data of Khelil et.al (KheN75) is very good at 1 - 1.6 MeV, the deviation between the two sets increases and reaches its maximum ∿ 15% at 2 MeV, whereas similar measurement of Liebert et.al at 2.5 and 3 MeV agrees

TABLE 5.2.3.7

K-SHELL THICK TARGET YIELDS AND DERIVED IONIZATION CROSS-SECTIONS, AND THEIR COMPARISONS WITH THE PREDICTIONS OF DIFFERENT THEORIES FOR THE ELEMENT ZINC
WITH UK=0.479 MU= 6.35 AND DE/DX VALUES FROM REFERENCE JAN166

E(P)	YIELD	YIELDFIT	DE/DX	SIGMA(I)	PWBA	PWBAB	PWBAC	PWBABC	BEA	CBEA
1.0	8.87E-05	8.90E-05	8.49E 02	1.20E-23	1.63E-23	1.09E-23	1.50E-23	1.00E-23	1.03E-23	1.08E-23
1.1	1.38E-04	1.37E-04	8.00E 02	1.58E-23	2.10E-23	1.43E-23	1.95E-23	1.33E-23	1.36E-23	1.41E-23
1.2	2.02E-04	2.03E-04	7.67E 02	2.05E-23	2.63E-23	1.82E-23	2.46E-23	1.70E-23	1.74E-23	1.80E-23
1.4	4.03E-04	4.01E-04	7.02E 02	3.19E-23	3.84E-23	2.73E-23	3.65E-23	2.59E-23	2.67E-23	2.73E-23
1.6	7.06E-04	7.12E-04	6.48E 02	4.61E-23	5.24E-23	3.81E-23	5.03E-23	3.66E-23	3.80E-23	3.89E-23
1.8	1.15E-03	1.16E-03	6.03E 02	6.29E-23	6.80E-23	5.05E-23	6.56E-23	4.87E-23	5.12E-23	5.25E-23
2.0	1.75E-03	1.78E-03	5.66E 02	8.14E-23	8.48E-23	6.41E-23	8.23E-23	6.22E-23	6.63E-23	6.80E-23
2.2	2.69E-03	2.56E-03	5.34E 02	1.00E-22	1.03E-22	7.88E-23	1.00E-22	7.67E-23	8.30E-23	8.53E-23
2.4	3.46E-03	3.52E-03	5.06E 02	1.19E-22	1.21E-22	9.43E-23	1.18E-22	9.22E-23	1.01E-22	1.04E-22
2.6	4.55E-03	4.62E-03	4.81E 02	1.35E-22	1.40E-22	1.11E-22	1.37E-22	1.08E-22	1.21E-22	1.24E-22
2.8	5.79E-03	5.81E-03	4.59E 02	1.49E-22	1.60E-22	1.27E-22	1.57E-22	1.25E-22	1.41E-22	1.45E-22
3.0	7.09E-03	7.04E-03	4.40E 02	1.58E-22	1.79E-22	1.45E-22	1.76E-22	1.42E-22	1.62E-22	1.68E-22

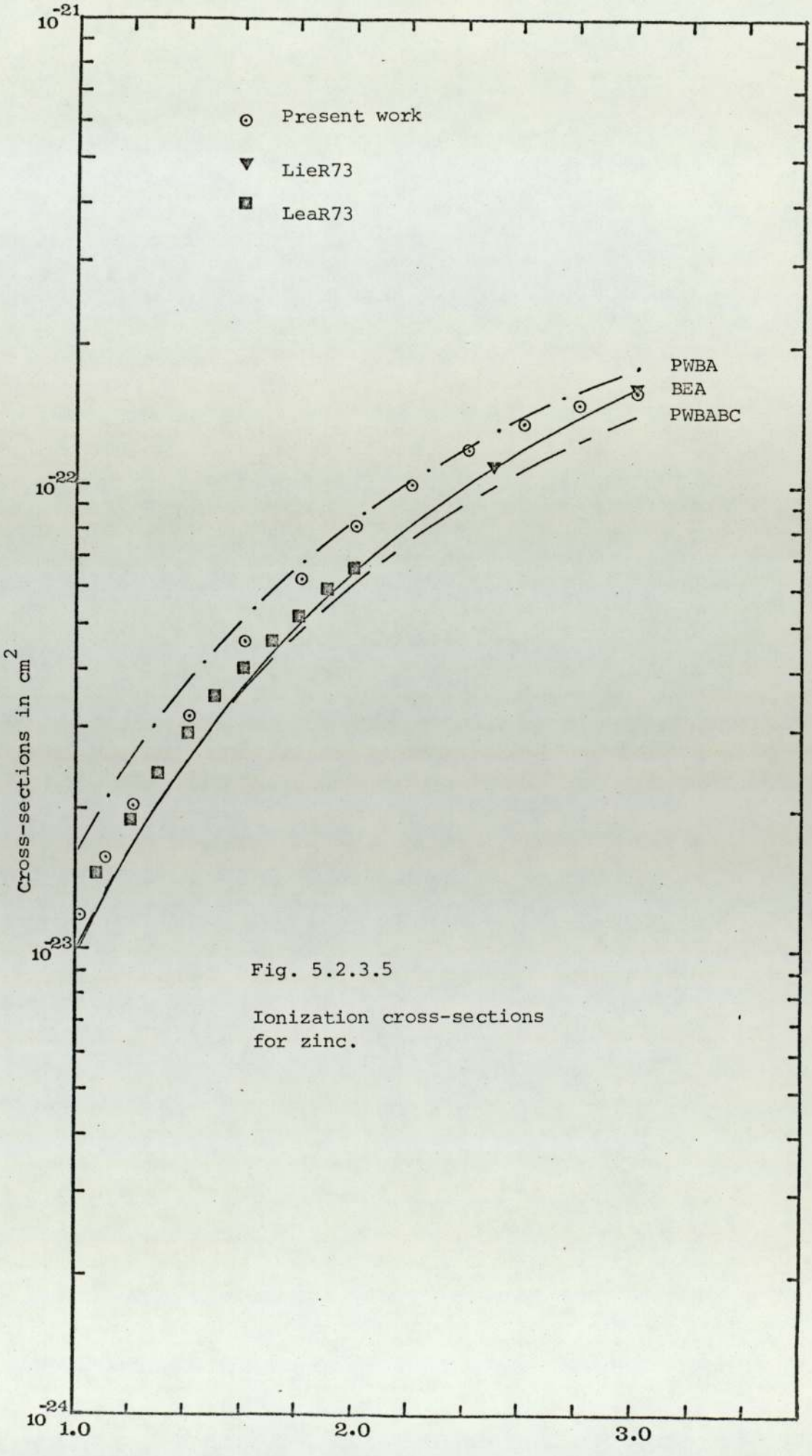

Fig. 5.2.3.5

Ionization cross-sections
for zinc.

TABLE 5.2.3.8

K-SHELL THICK TARGET YIELDS AND DERIVED IONIZATION CROSS-SECTIONS, AND THEIR COMPARISONS WITH THE PREDICTIONS OF DIFFERENT THEORIES FOR THE ELEMENT MOLYBDENUM WITH WK=0.764 MU= 1.75 AND DE/DX VALUES FROM REFERENCE JAN166

E(P)	YIELD	YIELDFIT	DE/DX	SIGMA(I)	PWBA	PWBAB	PWBAC	PWBABC	BEA	CREA
1.0	2.63E-06	2.63E-06	9.78E 02	3.01E-25	3.88E-25	2.71E-25	3.04E-25	2.13E-25	2.46E-25	2.82E-25
1.2	6.82E-06	6.86E-06	8.91E 02	5.50E-25	6.97E-25	4.97E-25	5.79E-25	4.13E-25	4.48E-25	4.98E-25
1.4	1.47E-05	1.46E-05	8.22E 02	9.09E-25	1.13E-24	8.15E-25	9.72E-25	7.04E-25	7.32E-25	7.96E-25
1.5	2.06E-05	2.04E-05	7.92E 02	1.13E-24	1.39E-24	1.01E-24	1.21E-24	8.86E-25	9.09E-25	9.79E-25
1.6	2.76E-05	2.79E-05	7.65E 02	1.40E-24	1.68E-24	1.23E-24	1.49E-24	1.09E-24	1.11E-24	1.19E-24
1.8	4.87E-05	4.88E-05	7.18E 02	2.06E-24	2.37E-24	1.76E-24	2.14E-24	1.59E-24	1.59E-24	1.68E-24
2.0	8.02E-05	8.01E-05	6.77E 02	2.87E-24	3.18E-24	2.40E-24	2.92E-24	2.20E-24	2.18E-24	2.27E-24
2.2	1.24E-04	1.24E-04	6.41E 02	3.81E-24	4.13E-24	3.14E-24	3.83E-24	2.92E-24	2.87E-24	2.98E-24
2.4	1.82E-04	1.82E-04	6.09E 02	4.81E-24	5.19E-24	4.00E-24	4.87E-24	3.75E-24	3.69E-24	3.81E-24
2.5	2.16E-04	2.18E-04	5.95E 02	5.30E-24	5.77E-24	4.47E-24	5.43E-24	4.20E-24	4.14E-24	4.26E-24
2.6	2.58E-04	2.56E-04	5.81E 02	5.77E-24	6.38E-24	4.96E-24	6.02E-24	4.68E-24	4.62E-24	4.75E-24
2.8	3.47E-04	3.44E-04	5.56E 02	6.61E-24	7.68E-24	6.03E-24	7.29E-24	5.72E-24	5.66E-24	5.81E-24
3.0	4.41E-04	4.43E-04	5.33E 02	7.21E-24	9.09E-24	7.19E-24	8.67E-24	6.86E-24	6.82E-24	6.99E-24

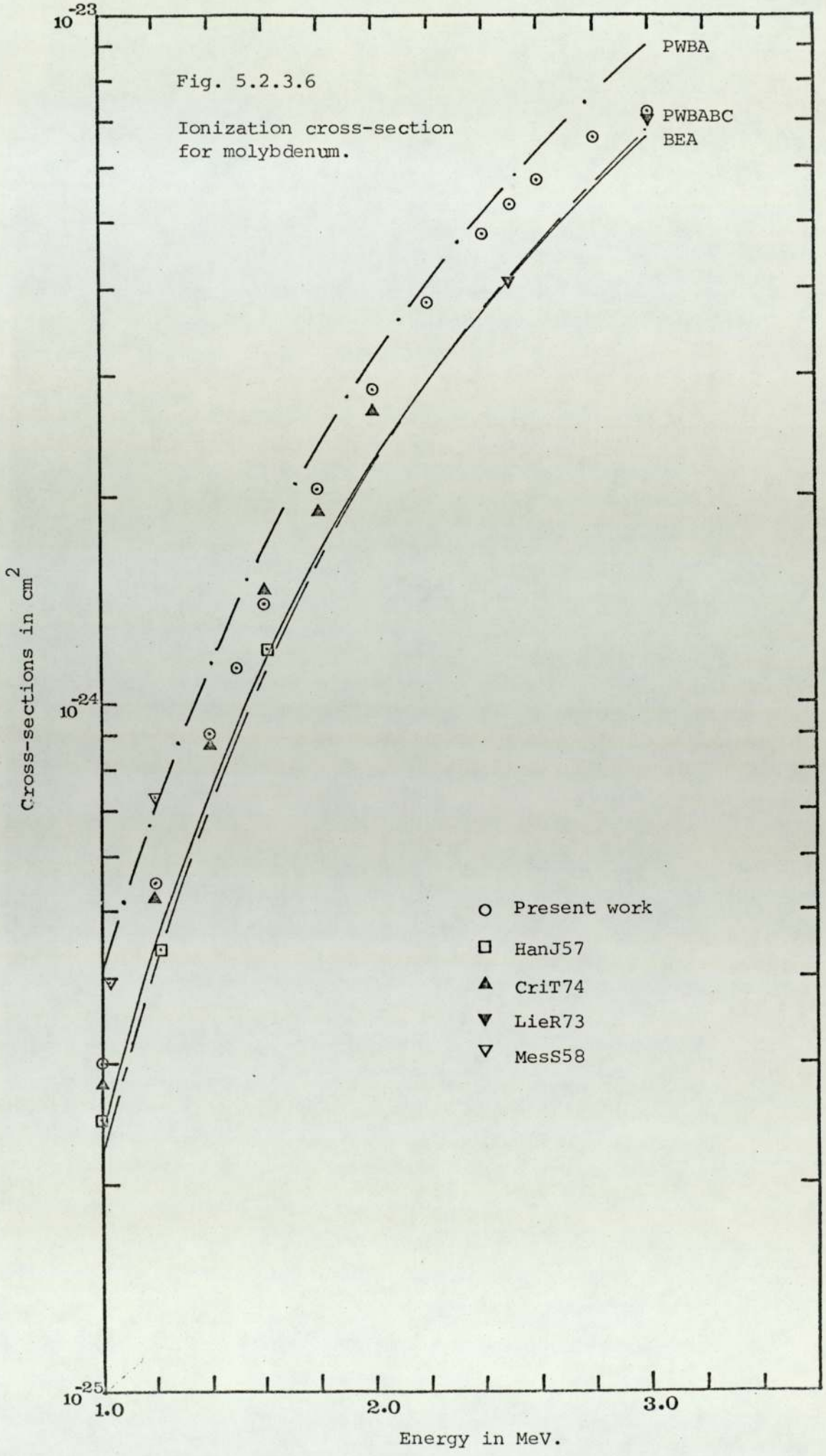
Fig. 5.2.3.6
Ionization cross-section for molybdenum.
PWBA
PWBABC
BEA
Present work
HanJ57
CriT74
LieR73
MesS58
Cross-sections in cm 2
10-23
10-24
10-25
1.0
2.0
3.0
Energy in MeV.

TABLE 5.2.3.9

K-SHELL THICK TARGET YIELDS AND DERIVED IONIZATION CROSS-SECTIONS, AND THEIR COMPARISONS WITH THE PREDICTIONS OF DIFFERENT THEORIES FOR THE ELEMENT SILVER WITH WK=0.830 MU=103.70 AND DE/DX VALUES FROM REFERENCE JAN166

E(P)	YIELD	YIELDFIT	DE/DX	SIGMA(I)	PWBA	PWBAB	PWRAC	PWRABC	BEA	CREA
1.0	7.10E-07	7.14E-07	9.73E 02	8.34E-26	1.01E-25	7.24E-26	7.16E-26	5.13E-26	6.65E-26	7.94E-26
1.1	1.22E-06	1.21E-06	9.24E 02	1.18E-25	1.40E-25	1.01E-25	1.04E-25	7.47E-26	9.21E-26	1.08E-25
1.2	1.99E-06	1.94E-06	8.84E 02	1.62E-25	1.87E-25	1.36E-25	1.44E-25	1.04E-25	1.24E-25	1.43E-25
1.3	2.86E-06	2.96E-06	8.47E 02	2.15E-25	2.44E-25	1.78E-25	1.93E-25	1.41E-25	1.61E-25	1.84E-25
1.4	4.37E-06	4.35E-06	8.14E 02	2.80E-25	3.10E-25	2.28E-25	2.52E-25	1.85E-25	2.06E-25	2.32E-25
1.5	6.16E-06	6.19E-06	7.85E 02	3.57E-25	3.87E-25	2.86E-25	3.21E-25	2.37E-25	2.58E-25	2.87E-25
1.6	8.58E-06	8.60E-06	7.58E 02	4.47E-25	4.75E-25	3.53E-25	4.00E-25	2.98E-25	3.17E-25	3.50E-25
1.7	1.17E-05	1.16E-05	7.33E 02	5.51E-25	5.74E-25	4.29E-25	4.91E-25	3.67E-25	3.85E-25	4.21E-25
1.8	1.54E-05	1.55E-05	7.10E 02	6.69E-25	6.84E-25	5.14E-25	5.93E-25	4.46E-25	4.61E-25	5.01E-25
1.9	2.04E-05	2.02E-05	6.89E 02	8.00E-25	8.06E-25	6.09E-25	7.07E-25	5.34E-25	5.46E-25	5.89E-25
2.0	2.62E-05	2.60E-05	6.69E 02	9.44E-25	9.40E-25	7.14E-25	8.32E-25	6.32E-25	6.40E-25	6.86E-25
2.1	3.34E-05	3.29E-05	6.51E 02	1.10E-24	1.09E-24	8.29E-25	9.70E-25	7.40E-25	7.44E-25	7.93E-25
2.2	4.14E-05	4.11E-05	6.33E 02	1.26E-24	1.24E-24	9.54E-25	1.12E-24	8.59E-25	8.58E-25	9.09E-25
2.3	4.80E-05	5.06E-05	6.17E 02	1.43E-24	1.41E-24	1.09E-24	1.28E-24	9.87E-25	9.81E-25	1.03E-24
2.4	6.19E-05	6.15E-05	6.02E 02	1.61E-24	1.60E-24	1.24E-24	1.46E-24	1.13E-24	1.11E-24	1.17E-24
2.5	7.44E-05	7.39E-05	5.88E 02	1.79E-24	1.79E-24	1.39E-24	1.64E-24	1.28E-24	1.26E-24	1.32E-24
2.6	8.74E-05	8.77E-05	5.74E 02	1.96E-24	2.00E-24	1.56E-24	1.84E-24	1.44E-24	1.41E-24	1.47E-24
2.7	1.03E-04	1.02E-04	5.61E 02	2.13E-24	2.22E-24	1.74E-24	2.05E-24	1.61E-24	1.58E-24	1.64E-24
2.8	1.20E-04	1.19E-04	5.50E 02	2.29E-24	2.45E-24	1.92E-24	2.27E-24	1.79E-24	1.75E-24	1.82E-24
2.9	1.38E-04	1.37E-04	5.38E 02	2.45E-24	2.69E-24	2.12E-24	2.51E-24	1.98E-24	1.94E-24	2.01E-24
3.0	1.55E-04	1.56E-04	5.27E 02	2.56E-24	2.94E-24	2.33E-24	2.75E-24	2.18E-24	2.14E-24	2.21E-24

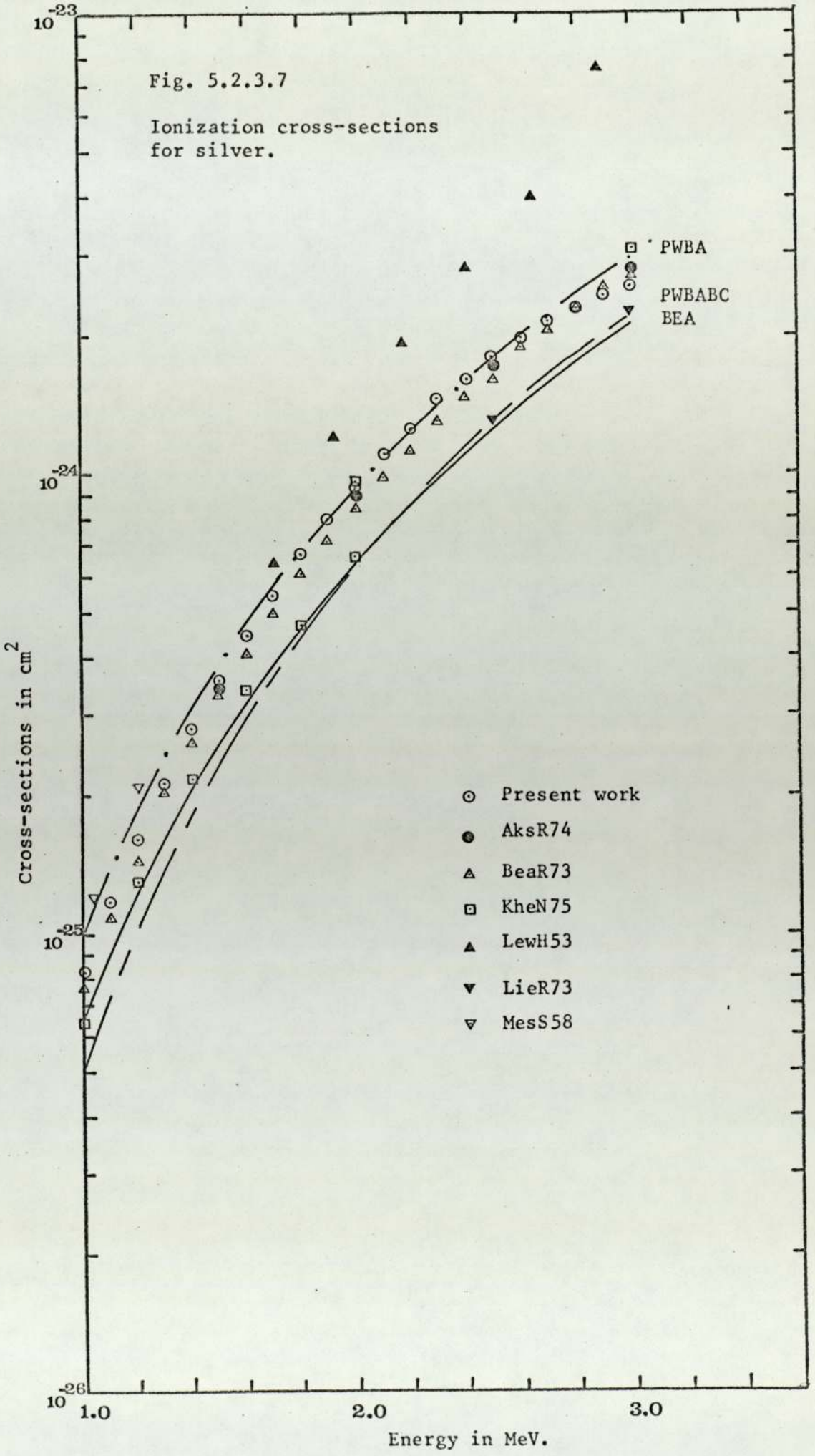
Fig. 5.2.3.7
Ionization cross-sections for silver.
PWBA
PWBABC
BEA
Present work
AksR74
BeaR73
KheN75
LewH53
LieR73
MesS58
Cross-sections in cm^2
10^{-23}
10^{-24}
10^{-25}
10^{-26}
1.0
2.0
3.0
Energy in MeV.

TABLE 5.2.3.10

K-SHELL THICK TARGET YIELDS AND DERIVED IONIZATION CROSS-SECTIONS, AND THEIR COMPARISONS WITH THE PREDICTIONS OF DIFFERENT THEORIES FOR THE ELEMENT CADMIUM WITH WK=0.840 MU= 1.41 AND DE/DX VALUES FROM REFERENCE JAN.66

E(P)	YIELD	YIELDFIT	DE/DX	SIGMA(I)	PWBA	PWBAB	PWBAC	PWBABC	BEA	CBEA
1.0	5.05E-07	5.07E-07	7.88E 02	5.45E-26	7.82E-26	5.62E-26	5.41E-26	3.89E-26	5.18E-26	6.23E-26
1.2	1.33E-06	1.30E-06	7.14E 02	1.07E-25	1.45E-25	1.06E-25	1.10E-25	8.00E-26	9.66E-26	1.13E-25
1.4	2.82E-06	2.90E-06	6.57E 02	1.87E-25	2.42E-25	1.78E-25	1.94E-25	1.43E-25	1.61E-25	1.83E-25
1.6	5.78E-06	5.74E-06	6.10E 02	3.01E-25	3.72E-25	2.77E-25	3.10E-25	2.31E-25	2.50E-25	2.78E-25
1.8	1.05E-05	1.04E-05	5.71E 02	4.51E-25	5.38E-25	4.06E-25	4.62E-25	3.48E-25	3.64E-25	3.98E-25
2.0	1.74E-05	1.74E-05	5.38E 02	6.35E-25	7.42E-25	5.65E-25	6.52E-25	4.96E-25	5.07E-25	5.46E-25
2.2	2.76E-05	2.76E-05	5.09E 02	8.51E-25	9.86E-25	7.58E-25	8.81E-25	6.77E-25	6.80E-25	7.25E-25
2.4	4.14E-05	4.14E-05	4.84E 02	1.09E-24	1.27E-24	9.84E-25	1.15E-24	8.91E-25	8.86E-25	9.35E-25
2.6	5.91E-05	5.92E-05	4.63E 02	1.35E-24	1.59E-24	1.25E-24	1.46E-24	1.14E-24	1.13E-24	1.18E-24
2.8	8.11E-05	8.15E-05	4.43E 02	1.61E-24	1.96E-24	1.54E-24	1.81E-24	1.42E-24	1.40E-24	1.46E-24
3.0	1.08E-04	1.08E-04	4.25E 02	1.86E-24	2.36E-24	1.87E-24	2.20E-24	1.74E-24	1.71E-24	1.77E-24

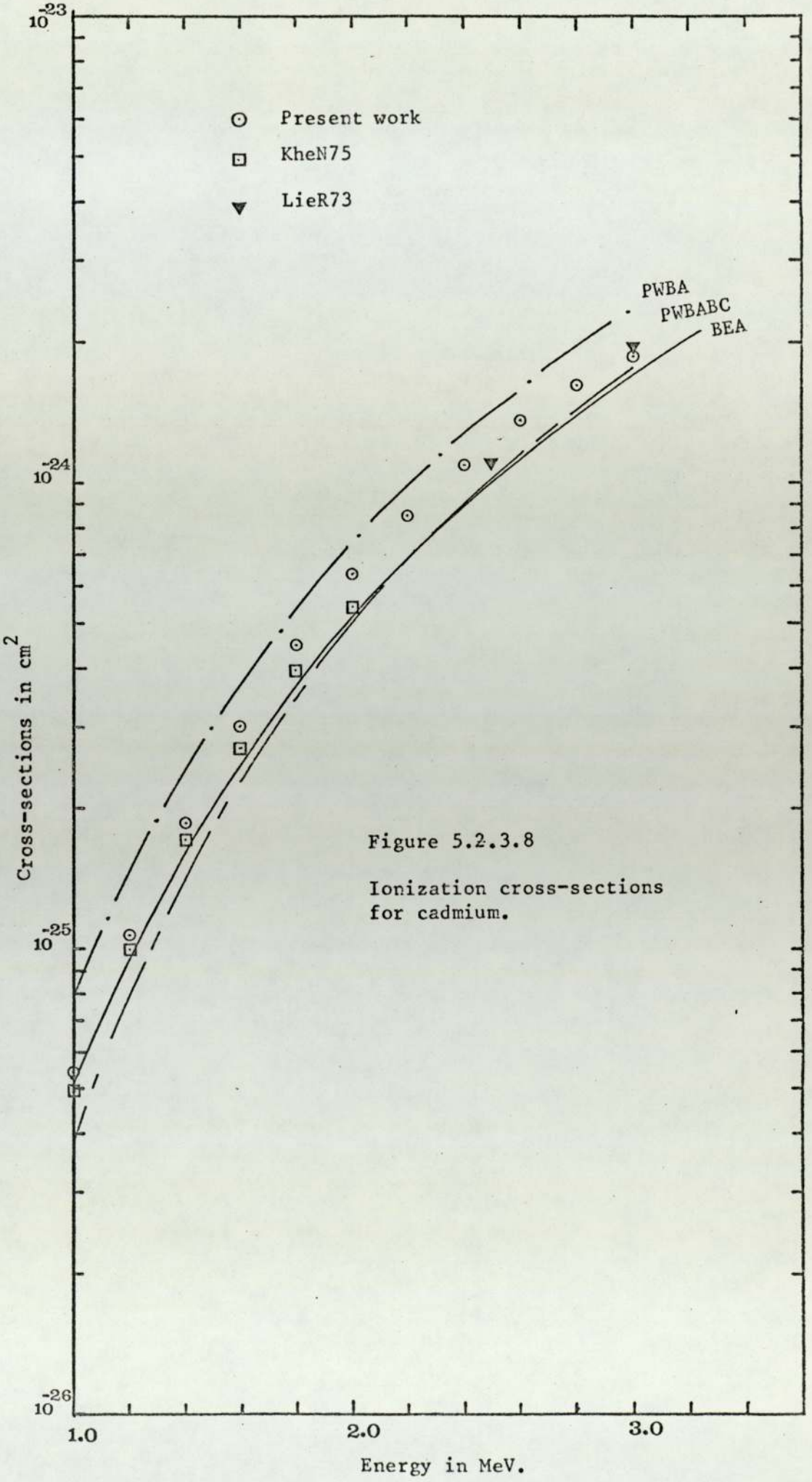

Figure 5.2.3.8

Ionization cross-sections for cadmium.

within the experimental error (Fig.5.2.3.8).

No measurement has been reported for indium in this energy region and the present data lies between the theoretical predictions (Fig.5.2.3.9).

For tin the agreement is excellent between the present measurement and thin target measurements of Bearse et.al (BeaR73) and Khelil et.al (KheN75) except at 1 MeV where present data is below Khelil's by $\sim$ 20% and above Bearse et.al (BeaR73) $\sim$ 17%. A solitary point of the thick target yield measurement of Messelt (MesS58) at 1.04 MeV is below the present measurement by $\sim$ 47%. Again the present measurement lies between the prediction of the theories (Fig.5.2.3.9).

To summarize, reasonable agreement was found between the present measurements and the thin target yield measurements of Aksselsson et.al (AksR74), Bissinger et.al (BisG72), and the thin target measurements made by North Texas University Group [(Lear et.al (LeaR73), Criswell et.al (CriT74), Khelil et.al (KheN75)] and similar measurements of Liebert et.al. (LieR73). The thin target measurements of Bodart et.al (BodF75) and McCoy et.al (McCJ75) are almost always systematically higher, whereas similar measurements of Bearse et.al (BeaR73) are always systematically lower than the present measurement except in case of silver and tin where the agreement is excellent.

A detailed summary of the proton induced cross-section for K shell ionization is provided in Appendix 1.

TABLE 5.2.3.11

K-SHELL THICK TARGET YIELDS AND DERIVED IONIZATION CROSS-SECTIONS, AND THEIR COMPARISONS
WITH THE PREDICTIONS OF DIFFERENT THEORIES FOR THE ELEMENT INDIUM
WITH WK=0.850 MU= 1.58 AND DE/DX VALUES FROM REFERENCE CONR75

E(P)	YIELD	YIELDFIT	DE/DX	SIGMA(I)	PWBA	PWBAB	PWBAC	PWBABC	BEA	CBEA
1.0	3.42E-07	3.42E-07	6.57E 02	4.21E-26	6.07E-26	4.38E-26	4.09E-26	2.96E-26	4.05E-26	4.91E-26
1.2	9.69E-07	9.75E-07	6.00E 02	8.56E-26	1.13E-25	8.28E-26	8.40E-26	6.14E-26	7.58E-26	8.91E-26
1.4	2.26E-06	2.24E-06	5.54E 02	1.50E-25	1.89E-25	1.40E-25	1.49E-25	1.10E-25	1.27E-25	1.46E-25
1.6	4.49E-06	4.51E-06	5.16E 02	2.41E-25	2.92E-25	2.19E-25	2.41E-25	1.80E-25	1.97E-25	2.21E-25
1.8	8.26E-06	8.21E-06	4.83E 02	3.61E-25	4.24E-25	3.21E-25	3.61E-25	2.72E-25	2.88E-25	3.17E-25
2.0	1.36E-05	1.38E-05	4.55E 02	5.11E-25	5.88E-25	4.48E-25	5.11E-25	3.90E-25	4.02E-25	4.36E-25
2.2	2.21E-05	2.20E-05	4.30E 02	6.90E-25	7.83E-25	6.03E-25	6.95E-25	5.35E-25	5.41E-25	5.80E-25
2.4	3.33E-05	3.32E-05	4.09E 02	8.94E-25	1.01E-24	7.86E-25	9.11E-25	7.07E-25	7.07E-25	7.49E-25
2.6	4.79E-05	4.78E-05	3.90E 02	1.11E-24	1.28E-24	9.97E-25	1.16E-24	9.08E-25	9.00E-25	9.46E-25
2.8	6.61E-05	6.64E-05	3.73E 02	1.34E-24	1.57E-24	1.24E-24	1.45E-24	1.14E-24	1.12E-24	1.17E-24
3.0	8.90E-05	8.89E-05	3.57E 02	1.57E-24	1.90E-24	1.51E-24	1.76E-24	1.40E-24	1.37E-24	1.43E-24

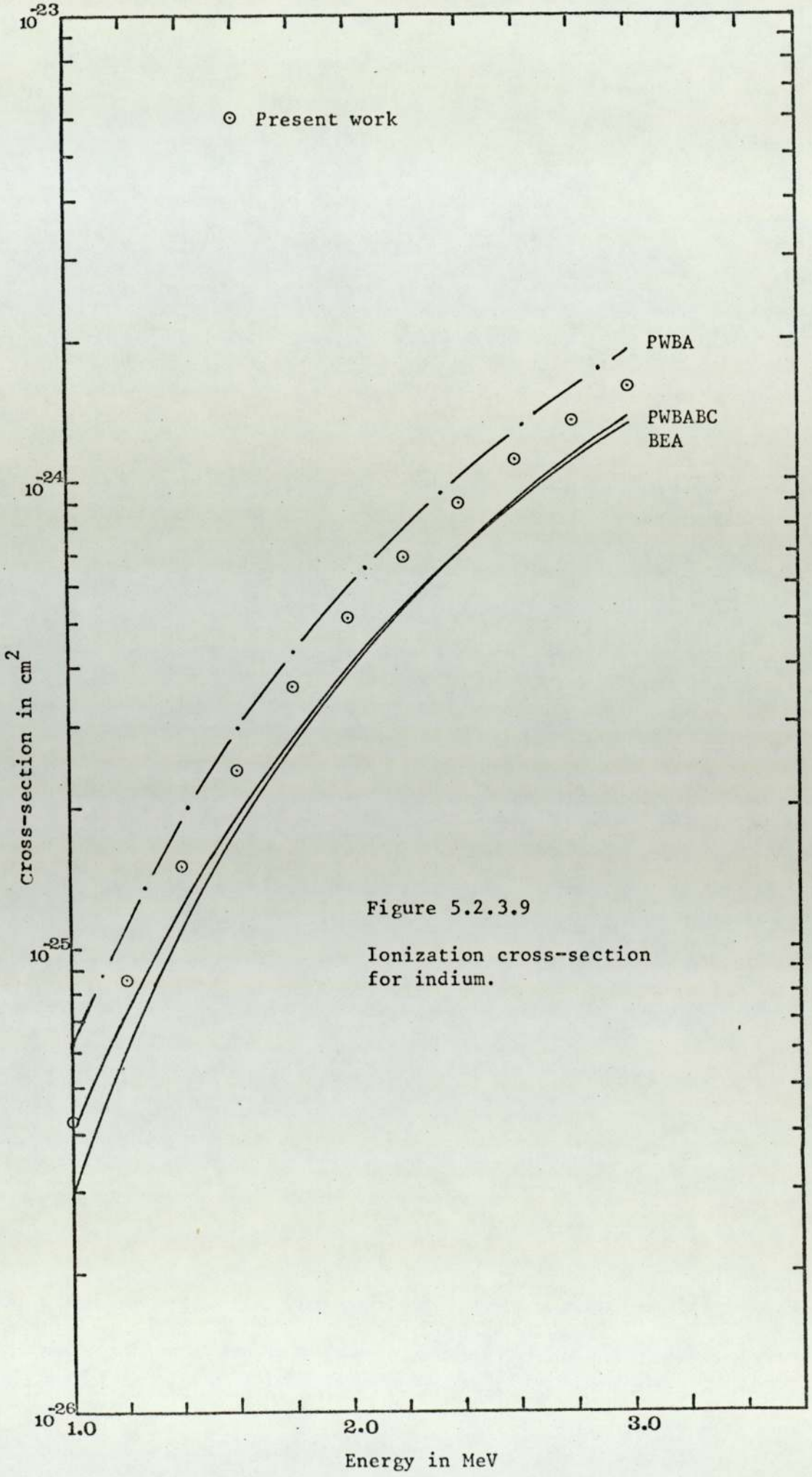

Figure 5.2.3.9

Ionization cross-section for indium.

TABLE 5.2.3.12

K-SHELL THICK TARGET YIELDS AND DERIVED IONIZATION CROSS-SECTIONS, AND THEIR COMPARISONS WITH THE PREDICTIONS OF DIFFERENT THEORIES FOR THE ELEMENT TIN WITH WK=0.859 MU= 1.48 AND DE/DX VALUES FROM REFERENCE JAN166

E(p)	YIELD	YIELDFIT	DE/DX	SIGMA(I)	PWBA	PWBAB	PWBAC	PWBABC	BEA	CBEA
1.0	2.55E-07	2.54E-07	6.47E 02	2.80E-26	4.73E-26	3.43E-26	3.11E-26	2.25E-26	3.18E-26	3.88E-26
1.2	7.12E-07	7.19E-07	5.87E 02	6.64E-26	8.86E-26	6.50E-26	6.44E-26	4.73E-26	5.97E-26	7.07E-26
1.4	1.78E-06	1.74E-06	5.40E 02	1.21E-25	1.49E-25	1.10E-25	1.15E-25	8.57E-26	1.01E-25	1.16E-25
1.6	3.48E-06	3.56E-06	5.01E 02	1.91E-25	2.30E-25	1.73E-25	1.87E-25	1.40E-25	1.56E-25	1.76E-25
1.8	6.54E-06	6.47E-06	4.69E 02	2.77E-25	3.36E-25	2.54E-25	2.82E-25	2.14E-25	2.29E-25	2.54E-25
2.0	1.07E-05	1.07E-05	4.42E 02	3.85E-25	4.67E-25	3.57E-25	4.02E-25	3.08E-25	3.21E-25	3.50E-25
2.2	1.69E-05	1.69E-05	4.18E 02	5.20E-25	6.24E-25	4.81E-25	5.49E-25	4.23E-25	4.32E-25	4.65E-25
2.4	2.57E-05	2.55E-05	3.97E 02	6.84E-25	8.09E-25	6.29E-25	7.23E-25	5.62E-25	5.66E-25	6.03E-25
2.6	3.69E-05	3.70E-05	3.79E 02	8.71E-25	1.02E-24	8.00E-25	9.25E-25	7.24E-25	7.22E-25	7.62E-25
2.8	5.14E-05	5.17E-05	3.63E 02	1.06E-24	1.26E-24	9.96E-25	1.16E-24	9.11E-25	9.01E-25	9.45E-25
2.9	6.03E-05	6.03E-05	3.55E 02	1.15E-24	1.39E-24	1.10E-24	1.28E-24	1.01E-24	1.00E-24	1.05E-24
3.0	6.99E-05	6.96E-05	3.48E 02	1.22E-24	1.53E-24	1.22E-24	1.41E-24	1.12E-24	1.11E-24	1.15E-24

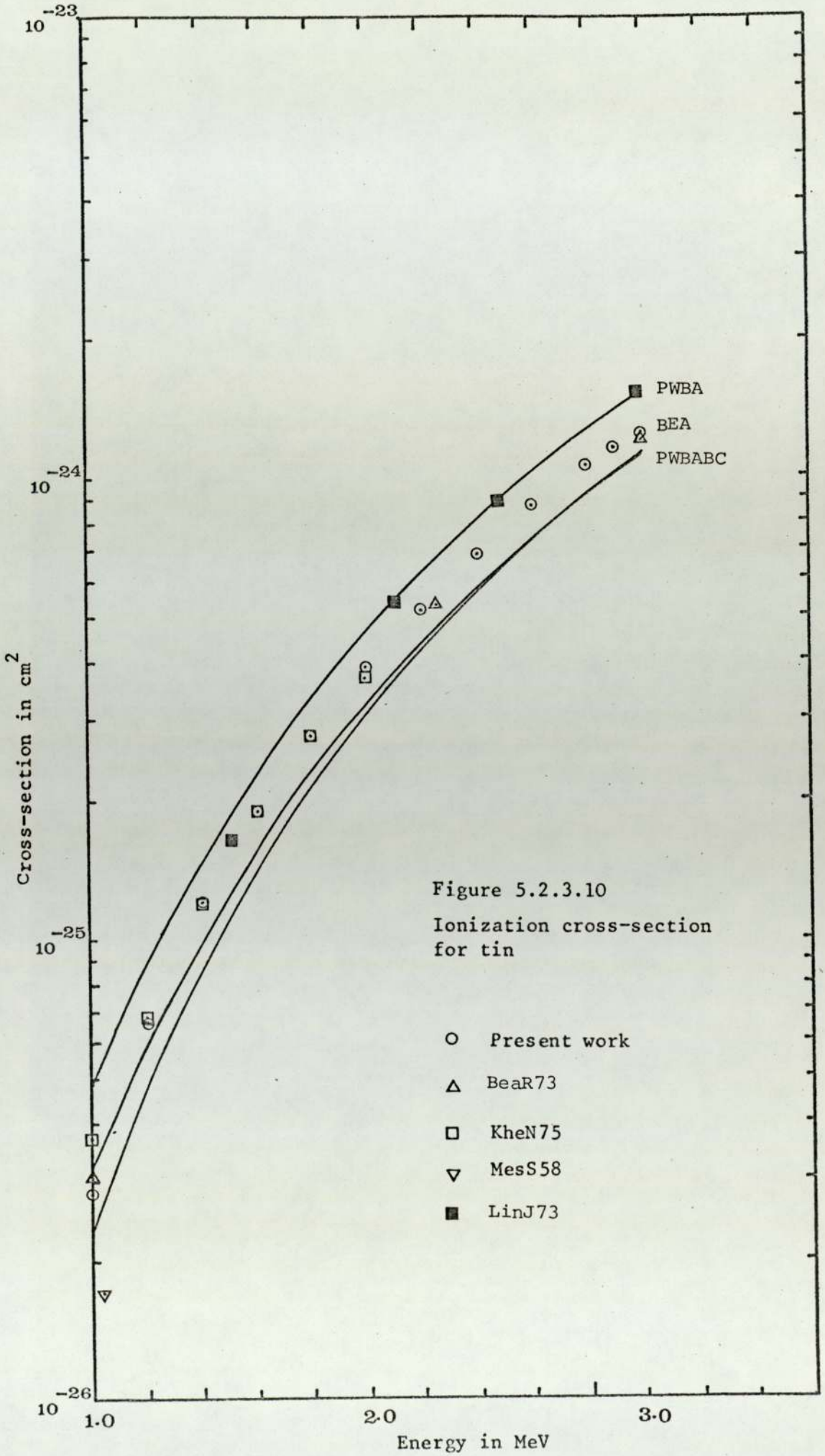

Figure 5.2.3.10

Ionization cross-section for tin

5.2.4 Experimental data and universal cross-sections.

The non-relativistic theoretical descriptions of the K-shell ionization by heavy charged particles namely PWBA and PWBA with binding energy and/or coulomb deflection corrections, BEA and CBEA, predict universal functions for all projectile target combinations in the range $E<450E_K$.

In this section present experimental cross-sections are reduced to the format of the universal functions of different theoretical predictions and are compared with them. For the sake of clarity the reduced cross-section at only 1, 2 and 3 MeV for all elements are plotted, other points are chosen to produce continuity in the plot.

In figures 5.2.4.1 to 5.2.4.4 comparisons are made between our data and the predictions of PWBA and the different modifications of PWBA proposed by Basbas et.al (BasG73).

In all these figures the curves represent a plot of $\sigma^{PWBA}/\sigma_{OK}/\theta_K)$ vs (η_K/θ_K^2) (Chapter III), taken from the tabulations reported by Basbas et.al (BasG73).

Comparison between our data and PWBA is made in figure 5.2.4.1, which shows that the PWBA curve lies above all our experimental points by about 15 - 50%, except in the case of titanium where measured data lie above the curve, and two points in silver where the agreement is very close.

In their work on the introduction of binding energy and coulomb deflection corrections to PWBA Basbas et.al showed a similar

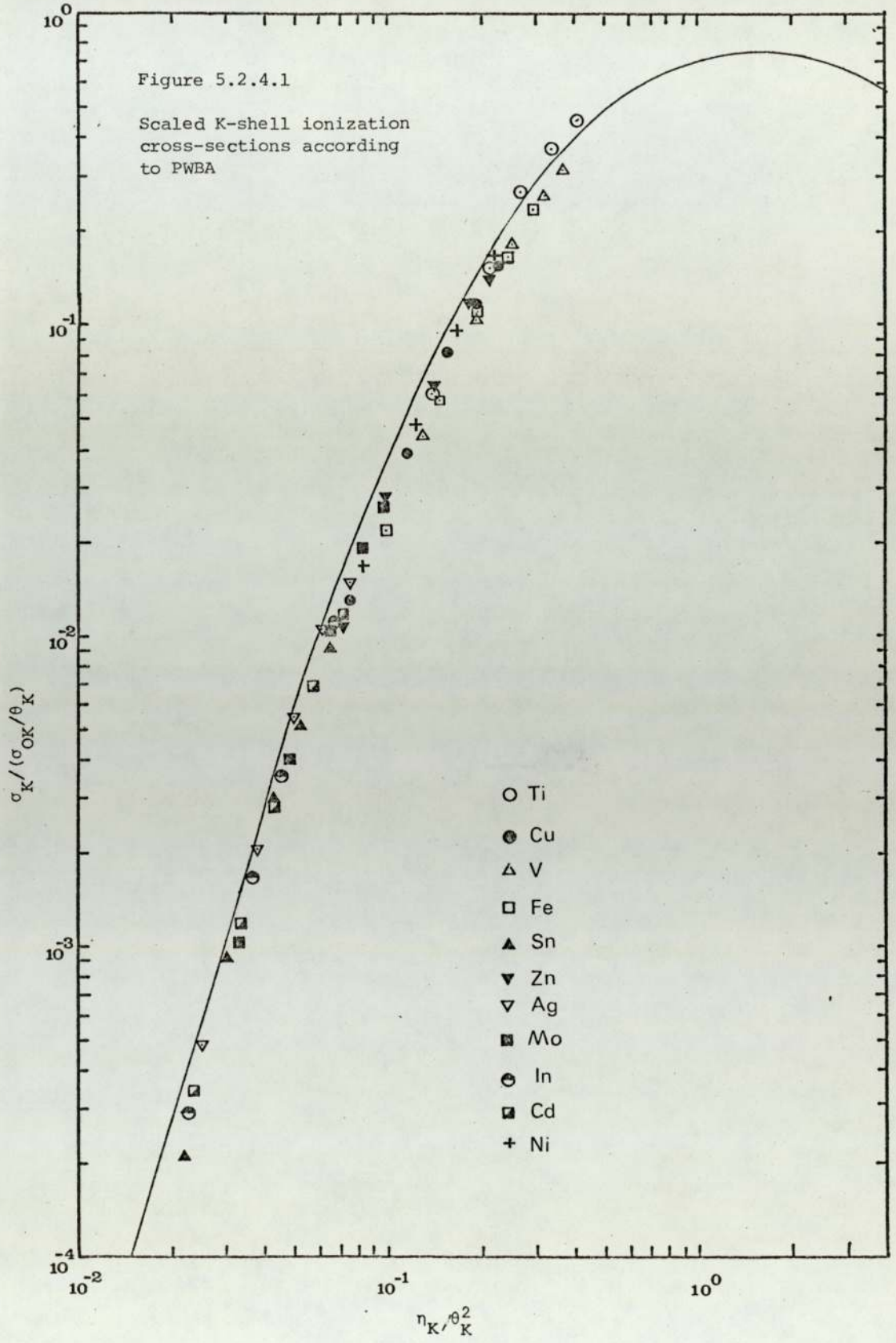
Figure 5.2.4.1
Scaled K-shell ionization cross-sections according to PWBA
10^0
10^{-1}
10^{-2}
10^{-3}
10^{-4}
10^{-2}
10^{-1}
10^0
$\sigma_K/(\sigma_{OK}/\theta_K)$
η_K/θ_K^2
Ti
Cu
V
Fe
Sn
Zn
Ag
Mo
In
Cd
Ni

discrepancy between their data and the PWBA universal function. There is, however, an important quantitative difference between the present data and theirs in that a) the deviation of their data from PWBA and b) the scatter of their data at any point are much greater than those of the present work. For example at $\eta_K/\theta_K^2 \sim 3 \times 10^{-2}$ the mean value of $\sigma_K/(\sigma_{oK}/\theta_K)$ in the present work is $\sim$ 70% of the theoretical value whereas the corresponding mean value reported by Basbas et.al (BasG73) is only $\sim$ 30% of the predicted value. Their data at the same point scatter between 1×10^{-4} and 6×10^{-4} whereas the corresponding spread in the present data is less than 30%. Their data however are based on the K shell ionization cross-section induced by H, D, $^3_2$He from low Z material such as aluminium carbon and oxygen whereas the present work consists of measurements on medium Z materials ($22 \lesssim Z \lesssim 50$) by 1 - 3 MeV protons. The measurements on copper by low energy protons (60 - 500 KeV) reported in their comparison lie above the rest of their data, which might be informative in explaining the disagreement between the two sets of data.

The effect of applying binding energy correction to the cross-section is shown in figure 5.2.4.2. The agreement between the experimental data and the universal curve is very good except for titanium and silver data.

A similar plot is made in figure 5.2.4.3 to show the effect of coulomb deflection correction on the present data. Compared to PWBA

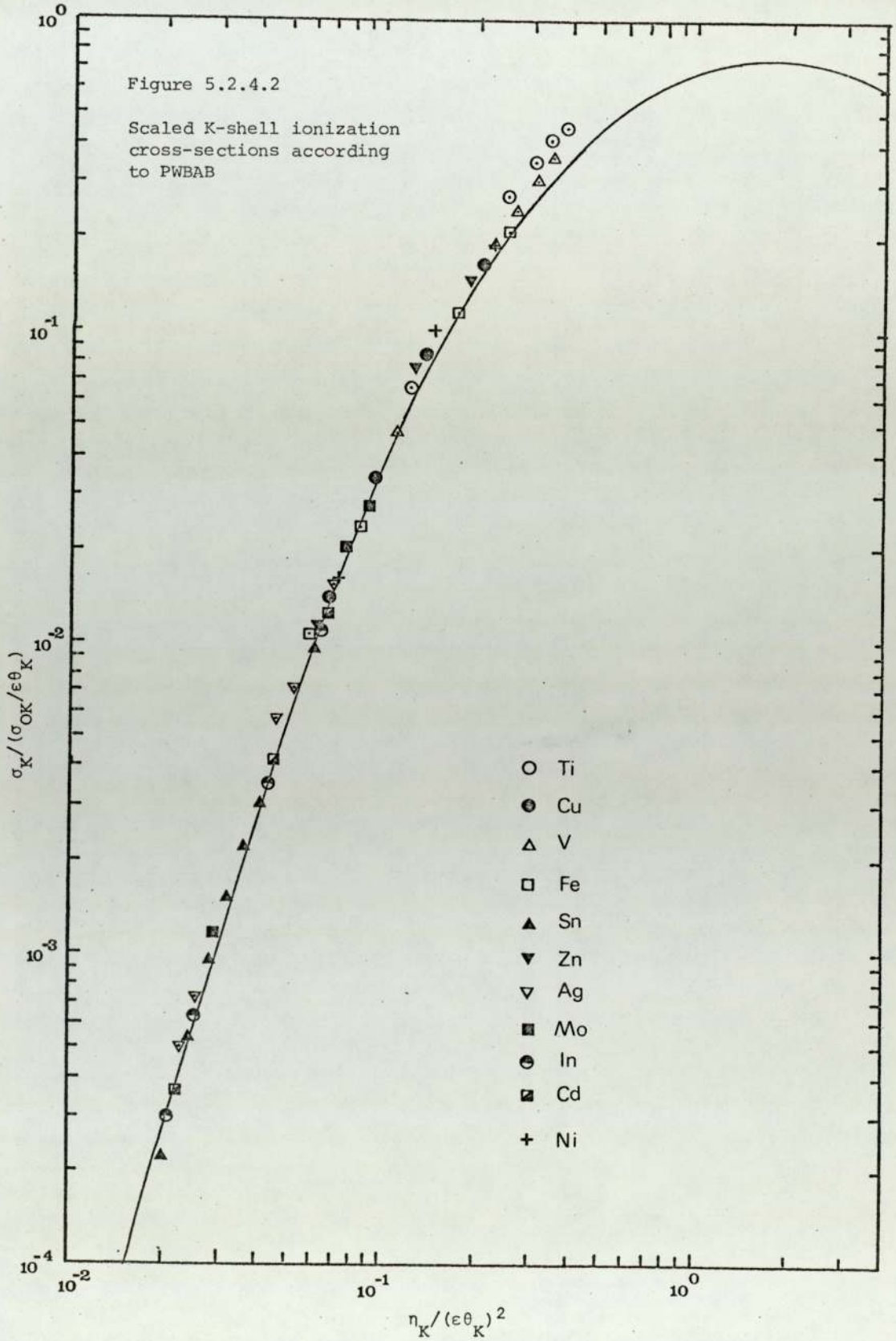
Figure 5.2.4.2
Scaled K-shell ionization cross-sections according to PWBAB
10^0
10^{-1}
10^{-2}
10^{-3}
10^{-4}
10^{-2}
10^{-1}
10^0
$\sigma_K/(\sigma_{OK}/\varepsilon\theta_K)$
$\eta_K/(\varepsilon\theta_K)^2$
Ti
Cu
V
Fe
Sn
Zn
Ag
Mo
In
Cd
Ni

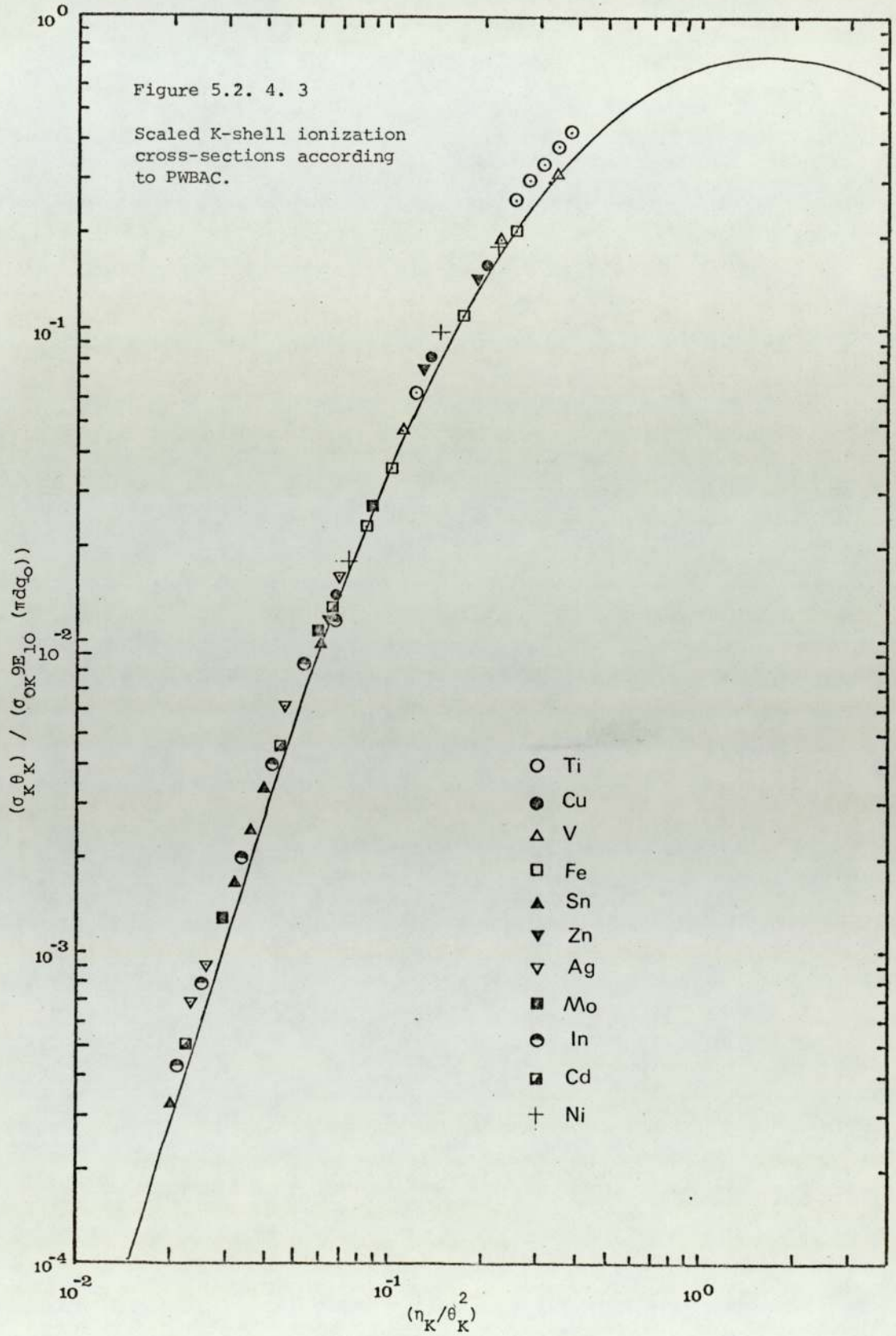
Figure 5.2. 4. 3
Scaled K-shell ionization cross-sections according to PWBAC.
10^0
10^{-1}
10^{-2}
10^{-3}
10^{-4}
$(\sigma_K \theta_K) / (\sigma_{OK} {}^9E_{10} (\pi d a_o))$
10^{-2}
10^{-1}
10^0
(η_K / θ_K^2)
Ti
Cu
V
Fe
Sn
Zn
Ag
Mo
In
Cd
Ni

the agreement between the experimental data treated with coulomb correction and the universal curve is much better. The agreement at $\eta_K/\theta_K^2 \geq .1$ is comparable with that of PWBAB but at $\eta_K/\theta_K^2 \leq .1$ PWBAC agreement with the curve is inferior.

The combined effect of binding energy and coulomb deflection corrections (PWBABC) on the experimental data and their comparison with the universal function is shown in figure 5.2.4.4, which shows that the PWBABC underestimate the cross-section significantly. The deviation of the experimental data reduced to the format of PWBABC is about the same order of magnitude as that of PWBA, but they are opposite in direction.

Since both of the corrections in the derivation of PWBABC namely binding energy correction (change in Z number) and coulomb deflection correction mainly involve the atomic numbers of the target elements the predictions of the theories are tested for their Z dependence at 3 specific energies, 1, 2 and 3 MeV. Fourth order polynomials were fitted to the experimental data at these three energies. The curves marked 1, 2 and 3 in figure 5.2.4.5 represent the cross-sections calculated from these polynomial at 1, 2 and 3 MeV. Theoretical PWBA and PWBABC cross-sections at 1, 2, 3 MeV for the elements studied are also plotted along with the curves. Since binding energy and coulomb deflection effects should be most pronounced for any element at 1 MeV in the present energy region studied, cross-sections for PWBAB and PWBAC for these elements are also plotted at 1 MeV. Comparison of PWBA and PWBABC at all these three energies shows that at a certain energy, as expected from the theories, they deviate more from each other as they progress towards higher atomic number, and the curves pass almost through the middle of the predictions of these two theories.

Inspection of the plot at 1 MeV shows an interesting feature.

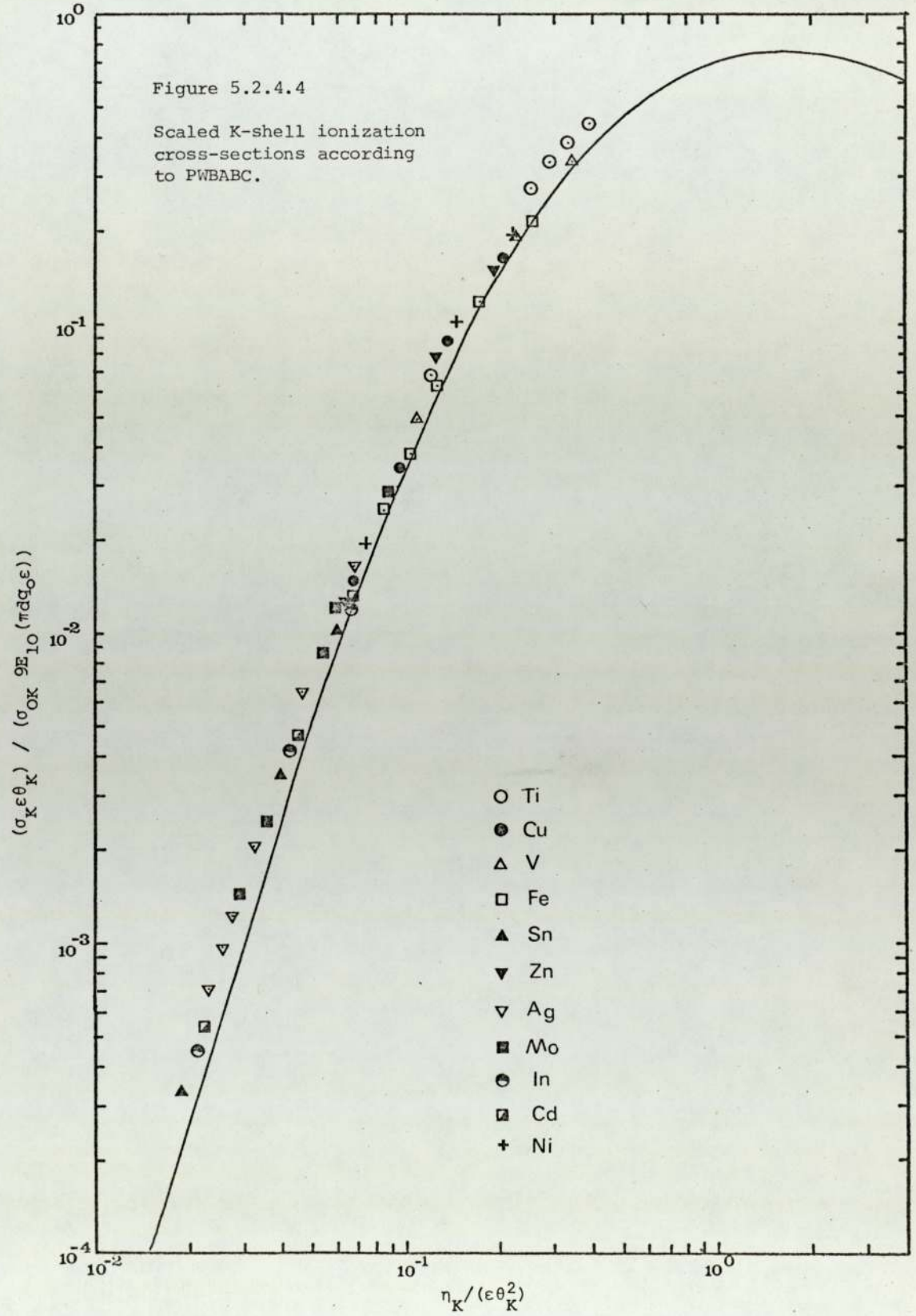
Figure 5.2.4.4
Scaled K-shell ionization cross-sections according to PWBABC.
10^0
10^{-1}
10^{-2}
10^{-3}
10^{-4}
10^{-2}
10^{-1}
10^0
$(\sigma_K \varepsilon \theta_K) / (\sigma_{OK} 9E_{10}(\pi d q_o \varepsilon))$
$\eta_K / (\varepsilon \theta_K^2)$
Ti
Cu
V
Fe
Sn
Zn
Ag
Mo
In
Cd
Ni

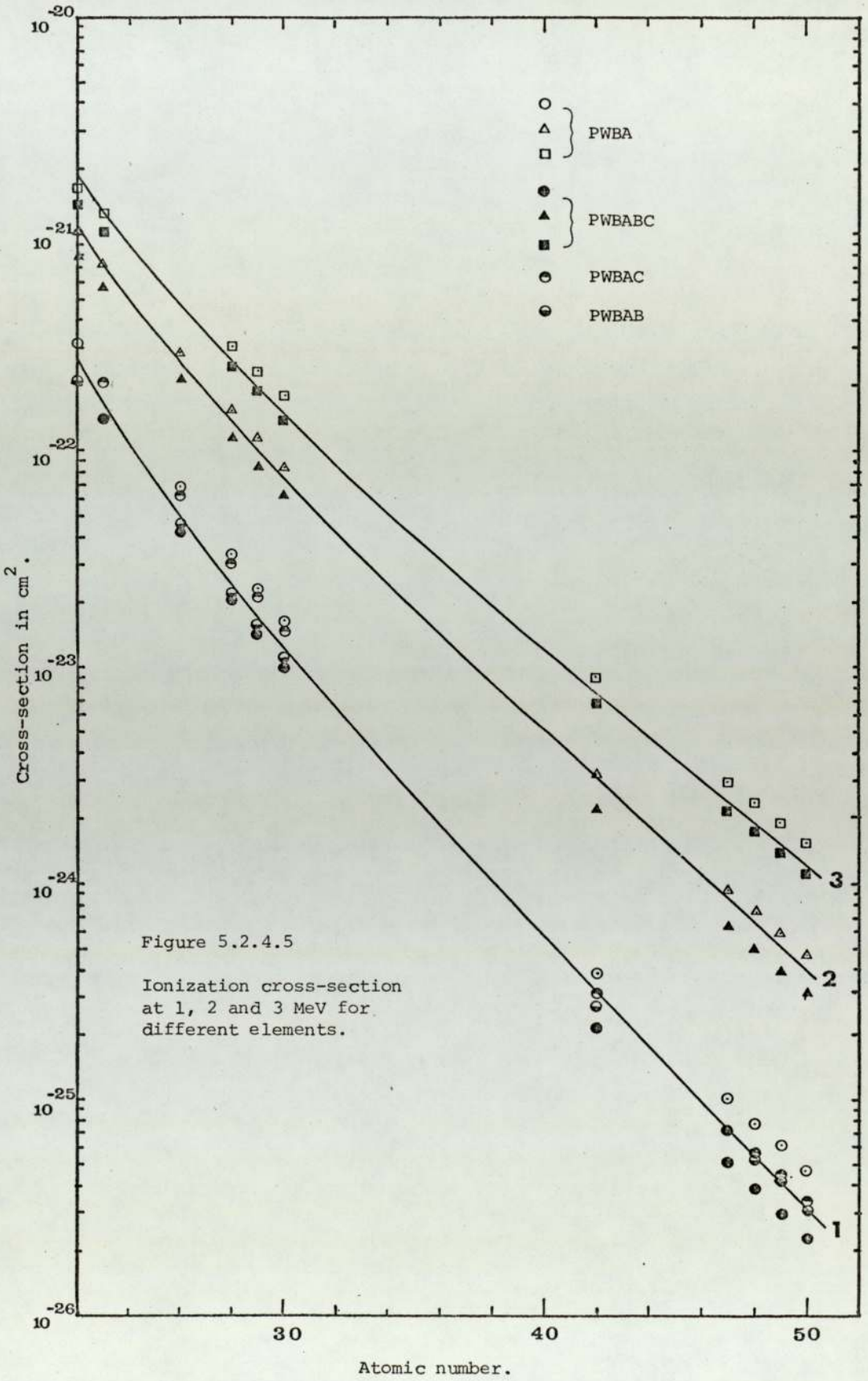

Figure 5.2.4.5

Ionization cross-section at 1, 2 and 3 MeV for different elements.

As expected at this energy, the coulomb deflection effect should be negligible for low Z element and should be more prominent for higher Z materials and hence any deviation of PWBABC from PWBA at low Z should almost wholly be attributed to binding energy effect, and at higher Z the total deviation of PWBABC from PWBA should contain both effects together. At low Z e.g. titanium and vanadium PWBAB and PWBAC are respectively indistinguishable from PWBABC and PWBA, whereas at higher Z they deviate from them and for Z $\sim$ 50 the corrections to PWBA by them are comparable.

On the basis of these discussions it can be inferred that both PWBA and PWBABC disagree significantly with the experimental data, while PWBA overestimates, PWBABC underestimates the cross-section by almost the same amount. Though PWBAB provide the best fit among the theories discussed, PWBAC produces comparable agreement.

Comparison is made between the universal function predicted by BEA theory and the experimental cross-sections reduced to BEA format in figure 5.2.4.6. The agreement is comparable to PWBAC in the region $(E/\lambda E_K) < 10^{-1}$ above which BEA tends to overestimate the cross-section. The agreement with the experimental data is better than both PWBA and PWBABC.

Similar comparison is also made for non-relativistic CBEA predictions (Fig.5.2.4.7), the curve represents the CBEA univeral function tabulated by Hansen et.al (HanJ73). The agreement between the theoretical prediction and the experimental data is comparable to PWBAB in the region $E/\lambda E_K^2 < 10^{-1}$ and follows BEA closely in the region $E/\lambda E_K^2 > 10^{-1}$.

To make a comparison between all the universal functions and the experimental data together, the cross-sections predicted by different theories and the present experimental cross-sections are reduced to

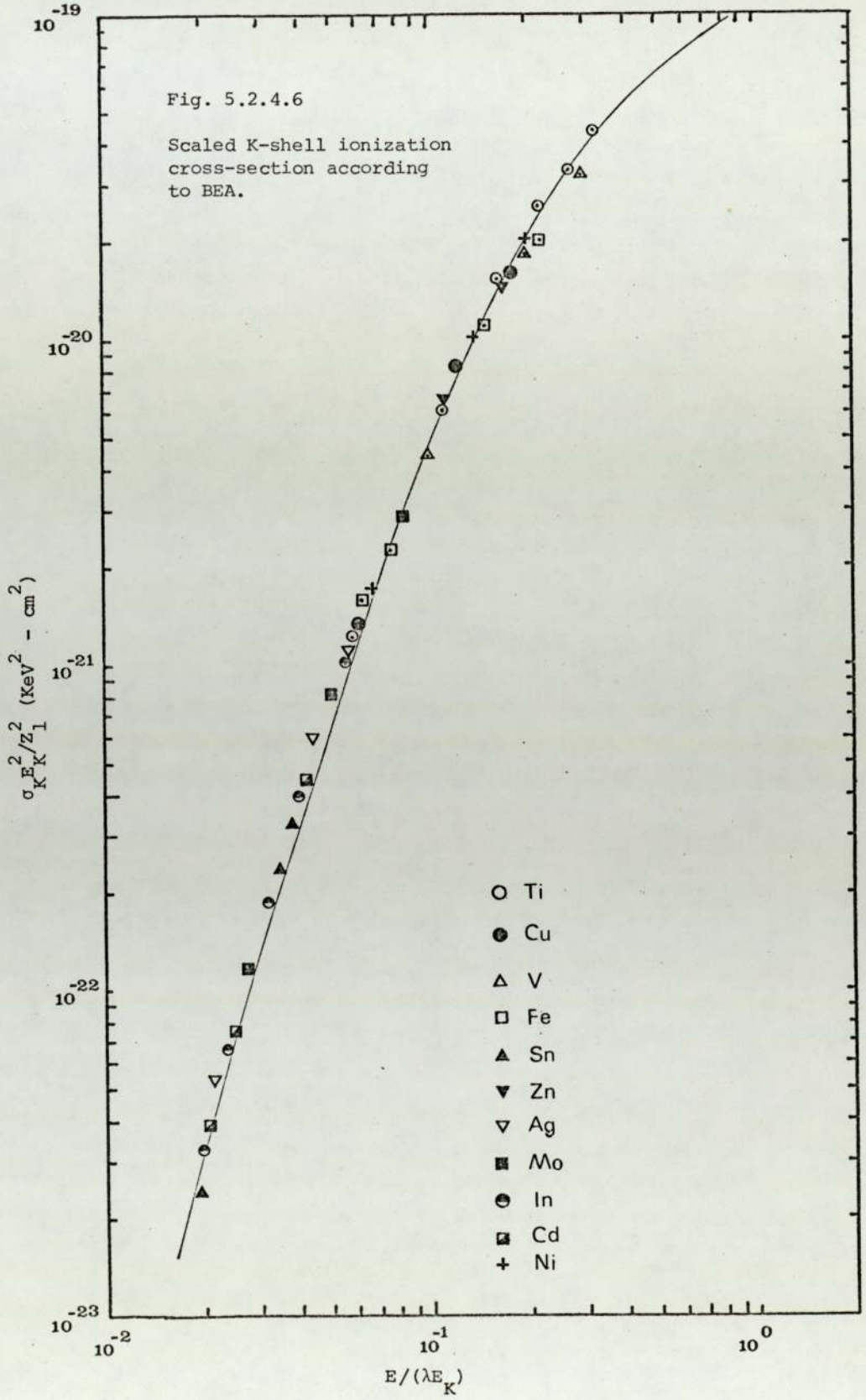
Fig. 5.2.4.6
Scaled K-shell ionization cross-section according to BEA.
10^{-19}
10^{-20}
10^{-21}
10^{-22}
10^{-23}
$\sigma_K E_K^2/Z_1^2$ (KeV^2 - cm^2)
10^{-2}
10^{-1}
10^{0}
$E/(\lambda E_K)$
Ti
Cu
V
Fe
Sn
Zn
Ag
Mo
In
Cd
Ni

Fig. 5.2.4.7

Scaled K-shell ionization cross-section according to CBEA.

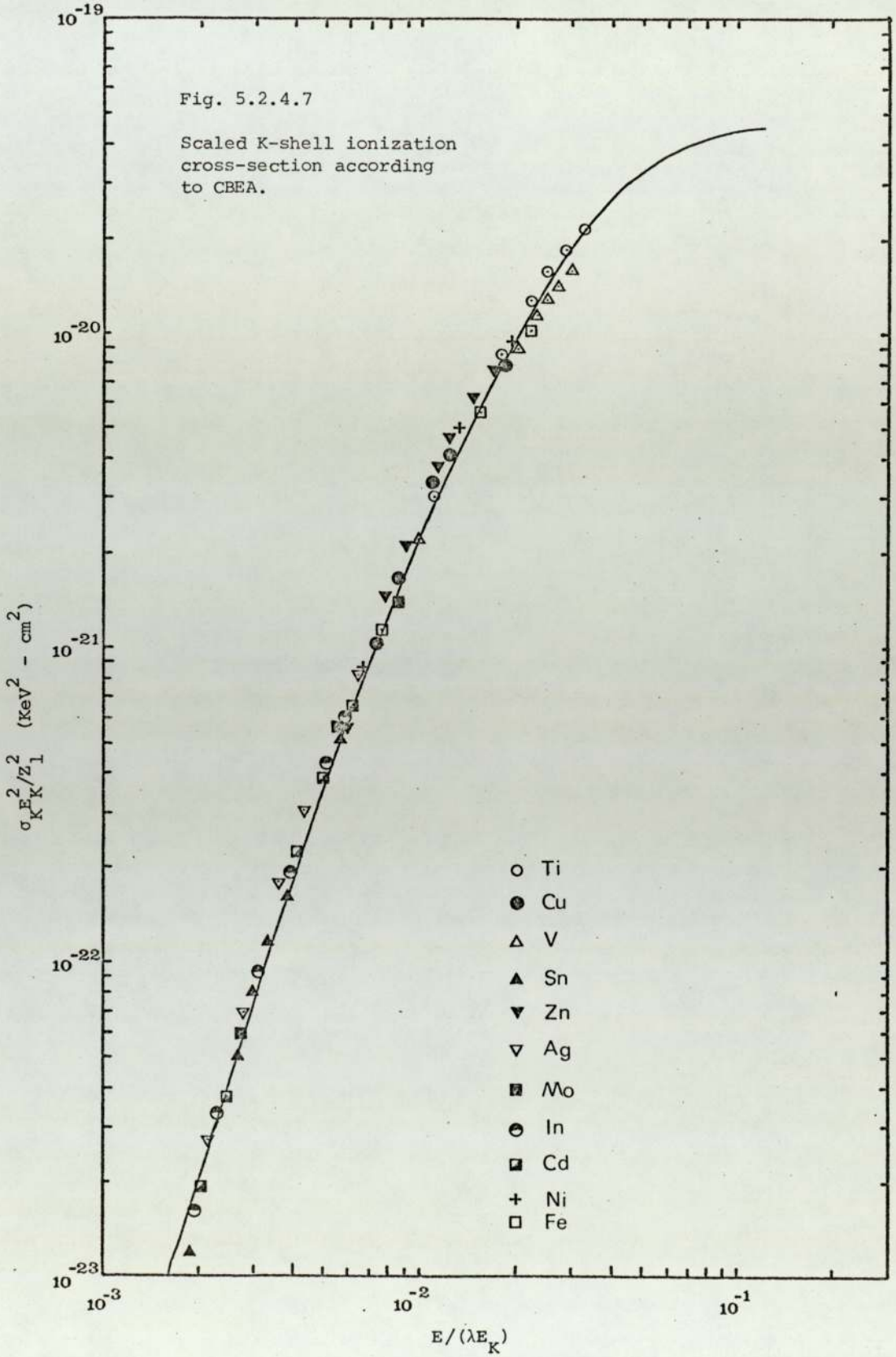

the format of BEA. A sixth order polynomial was fitted to the values of $\ell n(\sigma^{Expt}_{K} \times E_K^2)$ and $\ell n(E/\lambda E_K)$ for all elements at energies 1, 2 and 3 MeV.

The curve calculated from the polynomial is shown in figure 5.2.4.8 along with the prediction of different theories reduced to the format of BEA.

On the basis of a similar approach presenting the theoretical predictions reduced to BEA parameters as curves and plotting the scattered experimental points in the energy region 0.5 - 2 MeV for the proton induced ionization cross-section from thin target of Ag, Cd, Sn, Sb, Te, Ba, La Khelil and Gray (KheN75) favoured PWBAB to have overall best fit with their experimental data. However, the formation of universality of these data is not as good as that of present measurement and hence their prediction is more speculative.

On the basis of this discussion it should not be concluded that PWBAB provides the correct description of the K shell ionization cross-section, it can merely be stated that PWBAB gives the best empirical fit to the experimental data.

Recently calculations are being made for the relativistic corrections applicable to the ionization cross-sections for medium and high Z elements, Hansen et.al (HanJ73), Choi (ChoB71). These calculations show that, if applied, the relativistic corrections would increase the predicted cross-sections significantly. For example, Hansen (HanJ73), in his preliminary calculations for the relativistic corrections on silver, showed that such correction factors applied to the non-relativistic silver cross-sections at 1.25 MeV and 1.9 MeV are 1.48 and 1.31 respectively. These corrections applied to the PWBABC may be sufficient to remove the discrepancy between PWBABC and the experimental data.

It should be noted that the polynomial used to prepare the curve

Fig. 5.2.4.8

Experimental data reduced to BEA format and represented by a polynomial, theories reduced to BEA format.

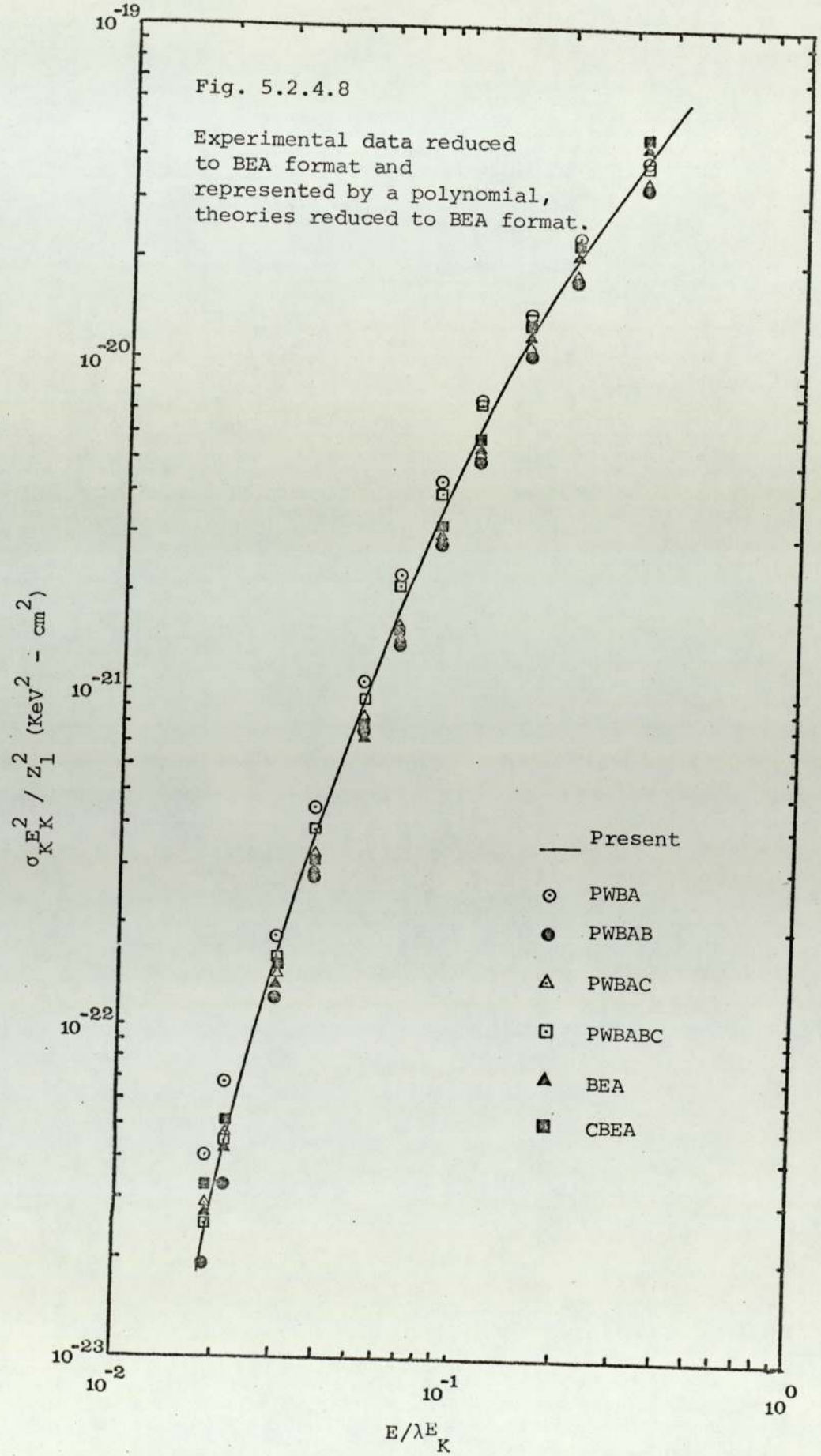

in figure 5.2.4.8 representing experimental ionization cross-section in the format of the BEA universal function can be used to calculate ionization cross-section for different elements in the limit

$$1.87E\text{-}2 \lesssim x \lesssim 3.3E\text{-}1 \quad \text{and for } 22 \lesssim Z \lesssim 50$$

$$\text{where} \quad x = \ell n\left(\frac{mE}{ME_K}\right)$$

The ionization cross-section is given by

$$\sigma_I(E) = \frac{1}{E_K^2} \text{Exp}(-18.48179 + 68.9357x + 73.2643\, x^2 + 40.196\, x^3 + 11.7229\, x^4 + 1.75928\, x^5 + .10499 x^6) \qquad 5.2.4.1$$

5.3 COMPARISON BETWEEN THIN AND THICK TARGET MEASUREMENTS:

In order to make a comparison between thick and thin target measurements consider the equations from which they are derived. The cross-sections for thick and thin targets respectively are given by:

$$\sigma_x = N \frac{d_t}{N_p d\Omega A \varepsilon} \left[\frac{dY}{dE} \cdot \frac{dE}{dx} + \mu Y \right] \qquad 5.3.1$$

$$\text{and} \quad \sigma_x = N \frac{d_t}{N_p d\Omega A \varepsilon} \frac{Y}{t} \qquad 5.3.2$$

where N_p is the number of incident protons, $d\Omega$ the geometrical efficiency, A, absorption corrections, ε, detector efficiency, d_t, dead time corrections, and N is the number of atoms/cc. These parameters with their uncertainties are present in both equations. t in this case is given in cm.

In order to compare the accuracy obtained in the two methods, the uncertainty in $\frac{dY}{dE}\frac{dE}{dx} + \mu Y$ is to be compared with the uncertainty in $\frac{Y}{t}$. It should be noted that in both the cases Y

contains only the statistical uncertainty.

The uncertainties in the parameters in the thick target measurements are discussed in section 5.2.2. The uncertainties in $\frac{dY}{dE}\frac{dE}{dx} + \mu Y$ are presented in table 5.2.2.2 for different elements. The maximum uncertainties at 1, 2 and 3 MeV are found to be $\sim$ 10%, $\sim$ 5% and $\sim$ 4% respectively.

For thin targets it is necessary to measure the thickness 't' accurately. In most of the recent works instead of directly measuring 't', it is eliminated by the use of Rutherford scattering formula for the incident proton beam.

N_R, the number of protons, scattered at an angle θ, to a detector subtending a solid angle $d\Omega_R$ to the point at which the beam hits the target is given by

$$N_R = Nt\, N_p\, \sigma_R(\theta)\, d\Omega_R \qquad 5.3.3$$

where N is the number of atoms/cc
and $\sigma_R(\theta)$ is the scattering cross-section at an angle θ.

Substituting N_p from equation 5.3.3 into equation 5.3.2 one obtains

$$\sigma_x = \frac{d_t}{A\varepsilon}\,\frac{Y}{N_R}\,\frac{d\Omega_R}{d\Omega}\,\sigma_R(\theta)$$

direct calculation of t is thus avoided.

Typical uncertainties in the measurement of t based on Rutherford scattering formula, as reported in recent works are for example 2 - 10% (KheN75), 1 - 3% (AksR74), 1 - 8% (GraT73). These uncertainties are probably slightly lower than the comparable uncertainty in thick target measurements.

This slight inferiority in accuracy for thick target measurements may be worth trading against the experimental advantages of using thick targets.

Preparation of self-supporting thin targets and subsequent handling of them needs extreme care. Rutherford scattering measurement of protons requires additional equipment. In addition, target deterioration and non-uniformity can be a serious problem in thin target measurements. Limitation on the use of high currents imposed by target heating sometimes restrict the thin target measurements to a very low yield. These problems are almost non-existent with the thick target measurements.

Although individual workers reporting thin target measurements claim uncertainties of < 10%, the differences between the authors are sometimes found to be as high as 60% (McCJ73 and BeaR73 on nickel). Similar comparisons cannot be made between thick target measurements in this energy region, due to the lack of reliable data. As can be seen from Appendix 1. almost all the thick target measurements reported in this energy region for the elements studied are based on inferior techniques.

It should be noted that the present thick target measurements are found to be consistent and compare well with the recent thin target measurements.

On the basis of this discussion it can be concluded that in the present energy range cross-sections with accuracy comparable to those from thin target methods can be derived from the thick target measurements.

CHAPTER VI

L Shell Measurements

6.1 INTRODUCTION

Recently there has been an increase in interest in the measurement of L shell ionization cross-sections by heavy charged particles. Vacancies produced in the three subshells LI, LII, LIII may be filled by the transition of an electron from a number of closely spaced energy levels in M, N, O and higher shells. The nomenclature of the subshells along with the major transitionsto LI, LII and LIII subshells are shown in figure 6.1.1.

The theoretical description of L shell ionization given in the Binary Encounter Approximation presented by Garcia et.al (GarJ73) is based on 1s hydrogenic wave functions and does not describe the finer details of subshell cross-sections. Working within the velocity space for electrons McGuire (McGE71) has developed the BEA theory for the description of L shell ionization. Hansen's (HanJ73) calculations of the L shell cross-sections in constrained BEA is based on more appropriate 2s and 2p hydrogenic wave functions. Calculations for non-relativistic PWBA cross-sections for L subshells have been reported by Choi et.al (ChoB73).

The last three approaches to the theoretical description predict a structure in the LI ionization cross-sections. They differ, however, in the energy of the exciting particle at which the maximum deflection occurs, and in the shape and extent of the structure. LII and LIII subshell ionization cross-sections on the other hand are monotonic increasing functionsof energy in all theories.

Apart from Lℓ and Lη transitions the resolution available with the present day Si(Li) detectors is not sufficient enough to separate X-rays due to individual transitions. The transitions appear in three groups Lα, Lβ and Lγ.

The main transitions comprising the Lα, Lβ and Lγ peaks are given

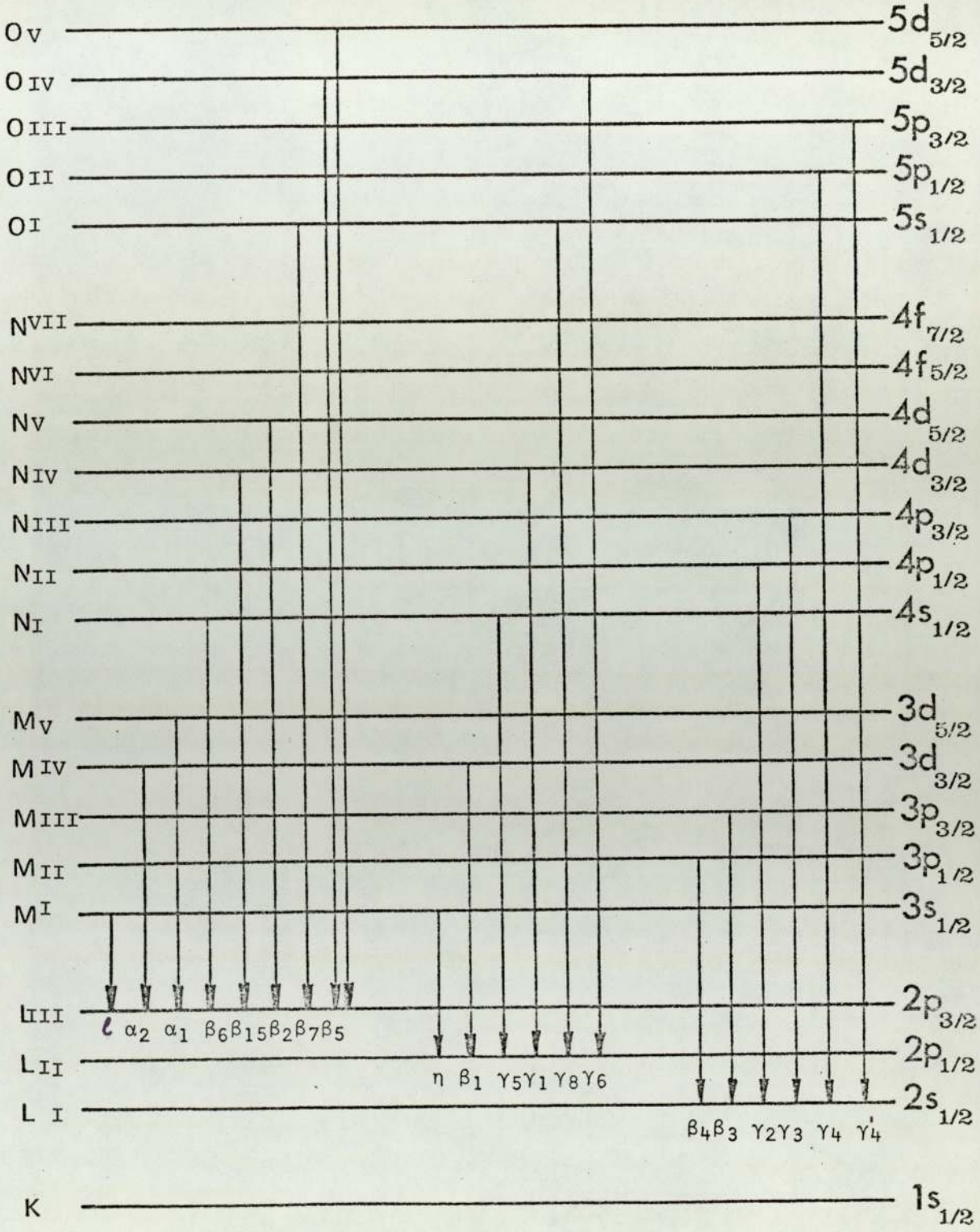

FIG. 6.1.1. L X-RAY TRANSITIONS

below:-

Table 6.1.1

Lα		Lβ		Lγ	
Nomenclature	Transition	Nomenclature	Transition	Nomenclature	Transition
$L\alpha_1$	M V - LIII	$L\beta_1$	MIV - LII	$L\gamma_1$	NIV - LII
$L\alpha_2$	MIV - LIII	$L\beta_2$	N V - LIII	$L\gamma_2$	NII - LI
		$L\beta_3$	MIII- LI	$L\gamma_3$	NIII- LI
		$L\beta_4$	MII - LI	$L\gamma_4$	OIII- LI
		$L\beta_5$	OIV,OV-LIII	$L\gamma_5$	NI - LII
		$L\beta_6$	N I - LIII	$L\gamma_6$	OIV - LII
		$L\beta_7$	O I - LIII	$L\gamma_8$	O I - LII
		$L\beta_{15}$	NIV - LIII		

and $L\ell$ and $L\eta$ are respectively the transitions MI - LIII and MI - LII.

The relation between total L shell X-ray production cross-section σ_{LX} and the three subshell ionization cross-sections σ_{LI}, σ_{LII}, σ_{LIII} is given by the equation 2.2.16. The relations between the L X-ray production cross-sections $\sigma_{L\ell}$, $\sigma_{L\alpha}$, $\sigma_{L\beta}$, $\sigma_{L\gamma}$ and σ_{LI}, σ_{LII} and σ_{LIII} are given by:

$$\sigma_{L\ell} = (\sigma_{LI} f_{13} + \sigma_{LI} f_{12} f_{23} + \sigma_{LII} f_{23} + \sigma_{LIII})\ \omega_3 F_{3\ell} \qquad 6.1.1$$

$$\sigma_{L\alpha} = (\sigma_{LI} f_{13} + \sigma_{LI} f_{12} f_{23} + \sigma_{LII} f_{23} + \sigma_{LIII})\ \omega_3 F_{3\alpha} \qquad 6.1.2$$

$$\sigma_{L\beta} = \sigma_{LI}\omega_1 F_{1\beta} + (\sigma_{LI} f_{12} + \sigma_{LII})\ \omega_2 F_{2\beta} + (\sigma_{LI} f_{13} + \sigma_{LI} f_{12} f_{23} + \sigma_{LII} f_{23} + \sigma_{LIII})\ \omega_3 F_{3\beta} \qquad 6.1.3$$

and

$$\sigma_{L\gamma} = \sigma_{LI}\omega_1 F_{1\gamma} + (\sigma_{LI} f_{12} + \sigma_{LII})\ \omega_2 F_{2\gamma} \qquad 6.1.4$$

where f_{12}, f_{13}, f_{23} are the Coster Kronig transitions (LI - LII),

(LI - LIII) and (LII - LIII) respectively, ω_1, ω_2, ω_3 are the subshell fluorescence yields of LI, LII and LIII subshells, and $Fi\phi = \Gamma_{i\phi}/\Gamma_i$ where Γ_i is the total radiative width of i^{th} subshell and $\Gamma_{i\phi}$ is the radiative width of the ϕ^{th} transition in the i^{th} subshell. A detailed review on ω_i, f_{ij} and $\Gamma_{i\phi}$ have been reported by Caruso (CarE75).

In the case of Lγ transitions the peak appears as two semi-resolved peaks, containing transitions $L\gamma_2$, $L\gamma_3$, $L\gamma_4$ to the LI subshell and transitions $L\gamma_1$ and $L\gamma_5$ to the LII subshell. Theoretical definitions of the production cross-sections of these two semiresolved peaks are:

$$\sigma_{L\gamma 2+3} + \sigma_{L\gamma 4} = \sigma_{LI}\omega_1 F_{1\gamma 2+3+4} \qquad 6.1.5$$

$$\text{and } \sigma_{L\gamma 5} + \sigma_{L\gamma I} = (\sigma_{LI} f_{12} + \sigma_{L2})\ \omega_2 F_{2\gamma 5+1} \qquad 6.1.6$$

The transition $L\gamma_6$ is unresolvable from $L\gamma_{2+3}$.

The composite nature of the Lα, Lβ and Lγ groups, containing major transitions, makes the measurements of subshell ionization cross-sections rather difficult. A number of authors (BusC73), (IshK74), (TawH74), (AksR74), (AbrF74), (TawH75) have measured the yield of composite groups Lα, Lβ and Lγ and of the well resolved lines Lℓ and Lη. The cross-sections derived from these yields were compared with existing theories. A common way of comparing the experimental data is to calculate the ratios between these cross-sections and compare them with the theories. The assumption behind these comparisons is that most of the uncertainty involved in the measurement is likely to be cancelled in the ratio calculations.

Using Lα cross-sections which comprise the transitions to the LIII subshell and computer analysing the semi-resolved Lγ peak into the transitions to LI and LII shells Datz et.al (DatS74), Madison et.al

(MadD74a), Chang et.al (ChaC75) measured the $2S_{\frac{1}{2}}$, $2P_{\frac{1}{2}}$ and $2P_{\frac{3}{2}}$ subshell ionization cross-sections in various heavy elements. They observed the structure in the LI shell ionization cross-section predicted by PWBA and CBEA theories.

All these comparisons with theories require precise knowledge of the subshell fluorescence yields ω_1, ω_2, ω_3, Coster-Kronig transition probabilities f_{12}, f_{13}, f_{23} and radiative widths. There is only a limited amount of experimental information available on these parameters and moreover there exist large discrepancies between measured values (CarE75).

6.2 MEASUREMENTS

6.2.1 Thick target yield

The experimental set-up and measuring procedure for the L X-ray thick target yield measurements are similar to those for K shell thick target yields discussed in section 5.1.2. Measurements have been made of L X-ray thick target yields from In, Sn, Nd, Dy, Pt and Au in the energy region of 1-3 MeV.

For the elements In and Sn Lα, Lβ and Lγ peaks could not be resolved and peak integration was made over the whole L X-ray region in the spectrum. For Neodymium only L_α and Lβ groups have been studied. For Dy, Pt, and Au, Lα, Lβ, Lγ groups and Lℓ transition were well resolved and studied separately. A specimen spectra for the L X-ray thick target yield is shown in figure 6.2.1.

Similar to the case of K shell thick target yields (sub section 5.1.2), the L X-ray experimental data were corrected for absorption in the airpath, target holder window and detector window. Due corrections were also made for geometry and dead time. The detector efficiency was found to be 100% for the L X-ray transitions studied. Equation 5.1.2.3 has been used for the estimate of thick target yields from

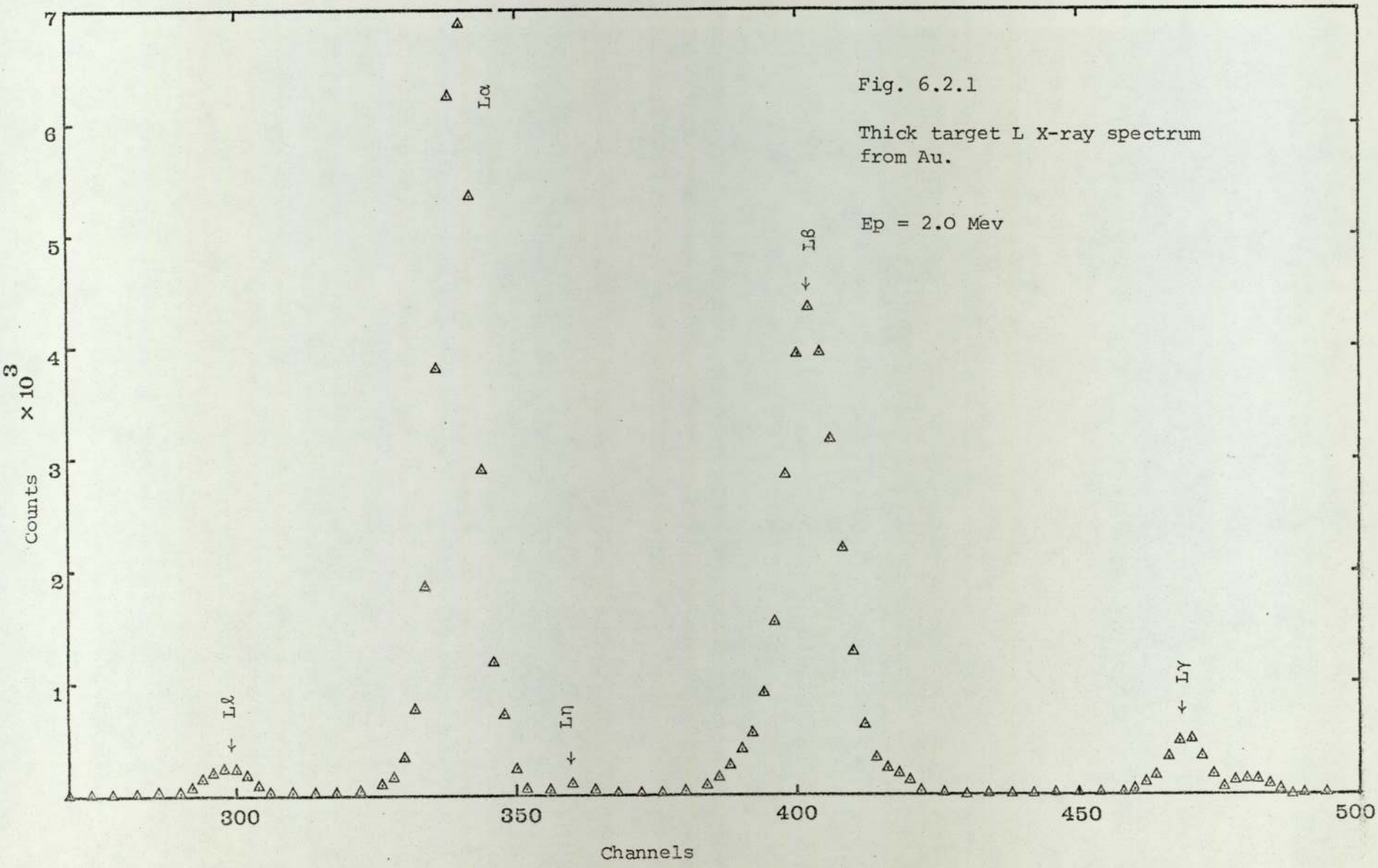

Fig. 6.2.1

Thick target L X-ray spectrum from Au.

Ep = 2.0 Mev

experimental data. The correction factors applied to the experimental data involving major uncertainties are presented in table 6.2.1.1. The table is prepared according to the discussions and criteria used in sub-section (5.1.3). The uncertainty in μ_{air} for In and Sn is, however, 5% (StoE74) and is different from that used in the subsection 5.1.3. In the cases where the absorption coefficient for a composite peak had to be calculated, (L X-ray for In and Sn and Lα, Lβ and Lγ for Nd. Dy, Pt, Au) the weighted energy of the composite peak has been used and was taken from the table of Storm and Israel (StoE74).

In the case of Lℓ and Lγ peaks, due to their low production cross-section compared to Lα and Lβ their statistical definitions are sometimes poor. The data, however, are found to be internally consistent within their statistical definition. The statistical uncertainty is presented in column 6 of table 6.2.1.1. The total uncertainty in column 10 is obtained by combining total systematic and total random errors.

6.2.2 Derivation of cross-section from thick target yields.

The L X-ray production cross-sections were derived from their respective thick target yield using the formula 5.2.1.3. Fourth to sixth order polynomials were fitted to the experimental data and $\frac{dY'_\mu}{dE}$ were derived from them. $\frac{dE}{dx}$ data was taken from the tabulations of Janni (JanJ66) for tin, neodymium, platinum and gold. dE/dx calculations done by Connell (ConB75) have been used for indium and dysprosium. μ values were calculated from the tabulations of Storm and Israel in the manner discussed in sub-sections 5.2.1. The total L X-ray production cross-section has been calculated by adding the component production cross-sections $\sigma_{L\ell}$, $\sigma_{L\alpha}$, $\sigma_{L\beta}$, $\sigma_{L\gamma}$.

An analysis has been made for the uncertainties involved in different parameters in the derivation of production cross-section following the discussion in section 5.2.2. The percentage uncertainty

Table 6.2.1.1

Major uncertainties in L X-ray thick target yield measurement along with the correction factors.

	C_{air}	C_{thw}	C_{dw}	Total Systematic	Statistics	Total random	Total
In	280 ± 32.5%	1.8 ± 4.3%	1.03	32.7%	1%	2.0%	32.8%
Sn	152 ± 28.6%	1.65 ± 3.7%	1.01	28.8%	2%	2.6%	28.9%
NdLα	5.3 ± 2.0%	1.14 ± 1.0%	1.00	2.2%	1%	2.0%	3.0%
NdLβ	3.45 ± 1.5%	1.11 ± .8%	1.00	1.7%	1%	2.0%	2.6%
DyLℓ	6.7 ± 2.2%	1.11 ± .8%	1.00	2.3%	5%	5.3%	5.8%
DyLα	3.74 ± 1.5%	1.07 ± .5%	1.00	1.7%	2%	2.6%	3.1%
DyLβ	2.53 ± 1.1%	1.05 ± .4%	1.00	1.3%	2%	2.6%	2.9%
DyLγ	1.77 ± .7%	1.03 ± .2%	1.00	.9%	3%	3.5%	3.6%
PtLℓ	1.62 ± .6%	1.05 ± .4%	1.00	.9%	4%	4.4%	4.5%
PtLα	1.38 ± .4%	1.04 ± .4%	1.00	.8%	1%	2.0%	2.2%
PtLβ	1.22 ± .2%	1.02 ± .2%	1.00	.6%	1%	2.0%	2.6%
PtLγ	1.13 ± .1%	1.01 ± .1%	1.00	.5%	2%	2.6%	2.6%
AuLℓ	1.43 ± .4%	1.05 ± .4%	1.00	.8%	4%	4.4%	4.5%
AuLα	1.27 ± .3%	1.03 ± .2%	1.00	.6%	1%	2.0%	2.1%
AuLβ	1.16 ± .1%	1.02 ± .2%	1.00	.5%	1%	2.0%	2.1%
AuLγ	1.04 ± .1%	1.01 ± .1%	1.00	.5%	3%	3.5%	3.5%

in the total L X-ray production cross-section for Dy, Pt and Au has been obtained by multiplying the uncertainties in $\sigma_{L\ell}$, $\sigma_{L\alpha}$, $\sigma_{L\beta}$ and $\sigma_{L\gamma}$ by appropriate weights and adding them quadratically. The results of the error analysis at 1, 2 and 3 MeV are presented in the table 6.2.2.1.

6.2.3 Thin target measurements.

To check the ratios $\sigma_{L\alpha}/\sigma_{L\ell}$, $\sigma_{L\alpha}/\sigma_{L\beta}$, $\sigma_{L\alpha}/\sigma_{L\gamma}$ derived from thick target yields, thin target measurements were made on dysprosium and gold. Targets of gold and dysprosium of thickness 10 - 15 $\mu g/cm^2$ were prepared by evaporation on .0075 cm thick 99.99% pure aluminium backing. The targets were mounted in the target holder and the detector was placed in contact with the target holder window to minimize absorption correction and maximize yield. To reduce the low energy brehmsstrahlung background .015mm thick aluminium foil was inserted between the detector and target holder. Since no absolute measurements were attempted, finer measurements on target thickness were not made. The only corrections applied to these measurements were dead time and absorption corrections.

6.3 RESULTS AND DISCUSSIONS

6.3.1 Introduction

The results of the total L X-ray production cross-sections on all elements studied are presented in figure 6.3.2.1 along with the work of other workers and the predictions of non relativistic PWBA and CBEA. Similar presentations are also made for Lα and Lβ cross-sections respectively in figures 6.3.3.1 and 6.3.3.2 for the elements Nd, Dy, Pt and Au. Lγ cross-sections for Dy, Pt, and Au are presented in figure 6.3.3.3. The ratios $\sigma_{L\alpha}/\sigma_{L\ell}$, $\sigma_{L\alpha}/\sigma_{L\beta}$ and $\sigma_{L\alpha}/\sigma_{L\gamma}$ along with the predictions of PWBA and CBEA and the ratios reported by other workers have been presented in figures 6.3.4.1 - 6.3.4.3. The ratios of $\sigma_{L\alpha}/\sigma_{L\ell}$, $\sigma_{L\alpha}/\sigma_{L\beta}$, $\sigma_{L\alpha}/\sigma_{L\gamma}$ calculated from the present thin target

Table 6.2.2.1

Major uncertainties in the derivation of proton induced L shell X-ray cross-sections. (All uncertainties are in percentage)

		1 MeV		2 MeV		3 MeV	
	ΔY_μ	ΔT	$\pm\Delta\sigma_x$	ΔT	$\pm\Delta\sigma_x$	ΔT	$\pm\Delta\sigma_x$
In	32.7	6.1	33.3	7.4	33.5	8.1	33.7
Sn	28.8	6.2	29.5	7.3	29.7	8.0	29.9
NdLα	2.2	4.7	5.2	4.6	5.1	5.0	5.5
NdLβ	1.7	5.1	5.4	4.4	4.7	4.9	5.2
NDL			4.9		4.6		4.8
DyLℓ	2.3	5.1	5.6	6.3	6.7	6.7	7.1
DyLα	1.7	4.7	5.0	4.5	4.8	5.1	5.4
DyLβ	1.3	4.8	5.0	3.3	3.6	3.4	3.6
DyLγ	.9	4.7	4.8	5.2	5.3	5.7	5.8
DyL			4.2		3.7		3.9
PtLℓ	.9	4.3	4.4	4.2	4.3	4.9	5.0
PtLα	.8	4.7	4.8	3.1	3.2	3.0	3.1
PtLβ	.6	5.2	5.2	3.3	3.4	2.7	2.8
PtLγ	.5	5.0	5.0	3.3	3.3	3.0	3.0
PtL			3.3		2.3		2.1
AuLℓ	.8	5.3	5.3	4.1	4.2	4.8	4.8
AuLα	.6	4.3	4.3	3.1	3.2	3.1	3.2
AuLβ	.5	4.7	4.7	3.3	3.3	2.8	2.9
AuLγ	.5	4.6	4.6	3.6	3.6	4.0	4.0
AuL			3.0		2.2		2.1

yield measurement on Dy and Au are also presented in these figures for comparison.These quantities are also presented in tables 6.3.1.1 - 6.3.1.4.

The theoretical curves for PWBA are prepared by using the calculations of Choi et.al (ChoB73) for σ_{LI}, σ_{LII}, σ_{LIII} and using the relations 6.1.1 - 6.1.4 . The table of Choi presents the values of f_{LI} and f_{LII} for a set of η_L and θ_L values, representing cross-sections (f_{Li}) at different energies (η_L) for different elements (θ_L). The cross sections σ_{LI}, σ_{LII} and σ_{LIII} at different energies, for the elements studied have been calculated from the table in two steps.

A suitable polynomial was fitted to the f_{LI} values for a set of θ_{LI} values, at a specific value of η_{LI}. The values of f_{LI} corresponding to the required values of θ_{LI} for LI subshells of the elements studied were then calculated from the polynomial. Similar calculations were made for different sets of f_{LI} values corresponding to different tabulated values of η_{LI}. Thus a set of f_{LI} values corresponding to the tabulated values of η_{LI} was found for each element. Similar calculations were made to obtain f_{LII} and f_{LIII} values for each element. It should be noted, however, that the f_{LIII} values were calculated from the function f_{LII} representing the 2p state of the atom.

In the second stage, cross-sections σ_{LI}, σ_{LII}, σ_{LIII} were calculated from these new tables as follows. The cross-sections σ_{LI} for the different elements were calculated at the energies corresponding to the tabulated values of η_{LI}. In between energy values were not calculated due to the presence of structure and the difficulty in fitting a suitable polynomial. The energies at which σ_{LI} were calculated were then used to calculate η_{LII}. The corresponding values of f_{LII} were then derived from a polynomial fitted to the η_{LII} and f_{LII} data. The cross-sections σ_{LII} were then computed from these f_{LII}. σ_{LIII} were computed in a similar way. Thus the present calculations of theoretical cross-sections σ_{LI}, σ_{LII} and σ_{LIII} were restricted at

energies defined by the tabulated values of η_{LI}.

These values of σ_{LI}, σ_{LII} and σ_{LIII} were used in equations 6.1.1 - 6.1.4 to compute the physical quantities used in the comparison.

For the calculation of σ_{LI}, σ_{LII} and σ_{LIII} predicted by CBEA theory, the tabulation of Hansen (HanJ73) was used. This gives universal functions for 2s and 2p non-relativistic hydrogenic wave functions. The energy parameter is in the form (mE/ME_{Li}) and the cross-section parameter is in the form $(\sigma E_{Li}^2/Z_1^2)$. A polynomial was fitted to the 2p universal function. As the 2s universal function contains structure, polynomial fitting to it was found unsuitable and the energies, E, and cross-sections σ_{LI} were calculated from the tabulated values. σ_{LII} and σ_{LIII} at the same energies were calculated from the polynomial fitted to the 2p universal function.

The values of f_{ij}, ω_i and $F_{i\phi}$ used in the calculation of different theoretical parameters are given in tables 6.3.1.5 and 6.3.1.6. The values of f_{ij} and ω_i are taken from the theoretical calculations of McGuire (McGE71) and $F_{i\phi}$ are taken from the tabulations of Scofield (ScoJ69). Where f_{ij}, ω_i or $F_{i\phi}$ for a specific element are not tabulated, they are estimated from the smooth curves drawn through the tabulated values.

6.3.2 Total L X-ray production cross-section.

In the present energy region the total L X-ray production cross-section, σ_{LX}, predicted by CBEA for the elements studied, are lower than those predicted by PWBA. For In, Sn and Nd the CBEA curve crosses PWBA at increasingly higher energies. For Dy, Pt and Au the CBEA predictions are lower than PWBA in the energy region studied. Agreement between these two theories improves as the energy increases.

The experimental σ_{LX} values are in general found to follow the

TABLE 6.3.1.1

EXPERIMENTAL L-SHELL X-RAY YIELDS AND DERIVED PRODUCTION CROSS-SECTIONS

ENERGY	INDIUM YIELD	INDIUM SIGMA(P)	TIN YIELD	TIN SIGMA(P)	NEODYMIUM YIELD Lα	NEODYMIUM SIGMA Lα	NEODYMIUM YIELD Lβ	NEODYMIUM SIGMA Lβ	NEODYMIUM SIGMA Lα/SIGMA Lβ
1.0	1.24E-03	1.56E-22	1.10E-03	1.39E-22	1.59E-04	1.98E-23	1.05E-04	1.23E-23	6.22E-01
1.2	2.01E-03	2.19E-22	1.84E-03	1.96E-22	2.93E-04	3.12E-23	2.08E-04	2.01E-23	6.46E-01
1.4	2.89E-03	2.80E-22	2.63E-03	2.55E-22	4.61E-04	4.41E-23	3.48E-04	2.98E-23	6.77E-01
1.6	3.86E-03	3.54E-22	3.51E-03	3.18E-22	6.62E-04	5.79E-23	5.26E-04	4.08E-23	7.05E-01
1.8	4.79E-03	4.22E-22	4.45E-03	3.82E-22	8.85E-04	7.23E-23	7.46E-04	5.31E-23	7.34E-01
2.0	5.62E-03	4.89E-22	5.32E-03	4.46E-22	1.11E-03	8.69E-23	9.88E-04	6.60E-23	7.59E-01
2.2	6.60E-03	5.53E-22	6.28E-03	5.07E-22	1.36E-03	1.01E-22	1.25E-03	7.93E-23	7.82E-01
2.4	7.44E-03	6.10E-22	7.07E-03	5.70E-22	1.59E-03	1.16E-22	1.52E-03	9.29E-23	8.00E-01
2.6	8.29E-03	6.61E-22	7.89E-03	6.17E-22	1.77E-03	1.31E-22	1.77E-03	1.05E-22	8.06E-01
2.8	8.87E-03	7.04E-22	8.48E-03	6.60E-22	2.07E-03	1.45E-22	2.08E-03	1.19E-22	8.16E-01
3.0	9.28E-03	7.37E-22	9.16E-03	6.96E-22	2.29E-03	1.61E-22	2.34E-03	1.32E-22	8.19E-01

TABLE 6.3.1.2

EXPERIMENTAL L X-RAY THICK TARGET YIELDS AND DERIVED X-RAY PRODUCTION CROSS-SECTIONS FOR DYSPROSIUM

ENERGY	YIELD Lα	SIGMA Lα	YIELD Lβ	SIGMA Lβ	YIELD Lγ	SIGMA Lγ	SIGMA Lx	SIGMA Lα /SIGMA Lβ	SIGMA Lα /SIGMA Lγ	SIGMA Lα /SIGMA Lℓ
1.0	9.23E-05	1.17E-23	5.78E-05	6.59E-24	5.07E-06	8.34E-25	1.96E-23	1.77E 00	1.40E 01	2.55E 01
1.1	1.28E-04	1.45E-23	8.26E-05	8.46E-24	7.17E-06	9.70E-25	2.45E-23	1.71E 00	1.49E 01	2.57E 01
1.2	1.71E-04	1.75E-23	1.11E-04	1.06E-23	1.00E-05	1.17E-24	2.99E-23	1.66E 00	1.50E 01	2.60E 01
1.4	2.68E-04	2.43E-23	1.89E-04	1.55E-23	1.56E-05	1.74E-24	4.25E-23	1.57E 00	1.39E 01	2.62E 01
1.6	3.93E-04	3.20E-23	2.95E-04	2.13E-23	2.39E-05	2.53E-24	5.71E-23	1.50E 00	1.27E 01	2.58E 01
1.8	5.27E-04	4.06E-23	4.23E-04	2.78E-23	3.54E-05	3.41E-24	7.35E-23	1.46E 00	1.19E 01	2.51E 01
2.0	6.88E-04	4.98E-23	5.70E-04	3.50E-23	4.76E-05	4.34E-24	9.12E-23	1.42E 00	1.15E 01	2.41E 01
2.2	8.78E-04	5.96E-23	7.43E-04	4.27E-23	6.09E-05	5.31E-24	1.10E-22	1.40E 00	1.12E 01	2.32E 01
2.4	1.03E-03	6.95E-23	9.34E-04	5.06E-23	7.41E-05	6.30E-24	1.30E-22	1.37E 00	1.10E 01	2.22E 01
2.5	1.13E-03	7.43E-23	1.03E-03	5.47E-23	8.07E-05	6.84E-24	1.39E-22	1.36E 00	1.09E 01	2.18E 01
2.6	1.23E-03	7.92E-23	1.13E-03	5.89E-23	9.07E-05	7.32E-24	1.49E-22	1.35E 00	1.08E 01	2.15E 01
2.7	1.31E-03	8.40E-23	1.22E-03	6.31E-23	9.54E-05	7.90E-24	1.59E-22	1.33E 00	1.06E 01	2.12E 01
2.8	1.41E-03	8.87E-23	1.34E-03	6.73E-23	1.05E-04	8.47E-24	1.69E-22	1.32E 00	1.05E 01	2.09E 01
2.9	1.49E-03	9.31E-23	1.44E-03	7.16E-23	1.13E-04	9.10E-24	1.78E-22	1.30E 00	1.02E 01	2.08E 01
3.0	1.58E-03	9.68E-23	1.54E-03	7.59E-23	1.20E-04	9.75E-24	1.87E-22	1.28E 00	9.92E 00	2.05E 01

TABLE 6.3.1.3

EXPERIMENTAL L X-RAY THICK TARGET YIELDS AND DERIVED X-RAY PRODUCTION CROSS-SECTIONS FOR PLATINUM

ENERGY	YIELD Lα	SIGMA Lα	YIELD Lβ	SIGMA Lβ	YIELD Lγ	SIGMA Lγ	SIGMA LX	SIGMA Lα /SIGMA Lβ	SIGMA Lα /SIGMA Lγ	SIGMA Lα /SIGMA Ll
1.0	2.76E-05	3.02E-24	1.63E-05	1.58E-24	2.13E-06	2.88E-25	5.01E-24	1.91E 00	1.05E 01	2.41E 01
1.2	5.59E-05	5.81E-24	3.37E-05	3.18E-24	4.09E-06	3.92E-25	9.69E-24	1.83E 00	1.48E 01	1.92E 01
1.4	9.80E-05	8.26E-24	6.18E-05	4.68E-24	6.79E-06	6.08E-25	1.40E-23	1.77E 00	1.36E 01	1.87E 01
1.6	1.50E-04	1.11E-23	9.97E-05	6.41E-24	1.09E-05	8.78E-25	1.89E-23	1.73E 00	1.26E 01	2.07E 01
1.8	2.15E-04	1.48E-23	1.47E-04	8.61E-24	1.61E-05	1.18E-24	2.53E-23	1.72E 00	1.25E 01	2.08E 01
2.0	2.96E-04	1.92E-23	2.11E-04	1.12E-23	2.21E-05	1.55E-24	3.29E-23	1.72E 00	1.24E 01	2.05E 01
2.2	3.96E-04	2.58E-23	2.89E-04	1.41E-23	3.05E-05	1.99E-24	4.10E-23	1.69E 00	1.20E 01	2.10E 01
2.4	5.05E-04	2.82E-23	3.89E-04	1.70E-23	4.06E-05	2.43E-24	4.90E-23	1.66E 00	1.16E 01	2.15E 01
2.6	5.94E-04	3.22E-23	4.65E-04	1.99E-23	4.70E-05	3.00E-24	5.67E-23	1.62E 00	1.07E 01	2.10E 01
2.8	7.25E-04	3.67E-23	5.88E-04	2.29E-23	5.98E-05	3.50E-24	6.49E-23	1.60E 00	1.05E 01	1.99E 01
3.0	8.36E-04	4.30E-23	6.92E-04	2.67E-23	7.04E-05	4.05E-24	7.57E-23	1.61E 00	1.06E 01	2.23E 01

TABLE 6.3.1.4

EXPERIMENTAL L X-RAY THICK TARGET YIELDS AND DERIVED X-RAY PRODUCTION CROSS-SECTIONS FOR GOLD

ENERGY	YIELD Lα	SIGMA Lα	YIELD Lβ	SIGMA Lβ	YIELD Lγ	SIGMA Lγ	SIGMA LX	SIGMA Lα /SIGMA Lβ	SIGMA Lα /SIGMA Lγ	SIGMA Lα /SIGMA Ll
1.2	4.84E-05	4.89E-24	2.94E-05	2.62E-24	3.28E-06	3.68E-25	8.12E-24	1.87E 00	1.33E 01	2.04E 01
1.4	8.49E-05	7.22E-24	5.27E-05	3.96E-24	6.03E-06	5.30E-25	1.21E-23	1.82E 00	1.36E 01	2.01E 01
1.6	1.31E-04	9.90E-24	8.58E-05	5.61E-24	9.50E-06	7.34E-25	1.67E-23	1.76E 00	1.35E 01	2.12E 01
1.8	1.93E-04	1.29E-23	1.30E-04	7.53E-24	1.34E-05	9.91E-25	2.21E-23	1.71E 00	1.30E 01	1.80E 01
2.0	2.62E-04	1.65E-23	1.85E-04	9.70E-24	1.99E-05	1.30E-24	2.84E-23	1.70E 00	1.27E 01	1.85E 01
2.2	3.46E-04	2.03E-23	2.50E-04	1.20E-23	2.64E-05	1.66E-24	3.49E-23	1.69E 00	1.22E 01	2.07E 01
2.4	4.34E-04	2.43E-23	3.27E-04	1.45E-23	3.47E-05	2.04E-24	4.19E-23	1.67E 00	1.19E 01	2.19E 01
2.6	5.31E-04	2.81E-23	4.16E-04	1.70E-23	4.16E-05	2.43E-24	4.89E-23	1.65E 00	1.16E 01	2.13E 01
2.8	6.31E-04	3.22E-23	5.02E-04	1.96E-23	5.29E-05	2.77E-24	5.62E-23	1.64E 00	1.16E 01	2.00E 01
3.0	7.34E-04	3.60E-23	6.00E-04	2.22E-23	6.02E-05	3.03E-24	6.30E-23	1.62E 00	1.19E 01	2.13E 01

Table 6.3.1.5

Subshell fluorescence yields and Coster Kroning transition coefficients

Element	w_1	w_2	w_3	f_{12}	f_{13}	f_{23}
Indium	.0116	.0612	.0693	.0506	.793	.159
Tin	.013	.0656	.0737	.052	.784	.162
Neodymium	.0746	.133	.135	.207	.303	.141
Dysprosium	.105	.194	.194	.205	.308	.138
Platinum	.108	.353	.325	.103	.535	.129
Gold	.105	.357	.327	.083	.644	.132

Table 6.3.1.6

Radiative transition Ratios $F_{i\phi}$

Element	$F_{3\ell}$	$F_{3\alpha}$	$F_{1\beta}$	$F_{2\beta}$	$F_{3\beta}$	$F_{1\gamma}$	$F_{2\gamma}$
Indium	.032	.909	.81	.88	.108	.165	.103
Tin	.0328	.853	.816	.865	.1082	.165	.109
Neodymium	.0328	.823	.76	.829	.1438	.207	.146
Dysprosium	.035	.83	.78	.83	.15	.21	.151
Platinum	.039	.791	.722	.810	.181	.221	.175
Gold	.04	.787	.719	.798	.172	.222	.179

PWBA curves and are lower than them. The difference between theory and experiment is in general found to be an increasing function of atomic numbers.

No measurements have been reported for In, Sn and Pt. Excellent agreement is observed between the present measurement and the thick target measurements of Khan et.al (KhaJ65) for the elements Nd and Dy. The thin target measurement of Abrath and Gray (AbrF74) between 1 - 2 MeV for Dy is systematically above the present values by $\sim$ 70%. They are also above the prediction of both theories. The thin target measurements of Shafroth et.al (ShaS73) agree with the present work on Au, within the experimental error over the entire energy range, whereas those of Akselsson et.al agree reasonably at 1.5 and 2 MeV, but are above the present measurement $\sim$ 30% at 2.5 and 3 MeV. The thick target work of Bernstein and Lewis (BerE54) also agree reasonably with the present measurement (Fig.6.3.2.1).

6.3.3 $\sigma_{L\alpha}$, $\sigma_{L\beta}$ and $\sigma_{L\gamma}$ cross-sections.

The present values of $\sigma_{L\alpha}$ are found to agree very well with the thin target measurements of Bearse et.al for Dy, and for Au they are within experimental error. ~~Agreement between~~ The thin target measurements of Akselsson et.al on Au are in agreement with the present work at 1.5 and 2.0 MeV but their results are higher than the present work at 2.5 and 3 MeV.

The only experimental measurement reporting numerical values of $\sigma_{L\beta}$ and $\sigma_{L\gamma}$ in the energy region 1-3 MeV for the elements studied are those of Akselsson et.al (AksR74) for Au. Again good agreement is found at 1.5 and 2.0 MeV but their values are higher at 2.5 and 3.0 MeV.

In general the results of $\sigma_{L\alpha}$, $\sigma_{L\beta}$, and $\sigma_{L\gamma}$ for all elements studied, follow systematically the predictions of PWBA. They are lower than the predictions of PWBA. For all elements deviation from PWBA is

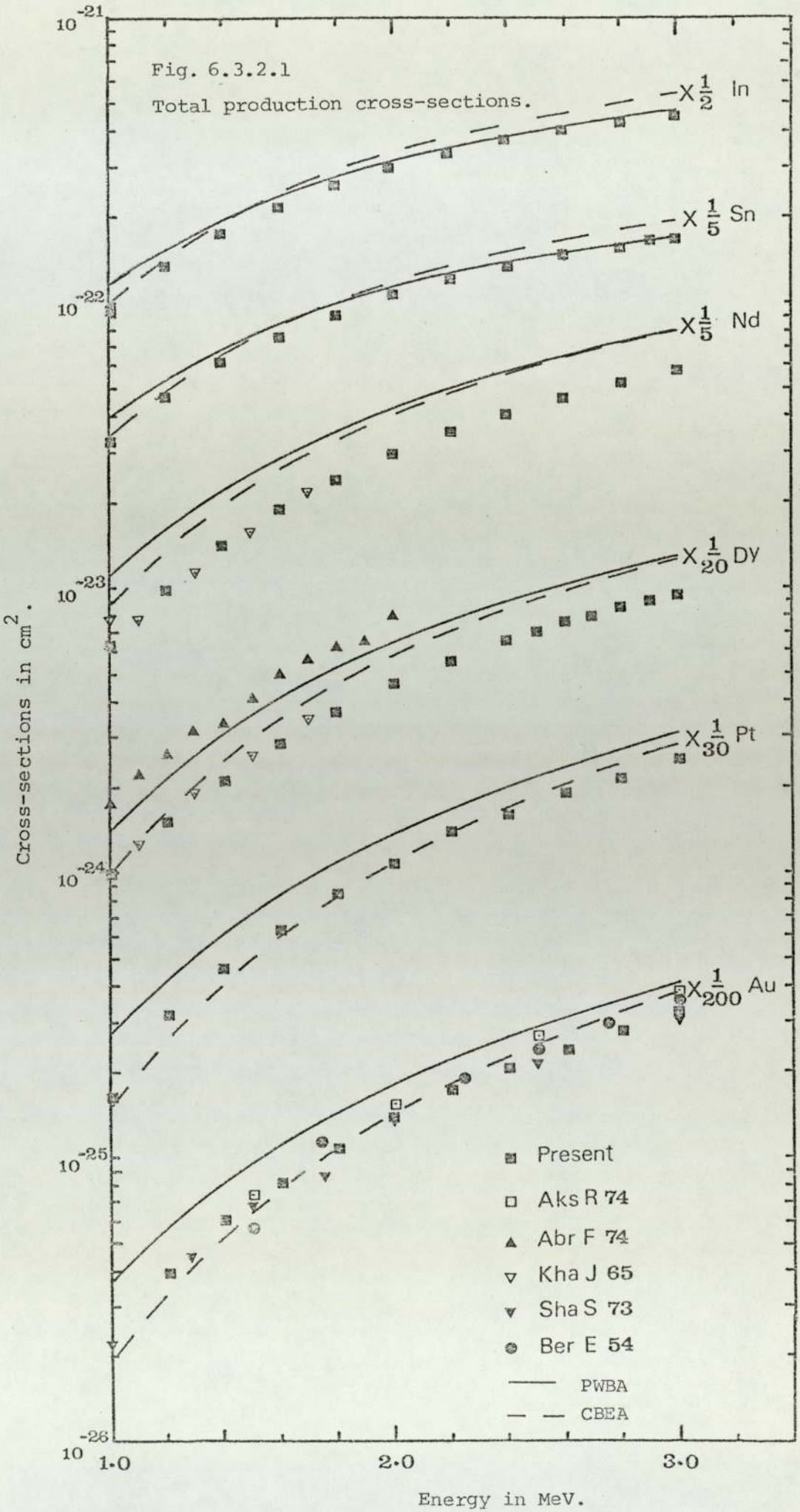
Fig. 6.3.2.1
Total production cross-sections.
10^{-21}
10^{-22}
10^{-23}
10^{-24}
10^{-25}
10^{-26}
$X\frac{1}{2}$ In
$X\frac{1}{5}$ Sn
$X\frac{1}{5}$ Nd
$X\frac{1}{20}$ Dy
$X\frac{1}{30}$ Pt
$X\frac{1}{200}$ Au
Present
Aks R 74
Abr F 74
Kha J 65
Sha S 73
Ber E 54
PWBA
CBEA
Cross-sections in cm^2.
1·0
2·0
3·0
Energy in MeV.

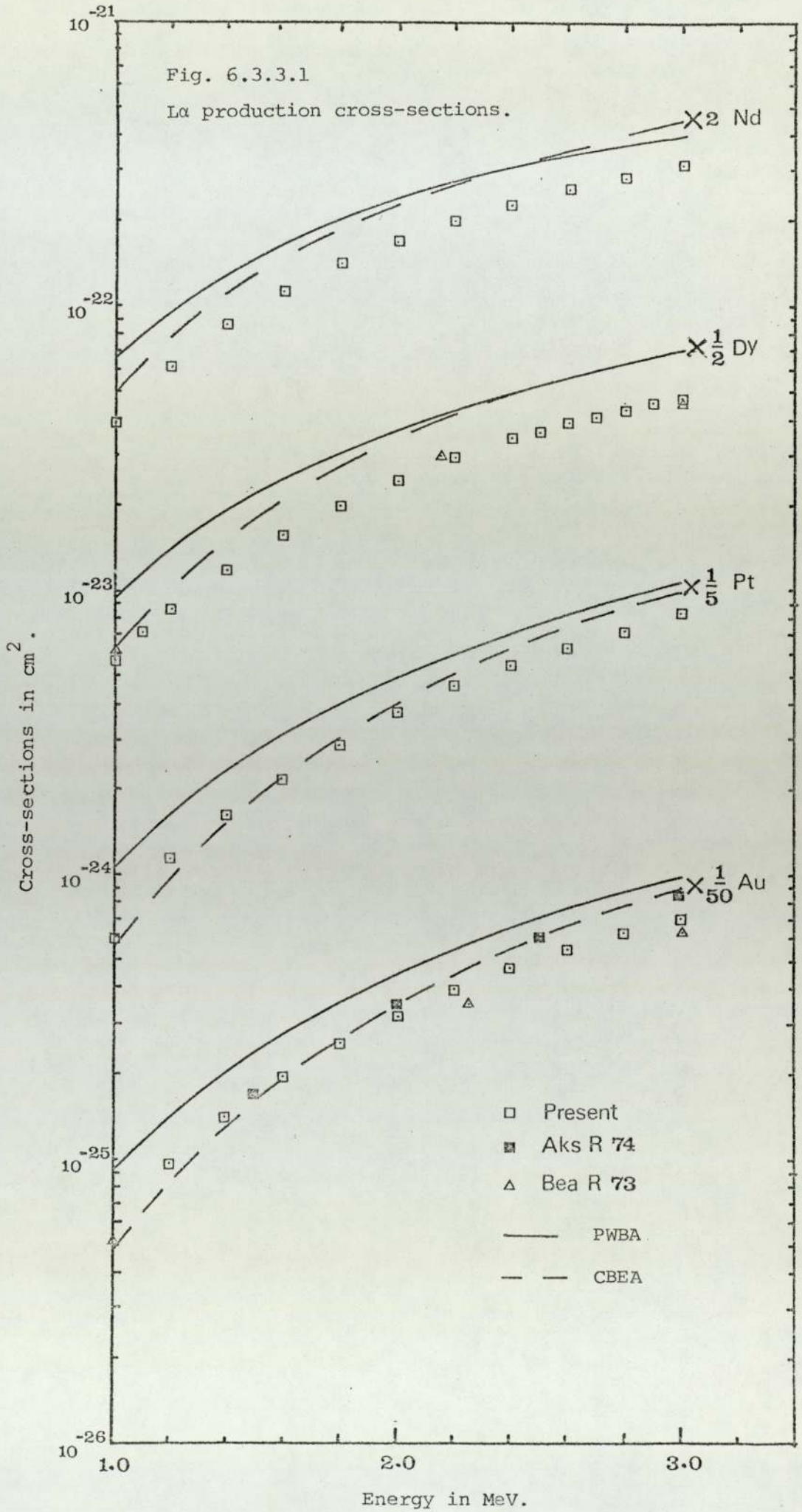
Fig. 6.3.3.1
Lα production cross-sections.
X2 Nd
X 1/2 Dy
X 1/5 Pt
X 1/50 Au
Present
Aks R 74
Bea R 73
PWBA
CBEA
Cross-sections in cm 2.
Energy in MeV.
10-21
10-22
10-23
10-24
10-25
10-26
1.0
2.0
3.0

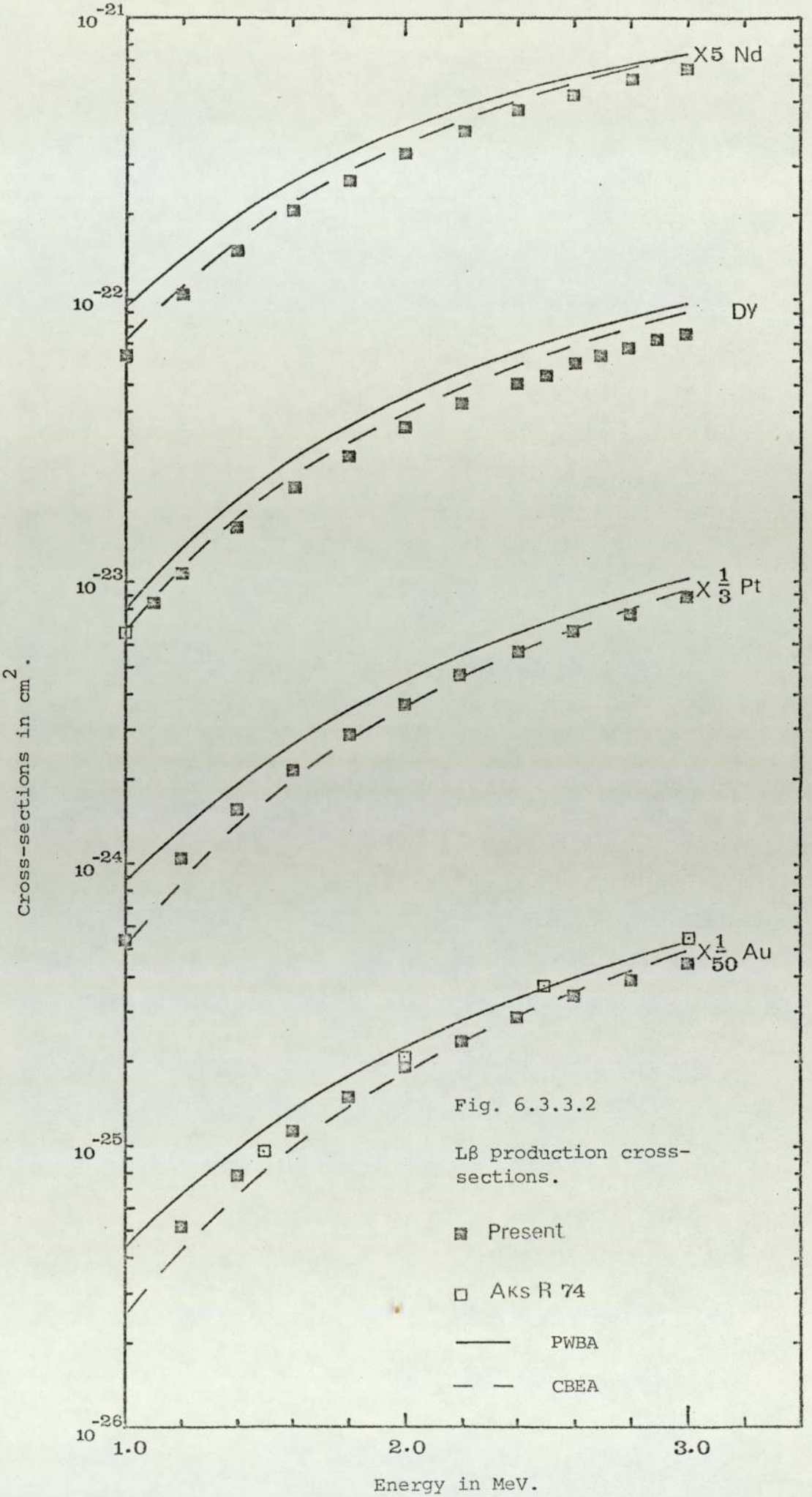

Fig. 6.3.3.2

Lβ production cross-sections.

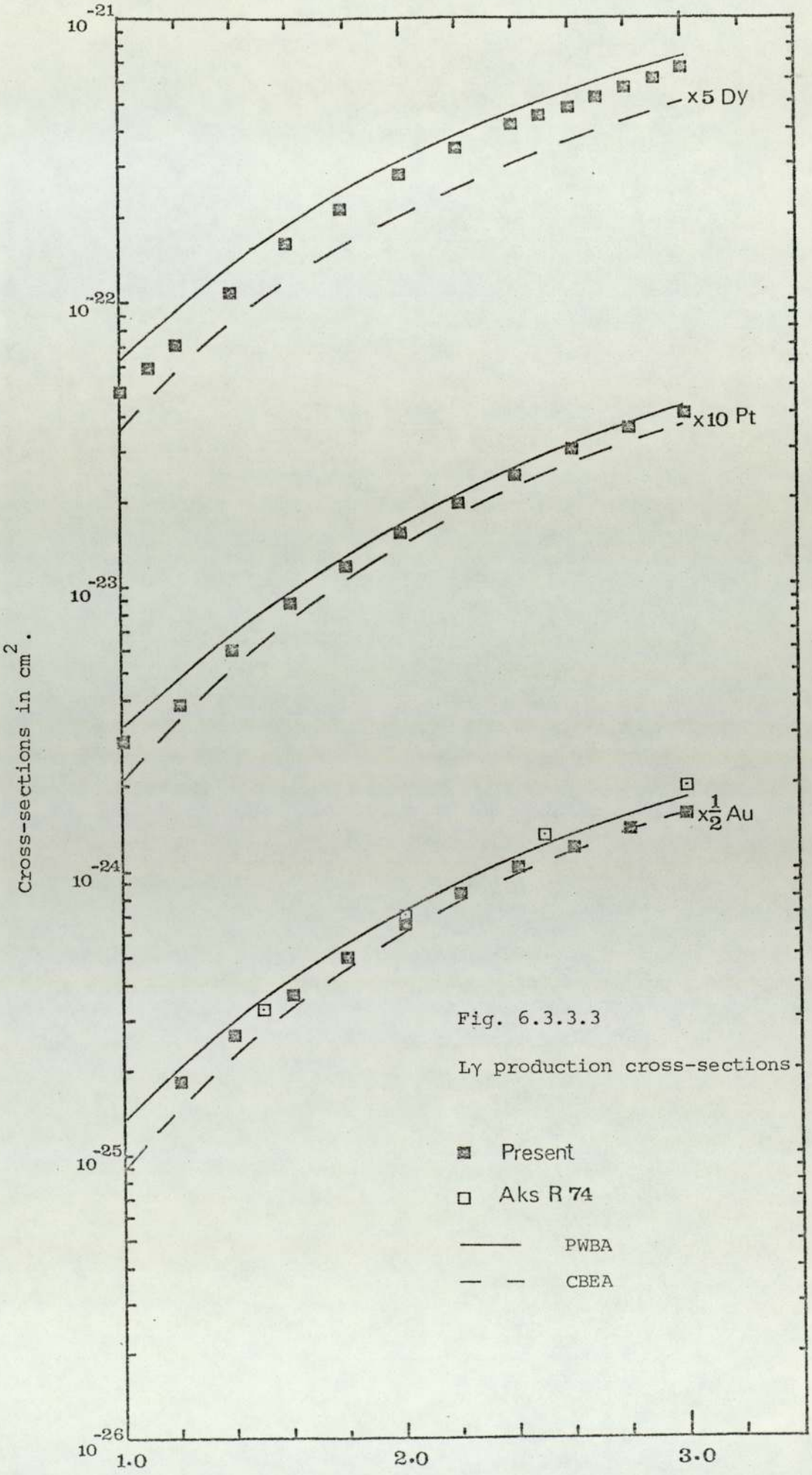

Fig. 6.3.3.3

Lγ production cross-sections

highest for $\sigma_{L\alpha}$ ($\sim$ 35 - 60%) and lowest for $\sigma_{L\gamma}$ (10 - 30%), whereas the deviations for $\sigma_{L\beta}$ are in between (15 - 45%). (Figs. 6.3.3.1 - 6.3.3.3).

6.3.4 Ratio measurements.

On the basis that the systematic uncertainties are expected to cancel each other, the ratios $\sigma_{L\alpha}/\sigma_{L\ell}$, $\sigma_{L\alpha}/\sigma_{L\beta}$ and $\sigma_{L\alpha}/\sigma_{L\gamma}$ are calculated. These should produce a better test for the theories. Since $\sigma_{L\alpha}$ and $\sigma_{L\ell}$ represent the transition to the same energy level LIII the ratios should be constant and should be equal to $\frac{F_{3\alpha}}{F_{3\ell}}$. These ratios for Dy, Pt and Au are plotted in figure 6.3.4.1 along with the ratio $\frac{F_{3\alpha}}{F_{3\ell}}$ and the measurements of other workers. These ratios are also presented in table 6.3.4.1 . For Dy though the mean value of $\sigma_{L\alpha}/\sigma_{L\ell}$ from thick target measurement shows good agreement with the theoretical value, the ratios show an energy dependence which is in disagreement with the theory. They also disagree with the thin target measurement of the present work and those of Abrath et.al (AbrF74). Further measurements are required to investigate this discrepancy. The mean value of the present thin target measurements also agrees with the theoretical values. Whereas the values of the present measurement scatter around the straight line predicted by theory, the measurements of Abrath et.al (AbrF74) are nearly constant but much lower than the theoretical values,figure 6.3.4.1.

The $\sigma_{L\alpha}/\sigma_{L\ell}$ values for Pt scatters nicely around the theoretical prediction and mean value is very close to theoretical value.

For Au the present thick and thin target values are again scattered around the theoretical curve. The amount of scattering is similar to the measurements reported by Akselsson et.al (AksR74) and Tawara et.al (TawH75). The agreement between the mean values and the theoretical value is very good (table 6.3.4.1).

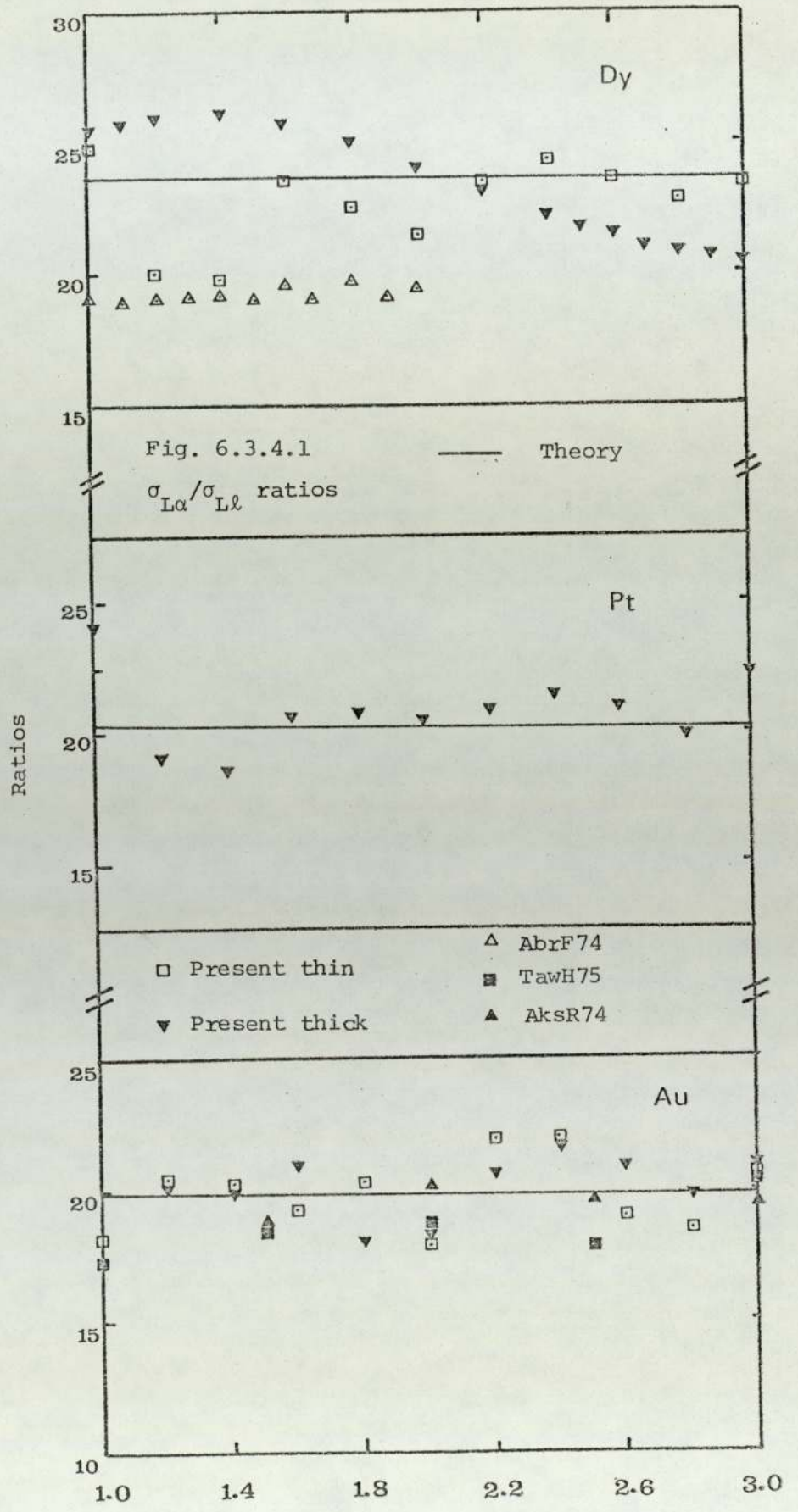

Fig. 6.3.4.1 $\sigma_{L\alpha}/\sigma_{L\ell}$ ratios

Table 6.3.4.1

Experimental mean values and theoretical values of $\sigma_{L\alpha}/\sigma_{L\ell}$ of the element Dy, Pt and Au

Element	Theoretical	Experimental			
	ScoJ69	Present		Others	
		thick	thin		
Dy	23.7	23.4	22.7	19.0	AbrF74
Pt	20.2	20.9			
Au	19.9	20.3	19.9	18.9	TawH75
				20.45	AksR74
				21.0	CloD73

The calculated ratio of $\sigma_{L\alpha}/\sigma_{L\beta}$ of Pt and Nd from thick target measurements and the same ratios for Dy and Au from both thick and thin target measurements are presented in figure 6.3.4.2. Also presented are the PWBA and CBEA calculations for $\sigma_{L\alpha}/\sigma_{L\beta}$.

No $\sigma_{L\alpha}/\sigma_{L\beta}$ measurement is found to be reported for Nd and Pt. For Dy our thick and thin target measurements disagree by $\sim$ 25% but they possess the same qualitative features. The thin target measurements of Close et.al (CloD73) lie in between the two sets and closer to thick target measurements.

For Au the present thick and thin target measurements agree reasonably well. The thick target data are almost coincident with the thin target measurements of Tawara et.al (TawH75), Close et.al (CloD73) and Akselsson et.al (AksR74) over the energy range studied. Similar measurements of Shafroth et.al (ShaS73) are systematically lower than the present measurements by $\sim$ 8%, which are again within the experimental errors (Fig. 6.3.4.2).

The thin and thick target ratios of $\sigma_{L\alpha}/\sigma_{L\gamma}$ of Dy and Au, thick target values for Pt, measurements of other workers and the predictions of PWBA and CBEA are presented in figure 6.3.4.3.

No measurement is found to be reported for Pt. Both the thick and thin target measurements for Dy show energy dependence similar to PWBA and agree with each other within experimental error.

For Au the agreement between the present thick and thin target measurements is reasonable. The thin target measurements of Akselsson et.al (AksR74), Tawara et.al (TawH75) and Close et.al (CloO73) are found to be in good agreement with the present thick target data. Similar measurements of Shafroth et.al (ShaS73) are systematically lower than the present thick target measurements by $\sim$ 10 - 15%.

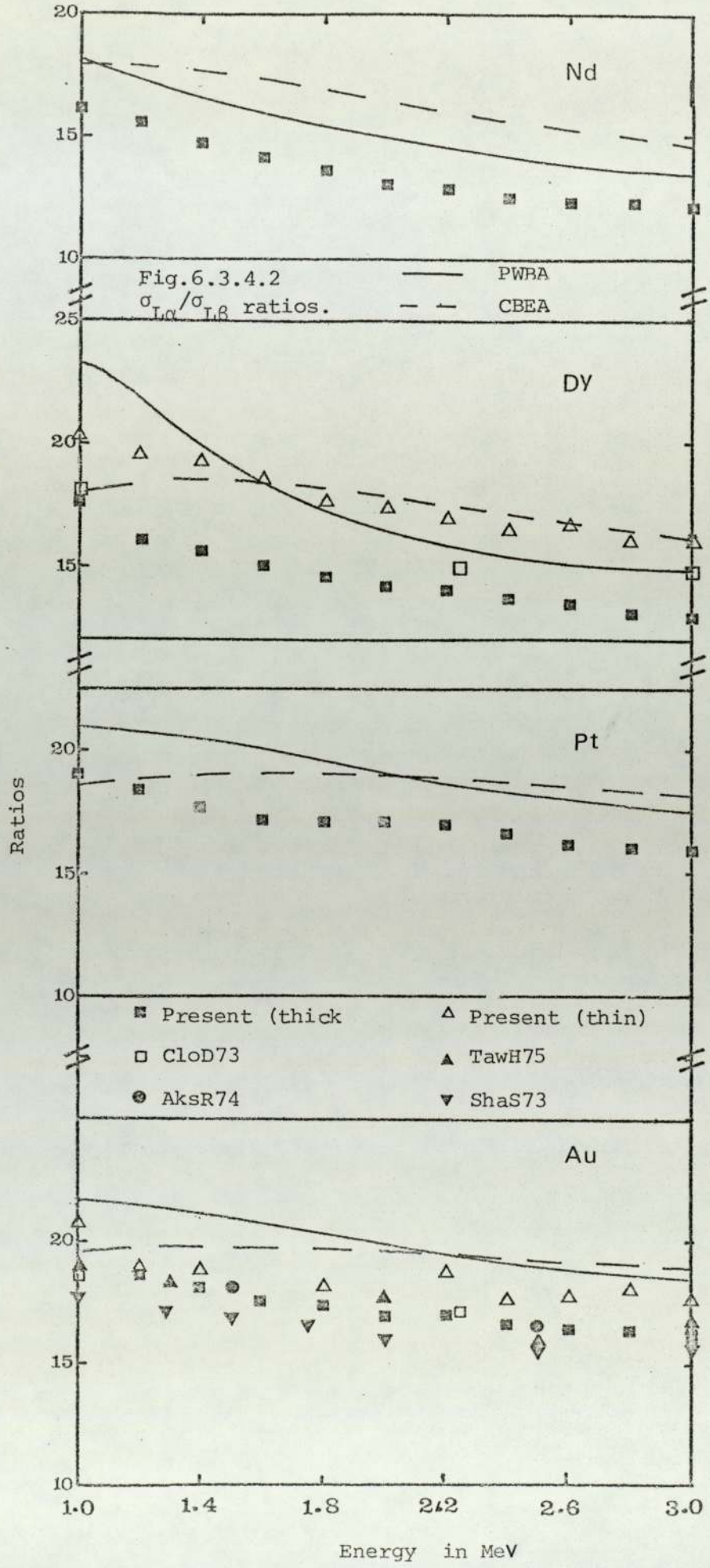

Fig.6.3.4.2 $\sigma_{L\alpha}/\sigma_{L\beta}$ ratios.

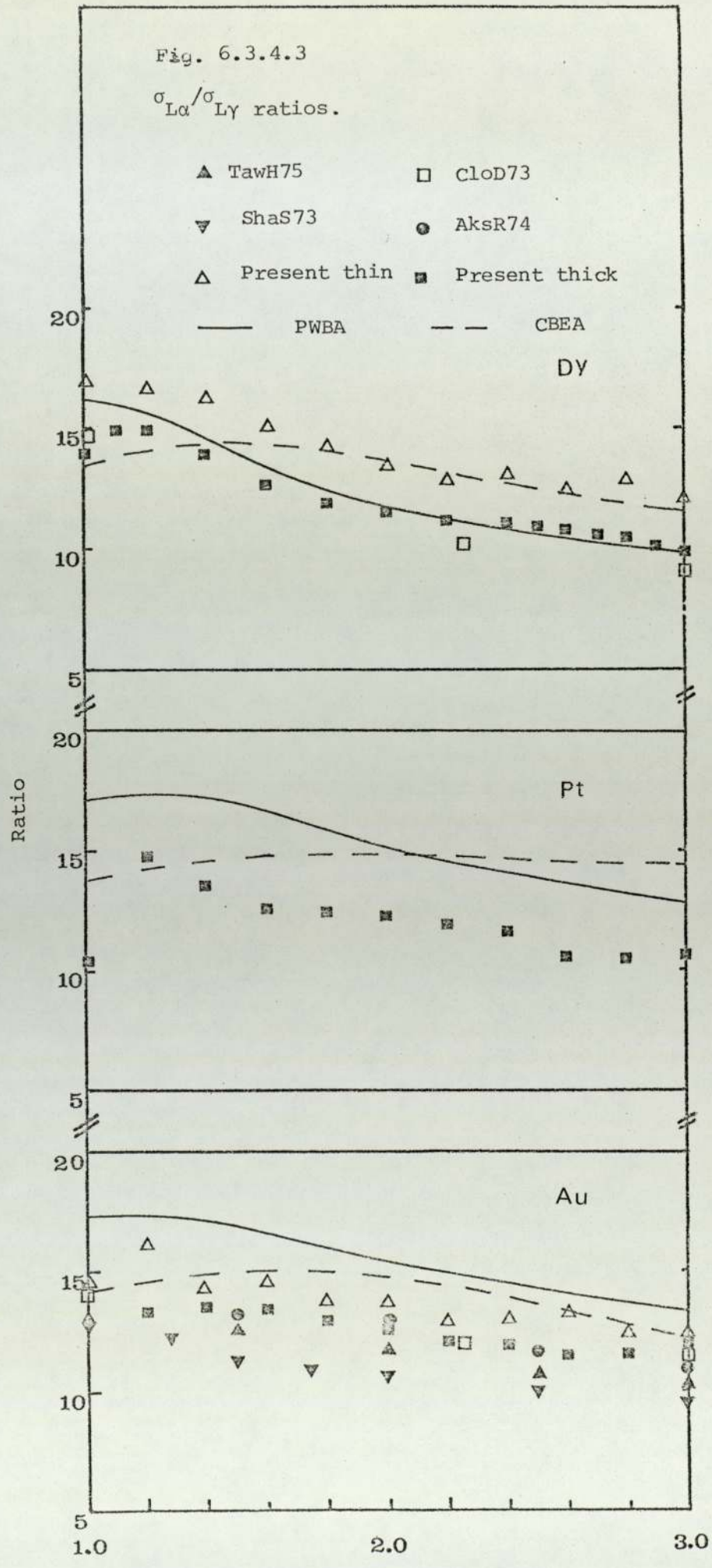
Fig. 6.3.4.3
$\sigma_{L\alpha}/\sigma_{L\gamma}$ ratios.
TawH75
CloD73
ShaS73
AksR74
Present thin
Present thick
PWBA
CBEA
Dy
Pt
Au
Ratio
20
15
10
5
1.0
2.0
3.0
Energy in MeV

6.3.5 Conclusions.

In most cases the present measurements are found to be in good agreement with the reported thick and thin target data. The present values of σ_{LX}, $\sigma_{L\alpha}$, $\sigma_{L\beta}$ and $\sigma_{L\gamma}$ are in general found to be systematically lower than the prediction of PWBA. This disagreement seems to have Z dependence and increases with the increase in Z number. Since CBEA values are in general lower than PWBA for the elements and energy region studied, the quantitative agreement between CBEA and the present data is sometime better at certain energies, but the energy dependence in all cases is better reproduced by PWBA than CBEA.

The ratio measurement also shows that the energy dependence is better described by PWBA.

6.4 CORRECTIONS TO THE THEORIES FOR L SHELL IONIZATION.

1. Relativistic effects.

The PWBA and CBEA theories as discussed in the case of K shell ionization, are uncorrected for relativistic effects arising due to the very high velocity of inner shell electrons, particularly for medium and high Z elements. Preliminary calculations, using the relativistic hydrogenic wave functions, have been made by Choi (ChoB71) and Hansen (HanJ73) for K and L shells. Alternatively, the correction can be made by applying a reduction factor to the binding energy of the electron (IshK74). These calculations indicate that the relativistic corrections, if applied, may increase the cross-sections predicted by non-relativistic PWBA significantly.

2. Binding effect and coulomb deflection effect.

The corrections applicable to PWBA cross-sections of K-shell due to binding and coulomb deflection effect have been discussed previously (Chapter III). Similar procedures have been described for

L shells by Brandt and Lapicki (BraW74). The effect of these corrections in PWBA is to decrease the cross-sections.

3. Retardation effects.

The retardation of the incident positive ion in the nuclear coulomb field reduces the cross-section. Garcia et.al (GarJ70) have reported a formula for the calculation of such effect.

4. Charge transfer effect.

In some cases inner shell electrons may be transferred to the orbit of projectile thus causing ionization. This effect has been calculated by Tawara et.al (TawH75) by using the Binary Encounter Approximation (GarJ68). For heavy elements the effect is usually < 1%.

5. Multiple ionization and fluorescence yield.

Due to the simultaneous ionization of different inner shells the value of the fluorescence yield changes. These changes were found to be very small (McGJ73).

Tawara et.al calculated the corrections (1 - 3) to be applied to the proton induced L shell ionization cross-section for bismuth. They found that the net effect is a correction factor of 10 - 20%. Their calculations are presented in the figure 6.4.1. Curves 1, 2, 3, 4 respectively show the correction terms due to relativistic, binding, coulomb and retardation effect. The curve marked NET incorporates all the corrections.

These corrections, if applied to the cross-section values predicted by the theories, will increase the difference between the present absolute measurements and the theories. These corrections, however, should not alter the theoretical ratios significantly and hence comments based on the ratios should not be affected.

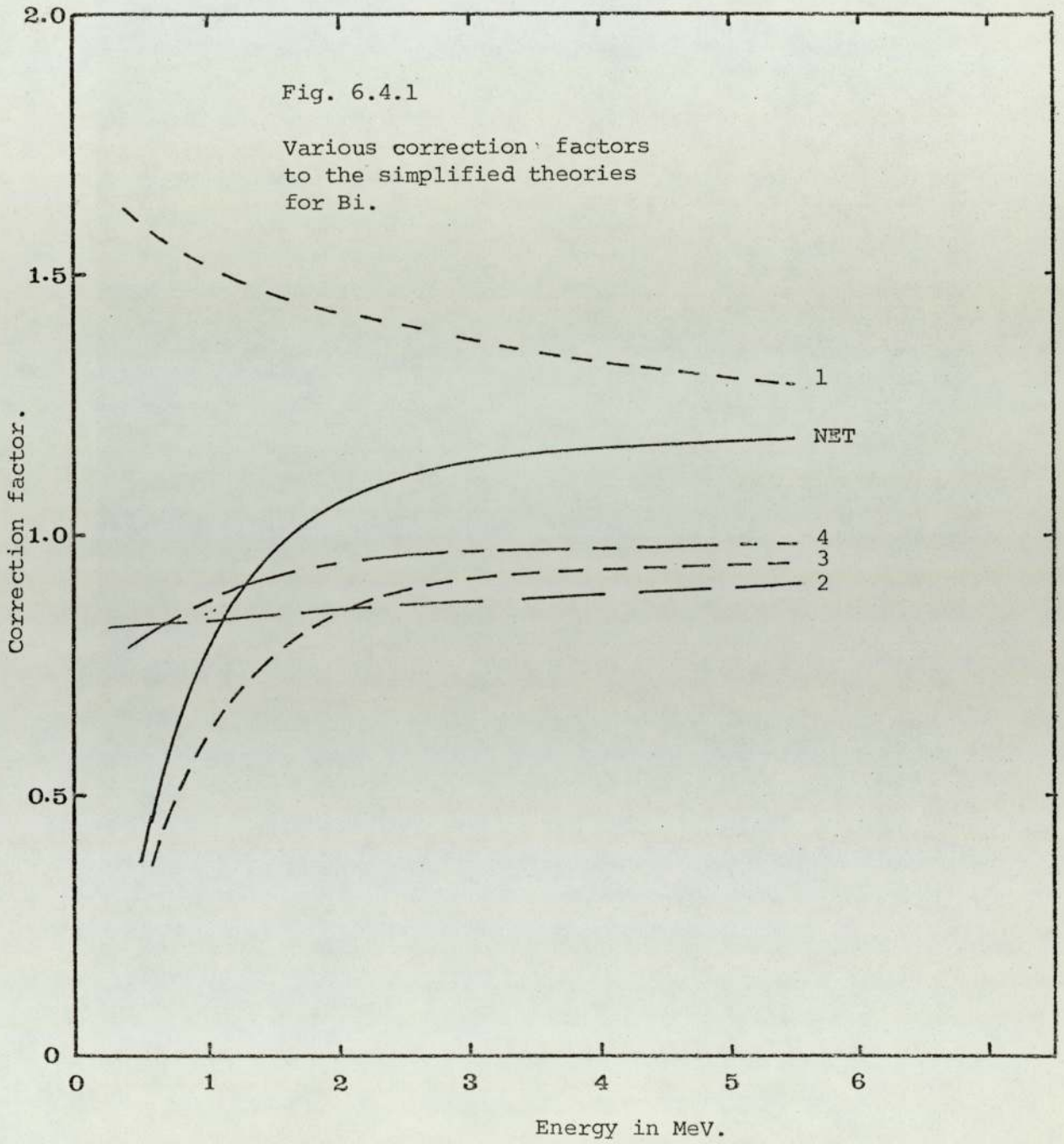

Fig. 6.4.1

Various correction factors to the simplified theories for Bi.

CHAPTER VII

Practical Analysis

7.1 INTRODUCTION

Proton induced X-ray analysis can be used to determine the trace element contents in thick, semi-thick and thin samples. If a thick target containing a number of elements is bombarded with n_p protons of energy E, the area $A_{\alpha i}$ under a K_α peak corresponding to i^{th} element in the resulting X-ray spectrum is given below:

$$A_{\alpha i}(E) = n_p \, \varepsilon_{\alpha i} \cdot \frac{\Omega}{4\pi} e^{-\Sigma \mu_i X_i} \int_{E_p}^{o} \sigma_{\alpha i x}(E) \, N_i \frac{dE}{S_m(E)} \, e^{-\mu X} \qquad 7.1.1$$

where $\varepsilon_{\alpha i}$ = the efficiency of the detector for the K_α radiation of the i^{th} element.

Ω = the solid angle of the detector.

$e^{-\mu_i x_i}$ = the attenuation of X-rays between the target and the front face of the detector.

$\sigma_{\alpha i x}(E)$ = the K_α production cross-section for the i^{th} element.

$S_m(E)$ = the stopping power of the matrix.

N_i = number of atoms/cc of the i^{th} element in the matrix.

$e^{-\mu X}$ = the absorption of the K_α X-ray of the i^{th} element in the matrix.

In practice the yield from the sample is very often compared with the yield from a standard material, s, containing a known concentration of the element of interest. The sample and the standard material are both bombarded with fixed numbers of protons of the same energy. The advantage with this method lies in the fact that, when the ratios are taken some of the parameters cancel out together with their uncertainties. If N_s is the number of atoms/cc of the element of interest in the standard matrix then in the case of homogenous samples, (using subscript

s for the standard), one can write:

$$\frac{A_{\alpha i}(E)}{A_{\alpha s}(E)} = \frac{N_i}{N_s} \frac{\int_{E_p}^{o} \sigma_{\alpha ix}(E) \frac{dE}{S_m(E)} e^{-\mu x}}{\int_{E_p}^{o} \sigma_{\alpha ix}(E) \frac{dE}{S_{ms}(E)} e^{-\mu_s x_s}} \qquad 7.1.2$$

If the element of interest is a high Z material in a low Z matrix in both the sample and the standard then the absorption in the matrix is negligible and equation 7.1.2 reduces to

$$\frac{A_{\alpha i}(E)}{A_{\alpha s}(E)} = \frac{N_i}{N_s} \frac{\int_{E_p}^{o} \sigma_{\alpha ix}(E) \frac{dE}{S_m(E)}}{\int_{E_p}^{o} \sigma_{\alpha ix}(E) \frac{dE}{S_{ms}(E)}} \qquad 7.1.3$$

The concentration of the element can then be determined provided the integrals are evaluated. This can be done numerically by using equation 5.2.4.1 for the cross-sections and using a polynomial fitted to tabulated values of $\frac{dE}{dx}$ for the specific matrix. Further discussions and simplifications have been reported by Deconninck et.al (DecD75).

In the case of thin samples, where the energy loss of the incident particle in passing through the sample is negligible, the analysis is easier. The area $a_{\alpha ix}$ for K_α radiation of the i^{th} element in a thin complex sample can be derived from equation 7.1.1 and is given by:

$$a_{\alpha ix}(E) = n_p \varepsilon_{\alpha i} \frac{\Omega}{4\pi} e^{-\Sigma \mu_i x_i} (N_i t_i) \sigma_{\alpha ix}(E) \qquad 7.1.4$$

where N_i is the number of atoms/cc of the i^{th} element present in the sample and t_i is the thickness of the sample in cm.

The thin target samples are analysed usually by comparing the yields of the various elements with a standard. The presence of an element, S, in the sample by a known amount may be used as an internal standard or the sample may be doped with a known amount of a standard S prior to the bombardment. The quantity of the added element should be small enough not to change the percentage of other elements significantly. The area under the K_α peak of the standard element S is given by:

$$a_{\alpha sx}(E) = n_p \varepsilon_{\alpha s} \frac{\Omega}{4\pi} e^{-\Sigma\mu_s X_s} (N_s t_s) \sigma_{\alpha sx}(E) \qquad 7.1.5$$

Using equation 7.1.4 and 7.1.5 the ratio $(N_i t_i)/(N_s t_s)$ can be found and is given by:

$$\frac{N_i t_i}{N_s t_s} = \frac{a_{\alpha ix}(E)}{a_{\alpha sx}(E)} \frac{e^{\Sigma\mu_i X_i}}{e^{\Sigma\mu_s X_s}} \frac{\sigma_{\alpha sx}(E)}{\sigma_{\alpha ix}(E)} \frac{\varepsilon_{\alpha s}}{\varepsilon_{\alpha i}} \qquad 7.1.6$$

Knowing $(N_s t_s)$ and other experimental parameters the determination of $(N_i t_i)$ requires a knowledge of the cross-section $\sigma_{\alpha ix}$ and $\sigma_{\alpha sx}$. The K_α production cross-section may be related to the more commonly reported ionization cross-section $\sigma_i(E)$ as follows:

$$\sigma_{\alpha ix}(E) = R_i \omega_i \sigma_i(E) \qquad 7.1.7$$

where ω_i is the K shell fluorescence yield and R_i is the K_α/K X-ray intensity ratios. These values can be obtained from standard references (BamW72, StoE70).

Substituting 7.1.7 in 7.1.6 and rearranging we get:

$$(N_i t_i) = \frac{a_{\alpha i x}(E)}{a_{\alpha s x}(E)} \frac{e^{\Sigma \mu_i X_i}}{e^{\Sigma \mu_s X_s}} \frac{R_s \omega_s \sigma_s(E)}{R_i \omega_i \sigma_i(E)} \frac{\varepsilon_{\alpha s}}{\varepsilon_{\alpha i}} (N_s t_s) \qquad 7.1.8$$

Empirical equations have been proposed by the present author for the calculation of K shell ionization cross-sections of various elements ($22 \leq Z \leq 50$) at proton energies 1.0, 1.5, 2.0, 2.5 and 3.0 MeV. These equations were obtained by fitting fourth order polynomials to the measured cross-section data. The cross-section σ_i can be obtained from the following equation:

$$\sigma_i(E) = \text{Exp}\left[a_o(E) + a_i(E)\, x_i + a_2(E)\, x_i^2 + a_3(E)\, x_i^3 + a_4(E)\, x_i^4 \right] \qquad 7.1.9$$

where $x = \ln Z$. The coefficients at five energies 1.0, 1.5, 2.0, 2.5 and 3.0 MeV are given in table 7.1.1. The polynomials at 1.0, 2.0 and at 3.0 MeV are plotted in Fig.7.1.1 along with the measured cross-sections and those of North Texas University Group. Similar polynomials can be proposed for the cross-sections where measurements are made for heavy elements using Lα transitions.

7.2 ANALYSIS

Different types of samples were studied to gain experience of proton induced X-ray analysis. The samples were chosen to be representative of the different types of samples normally encountered. The following samples were analysed:

i) Commercially available aluminium foil.

ii) Urine from various persons.

iii) A thin film of niobium on an aluminium substrate, prepared by sputtering of niobium in a krypton atmosphere.

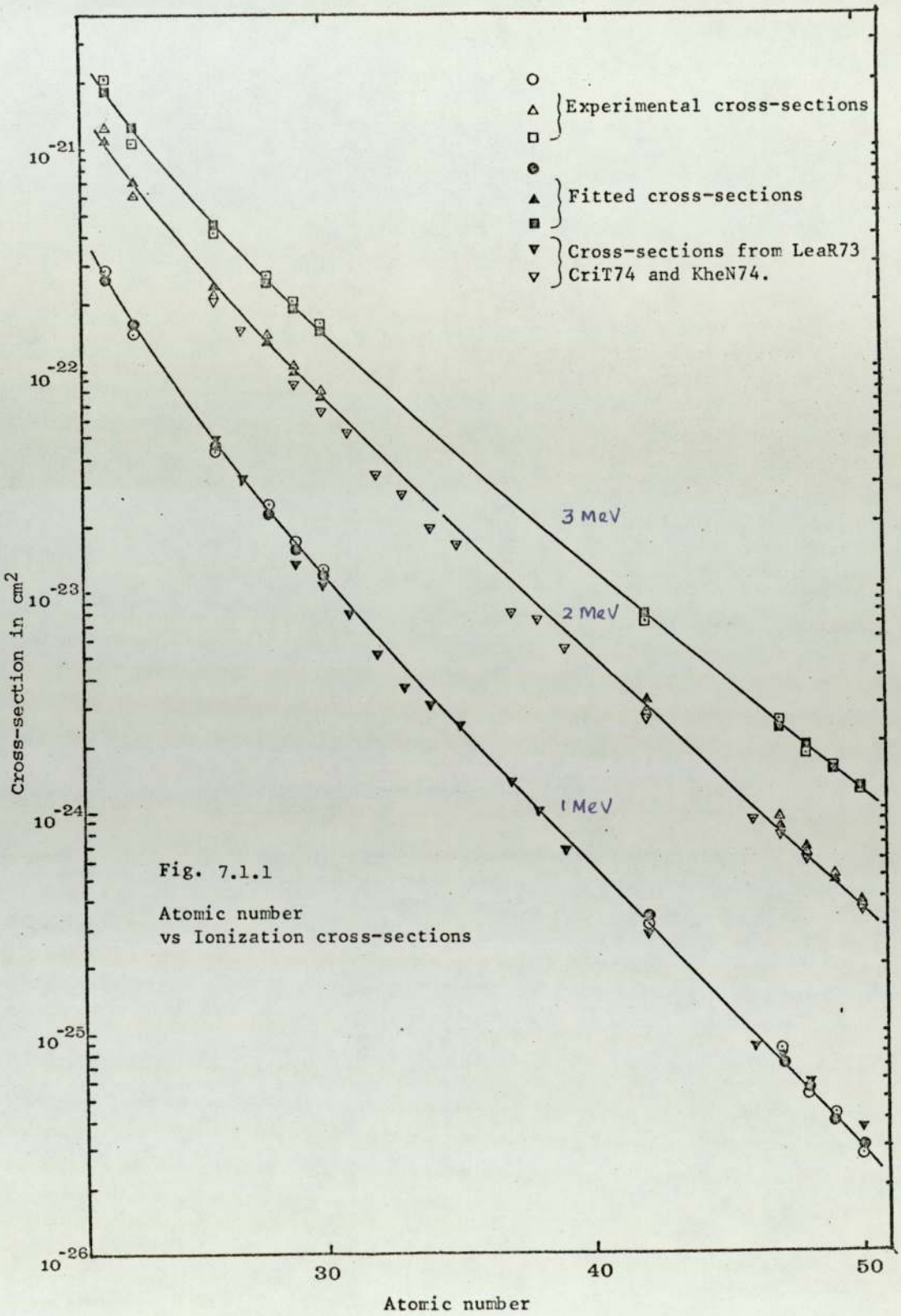

Fig. 7.1.1

Atomic number
vs Ionization cross-sections

Table 7.1.1

Coefficients of the polynomials for the calculation of ionization cross-sections at different energies.

Energy in MeV	a_o	a_1	a_2	a_3	a_4
1.0	345.616695	- 370.732930	127.930910	-18.751734	.8997905
1.5	910.967987	-1047.09943	430.789081	-78.849705	5.363094
2.0	907.686764	-1030.99674	417.841408	-75.070829	4.992184
2.5	850.409326	- 965.627357	389.969960	-69.799079	4.621429
3.0	815.084873	- 941.963786	387.572099	-70.908907	4.819339

7.2.1 Aluminium sample: Commercially available aluminium foil 750μm thick of 99.97% purity was analysed with a view to dtermining the concentration of iron impurity. This is a case of analysis of a high Z element in a thick low Z matrix.

To perform the analysis spectroscopically pure iron layers of thickness ∿ 4.81μg/cm^2, ∿ 10μg/cm^2 and 15μg/cm^2 were evaporated onto the aluminium foil. These targets were then bombarded by 2.5, 2.0 and 1.5 MeV protons in the same geometrical arrangements and experimental conditions. The areas under the FeK_α peaks for each target for 1μc of charge on the target were obtained.

The following assumptions were made in the analysis:

i) The FeK_α X-rays produced by proton bombardment suffer insignificant absorption in the aluminium matrix.

ii) Deposition of upto 15μg/cm^2 of iron on the surface does not introduce significant absorption of the emerging K_α X-rays.

Where the i^{th} element is distributed uniformly through a thick target and a thin layer is also present on the surface of the thick target, the area $A_i(E)$ under the K_α peak is given by:

$$A_i(E) = K\sigma_i(E)\ (N_i' t_i') + K N_i \int_{E_p}^{o} \sigma_i(E)\ \frac{dE}{S_m(E)} \qquad 7.2.1.1$$

where N_i' is the number of atoms /cc of the i^{th} element in the thin layer and t_i' is the thickness of the layer and N_i is the number of atoms /cc of the element of interest in the matrix, and K contains all the geometrical and absorption factors, R_i and ω_i.

Since most of the contribution to the thick target yields come from the depth in which the protons lose 30% of their energy the upper limit of the integral in equation 7.2.1.1 can be replaced by $.7E_p$

and the approximate equation is given by:

$$A_i(E) = K\sigma_i(E)\ (N_i' t_i') + K N_i \int_{E_p}^{.7E_p} \sigma_i(E) \frac{dE}{S(E)} \qquad 7.2.1.2$$

The values of the integral at 2.5, 2.0 and 1.5 MeV were evaluated numerically. The equation 5.2.4.1 was used for σ_i at these energies and tabulated values of $\frac{dE}{dx}$ were used. Knowing the values of the integral, equation 7.2.1.2 was solved for N_i using two values of $A_i(E)$ at two thicknesses. The values of concentrations of Fe atoms in the aluminium were found to be 3.9×10^{18} atoms/cc, 4.0×10^{18} atoms/cc and 3.8×10^{18} atoms/cc from measurement at 2.5, 2.0 and 1.5 MeV respectively. The mean is 3.9×10^{18} atom/cc which is 63 ppm in aluminium foil. The estimated uncertainty is of the order of 10%.

7.2.2 Urine Samples:

The urine samples code named (a) Upal (b) Sturt and (c) Seasm were studied and a comparison of trace elements present made. In order to establish an internal standard for the measurement, the urine samples were doped by introducing a known amount of cadmium. The samples were bombarded prior to doping to make sure that no detectable amount of cadmium existed in the untreated samples. Cadmium in the form of $CdNO_3$ was introduced into the samples in such an amount so as to make the $CdNO_3$ content in the urine 60µg/cc.

About 100µl of each of the urine samples were dried on spectroscopically pure aluminium foils to produce thin targets. Each of these targets were bombarded for about half an hour. The resulting spectra are shown in figure 7.2.2.1. The data of Sturt and Seasm were normalised to that of Upal using the CdK_α peak. The quantitative analysis of trace elements in the samples were made using the equations 7.1.8 and 7.1.9.

The amounts of various elements found in different samples are

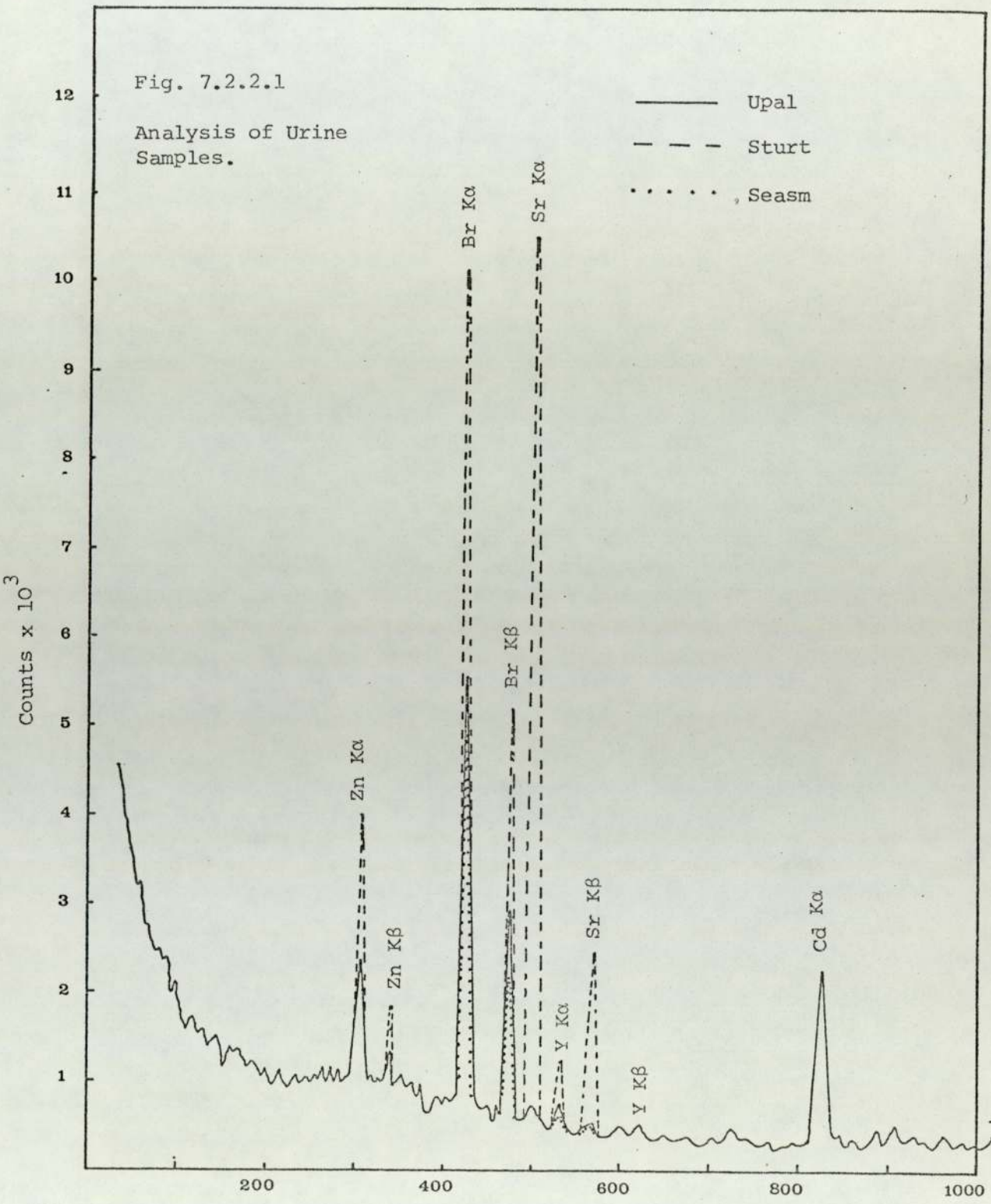
Fig. 7.2.2.1
Analysis of Urine Samples.
Upal
Sturt
Seasm
Counts x 10^3
12
11
10
9
8
7
6
5
4
3
2
1
Zn Kα
Zn Kβ
Br Kα
Br Kβ
Sr Kα
Y Kα
Sr Kβ
Y Kβ
Cd Kα
200
400
600
800
1000

Table 7.2.2.1

Trace element contents in the urine samples/cc

	Sturt	Upal	Seasm
Y	2µg ± 8%	.9µg ± 8%	.7µg ± 8%
Sr	13µg ± 8%		
Br	5.5µg ± 8%	2.8µg ± 8%	1.7µg ± 8%
Zn	.53µg ± 8%	.26µg ± 8%	

given in table 7.2.2.1.

7.2.3 Niobium target

The purpose of the study of the niobium target was primarily to detect any presence of krypton and if present to determine its concentration.

A thin target of niobium ($\sim$ 10 - 15 $\mu g/cm^2$) was prepared on a spectroscopically pure thin aluminium foil by sputtering in a krypton atmosphere. The target was supplied by the thin film group of the Department of Physics, University of Aston in Birmingham.

The target was bombarded by 2 MeV protons and the X-rays detected. The resulting X-ray spectrum clearly showed the presence of krypton (Fig.7.2.3.1). The area under the K_α peak of niobium and krypton were found. The percentage contents of the krypton in niobium was calculated using the formula 7.1.8. Since the melinex window of the target holder and beryllium window of the detector were transparent to niobium and krypton K_α peaks (energies 16.62 keV and 12.6 keV respectively) and the detector was placed in contact with the target holder window, absorption corrections were negligible. Values of $\varepsilon_{\alpha i}$ were determined and the niobium and krypton ionization cross-sections at 2.0 MeV were calculated from the equation 7.1.9. The weight concentration was found to be $\sim$ .18%. The uncertainty in the result was estimated to be $\sim$ 10%.

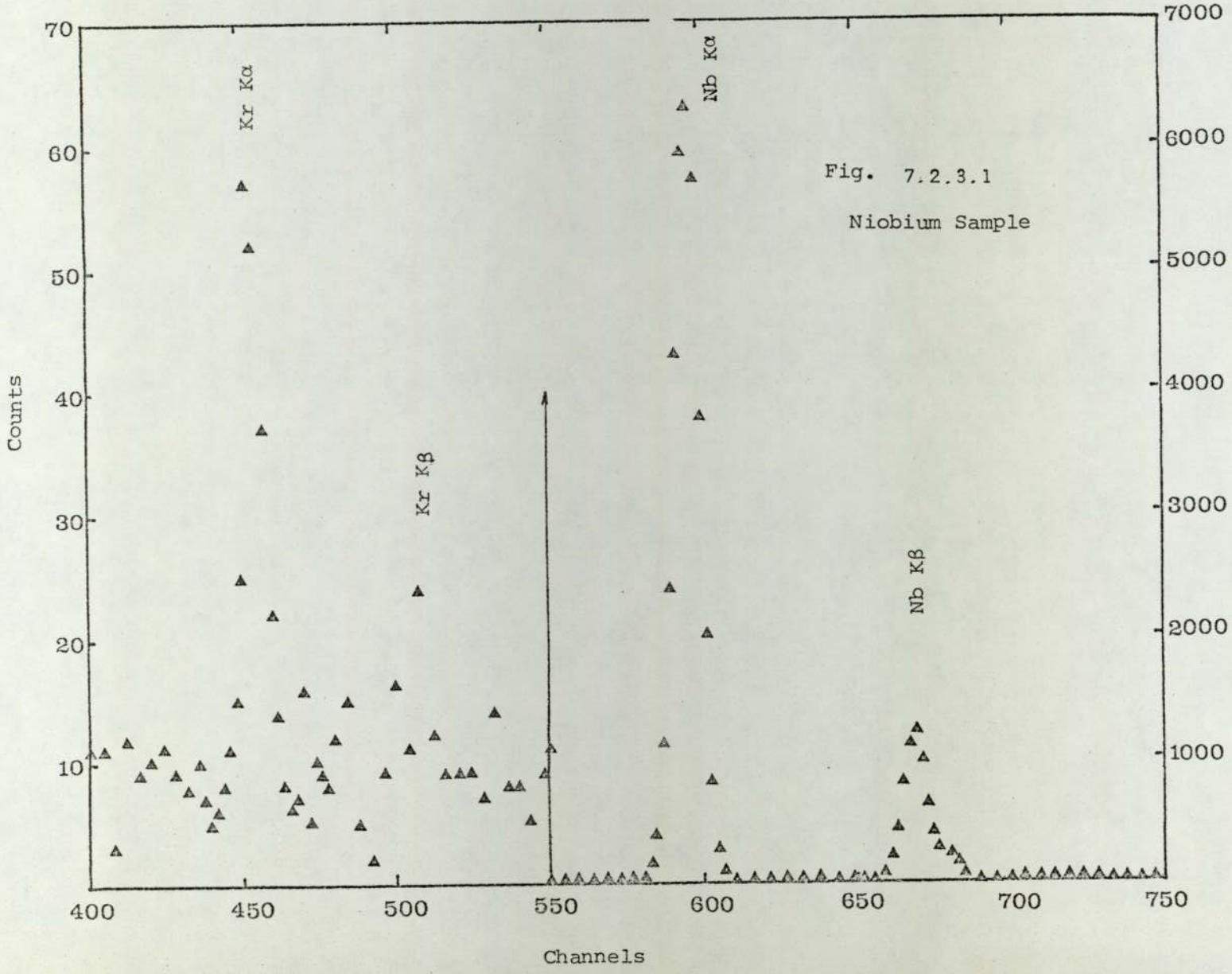

Fig. 7.2.3.1

Niobium Sample

Appendix 1

Summary of the Proton Induced K X-ray Emission Studies

Element	Z	Ep (KeV)	Target	Detector	Reference	Comments
Beryllium	4	50-100	thk	pc	ChrL67	
		10-200	thk	pc	TerM72	
Carbon	6	1500	thk	pc	OgiW64	
		15-1908	thk	pc	KhaJ65	
		25-100	thk	pc	SteA65	
		50-100	thk	pc	ChrL67	
		40-110	thk	pc	SteA67	
		20-80	thk	pc	DerR68	
		60-200	thk		TerM70	
		15-50	thk	pc	TerM70a	
		20-160	thn	Si(Li)	WegW73	
Oxygen	8	60-110	thk	pc	SteA65, SteA67	
		25-75	thn	pc	MarC67	
		20-100	thn	pc	HarR69, HarR68	
		100	gas	pc	HarR68	
		500-2500	gas	pc	PooD68	
Fluorine	9	300-200	gas		TobL72b	
Neon	10	28-200	gas		TobL72b	
		28-145	gas	pc	HarK73	
Magnesium	12	25-1700	thk	pc	KhaJ64, KhaJ65	
		125-200	thk	pc	BraW66	
		125-200	thk	pc	BraW66	
		1000-5000	thn	pc	SelB69	

Element	Z	Ep (KeV)	Target	Detector	Reference	Comments
Aluminium	13	1500	thk	pc	OgiW64	
		25-1700	thk	pc	KhaJ64a, KhaJ65	
		30-300	thk	pc	BraW66	
		70-100	thk	pc	KhaJ66b	
		70-170	thk	pc	PetO36	
		100	thk	pc	BraW65	
		60-110	thk	pc	SteA65	
		60-200	thk		BraW66	
		75-100	thk	pc	KhaJ66b	
		50-100	thn	pc	ChrL67	
		25-75	thn	pc	MarC67	
		50-100	thk	pc	SteA67	
		500-2500		pc	PooD68	
		25-200	thk	pc	BraW69	
		40-100	thn	pc	HarR69	
		1000-5000	thn	pc	SelB69	
		80-200	thk	pc	NeeP70a	
		100-250	thk	pc	ShiK70	
		90-180	thk	pc	ShiK71	
		180-160	thk	pc	ShiK71	
		200-3000	thk	pc	BasG73	
Silicon	14	100	thk	pc	CaiJ69	
		50-160	thk	Si(Li)	WegW73	
Argon	18	28-145	gas	pc	HarK73	
		1500-500	gas	pc	WinL73	
Calcium	20	2000-25000	thn	pc	BisG70	
		6000-15000		Si(Li)	BurD70	
Scandium	21	1000-5000	thn	Si(Li)	LinJ73	
		1000-5000	thn	Si(Li).	McCJ73	

Element	Z	Ep (KeV)	Target	Detector	Reference	Comments
Titanium	22	200-500	thk	NaI(Tl)	JopR62	
		1500	thk	pc	OgiW64	
		2000-25000	thn	pc	BisG70	
		1500	thn	Si(Li)	JohT70	
		100-250	thk	pc	ShiK70	
		100-150	thn	Si(Li)	DugJ71	
		90-170	thk	pc	ShiK71	
		1000-3000	thn	Si(Li)	BeaR73	Kα measured
		1000-5000	thn	Si(Li)	McCJ73	
		1500-10930	thn	Si(Li)	AksR74	
		130-415	thk	Si(Li)	WheR74	
		500-2000	thn	Si(Li)	BodF75	
		1000-3000	thk	Si(Li)	Present	
Vanadium	23	75	thk	pc	SteA67	
		100-150	thn	Si(Li)	DugJ72	
		6000-15000		Si(Li)	BurD70	Kα measured
		2500	thn	Si(Li)	BeaR73	
		500-2000	thn	Si(Li)	BodF75	
		1000-3000	thk	Si(Li)	Present	
Chromium	24	100-150	thn	Si(Li)	DugJ72	
Manganese	25	100-150	thn	Si(Li)	DugJ72	
		2500-12000	thn	Si(Li)	LieR73	
		130-415	thk	Si(Li)	WheR74	
Iron	26	400-700	thk	GM	UrbJ55	
		140-1300	thk	NaI(Tl)	MesS58	
		441	thk	NaI(Tl)	JopR62	
		1500	thk	pc	OgiW64	
		75	thk	pc	SteA67	
		700-2500	thn		FahA71	
		100-150	thn	Si(Li)	DugJ72	
		160000	thn	Si(Li)	JarO72	
		1000-3000	thn	Si(Li)	BeaR73	Kα measured
		500-2000	thn	Si(Li)	LeaR73	
		2500-12000	thn	Si(Li)	LieR73	

Element	Z	Ep (KeV)	Target	Detector	Reference	Comments
Iron (contd)	26	1000-5000	thn	Si(Li)	McCJ73	
		1500-10930	thn	Si(Li)	AksR74	
		130-415	thk	Si(Li)	WheR74	
		500-2000	thn	Si(Li)	BodF75	
		1000-3000	thk	Si(Li)	Present	
Cobalt	27	400-700	thk	GM	Urb 55	
		100-150	thn	Si(Li)	DugJ72	
		500-2000	thn	Si(Li)	LeaR73	
		1500-10930	thn	Si(Li)	AksR74	
Nickel	28	400-700	thk	GM	UrbJ55	
		6000-15000	thk	Si(Li)	RicP69	
		5000-28000	thn	pc	BisG70	
		100-300	thk	pc	ShiK70	
		100-150	thn	Si(Li)	DugJ72	
		1000-3000	thn	Si(Li)	BeaR73	Kα measured
		1000-5000	thn	Si(Li)	McCJ73	
		280-420	thk	pc,Si(Li)	DysN73	
		2500-12000	thn	Si(Li)	LieR73	
		1500-10930	thn	Si(Li)	AksR74	
		90-415	thk	Si(Li)	WheR74	
		500-2000	thn	Si(Li)	BodF75	
		1000-3000	thk	Si(Li)	Present	
Copper	29	400-700	thk	GM	UrbJ55	
		200-1215	thk	NaI(Tl)	HanJ56	
		400-1000	thn	pc	SinB57a	
		140-1200	thk	NaI(Tl)	MesS58	
		200-500	thk	NaI(Tl)	JopR62	
		150-500	thk	pc	KhaJ64a	
		10-50	thk	pc	KhaJ64b	
		1500	thk	pc	OgiW64	
		75-100	thk	pc	SteA67	
		500-2500	thk	pc	PooD68	
		6000-19000		Si(Li)	RicP69, RicP70	
		150-250	thk	pc	ShiK70	
		700-2500	thn		FahA71	

Element	Z	Ep (KeV)	Target	Detector	Reference	Comments
Copper (contd)	29	125-150	thn	Si(Li)	DugJ71	
		160000	thn	Si (Li)	JarO72	
		1000-3000	thn	Si(Li)	BeaR73	Kα measured
		210-420	thk	pcSi(Li)	DysN73	
		500-2000	thn	Si(Li)	LeaR73	
		2500-12000	thn	Si(Li)	LieR73	
		1500-10930	thn	Si(Li)	AksR74	
		130-415	thk	Si(Li)	WheR74	
		500-2000	thn	Si(Li)	BodF75	
		1000-3000	thk	Si(Li)	Present	
Zinc	30	400-700	thk	GM	UrbJ55	
		700-2500	thn		FahA71	
		2500-1200	thn	Si(Li)	LieR73	
		450-2000	thn	Si(Li)	LeaR74	
		150-415	thk	Si(Li)	WheR74	
		1000-3000	thk	Si(Li)	Present	
Gallium	31	500-2000	thn	Si(Li)	LeaR73	
Germanium	32	1000-3000	thn	Si(Li)	BeaR73	Kα measured
Arsenic	33	470-2000	thn	Si(Li)	LeaR73	
		1000-5500	thn	Si(Li)	LinJ73	
		470	thn	Si(Li)	LeaR74	
Selenium	34	400-2000	thn	Si(Li)	CriT74	
Bromine	35	600-2000	thn	Si(Li)	CriT74	
Krypton	36	1500-5000	gas	Si(Li)	WinL73	
Rubidium	37	400-2000	thn	Si(Li)	CriT74	
		1000-3000	thn	Si(Li)	BeaR73	Kα measured
Strontium	38	600-2000	thn	Si(Li)	CriT74	
Yttrium	39	2500-12000	thn	Si(Li)	LieR73	
		600-200	thn	Si(Li)	CriT74	

Element	Z	Ep (KeV)	Target	Detector	Reference	Comments
Zirconium	40	200-500	thk	NaI(Tl)	JopR62	
		160000	thn	Si(Li)	JarO72	
		1000-3000	thn	Si(Li)	BeaR73	Kα measured
Molybdenum	42	2400	thk	NaI(Tl)	LewH53	
		250-1610	thk	NaI(Tl)	HanJ56	
		240-1200	thk	NaI(Tl)	MesS58	
		441	thk	NaI(Tl)	JopR62	
		75	thk	pc	SteA67	
		160000	thn	Si(Li)	JarO72	
		400-2000	thk	pc,Si(Li)	DysN73	
		2500-12000	thn	Si(Li)	LieR73	
		400-2000	thn	Si(Li)	CriT74	
		1000-3000	thk	Si(Li)	Present	
Rhodium	45	160000	thn	Si(Li)	JarO72	
Palladium	46	600-2000	thn	Si(Li)	CriT74	
Silver	47	1700-2880	thk	NaI(Tl)	LewH53	
		600-1000	thn	NaI(Tl)	SinB57a	
		260-1200	thk	NaI(Tl)	MesS58	
		160000	thn	Si(Li)	JarO72	
		1000-3000	thn	Si(Li)	BeaR73	
		375-445	thk	pc,Si(Li)	DysN73	
		2500-12000	thn	Si(Li)	LieR73	
		1500-10930	thn	Si(Li)	AksR74	
		600-2000	thn	Si(Li)	KheN75	
		1000-3000	thk	Si(Li)	Present	
Cadmium	48	2500-12000	thn	Si(Li)	LieR73	
		600-2000	thn	Si(Li)	KheN75	
		1000-3000	thk	Si(Li)	Present	
Indium	49	1000-3000	thk	Si(Li)	Present	

Element	Z	Ep (Kev)	Target	Detector	Reference	Comments
Tin	50	260-1040	thk	NaI(Tl)	MesS58	
		160000	thn	Si(Li)	JarO72	
		1000-3000	thn	Si(Li)	BeaR73	
		1500-6000	thn	Si(Li)	LinJ73	
		600-2000	thn	Si(Li)	KheN75	
		1000-3000	thk	Si(Li)	Present	
Antimony	51	1000-3000	thn	Si(Li)	BeaR73	
		1500-5000	thn	Si(Li)	LinJ73	
Xenon	54	4500-5000	gas	Si(Li)	WinL73	
Barium	56	160000	thn	Si(Li)	JarO72	
Samarium	62	160000	thn	Si(Li)	JarO72	
Terbium	65	16000	thn	Si(Li)	JarO72	
Tantalum	73	1920-3150	thk	NaI(Tl)	LewH53	
		140-1250	thk	NaI(Tl)	MesS58	
		160000	thn	NaI(Tl)	JarO72	
Platinum	78	160000	thn	Si(Li)	JarO72	
Gold	79	2400	thk	NaI(Tl)	LewH53	
		160000	thn	Si(Li)	JarO72	
Lead	82	1920-2880	thk	NaI(Tl)	LewH53	
		160000	thn	Si(Li)	JarO72	
Uranium	92	160000	thn	Si(Li)	JarO72	

Appendix 2

Summary of the Proton Induced L X-ray Emission Studies

Element	Z	Ep (KeV)	Target	Detector	Reference	Comments
Argon	18	70-100	gas	pc	SarF70	
Vanadium	23	60-200	thn	pc	NeeP70	
Iron	26	70	thk	pc	SteA67	
Nickel	28	60-200	thn	pc	NeeP70	
		100-250	thk	pc	ShiK70	
Copper	29	25-1700	thk	pc	KhaJ64b,KhaJ66a	
		75-115	thk	pc	BraW65	
		70-100	thk	pc	KhaJ66b	
		75-200	thk	pc	BraW66	
		260-1500	thk	pc	KhaJ67	
		25-100	thk	pc	SteA67	
		100	thk	pc	CaiJ69	
		60-200	thn	pc	NeeP70	
		100-250	thk	pc	ShiK70	
		90-180	thk	pc	ShiK71	
Zinc	30	60-200	thn	pc	NeeP70	
Krypton	36	1500-5000	gas	Si(Li)	WinL73	
Zirconium	40	441	thk	NaI(Tl)	JopR62	
		100-250	thk	pc	ShiK70	
Molybdenum	42	200-500	thk	NaI(Tl)	JopR62	
		75	thk	pc	SteA67	
		100-250	thk	pc	ShiK70	
		90-170	thk	pc	ShiK71	
Selenium		60-200	thn	pc	NeeP70	

Element	Z	Ep (KeV)	Target	Detector	Reference	Comments
Rhodium		60-200	thn	pc	NeeP70	
Silver	47	400-1000	thn	pc	SinB57b	
		441	thk	NaI(Tl)	JopR62	
		15000	thk	pc, NaI(Tl)	OgiW64	
		2000-28000	thn	pc	BisG70	
		100-250	thk	pc	ShiK70	
		700-7500	thn		FahA71	
		120-210	thk	pc	ShiK71	
		1500-10930	thn	Si(Li)	AksR74	
Cadmium	48	200-500	thk	NaI(Tl)	JopR62	
		100-250	thk	pc	ShiK70	
Indium	49	1000-3000	thk	Si(Li)	Present	
Tin	50	75	thk	pc	SteA67	
		150-250	thk	pc	ShiK70	
		1400-4400	thk	Si(Li)	IshK74	
		1000-3000	thk	Si(Li)	Present	
Tellurium	52	441	thk	NaI(Tl)	JopR62	
Xenon		1500-5000	thn	Si(Li)	WinL73	
Barium	56	441	thk	NaI(Tl)	JopR62	
Cerium	58	1000-3000	thn	Si(Li)	BeaR73	
		1000-3000	thn	Si(Li)	CloD73	
Praseodymium	59	300-2000	thn	Si(Li)	AbrF74	
Neodymium	60	500-1700	thk	pc	KhaJ65	
		1000-3000	thk	pc	KhaJ65	

Element	Z	Ep (KeV)	Target	Detector	Reference	Comments
Samarium	62	500-1700	thk	pc	KhaJ65	
		1000-3000	thn	Si(Li)	BeaR73	
		1000-3000	thn	Si(Li)	CloD73	
		300-2000	thn	Si(Li)	AbrF74	
Gadolinium	64	441	thk	NaI(Tl)	JopR62	
		500-1700	thk	pc	KhaJ65	
		300-2000	thn	Si(Li)	AbrF74	
Terbium	65	500-1700	thk	pc	KhaJ65	
Dysprosium	66	500-1700	thk	pc	KhaJ65	
		1000-3000	thn	Si(Li)	BeaR73	
		1000-3000	thn	Si(Li)	CloD73	
		300-2000	thn	Si(Li)	AbrF74	
		1000-3000	thk	Si(Li)	Present	
Holmium	67	500-1700	thk	pc	KhaJ65	
Erbium	68	441	thk	NaI(Tl)	JopR62	
Thullium	69	441	thk	NaI(Tl)	JopR62	
		1000-3000	thn	Si(Li)	BeaR73	
		100-3000	thn	Si(Li)	CloD73	
Ytterbium	70	441	thk	NaI(Tl)	JopR62	
Lutecium	71	441	thk	NaI(Tl)	JopR62	
Hafnium	72	441	thk	NaI(Tl)	JopR62	

Element	Z	Ep (KeV)	Target	Detector	Reference	Comments
Tantalum	73	1500-4250	thk		BerE54	
		200-500	thk	NaI(Tl)	JopR62	
		1500	thk	pc,NaI(Tl)	OgiW64	
		1000-3000	thn	Si(Li)	BeaR73	
		1400-4400	thn	Si(Li)	IshK74	
Tungsten	74	441	thk	NaI(Tl)	JopR62	
		230-420	thk	pc,Si(Li)	DysN73	
		1000-3700	thn	Si(Li)	CloD73	
Rhenium	75	441	thk	NaI(Tl)	JopR62	
Osmium	76	441	thk	NaI(Tl)	JopR62	
Indium	77	441	thk	NaI(Tl)	JopR62	
Platinum	78	441	thk	NaI(Tl)	JopR62	
		1000-3000	thk	Si(Li)	Present	
		1000-3000	thk	Si(Li)	Present	
Gold	79	1500-4250	thk	NaI(Tl)	BerE54	
		200-500	thk	NaI(Tl)	JopR62	
		70-200	thk	pc	NeeP70b	
		1000-5000	thn	Si(Li)	DugJ71	
		700-2500	thn		FahA71	
		500-3000	thn	Si(Li)	BisG72a	
		1000-3000	thn	Si(Li)	BeaR73	
		1000-3000	thn	Si(Li)	CloD73	
		500-30000	thn	Si(Li)	ShaS73	
		1500-5000	thn	Si(Li)	AksR74	
		250-5200	thn	Si(Li)	DatS74	
		1000-4500	thn	Si(Li)	TawH75	
		1000-3000	thk	Si(Li)	Present	
Mercury	80	441	thk	NaI(Tl)	JopR62	

Element	Z	Ep (Kev)	Target	Detector	Reference	Comments.
Lead	82	1500-4250	thk	NaI(Tl)	BerE54	
		441	thk	NaI(Tl)	JopR62	
		75	thk	pc	SteA67	
		1000-3000	thn	Si(Li)	BeaR73	
		1000-3000	thn	Si(Li)	CloD73	
		500-4000	thn	Si(Li)	MadD74	
		500-14000	thn	Si(Li)	BusC73	
Bismuth	83	441	thk	NaI(Tl)	JopR62	
		1000-5000	thn	Si(Li)	DugJ71	
		1000-3000	thn	Si(Li)	CloD74	
		500-4000	thn	Si(Li)	MadD74	
		1000-4500	thn	Si(Li)	TawH75	
Thorium	90	1000-3000	thn	Si(Li)	BeaR73	
		1000-3700	thn	Si(Li)	CloD73	
Uranium	92	1500-4000	thk	NaI(Tl)	BerE54	
		441	thk	NaI(Tl)	JopR62	
		75	thk	pc	SteA67	
		1000-5000	thn	Si(Li)	DugJ71	
		1000-3000	thn	Si(Li)	CloD73	
		1000-4500	thn	Si(Li)	TawH75	

REFERENCES

AbrF74 : F. Abrath and T. J. Gray, Phys.Rev.A. Vol.9, P.682.

AksR74 : R. Akselsson and T. B. Johansson, Z.Physik, Vol.266, P.245.

AldK56 : K. Alder, T. Huus, B. Mottelson and A. Winter, Rev.Mod.Phys., Vol.28, P.432.

BamW72 : W. Bambynek, B. Crasemann, R. W. Fink, H. V. Freund, H. Mark,C. D. Swift, R. E. Price, P. V. Rao, Rev.Mod.Phys., Vol.44, No.4, P.716.

BanJ59 : J. Bang and J. M. Hansteen, Kgl. Danske Videnskab Selskab, Mat-Fys. Medd., Vol.31, No.13.

BasG73 : G. Basbas, W. Brandt and R. Laubert, Phys.Rev.Vol.A7, P.983.

BarB74 : B. K. Barns, L. E. Beghian, G. H. R. Kegel, S. C. Mathur, A. Mittler and P. W. Quinn, Proc. of the 3rd Conf. on Appli. of Small Accelerator, Denton, Texas, Oct.21-23.

BeaR73 : R. C. Bearse, D. A. Close, J. J. Malanify and C. J. Umbarger, Phys.Rev.A, Vol.7, No.4, P.1269.

BeiA63 : A. Beiser, Concepts of Modern Physics, Kogakusha Company Ltd, Tokyo.

BerE54 : E. M. Bernstein and H. W. Lewis, Phys.Rev., Vol.95, P.83.

BisG70 : G. A. Bissinger, J. M. Joyce, E. J. Ludwig, W. S. McEver and S. M. Shafroth, Phys.Rev. Vol.A1, P.841.

BisG72 : G. A. Bissinger, S. M. Shafroth and A. W. Walter, Phys.Rev. Vol.A5, P.2046.

BisG72a: G. A. Bissinger, A. B. Baskin, B. H. Choi, S. M. Shafroth, J. M. Howard and A. W. Waltner, Phys.Rev.A, Vol.6, No.2, P.545.

BodF75 : F. Bodart, G. Deconninck, S. Wilk, X-ray Spectrometry, Vol.4.

BraW65 : W. Brandt, J. M. Khan, D. L. Potter and R. D. Worley, Phys.Rev. Lett. Vol.14, P.42.

BraW66 : W. Brandt, R. Laubert and I. Sellin, Phys.Rev. Vol.151, P.56

BraW69 : W. Brandt and R. Laubert, Phys.Rev., Vol.178, P.225.

BraW72 : W. Brandt, Proc. of the 3rd Int. Conf on Atomic Physics (S.J.Smith, ed) P.155, Plenum Press, New York.

BraW74 : W. Brandt and G.Lapicki, Phys.Rev. Vol.A10, P.474.

BurW57 : W. Buhring and O. Haxel, Z Physik, Vol.148, P.653.

BurD70 : D. Burch and P. Richard, Phys.Rev. Letters Vol.25, P.983.

BusC73 : C. E. Busch, A. B. Baskin, P. H. Nettles, S. M. Shafroth and A. W. Waltner, Phys.Rev. Vol.A7, P.1601.

CaiJ69 : J. A. Cairns,D. F. Holloway and R. S. Nelson, Proc. Int. Conf. At Coll. Phenom Solids, P.541. (D. W. Palmer, M. W. Thompson and P. D. Townsend eds.) North Holland.

CarE75 : E. Caruso, Energia Nucleare, Vol.22, P.382.

ChaC75 : C. N. Chang, J. F. Morgan, S. L. Blatt, Phys.Rev.A. Vol.11, No.2, P.607.

ChoB71 : B. H. Choi, Phys.Rev. Vol.A4, P.1002.

ChoB73 : B. H. Choi, E. Merzbacher, G. S. Khandelwal, Atomic Data, No.5, P.291

ChrL67 : L. J. Christensen, J. M. Khan and W. F. Brunner, Rev.Sci.Inst. Vol.38, P.20.

CloD73 : D. A. Close, R. C. Bearse, J. J. Malanify, and C. J. Umberger, Phys. Rev. A Vol.8, P.1873

ConB75 : B. O'Connel, Ph.D. thesis, University of Aston in Birmingham (unpublished).

CooJ71 : J. A. Cooper; Nucl.Instr. and Methods, Vol.106, P.525.

CriT74 : T. L. Criswell and T. J. Gray, Phys.Rev.A. Vol.10, No.4, P.1145.

DatS74 : S. Datz, J. L. Duggan, L. C. Feldman, E. Laegegaard, J. U. Anderson, Phys.Rev. Vol.A9, P.192.

DecD75 : G. Deconninck, G. Demortier, F. Bodart, Atomic Energy Review, Vol.13, Part 2, P.367.

DehF66 : F. J. de Heer, J. Schutten and H. Moustafa, Physica, Vol.32, P.1766.

DerR68 : R. C. Der, T. M. Kavanagh, J. M. Khan, B. P. Curry and R. J. Fortner, Phys.Rev. Letts. Vol.21, P.1731.

DugJ71 : J. L. Duggan, W. L. Beck, L. Albrecht, L. Munz, J. D. Spaulding, 20th Annual Denver Conf. on Appl. of X-ray Analysis, August 11-13.

DugJ72 : J. L. Duggan, W. L. Beck, L. Albrecht, L. Munz and J. D. Spaulding, Advances in X-ray Analysis Vol.15, P.407.

DysN73 : N. A. Dyson, J.Phys.B: Atom Molec.Phys. Vol.6, P.562.

ElaE65 : E. Elad, Nucl.Instr. and Methods, Vol.37, P.327.

FahA71 : A. Fahlenius and P. Jauho, Ann.Acad.Sci. Fennicae Avi. Vol.367, P.3.

FloR72 : R. G. Flocchini, P. J. Feeney, R. J. Sommerville and T. A. Cahill, Nucl.Instr. Methods, Vol.100, P.397.

FolF74 : F. Folkmann, C. Gaarde, T. Huus and K. Kemp, Nucl.Instr. Methods, Vol.116, P.487.

FolF74a: F. Folkmann, J. Borggreen and A. Kjeldgaard, Nucl.Instr. Methods, Vol.119, P.117.

GarJ68 : J. D. Garcia, E. Gerjouy and J. E. Welker, Phys.Rev., Vol.165, P.72.

GarJ70 : J. D. Garcia, Phys.Rev. Vol.A1, P.280.

GarJ70a: J. D. Garcia, Phys.Rev., Vol.A1, P.1402.

GarJ71 : J. D. Garcia, Phys.Rev., Vol.A4, P.955.

GarJ73 : J. D. Garcia, R. J. Fortner, T. M. Kavanagh, Rev.Mod.Phys., Voll.45, No.2, P.111.

GerE66 : E. Gerjouy, Phys.Rev. Vol.148, P.54.

GorB71 : B. M. Gordon and H. W. Kraner, Chemical Analysis by Charged Particle Bombardment, Namur, Belgium.

GouF71 : F. S. Goulding and J. M. Jaklevic, University of California Research Laboratories, Report UCRL-20625.

GraT73 : Tom J. Gray, R. Lear, R. J. Dexter, F. N. Schwettmann, K. C. Wiemer, Thin Solid Films, Vol.19, P.103.

GraT74 : T. J. Gray, F. D. McDaniel and R. K. Gardner, Bull. Am. Phys. Soc. Vol.19, P.1107.

HanH64 : H. Hansen, H. Weigmann and A. Flammersfeld, Nucl.Phys. Vol.48, P.241.

HanH66 : H. Hansen and A. Flammersfeld, Nucl.Phys. Vol.79, P.135.

HanJ57 : J. M. Hansteen and S. Messelt, Nucl.Phys. Vol.2, P.526.

HanJ73 : J. S. Hansen, Phys.Rev. Vol.8, No.2, P.822.

HarR68 : R. R. Hart, N. T. Olson and H. P. Smith, Jr., J.Appl.Phys. Vol.39, P.5538.

HarR69 : R. R. Hart, F. W. Reuter, III, H. P. Smith, Jr. and J. M. Khan, Phys.Rev. Vol.179, P.4.

HarK73 : K. G. Harrison, H. Tawara and F. J. de Heer, Physica, Vol.66, P.16.

HarT73 : T. L. Hart and R. L. Watson, (Unpublished).

IshK74 : K. Ishi, S. Morita,H. Tawara, H. Kaji and T. Shiokawa, Phys.Rev. Vol.A10, P.774.

JanJ66 : J. F. Janni, Technical Report No.AFWL-TR-65-150, Air Force Weapons Lab., Research and Technology Div., Air Force Systems Command, Kirtland Air Force Base, New Mexico.

JakJ70 : J. M. Jaklevic and F. S. Goulding, University of California Research Laboratories Report UCRL - 20152.

JarO72 : O. N. Jarvis, C. Whitehead and M. Shah, Phys.Rev. Vol.A5, P.1198.

JohT70 : T. B. Johansson, R. Akselsson and S. A. F. Johansson, Nucl.Instr.Meth., Vol.84, P.141.

JohT72 : T. B. Johansson, R. Akselsson and S. A. E. Johansson, Advances in X-ray Analysis, Vol.15, P.373.

JolR71 : R. K. Jolly and H. B. White, Nucl.Instr. Methods, Vol.97, P.103.

JopR62 : R. C. Jopson, H. Mark and C. D. Swift, Phys.Rev. Vol.127, P.1612.

KeVI72 : Kevex Instruction Manual.

KhaG69 : Khandelewal, Choi, Merzbacher, Atomic data, Vol.1.

KhaJ64a: J. M. Khan and D. L. Potter, Phys.Rev. Vol.133, P.A890.

KhaJ64b: J. M. Khan, D. L. Potter and R. D. Worley, Phys.Rev. Vol.134, P.A316.

KhaJ64c: J. M. Khan, D. L. Potter and R. D. Worley, Phys.Rev. Vol.135, P.A511.

KhaJ64d: J. M. Khan, D. L. Potter and R. D. Worley, Phys.Rev. Vol.136, P.A108.

KhaJ65 : J. M. Khan, D. L. Potter and R. D. Worley, Phys.Rev. Vol.139, P.A1735.

KhaJ66a: J. M. Khan, D. L. Potter and R. D. Worley, Phys.Rev. Vol.145, P.2-3.

KhaJ66b: J. M. Khan, D. L. Potter, R. D. Worley and H. P. Smith,Jr., Phys.Rev. Vol.148, P.413.

KhaJ67 : J. M. Khan, D. L. Potter, R. D. Worley and H. P. Smith, Jr., Phys.Rev., Vol.163, P.87.

KheN75 : Najat A. Khelil and Tom J. Gray, Phys.Rev. Vol.A11, No.3, P.893.

KomP68 : P. Komarek, Acta.Phys. Augtr. Vol.27, P.369,

LarN62 : N. L. Lark, Bull.Am.Phys.Soc. Vol.7, P.623.

LeaR73 : R. Lear and Tom J. Gray, Phys.Rev.A. Vol.8, P.2469.

LewH53 : H. W. Lewis, B. E. Simmons and E. Mezbacher, Phys.Rev. Vol.91, P.943.

LewC72 : C. W. Lewis, R. L. Watson and J. B. Natowitz, Phys.Rev. Vol.A5, P.1773.

LieR73 : R. B. Liebert, T. Zabel, D. Miljanic, H. Larson, V. Valkovic, G. C. Phillips, Phys.Rev.A. Vol.8, No.5. P.2336-2341.

LinJ73 : J. Lin, J. L. Duggan and R. F. Carlton, Proc.In.Conf. Inner-Shell Ionization Phenomena, Vol.2, P.998, Conf-720404(USAEC).

MadD74 : Don H. Madison and E. Merzbacher, Private communication.

MadD74a: D. H. Madison, A. B. Baskin, C. E. Busch and S. M. Shafroth, Phys.Rev. Vol.A9, P.675.

ManN74 : N. F. Mangelson, K. K. Nielson, M. W. Hill, D. J. Eatough, L. D. Hansen, Proc. of the Conf. on Appl. of Small Accelerators, Denton, Texas, Oct. 21-23.

MarC67 : C. L. Marks, W. P. Saylor and A. A. Sterk, Proc. Second. Symp. Low-Energy X- and Gamma Sources and Appl., P.587 (USAEC report ORNL-IIC-10)

McGE71 : E. J. McGuire, Phys.Rev., Vol.A3, P.587.

McGJ73 : J. H. McGuire and P. Richard, Phys.Rev. Vol.A8, P.1374.

McCJ73 : J. D. McCoy, J. L. Duggan, E. L. Robinson, C. J. Cipolla, Nuclear Techniques in Basic Metal Industries, (Proc. Symp. Helsinki).

McKR75 : R. H. McKnight, S. T. Thornton and R. R. Karlowicz, Nucl.Instr. and Methods, Vol.123, P.1.

MerE58 : E. Merzbacher and H. W. Lewis, Handbook of Physics, Edited by S. Flügge (Springer, Berlin) Vol.34, P.166.

MesS58 : S. Messelt, Nucl.Phys., Vol.5, P.535.

MilR74 : R. H. Miller and J. R. Greening, J.Phys.B: Atom. Molec. Phys., Vol.7, No.17, P.2332.

MugA72 : A. H. F. Muggleton, Nucl.Instr. and Methods, Vol.101, P.113.

NeeP70a: P. B. Needham, Jr., and B. D. Sartwell, Phys.Rev. Vol.A2, P.27.

NeeP70b: P. B. Needham, Jr., and B. D. Sartwell, Phys.Rev. Vol.A2, P.1686.

NorL70 : L. C. Northcliffe and R. L. Schilling, Nuclear Data Tables, Vol.A7, P.233.

OgiW64 : W. T. Ogier, G. J. Lucas, J. S. Murray and T. E. Holzer, Phys.Rev. Vol.135, P.A1070.

OlsD73 : D. K. Olsen, C. Fred Moore and Patrick Richard, Phys.Rev.A. Vol.7, No.4. P.1244.

PerS73 : S. K. Perry and F. P. Brady, Nucl.Instr.Methods, Vol.108, P.389.

PetO36 : O. Peter, Annalen der Physik, Vol.5, P.299.

PooD68 : D. M. Poole and J. L. Shaw, Fifth International Congress on X-ray optics and eflicroanalysis, P.319-324, Springer-Verlag, Berlin.

RicP69 : P. Richard, I. L. Morgan, T. Furuta and D. Burch, Phys.Rev. Letters, Vol.23, P.1009.

RicP70 : P. Richard, T. I. Bonner, T. Furuta, I. L. Morgan and J. R. Rhodes, Phys.Rev. Vol.1A, P.1044.

RutC73 : C. H. Rutledge and R. L. Watson, Atomic Data and Nuclear Data Tables, Vol.12, P.195.

SarF70 : F. W. Saris and D. Onderdelindin, Physica, Vol.49, P.411.

ScoJ69 : J. H. Scofield, Phys. Rev. Vol. 179, P.9.

SelB69 : B. Sellers, F. A. Hanser and H. H. Wilson, Phys.Rev. Vol.182, P.90.

Shas73 : S. M. Shafroth, G. A. Bissinger and A. W. Waltner, Phys.Rev.A. Vol.7, P.566.

ShiK70 : K. Shima, M. Sakisaka, M. Kokado, T. Yamamato and I. Makino, Jap.J.App.Phys, Vol.9, P.1297.

ShiK71 : K. Shima, I. Makino and M. Sakisaka, J. Phys.Soc. Japan, Vol.30, P.611.

SinB57a: B. Singh, Phys.Rev. Vol.107, P.711.

SinB57b: B. Singh, Phys.Rev. Vol.108, P.1449.

SteA65 : A. A. Sterk, Advances in X-ray Analysis, Vol.8, P.189

SteA67 : A. A. Sterk, C. L. Marks and W. P. Saylor, Advances in X-ray Analysis, Vol.10, P.399.

StoN72 : N. Stotterfoht, Proc.Int.Conf. on Inner-Shell Ionization Phenomena, Vol.2, P.979, Conf-720404 (USAEC).

StoN73 : N. Stotterfoht, D. Schneider and K. G. Harrison, to be published.

StoE74 : E. Storm and H. I. Israel, Nuclear Data Tables, Vol.A7, P.566.

TawH74 : H. Tawara, K. Ishi, S. Morita, H. Kaji, C. N. Shu and T. Shiokawa, Phys.Rev. Vol.A9, P.1617.

TawH75 : H. Tawara, K. Iohi, S. Morita, H. Kaji, T. Shiokawa, Phys.Rev.A. Vol.11, No.5, P.1560.

TerM70 : M. Terasawa, T. Inouye and H. Kamei, J. Phy. Soc. Jap., Vol.29, P.1394.

TerM71 : M. Terasawa, T. Tamura and H. Kamada, VII ICPEAC Abstracts (North Holland Publishing Co. Amsterdam) P.410.

TerM72 : M. Terasawa, T. Tamura and H. Kamada, J. Phys. Soc. Jap., Vol.33, P.1420.

ThoJ74 : Jean Paul Thomas, L. Porte, J. Engerran, J. C. Viala, J. Tousset, Nucl.Instr.Methods, Vol.117, P.579.

TobL72a: L. H. Toburen, Phys.Rev. Vol.A5, P.2482.

TobL72b: L. H. Toburen, Proc.Inst.Conf. on Inner-Shell Ionisation Phenomena, Vol.2, P.979. Conf-720404 (USAEC).

UrbJ55 : J. Urbanec and C. Simone, Czech.J.Phys. Vol.5, P.40.

ValV74 : V. Valkovic, R. B. Liebert, T. Zabel, H. T. Larson, D. Miljanic, R. M. Wheeler and G. C. Phillips, Nucl.Instr.Methods, Vol.114, P.573.

VerJ71 : J. W. Verba, J. W. Sunier, B. T. Wright, I. Slaus, A. B. Holman, J. G. Kulleck, Chemical Analysis by charged particle Bombardment, Namur, Belgium.

VriL69 : L. Vriens, Case Studies in Atomic Collision Physics 1, E. W. McDanniel and M. R. C. McDowell, North Holland (Amsterdam).

WalR74 : R. L. Walters, R. D. Willis, W. F. Gutnecht, J. M. Joyce, Analytical Chemistry, Vol.117, P.579.

WatR70 : R. L. Watson, C. W. Lewis and J. B. Natowitz, Nucl.Phys., Vol.A154, P.561.

WatR73 : R. L. Watson and L. H. Toburen (Rutledge compilation).

WeaD74 : D. R. Weaver, Birmingham Radiation Centre, U.K.Publication, Report No.74-01.

WegW73 : W. F. Van der Weg, W. H. Kool, H. E. Rosendaal, F. W. Saris, Rad.Eff. Vol.17, P.245.

WheR74 : R. M. Wheeler, R. P. Chaturvedi and A. R. Zander, (Personal Communication).

WilC67 : C. F. Williamson, J. P. Boujot and J. Picard, Tables of Range and Stopping power of chemical elements for charged particles of energy 0.05 to 500 MeV, No.CEA-R3042, C.E.A. Saclay,France.

WinL73 : L. M. Winters, J. R. MacDonald, M. D. Brown, L. D. Elsworth and T. Chiao, Phys.Rev. Vol. A7, P.1276.

WolR73 : R. Woldseth, Kevex Corporation, Burlingame, California.